KEY TECHNOLOGIES FOR ADVANCED CELLULAR BASE STATION ANTENNAS

Haihan Sun
Faculty of Engineering and Information Technology
University of Technology Sydney

A thesis submitted for the degree of
Doctor of Philosophy

May 2019

Certification of Original Authorship

I, Haihan Sun, declare that this thesis, is submitted in fulfilment of the requirements for the award of Doctor of Philosophy, in the Faculty of Engineering and Information Technology at the University of Technology Sydney.

This thesis is wholly my own work unless otherwise reference or acknowledged. In addition, I certify that all information sources and literature used are indicated in the thesis.

This document has not been submitted for qualifications at any other academic institution.

This research is supported by the Australian Government Research Training Program.

Production Note:
Signature: Signature removed prior to publication.
Date: 27 May 2019

Acknowledgements

First of all, I would like to express my deepest gratitude to my supervisor Prof. Yingjie Jay Guo for his continuous guidance and support throughout my PhD study. Prof. Guo has provided me with an excellent research environment and has given me insightful advice and innovative ideas for my research projects. His profound knowledge of antennas and wireless communications, insight into academic frontiers, and rigorous academic attitude have deeply inspired and influenced me.

I am profoundly grateful to Prof. Bevan Jones for providing me with industrial guidance. He led me into the field of base station antennas and taught me how to combine scientific knowledge with industrial realizations. I am greatly inspired by his deep insights into technical issues. I would not have been able to carry out some industrial-orientated projects without his guidance.

I would like to thank my co-supervisor Dr. Can Ding and my collaborator Dr. He Zhu for their valuable suggestions on this work, support with testing and experiments, and advice on papers and thesis writing.

I would like to thank Prof. Trevor Bird and Prof. Richard W. Ziolkowski for their support and encouragement during my PhD study. Their dedication to scientific research inspires our young researchers greatly. I would like to thank Prof. Zheng Li for his valuable suggestions on my work. My sincere thanks also go to Dr. Pei-Yuan Qin, Dr. Wei Lin, Prof. Yanhui Liu, Prof. Jianquan Huang, and fellow doctoral students at Global Big Data Technologies Centre (GBDTC), especially Mr. Shulin Chen, Mr. Tianyu Yang, Miss Lizhao Song, Mr. Jiwei Lian, and Miss Xuan Wang, for their kind help and support.

In addition, I would like to thank my friends who have brought joy to my life. Those thanks especially go to Miss Marie Joshua Tapas, Miss Tomoyo Moriwaki, Miss Chao Lan, Miss Yang Qian, Miss Jiayi Shi, Mr Wei Huang, Dr. Kireesan Sornalingam, Mr Ye Shi, and Mr Henry Cheung.

Last but not least, I would like to express my forever thanks to my parents for their unconditional love, unreserved support and encouragement throughout my life.

List of Publications

Peer-Reviewed Journal Papers

1. **H. Sun**, C. Ding, B. Jones, and Y. J. Guo, "A wideband base station antenna element with stable radiation pattern and reduced beam squint," *IEEE Access*, vol. 5, pp. 23022 – 23031, 2017.
2. **H. Sun**, H. Zhu, C. Ding, and Y. J. Guo, "Wideband planarized dual-linearly-polarized dipole antenna and its integration for dual-circularly-polarized radiation," *IEEE Antennas and Wireless Propagation Letters*, vol. 17, pp. 2289 – 2293, Dec. 2018.
3. **H. Sun**, C. Ding, H. Zhu, B. Jones, and Y. J. Guo, "Suppression of cross-band scattering in multiband antenna arrays," *IEEE Transactions on Antennas and Propagation*, vol. 67, pp. 2379 - 2389, Jan. 2019.
4. C. Ding, **H. Sun**, R. W. Ziolkowski, and Y. J. Guo, "Simplified tightly-coupled cross-dipole arrangement for base station applications," *IEEE Access*, vol. 5, pp. 27491 – 27503, 2017.
5. T. S. Bird, V. Lingasamy, K. T. Selvan, and **H. Sun**, "Improved finite-range gain formula for open-ended rectangular waveguides and pyramidal horns," *IET Microwaves, Antenna & Propagation*, vol. 14, issue 14, pp. 2054 – 2058, 2017.
6. C. Ding, **H. Sun**, R. W. Ziolkowski, and Y. J. Guo, "A dual-layered loop array antenna for base stations with enhanced cross-polarization discrimination (XPD)," *IEEE Transactions on Antennas and Propagation*, vol. 66, pp. 6975 - 6985, Dec. 2018.
7. H. Zhu, **H. Sun**, B. Jones, C. Ding, and Y. J. Guo, "Wideband dual-polarized multiple beam-forming antenna arrays," *IEEE Transactions on Antennas and Propagation*, vol. 67, pp. 1590 – 1604, Dec. 2018.
8. **H. Sun**, H. Zhu, C. Ding, B. Jones, and Y. J. Guo, "Choking techniques for scattering suppression in multi-band base station antenna arrays," *IEEE Transactions on Antennas and Propagation*. (Under review)
9. **H. Sun**, B. Jones, C. Ding, and Y. J. Guo, "A method to enhance the bandwidth and reduce the size of dual-polarized antennas," *IEEE Transactions on Antennas and Propagation*. (Under review)

Peer-Reviewed Conference Papers

1. **H. Sun**, C. Ding, Y. J. Guo, and R. Mittra, "A wideband dipole antenna based on a non-uniformly segmented structure," *European Conference on Antennas and Propagation (EuCAP)*, 2017.
2. **H. Sun,** C. Ding, T. Yang, Y. J. Guo, and P. Q, "A wideband base station antenna with stable radiation pattern," *Australian Microwave Symposium (AMS)*, ***Best Student Paper***, 2018.
3. **H. Sun**, C. Ding, and Y. J. Guo, "A novel dual-polarized planar antenna," *IEEE International Symposium on Antennas and Propagation (APS)*, ***Honourable Mention in Student Paper Competition***, 2018.
4. **H. Sun**, C. Ding, and Y. J. Guo, "A wideband base station antenna with reduced beam squint," *European Conference on Antenna and Propagation (EuCAP)*, 2018.
5. **H. Sun**, C. Ding, T. S. Bird, and Y. J. Guo, "A base station antenna element with simple structure but excellent performance," *Australian Microwave Symposium (AMS)*, 2018.
6. **H. Sun**, C. Ding, H. Zhu, B. Jones, and Y. J. Guo, "Suppression of cross-band scattering in multi-band base station antenna arrays," *Australian Symposium on Antennas (ASA)*, ***Student Prize for Best Oral Presentation***, 2019.
7. C. Ding, **H. Sun**, Y. J. Guo, P. Qin, and Y. Yang, "Beamwidth control of base station antennas employing reflectors and directors," *International Symposium on Antennas and Propagation (ISAP)*, 2015.
8. D. Guan, C. Ding, **H. Sun**, and F. Yuan, "Wide-band SIW cavity-backed circular polarized array antennas with sequential rotation technique," *International Conference on Electromagnetics in Advanced Applications (ICEAA)*, 2016.
9. C. Ding, B. Jones, **H. Sun**, P. Y. Qin, Y. J. Guo, and L. Ji, "Wideband feeding method for full-wave dipole," *2017 IEEE International Symposium on Antennas and Propagation (APS)*, 2017.
10. C. Ding, **H. Sun**, Y. J. Guo, and R. W. Ziolkowski, "A general design and optimization method of tightly-coupled cross-dipoles for base station," *European Conference on Antenna and Propagation (EuCAP)*, 2018.

To my parents

Table of Contents

Acknowledgements ..... **II**
List of Publications ..... **III**
Table of Contents ..... **VI**
List of Figures ..... **IX**
List of Tables ..... **XX**
List of Abbreviations ..... **XXI**
Abstract ..... **XXII**
Chapter 1: Introduction **1**
1.1 Background 1
1.1.1 Cells 1
1.1.2 Antenna Beams 2
1.1.3 Phased Array 5
1.1.4 Diversity Systems 8
1.1.5 Antenna Bands 8
1.1.6 Specifications of Cellular BSAs 9
1.2 Motivation and Contribution 9
1.2.1 Motivation 9
1.2.2 Original Contribution 10
1.3 Thesis Outline 11
Chapter 2: Literature Review **15**
2.1 Dual-Polarized Antenna Elements 15
2.2 Multi-Band Antenna Arrays 22
2.3 Butler Matrix Beam-Forming Networks 25
Chapter 3: Square-Dipole-Array Antennas **29**
3.1 Introduction 29
3.2 Square-Folded-Dipole-Array Antenna 29
3.2.1 Antenna Configuration 29
3.2.2 Working Principle 30
3.2.3 Feed Network 35
3.2.4 Experimental Results 41
3.3 Simplified Square-Dipole-Array Antenna 44
3.3.1 Antenna Configuration 44
3.3.2 Analysis and Optimization 46

3.3.3 Experimental Results 49
3.4 Comparison 51
3.5 Summary 52
Chapter 4: Cross-Dipole Antennas 53
4.1 Introduction 53
4.2 Simplified Tightly-Coupled Cross-Dipole Antenna 54
4.2.1 Model Description 54
4.2.2 Coupling Analysis 55
4.2.3 Design Methodology 60
4.2.4 Antenna Design 69
4.3 Bandwidth Enhancement of Cross-Dipole Antennas 74
4.3.1 Antenna I: Loop-Connected Isolated Cross-Dipole Element 74
4.3.2 Antenna II: Loop-Connected Tightly-Coupled Cross-Dipole Element 81
4.3.3 Comparison 86
4.4 Summary 87
Chapter 5: Dual-Dipole Antennas 89
5.1 Introduction 89
5.2 Working Mechanism of the Dual-Dipole Radiators 90
5.3 Three-Layer Planarized Dual-Dipole Antenna 92
5.3.1 Antenna Configuration 92
5.3.2 Feed Network 93
5.3.3 Experimental Results 95
5.4 Two-layer Planarized Dual-Dipole Antenna 97
5.4.1 Antenna Configuration 97
5.4.2 Experimental Results 99
5.5 The Integration of Planarized Dual-Dipole Antennas 101
5.5.1 Configuration of the Wideband Coupler 102
5.5.2 Configuration of the Integrated Dual-CP Antenna 104
5.5.3 Experimental Results 106
5.6 Summary 109
Chapter 6: Multi-Band Base Station Antenna Arrays 111
6.1 Introduction 111
6.2 Statement of Cross-band Scattering Problem 111
6.3 Choking Techniques to Suppress Cross-Band Scattering 114
6.3.1 Choke 1: The Spirals 115

6.3.2 Choke 2: The Coaxial Chokes 118
6.3.3 Choke 3: The Stripline Chokes 121
6.3.4 Discussion 123
6.4 Application I: Interleaved 3G and 4G Base Station Antenna Array 124
6.4.1 Design of Stripline-Choked LB Element 125
6.4.2 Experimental Results 137
6.5 Application II: Interleaved 4G and 5G Base Station Antenna Array 141
6.5.1 Design of Spiral LB Element 142
6.5.2 Experimental Results 146
6.6 Summary 152
Chapter 7: Multi-Beam Base Station Antenna Arrays 153
7.1 Introduction 153
7.2 Beam-Forming Antenna Array System 154
7.3 Wideband Beam-Forming Network 156
7.3.1 Three-Beam Butler Matrix 157
7.3.2 Wideband Power Dividers 169
7.4 Beam-Forming Arrays 172
7.4.1 Configuration and Performance of the Radiating Element 173
7.4.2 Configuration of Beam-Forming Arrays 175
7.4.3 Experimental Results 176
7.5 Summary 180
Chapter 8: Conclusion and Future Work 181
8.1 Conclusion 181
8.2 Future Work 183
References 185

List of Figures

Figure 1.1 Configuration of a typical base station array [2]. 1
Figure 1.2 Three-sector cell plan. 2
Figure 1.3 Cross-dipole with reflector for azimuth pattern forming. 2
Figure 1.4 (a) Illustration of coverage of mechanical tilt [3], and (b) horizontal radiation pattern with different downtilt angles of mechanical tilt. 3
Figure 1.5 (a) Illustration of coverage of electrical tilt [3], and (b) horizontal radiation pattern with different downtilt angles of electrical tilt. 4
Figure 1.6 Contour of the normalized radiation pattern of a cross-dipole placed above a ground plane. 4
Figure 1.7 Arrangement of N-element linear array. 5
Figure 1.8 Field patterns with (a) N = 4, and (b) N = 8. 6
Figure 1.9 Field pattern with electrical downtilt of 10°. 6
Figure 1.10 Field patterns with (a) uniform amplitude distribution, and (b) sinusoidal amplitude distribution. 7
Figure 1.11 Field patterns with (a) $d = 0.5\lambda$, and (b) $d = 1.5\lambda$. 7
Figure 2.1 Configurations of dual-polarized patch antennas reported in the literatures (a) [8], and (b) [10]. 16
Figure 2.2 Configurations of dual-polarized cross-dipole antennas reported in the literatures (a) [13], (b) [15], (c) [16], and (d) [17]. 17
Figure 2.3 Configurations of dual-polarized ME-dipole antennas reported in the literatures (a) [31], and (b) [34]. 18
Figure 2.4 Configurations of dual-polarized square-dipole-array antennas reported in the literatures (a) [38], and (b) [39]. 19
Figure 2.5 Configurations of dual-polarized slot antennas reported in the literatures (a) [42], (b) [44], and (c) [49]. 20
Figure 2.6 Configurations of dual-dipole antennas reported in the literatures (a) [51], (b) [52], (c) [53], and (d) [54]. 21
Figure 2.7 Configurations of dual-band antenna elements reported in the literatures (a) [57], and (b) [58]. 22

Figure 2.8 Different base station antenna array schemes: (a) Up-and-down scheme, (b) embedded scheme, and interleaved schemes with (c) one HB columns and one LB column and (d) two HB columns and one LB column. 24
Figure 2.9 Schematic for the beam-forming arrays. 26
Figure 2.10 Butler matrix designs using microstrip lines [77], striplines [78] and CPW [79]. 27
Figure 3.1 (a) Perspective view of the proposed antenna, and (b) top view of the aperture. 30
Figure 3.2 (a) Configuration of the radiator without feed network, and (b) the current distribution on the radiator at 2.2 GHz. 31
Figure 3.3 (a) The simulated and (b) the calculated HPBW variations of HP, VP, −45°-polarized patterns of the element in the horizontal plane with an infinite ground plane. 31
Figure 3.4 The variation of co-polar HPBWs across the band with (a) different distance D between the folded dipole elements, (b) different antenna height H, and (c) different widths W of ground plane. 33
Figure 3.5 The HP, VP and co-polar HPBWs of the antenna element placed on a ground plane of width 170 mm. 34
Figure 3.6 Current distribution illustration of (a) a cross-dipole, and (b) the four folded dipole elements; contour plot of beam of (c) a cross-dipole, and (d) the four folded dipole elements in u-v coordinates. 34
Figure 3.7 (a) Feed method, and (b) the equivalent circuit model of the impedance. 36
Figure 3.8 Input impedance of the folded dipole elements (Z) on the Z-Smith for parameters (a) D, (b) H, (c) OP, (d) IP. 37
Figure 3.9 Configuration of the matching circuit. 38
Figure 3.10 Calculated $|S_{11}|$ of the matching circuit model. 38
Figure 3.11 The impedance of (a) the folded dipole input, (b) the folded dipole input and the line transformer I, (c) the folded dipole input, line transformer I, and balun, (d) the folded dipole input, the line transformer I, balun, and line transformer II on the Smith chart from 1.60GHz to 2.80 GHz. 39
Figure 3.12 Realization of the matching circuit. (a) Top view of antenna aperture, and perspective views of the feed network for (b) +45° polarization, and (c) −45° polarization. 40

Figure 3.13 (a) Front view, and (b) side view of the prototype of the proposed antenna. 41
Figure 3.14 Simulated and measured S-parameters. 42
Figure 3.15 Simulated and measured radiation patterns in the horizontal plane at (a) 1.7 GHz, (b) 2.2 GHz, and (c) 2.7 GHz. 42
Figure 3.16 Simulated and measured HPBWs and gains. 43
Figure 3.17 Simulated and measured beam squint at 10° down-tilt. 43
Figure 3.18 Antenna configuration: (a) perspective view; (b) top view; (c) detached view of balun A; (d) detached view of balun B. 45
Figure 3.19 (a) Schematic current distribution and (b) equivalent circuit model of the concentrically arrange dipoles without feed network. 46
Figure 3.20 Variation of the (a) real and (b) imaginary parts of the antenna input impedance with different W_g. 47
Figure 3.21 Variation of the (a) real and (b) imaginary parts of the antenna input impedance with different L_g. 47
Figure 3.22 Simulated (a) HPBW (b) cross-polarization level within main lobe with optimized gap size. 48
Figure 3.23 Equivalent circuit and the physical implementation of the antenna feed network. (Optimized values for circuit elements: TL_M: 250 Ω, 8.3 mm; LL: 100 Ω, 6.6 mm; SL: 416.7 Ω, 50.7 mm; OL: 113.6 Ω, 20.5 mm; TL: 91.77 Ω, 23.2 mm.) 49
Figure 3.24 The calculated, simulated and measured S-parameters of the antenna. 49
Figure 3.25 Prototype of the antenna. 50
Figure 3.26 Simulated and measured radiation patterns. (a) 1.7 GHz, (b) 2.2 GHz, and (c) 2.7 GHz. 50
Figure 3.27 Simulated and measured HPBW and gain. 51
Figure 4.1 Cross-dipole geometry. (a) Model-A: tightly-coupled cross-dipoles consisting of a driven dipole and a parasitic dipole. (b) Model-B: driven dipole only. 54
Figure 4.2 Variations of the impedance of Model-A and Model-B in the target band. (a) Resistance. (b) Reactance. 55
Figure 4.3 Current distributions on the traces of the models. (a) Model-A. (b) Model-B. 56

Figure 4.4 Simulated currents. (a) Current magnitudes on the middle branches of Model-A and Model-B. (b) Current magnitudes on the side branches of Model-A and Model-B. (c) Current phases on three different branches of Model-A. 57
Figure 4.5 3D radiation pattern of the proposed tightly-coupled cross-dipole. 58
Figure 4.6 Comparison of *x*- and *y*-aligned radiation patterns of Model-A and Model-B. 60
Figure 4.7 Representation of the current distributions. (a) Schematic for the tightly-coupled cross-dipole antenna. (b) Equivalent six-element dipole array for model-A. (c) Reduced, equivalent three-element dipole array model. 61
Figure 4.8 Simulated radiation patterns. (a) E-plane pattern and (b) H-plane pattern of a single half-wavelength dipole placed a quarter-wavelength above an infinite ground plane and oriented parallel to it. (c) Three-element array factor pattern alone. (d) Model-A-based cross-dipole radiation pattern. 64
Figure 4.9 Revised and simplified cross-dipole configuration. 65
Figure 4.10 HPBW plotted on the Z-Smith diagram for the parameters: (a) L, (b) s, (c) W, (d) W', (e) h, and (f) G. 66
Figure 4.11 Input impedance plotted on the Z-Smith diagram for the parameters: (a) L, (b) s, (c) W, (d) W', (e) h, and (f) G. 67
Figure 4.12 Optimized simplified cross-dipole antenna. (a) Perspective view. (b) Details of the two feed networks implemented using PCBs. (c) Circuit theory model of the matching circuit. 70
Figure 4.13 Photos of the antenna and measurement system. (a) Fabricated and assembled antenna prototype. (b) Mounting the antenna. (c) Antenna under test (AUT). 71
Figure 4.14 Simulated and measured reflection coefficients of the two ports. 72
Figure 4.15 Simulated and measured co- and cross-polarization radiation patterns at (a) 1.7, (b) 2.2, and (c) 2.7 GHz. 73
Figure 4.16 Simulated and measured HPBW for the two polarizations across the target band. 73
Figure 4.17 Configuration of the radiator of the loop-loaded isolated cross-dipole. 74
Figure 4.18 (a) Design procedure of the loop-connected radiator. (b) Impedance of radiators at different steps from 1.65 GHz to 2.75 GHz in Smith Chart. 75

Figure 4.19 (a) Circuit model of a practical feed network for dipole, (b) matching results for Models B and E. 77
Figure 4.20 Current distribution at 2.2 GHz on the loop-loaded isolated cross-dipole radiator. 77
Figure 4.21 Impedance of the radiator from 1.7 GHz to 2.7 GHz with different values of (a) LD, (b) WD, (c) LL, (d) WL, and (e) G. 78
Figure 4.22 (a) Perspective view of the antenna I. Plots of (b) balun 1, and (c) balun 2. (d) Fabricated prototype of the antenna I. 79
Figure 4.23 Simulated and measured S-parameters of antenna I. 80
Figure 4.24 Horizontal radiation patterns of +45°-polarized radiation of antenna I at (a) 1.7 GHz, (b) 2.2 GHz, and (c) 2.7 GHz. 81
Figure 4.25 Simulated and measured HPBW and realized gain of the antenna I. 81
Figure 4.26 Radiator of loop-loaded tightly-coupled cross-dipoles. (R = 14.4 mm, A = 83.6°, L= 28 mm, W= 0.8 mm, and G = 0.56 mm) 82
Figure 4.27 (a) Design procedure of radiator. (b) Impedance of radiators at different steps from 1.7 GHz to 3.2 GHz in Smith Chart. (c) Matching results for Models F and G using circuit in Figure 4.19(a). 83
Figure 4.28 Influence of length of loop *L* to the radiator's impedance. 83
Figure 4.29 (a) Perspective view of the antenna II. Plots of (b) balun 3, and (c) balun 4. (d) Fabricated prototype of the antenna II. 84
Figure 4.30 S-parameters of loop-loaded tightly-coupled cross-dipole. 85
Figure 4.31 Radiation patterns of the loop-loaded tightly-coupled cross-dipole at (a) 1.7 GHz, (b) 2.2 GHz, (c) 2.7 GHz, and (d) 3.2 GHz. 85
Figure 4.32 (a) HPBW, and (b) gain of the loop-loaded tightly-coupled cross-dipole... 86
Figure 5.1 (a) Traditional, and (b) new configurations of communication systems consisting antennas and RF modules. 89
Figure 5.2 (a) Configurations of the radiators; and (b) the simulated current distribution when excite dipole 1 and 2. 91
Figure 5.3 Comparison of the calculated HPBWs from the mathematic models of the one dipole and two dipoles configurations, and the simulated HPBWs of the actual antenna with four dipoles. 92
Figure 5.4 Antenna configuration: (a) Perspective view; Top views of the (b) top, (c) middle, and (d) bottom metallic layers. 93

Figure 5.5 Circuit representation of the feed network. 94
Figure 5.6 SWR results of the circuit model and physical model..... 94
Figure 5.7 Physical realization model. 94
Figure 5.8 Prototype of the three-layer planarized dual-LP antenna. 96
Figure 5.9 Circuit matching results, and the simulated and measured S parameters. 96
Figure 5.10 Simulated and measured radiation patterns. (a) 1.7 GHz, (b) 2.2 GHz, (c) 2.7 GHz. 97
Figure 5.11 Simulated and measured HPBWs and gains. 97
Figure 5.12 Configuration of the wideband ±45°-polarized antenna. 98
Figure 5.13 (a) Equivalent circuit, and (b) physical realization of the feed network. 98
Figure 5.14 Simulated reflection coefficients of the antenna with ideal circuit feed network and its physical realization. 99
Figure 5.15 Prototype of the dual-linearly polarized antenna. 99
Figure 5.16 Simulated and measured S parameters. 100
Figure 5.17 Simulated and measured radiation patterns. (a) 1.7 GHz, (b) 2.2 GHz, and (c) 2.7 GHz. 100
Figure 5.18 Simulated and measured HPBWs and gains. 101
Figure 5.19 (a) Circuit design and (b) the printed circuit board realization of the wideband coupler. 102
Figure 5.20 Simulated (a) magnitude of S_{11} and S_{21}, (b) magnitude of S_{31} and S_{41}, and (c) phases of S_{31} and S_{41} of the wideband coupler. 103
Figure 5.21 Configuration of the wideband dual-circularly-polarized antenna: (a) high-angle perspective view, (b) low-angle perspective view, and (c) detail view of the vertical coupler. 104
Figure 5.22 Current distribution on the coupler with (a) a traditional ground plane and (b) a defected ground plane, and (c) the resultant AR for the two cases. 106
Figure 5.23 Prototype of the dual-circularly polarized antenna: (a) top view, (b) side view, and (c) perspective view. 106
Figure 5.24 Simulated and measured reflection coefficients of the dual-circularly-polarized antenna. 107
Figure 5.25 Simulated and measured axial ratio of the dual-circularly-polarized antenna. 107

Figure 5.26 Simulated and measured radiation patterns of LHCP at (a) 1.5 GHz, (b) 2.2 GHz, and (c) 3.0 GHz. 108
Figure 5.27 Simulated and measured HPBWs and Gains of the dual-circularly-polarized antenna. 108
Figure 6.1 Configuration of the interleaved BSA array section: (a) top view, and (b) perspective view. 112
Figure 6.2 Simulated S-parameters for the LB and HB antennas when working alone. 113
Figure 6.3 Current distribution on the array section when HB array on the right column is excited. 113
Figure 6.4 Horizontal radiation patterns of the HB array i) without, and ii) with the unaltered LB element at (a) 1.7 GHz, (b) 1.8 GHz, and (c) 1.9 GHz. 114
Figure 6.5 One example of the choked radiator. 115
Figure 6.6 (a) Configuration of spiral structure. (b) Demonstration of spiral structure illuminated by plane wave. 116
Figure 6.7 Maximum induced current on the spiral structure with different (a) gap *g*, (b) inner diameter *d*, and (c) width of strip *w*. 117
Figure 6.8 Maximum induced current on the spiral structure resonating at 3.5 GHz with different combinations of parameters. 118
Figure 6.9 Configuration of coaxial chokes. 118
Figure 6.10 Maximum induced current on the arm with coaxial chokes with different (a) *l_choke*, (b) *d_in*, and (c) *d_out*. 120
Figure 6.11 Maximum induced current on the arm with coaxial chokes with resonant point at 3.5 GHz but with different combinations of parameters. 120
Figure 6.12 Configuration of choke 3 with conducting lines. 121
Figure 6.13 Maximum induced current on the radiator with conducting lines with different (a) *w*, (b) *h*, and (c) *s*. 122
Figure 6.14 . Magnitudes of the induced currents on the arm with stripline chokes with resonant point at 3.5 GHz but with different combinations of parameters: (a) different combination of *s* and *h* when fix *w*, and (b) different combination of *w* and *h* when fix *s* (unit: mm). 123
Figure 6.15 Dual-band dual-polarized base station antenna array configuration with interleaved scheme. 124

Figure 6.16 Circuit model of the choke. 125
Figure 6.17 (a) Top, and (b) side view of the realized choke. 126
Figure 6.18 (a) Model 1: a strip with a length of around $\lambda/2$ at 2.0 GHz (middle frequency at high band) and a width of 11 mm; Model 2: the strip in Model 1 cut in the middle and bridged with an inductive line. (b) Comparison of induced HB current on the strip in Model 1, and on the strip in Model 2 with different value of *l*. (c) Comparison of induced HB current on the strip in Model 1, and on the strip in Model 2 with different value of *g*. (d) Comparison of induced HB currents on the strip in Model 2 with optimized {*g, l*} values for open circuit point at 2.0 GHz. 128
Figure 6.19 (a) Model 3: a strip with a length of around $\lambda/2$ at 0.89 GHz (middle frequency at low band) and a width of 11 mm; Model 4: the strip in Model 3 cut in the middle and bridged with a choke. (b) Comparison of induced LB current on the strip in Model 3, and on the strip in Model 4 with different values of *w*. (c) Induced LB current on the strip in Model 4 with optimized {*g, l, w*} values for open circuit point at 2.0 GHz and short circuit point at 0.89 GHz. 129
Figure 6.20 (a) The LB dipole arms with different number of cuts. (b) Top view of the LB dipole arm with chokes inserted in. 131
Figure 6.21 (a) Model to determine effect of segment length *l_s* in free space illuminated by HB plane wave. (b) Maximum induced HB current on the segment with different *l_s*. 131
Figure 6.22 Configuration of optimized choked LB radiator. 132
Figure 6.23 The E-field cuts in the *zx*-plane under the circumstances of i) only HB array, ii) HB array with unaltered LB radiators, and iii) HB array with choked LB radiators. 133
Figure 6.24 Comparison of HB radiation patterns under the circumstances of i) only HB array, ii) HB array with unalthered LB radiators, and iii) HB array with choked LB radiators at (a) 1.7 GHz, (b) 1.9 GHz, (c) 2.1 GHz, and (d) 2.3 GHz. 133
Figure 6.25 (a) Perspective view of the choked LB antenna. Configurations of (b) balun 1, and (c) balun 2. (The baluns are printed on both sides of a substrate with a dielectric constant of 4.4, a loss tangent of 0.0025, and a thickness of 1.5 mm.) 135

Figure 6.26 S-parameters of the choked LB element and the unaltered LB element. .. 136
Figure 6.27 Radiation patterns of the choked LB element and the unaltered LB element at (a) 0.82 GHz, (b) 0.88 GHz, (c) 0.92 GHz, and (d) 0.96 GHz. 136
Figure 6.28 (a) Top, and (b) side views of the dual-band dual-polarized interleaved array. 137
Figure 6.29 Simulated and measured reflection coefficients of the HB array. 138
Figure 6.30 Simulated and measured radiation patterns of the HB array. (a) Port 1 at 1.7 GHz. (a) Port 2 at 1.7 GHz. (c) Port 1 at 2.0 GHz. (d) Port 2 at 2.0 GHz. (e) Port 1 at 2.3GHz. (f) Port 2 at 2.3 GHz. 139
Figure 6.31 Simulated and measured horizontal HPBW and realized gain of the HB array. 139
Figure 6.32 Simulated and measured S-parameters of the choked LB antenna..... 140
Figure 6.33 Simulated and measured radiation pattern of the choked LB antenna. (a) Port 1 at 0.82 GHz. (b) Port 2 at 0.82 GHz. (c) Port 1 at 0.88 GHz. (d) Port 2 at 0.88 GHz. (e) Port 1 at 0.96 GHz. (f) Port 2 at 0.96 GHz. 141
Figure 6.34 Simulated and measured HPBW and realized gain of the choked LB antenna. 141
Figure 6.35 (a) Configuration of spiral structure. (b) Current suppression capability at around 3.7 GHz. 142
Figure 6.36 Arrangement of the interleaved dual-band array with spiral LB radiators. 143
Figure 6.37 The E-field cuts in the *zx*-plane under the circumstances of i) only HB array, ii) HB array with unaltered LB radiators (dipole arm in strip form), and iii) HB array with spiral LB radiators. 143
Figure 6.38 Comparison of HB radiation pattern in the horizontal plane (*zx*-plane) under the circumstances of i) only HB array, ii) HB array with unaltered LB radiators, and iii) HB array with spiral LB radiators at (a) 3.3 GHz, (b) 3.4 GHz, (c) 3.6 GHz, (d) 3.7 GHz. 144
Figure 6.39 (a) Perspective view of the spiral LB antenna. (b) Configuration of two baluns for spiral LB antenna. 145
Figure 6.40 S-parameters of the spiral LB antenna. 146
Figure 6.41 Horizontal radiation patterns of spiral LB antenna at 1.7 GHz, 1.9 GHz, and 2.2 GHz. 146

Figure 6.42 (a) Perspective view of the dual-band antenna array model. (b) View of the feed network for the dual-band antenna array. (c) Front view, and (b) side view of the fabricated antenna array prototype. 147
Figure 6.43 (a) Simulated and (b) measured reflection coefficients for HB ports. (c) Simulated and (d) measured isolations between HB ports. 148
Figure 6.44 Normalized simulated and measured radiation patterns in the horizontal plane for the HB antennas. (a) Port 1 at 3.3 GHz, (b) port 2 at 3.3 GHz, (c) port 1 at 3.5 GHz, (d) port 2 at 3.5 GHz, (e) port 1 at 3.7 GHz, and (f) port 2 at 3.7 GHz. 149
Figure 6.45 (a) Simulated and (b) measured HPBW in the horizontal plane. (c) Simulated and (d) measured gain for the HB antennas in the two columns. 150
Figure 6.46 Simulated and measured S-parameters for the LB antenna. 150
Figure 6.47 Normalized simulated and measured radiation patterns in the horizontal plane for the LB antenna. (a) Port 5 at 1.7 GHz, (b) port 6 at 1.7 GHz, (c) port 5 at 1.9 GHz, (d) port 2 at 1.9 GHz, (e) port 1 at 2.2 GHz, and (f) port 2 at 2.2GHz. 151
Figure 6.48 Simulated and measured HPBW and gain for the LB antenna. 152
Figure 7.1 Configurations of two beam-forming arrays for LTE base stations: (a) using 5-element array; (b) using 6-element array. 155
Figure 7.2 Configuration of the proposed wideband three-beam Butler matrix for LTE base stations. 156
Figure 7.3 Equivalent transmission line models of two quadrature couplers: (a) traditional type; (2) tandem type. 159
Figure 7.4 Configuration of (a) Cross-sectional view of the stripline implementation used in the design of quadrature coupler; (b) 3D model of the constructed quadrature coupler. 161
Figure 7.5 Simulated reflection coefficients of the antenna with ideal circuit feed network and its physical realization. 162
Figure 7.6 Equivalent transmission line models of the wideband phase shifter: (a) phase shifter; (b) reference line. 163
Figure 7.7 3D model of the constructed phase shifter. 164
Figure 7.8 Synthesized and full-wave simulation results of the phase shifter: (a) S-parameters; (b) differential phase. 165

Figure 7.9 3D model of the proposed three-beam Butler matrix for LTE base stations. 166
Figure 7.10 Simulated S-parameters of the fabricated Butler matrix: (a) return loss and isolations; (b) transmission coefficients; (c) differential phases. 167
Figure 7.11 Photograph of the fabricated Butler matrix prototype. 168
Figure 7.12 Measured S-parameters of the fabricated Butler matrix: (a) return loss and isolations; (b) transmission coefficients; (c) differential phases. 169
Figure 7.13 Wideband Wilkinson dividers: (a) the printed circuit board realization; (b) equivalent circuit. 170
Figure 7.14 Simulated (a) magnitude of S_{11} and S_{21}, (b) magnitude of S_{31} and S_{41}, and (c) phases of S_{21} and S_{31} of the wideband power divider. 172
Figure 7.15 Configuration of (a) the ±45°-polarized antenna element; (b) radiator; (c) balun 1; and (d) balun 2. 173
Figure 7.16 Simulated S-parameters of the ±45°-polarized single antenna element. ... 174
Figure 7.17 Simulated radiation pattern at 1.8 GHz, 2.2 GHz, and 2.6 GHz for the ±45°-polarized antenna element. 174
Figure 7.18 Simulated HPBW and gain for the ±45°-polarized antenna element. 175
Figure 7.19 Configuration of (a) 5-element antenna array, and (b) 6-element antenna array. 176
Figure 7.20 The tested LTE beam-forming array including the beam-forming network and 6-element antenna array: (a) test environment; (b) overall structure. . 176
Figure 7.21 Measured return loss and isolation at input ports of two beam-forming arrays: (a) using 5-element array; (b) using 6-element array. 177
Figure 7.22 Simulated and measured radiation patterns at 1.8 GHz, 2.2 GHz, and 2.6 GHz for the 6-element antenna array fed by the beam-forming network: (a) beam 1 at 1.8 GHz; (b) beam 2 at 1.8 GHz; (c) beam 3 at 1.8 GHz; (d) beam 1 at 2.2 GHz; (e) beam 2 at 2.2 GHz; (f) beam 3 at 2.2 GHz; (g) beam 1 at 2.6 GHz; (h) beam 2 at 2.6 GHz; (i) beam 3 at 2.6 GHz. 178

List of Tables

Table 1.1 Frequency Bands, Short References, and Services 9
Table 2.1 Comparison of Wideband Butler Matrices 28
Table 3.1 Optimized Parameters of the Radiator 30
Table 3.2 Optimized Parameters for the Physical Implementation of the Matching Network 40
Table 3.3 Comparison of Antenna Performances 51
Table 4.1 Comparison of the Radiation Performance of Model-A and Model-B..... 56
Table 4.2 Optimized Dimensions of the Simplified Cross-dipole Antenna 65
Table 4.3 Optimized Dimensions of the Two Feed Networks..... 71
Table 4.4 Comparison of Antennas' Performances 86
Table 5.1 Optimized Parameters of the Matching Elements. 95
Table 5.2 Optimized Parameters of the Matching Elements 99
Table 5.3 Optimized Parameters for Coupler 103
Table 5.4 Comparison of Dual-CP Antennas' Performance..... 109
Table 6.1 SSBW of Spiral with Different Combinations of Parameters 118
Table 6.2 SSBW of Coaxial Chokes with Different Combinations of Parameters..... 120
Table 6.3 SSBW of Stripline Chokes with Different Parameter Combinations 123
Table 6.4 Optimized Parameters of the Choked Antenna..... 132
Table 6.5 Optimized Parameters of Baluns for the Choked Antenna 135
Table 7.1 Power and Phase Distribution on the 5-Element Array 155
Table 7.2 Power and Phase Distribution on the 6-Element Array 156
Table 7.3 Related Parameters of Two Quadrature Couplers 161
Table 7.4 Related Parameters of Two Power Dividers 172
Table 7.5 Optimized Parameters of the ±45°-polarized antenna element..... 174
Table 7.6 Overall Performance of the 6-element Array Fed By the Beam-Forming Network 179

List of Abbreviations

AR	Axial Ratio
BSA	Base Station Antenna
CP	Circularly-Polarized
GLL	Grating Lobe Level
FBR	Front-to-Back Ratio
HB	High Band
HPBW	Half-Power Beamwidth
ICD	Isolated Cross-Dipole
LB	Low Band
LHCP	Left-Handed Circular Polarization
LP	Linearly-Polarized
ME-dipole	Magneto-Electric Dipole
MIMO	Multiple-Input Multiple-Output
PDR	Power Division Ratio
RHCP	Right-Handed Circular Polarization
SLL	Side Lobe Level
TCCD	Tightly-Coupled Cross-Dipole
XPD	Cross Polarization Discrimination
3G	Third Generation of Cellular Mobile Communications
4G	Fourth Generation of Cellular Mobile Communications
5G	Fifth Generation of Cellular Mobile Communications

Abstract

Cellular base station antennas (BSAs) are critical components in mobile communication systems. As the cellular mobile communication systems evolve rapidly to the fifth generation (5G), BSAs that can simultaneously support different standards and have high data capacity are in high demand. Multi-band arrays and multi-beam arrays are good solutions, but they place additional stringent requirements on the antennas. Firstly, high performance characteristics of antenna elements are required. Secondly, cross-band scattering, which is a long-existing issue in multi-band antenna arrays, needs to be suppressed to maintain the performance and stability of antenna systems. Thirdly, for multi-beam antenna arrays, they are desired to have wide operating bandwidth and consistent patterns with low side-lobe levels. All of these are difficult to achieve. This thesis addresses the challenges mentioned above by making three main contributions.

The first contribution is the improvement of the base station antenna elements. Three configurations have been thoroughly studied, including square-dipole-array, cross-dipole and dual-dipole configurations. Different methods are investigated to enhance bandwidth, stabilize radiation patterns, or minimize beam squint, and the outcomes of these are implemented in antenna designs. In addition, circuit models of feed networks are proposed to facilitate wideband impedance matching. Two antennas featuring planarized configurations are designed for the ease of system integration. In total, eight antenna elements have been designed, fabricated and tested to achieve the desired wideband radiation performances.

The second contribution is the development of new approaches to minimize cross-band interference in multi-band BSA arrays. Chokes that can minimize scattering currents are implemented in the antenna designs. The working principles and capabilities of suppressing scattering of three different types of chokes are analyzed. Based on these techniques, two dual-band antenna arrays have been designed. Experimental results verify that cross-band scattering is suppressed and both arrays have stable radiation patterns across wide operating bandwidths. The techniques presented for suppressing cross-band scattering guarantee the co-existence of antennas for different services, and facilitate the evolution of communication standards.

The third contribution is the development of multi-beam antenna arrays to increase system capacity with a wide coverage area. Cross-dipoles with a compact configuration

and stable radiation performances are chosen as array elements. Wideband beam-forming networks formed by Butler matrices and power dividers are used to provide correct phase increments and power levels for elements. Three-beam antenna arrays have been designed with required beamwidth and crossover level. The proposed designs can be used in a wide range of LTE base stations to increase system capacity.

Chapter 1: Introduction

1.1 Background

Cellular base station antennas (BSA) are critical components in mobile communication systems. They provide a link between a base station and a mobile device and act as an essential tool for the control of frequency re-use and the optimization of channel capacity in a mobile radio network [1]. Their performance is directly related to the efficiency of communication networks. BSAs are typically mounted on tall towers or buildings to avoid obstacles between the phones and the cell tower, as shown in Figure 1.1 [2]. They have become a familiar feature in nearly every corner of the world. Concepts and specifications of antenna performance characteristics related to BSAs are presented as follows.

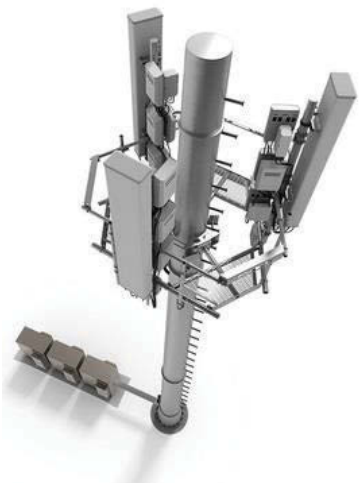

Figure 1.1 Configuration of a typical base station array [2].

1.1.1 Cells

A cellular radio cell is a geographical area that is served by the same radio resource. Cells' shape is directly related to the antennas' azimuth beamwidth and pointing direction. Typically, interlocking hexagons are used to represent cells, as shown in Figure 1.2. The circles in the diagram represent cell sites, where the base station towers and their antennas are located. Each cell site serves three cells, and each cell is served by a separate antenna. Therefore, three antennas with azimuth coverage of 120° are needed. Further

cell sites provide further radio coverage with sets of three cells. These cells together provide radio coverage over larger geographical areas.

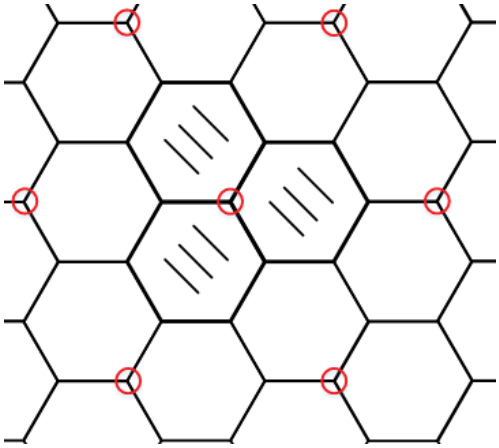

Figure 1.2 Three-sector cell plan.

In the areas of high traffic density, the capacity of the cell needs to be increased to meet demand. One solution is to split existing cells, allowing more new sites implemented and reducing the coverage radius of the original site.

1.1.2 Antenna Beams

An antenna beam can be characterized by its azimuth pattern and elevation pattern. For the three-sector cell plan, the azimuth pattern is required to provide 120° coverage (a 3 dB beamwidth of 65°, and a 10 dB beamwidth of 120°), and the elevation pattern is expected to cover 5°-15°. Therefore, a BSA typically comprises a vertical array of radiating elements to achieve desired antenna beams.

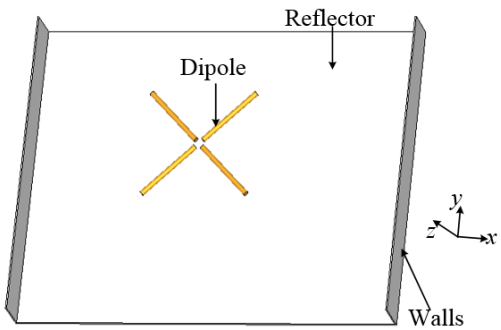

Figure 1.3 Cross-dipole with reflector for azimuth pattern forming.

The azimuth radiation pattern is determined by the design of individual antenna

elements. A typical base station antenna element is shown in Figure 1.3, which is formed by two half-wavelength dipoles crossing each other and backed by a reflector with a distance of half wavelength. The width of the reflector is about one wavelength. The surrounding walls are sometimes adopted to reduce back lobe level. For this configuration, the 3 dB and 10 dB beamwidths are around 65° and 120°, respectively.

The vertical beam normally covers 5°-15° as elevation coverage is only needed over a limited region below the horizon. It is usually directed slightly downwards to limit cell size, increase capacity within the intended coverage area and reduce interference with neighboring cells [1]. This phenomenon is known as beamtilt of the BSA. The beamtilt angle is normally in the range of 0-10°. Beamtilt is realized by two methods, namely mechanical tilt and electrical tilt.

The **mechanical tilt** is realized by physically or manually downtilting the BSA. This method is of limited use as it introduces undesirable pattern distortion. As depicted in Figure 1.4(a), with mechanical tilt, the front part is tilted downward while the back part is tilted upward, which gives rise to the unwanted inter-sector interference. As shown in Figure 1.4(b), mechanical tilt cannot provide consistent coverage reduction in all horizontal directions. The coverage is reduced more in the boresight and less at other directions, and the horizontal half-power beamwidth (HPBW) increases with a rising downtilt angle.

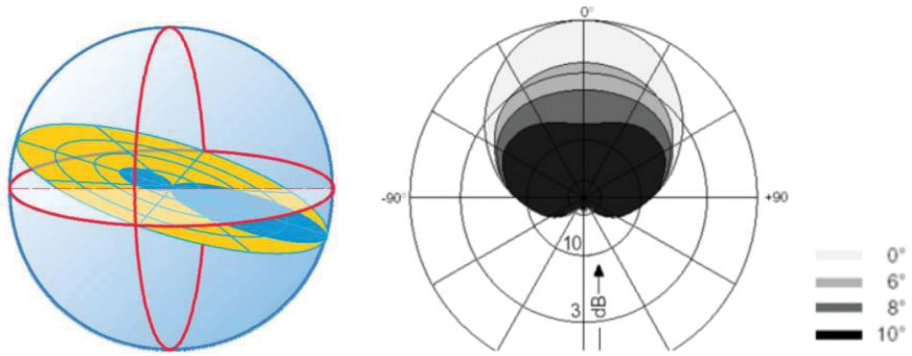

(a) (b)

Figure 1.4 (a) Illustration of coverage of mechanical tilt [3], and (b) horizontal radiation pattern with different downtilt angles of mechanical tilt.

The **electrical tilt** is realized by manipulating phases of the array elements using phase shifters. By introducing different progressive phase shifts to array elements, the beam of the array can be tilted to different directions. As shown in Figure 1.5, electrical downtilt

brings all the beams downward from the horizon, and have same coverage reduction in all horizontal directions. Nowadays, the electrical tilt can be remotely controlled by using actuators to drive phase shifters, which greatly facilitate the adjustment of antenna tilting beams.

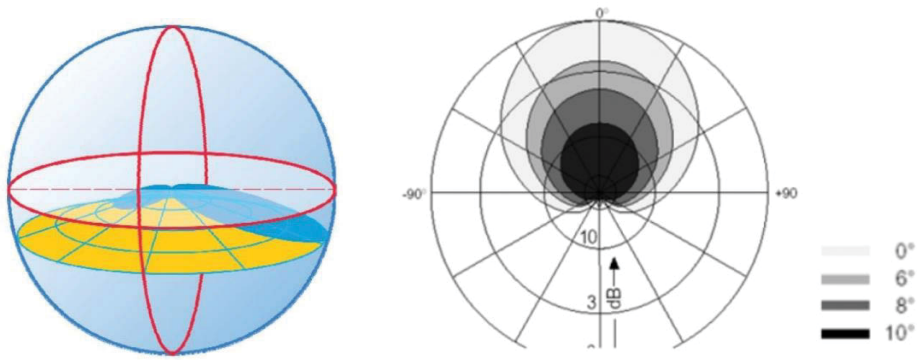

(a) (b)

Figure 1.5 (a) Illustration of coverage of electrical tilt [3], and (b) horizontal radiation pattern with different downtilt angles of electrical tilt.

Electrical beamtilt usually uses phased array technologies. The elevation beam characteristics are directly related to the number of array elements, the distance between elements, and the magnitude and phase distributions for each array element. The characteristics of a phased array will be detailed in 1.1.3.

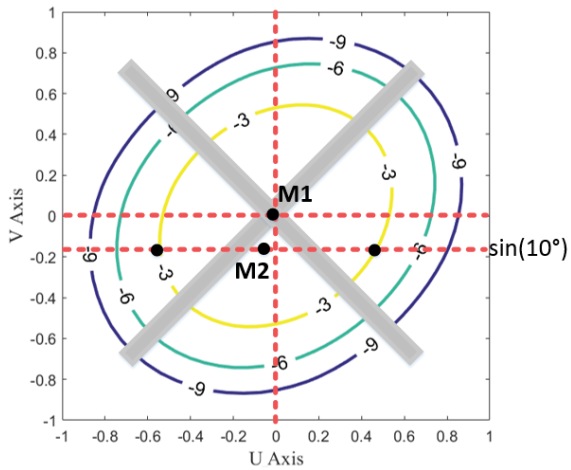

Figure 1.6 Contour of the normalized radiation pattern of a cross-dipole placed above a ground plane.

Beam squint is a parameter that measures the difference between the mechanical boresight and the azimuth beam pointing angle of the antenna in the horizontal direction,

representing the symmetry of the main beam. Elliptical beam shape of array elements is the main source of squint. For a simple dipole, it has the characteristic that the beamwidth in the E-plane is substantially narrower than that in the H-plane. When used in an array, this leads to problems of unbalanced grating lobes and squint when the beam is tilted. As an example, Figure 1.6 shows a contour plot of the radiation pattern of a cross-dipole in u-v coordinates ($u = \sin\theta\cos\phi, v = \sin\theta\sin\phi$). Without down-tilt, the beam peak (M1) is in the direction of the mechanical boresight. With a down-tilt angle of 10°, the beam peak (M2) shifts away from the mechanical boresight, thus resulting in a squint. The beam of the orthogonal polarization moves in the opposite direction which leads to different coverage for the two polarizations and degradation in multiple-input and multiple-output (MIMO) performance. In the cellular industry, the beam squint of a base station antenna array is typically required to be less than 5° for a down-tilt range from 0 to 10°.

1.1.3 Phased Array

The gain of a BSA is typically many times larger than that provided by a single radiating element, so it is necessary to use antenna arrays to achieve the required gain and pattern characteristics. Phased arrays are particularly suitable for the beamforming. By controlling the magnitude and phase difference between the antenna elements, the characteristics such as beam pointing direction, beamwidth, side lobe and grating lobe levels can be adjusted.

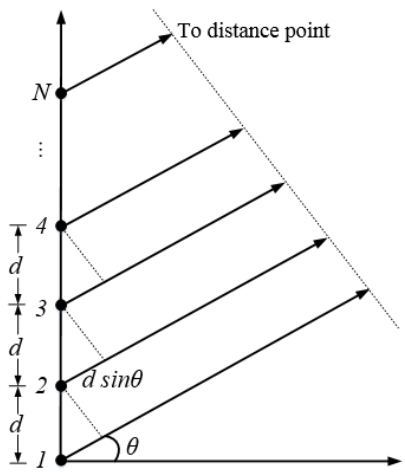

Figure 1.7 Arrangement of N-element linear array.

An N-element linear phased array with isotropic sources shown in Figure 1.7 is used to illustrate the characteristics of the phased array. The distance between neighboring elements is d. The amplitude for element i is a_i. Each following element has a progressive phase of δ. If we take the first element as the reference for phase, then at a distance point, the signal from the element i is advanced by $(i-1)(\beta d \sin\theta + \delta)$, where $\beta = \frac{2\pi}{\lambda}$. The field pattern at far field can be expressed as

$$F = \sum_{i=1}^{N} a_i e^{j(i-1)(\beta d \sin\theta + \delta)} \tag{1.1}$$

The beam characteristics such as beamwidth, beam tilting angle, side lobe and grating lobe levels are closely related to parameters N, δ, a_i, d.

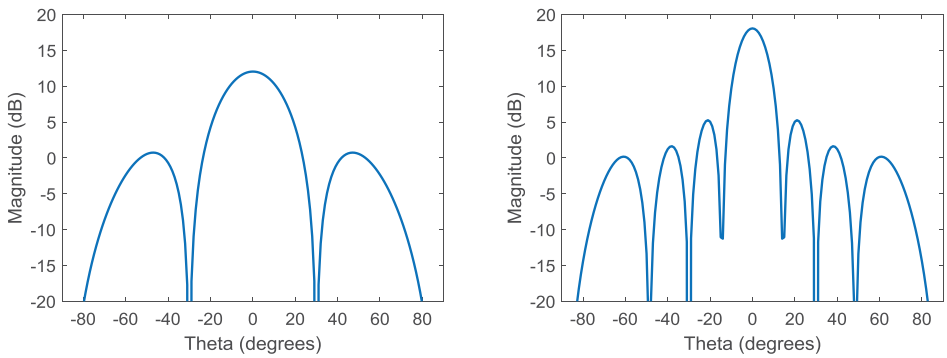

(a) (b)

Figure 1.8 Field patterns with (a) N = 4, and (b) N = 8.

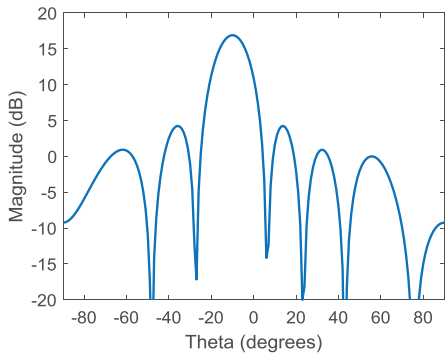

Figure 1.9 Field pattern with electrical downtilt of 10°.

Beamwidth: The beamwidth is mainly determined by the number of antenna elements N. We set $a_i = 1$, $d = 0.5\lambda$, and $\delta = 0$, and calculate the field pattern for $N = 4$ and 8.

The results are shown in Figure 1.8. The beamwidth becomes narrower and the directivity is larger with more numbers of elements.

Beam tilting angle: Electrical beamtilt is realized by providing a progressive phase variation across the array using phase shifters. A phase increment of $\delta = \beta d \sin\alpha$ between adjacent elements provides a downtilt angle of α. We set $a_i = 1$, $d = 0.5\lambda$, and $N = 7$, and the calculated result of electrical downtilt 10° is shown in Figure 1.9.

Side lobes: The side lobes can be controlled by the amplitude distribution of the antenna elements. A uniform amplitude distribution yields the maximum directivity with a side lobe level around -13 dB. By tapering the amplitude distribution that the signal power at the end of the array is less than that at the center of the array, the side lobe level can be reduced with a sacrifice of the maximum directivity. The patterns obtained with uniform amplitude distribution and sinusoidal amplitude distribution for $d = 0.5\lambda$, $N = 7$, and $\delta = 0$ are compared in Figure 1.10.

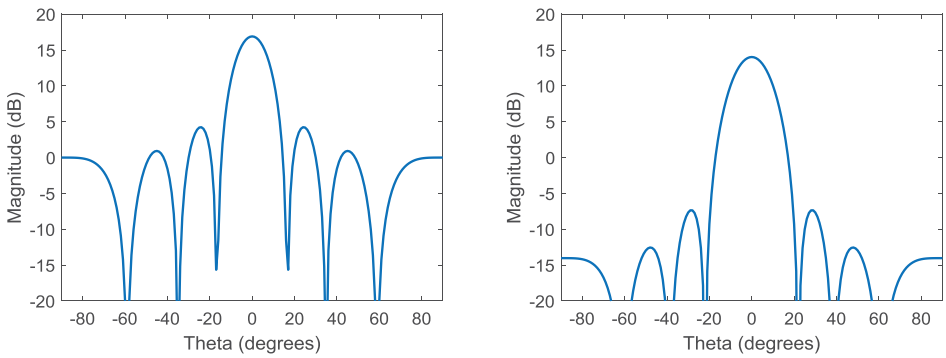

(a) (b)

Figure 1.10 Field patterns with (a) uniform amplitude distribution, and (b) sinusoidal amplitude distribution.

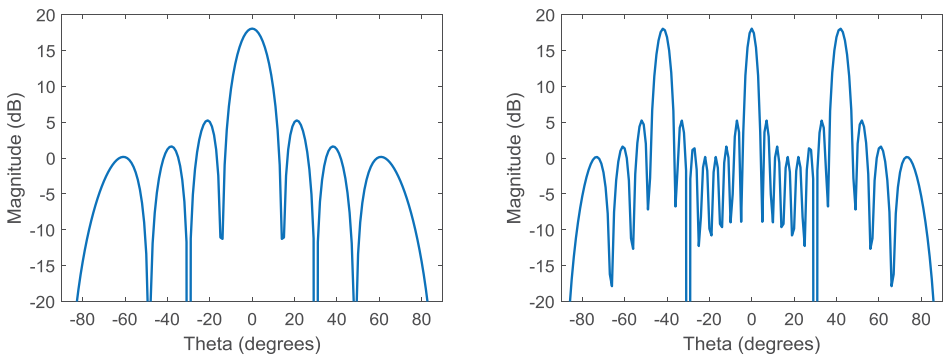

(a) (b)

Figure 1.11 Field patterns with (a) $d = 0.5\lambda$, and (b) $d = 1.5\lambda$.

Grating lobes: When the spacing between adjacent array elements is larger than half wavelength, the array may have equally strong radiation in other directions other than the desired direction. These unwanted radiation beams are called grating lobes. Normally the spacing is restricted in the range between $\lambda/2$ and λ. If an array needs to be electrical downtilted, the element spacing must be near $\lambda/2$ to avoid grating lobes. For $a_i = 1$, $N = 8$, and $\delta = 0$, calculated field patterns with $d = 0.5\lambda$ and 1.5λ are compared in Figure 1.11.

1.1.4 Diversity Systems

Signal fading is always a big issue in wireless communication systems. For cellular mobile communication systems, as the transmit power of a mobile phone is much less than that of a base station, the uplink signal (from a mobile phone to a base station) has a worse signal to noise ratio than the downlink signal (from a base station to a mobile phone). Diversity serves as a good solution to compensate the fading effects and improve the handsets' performances. The basic idea for the diversity is that system uses two or more antennas instead of using just one to ensure at least one antenna have a strong signal. There are two diversity systems for the cellular base station antennas, namely the spatial diversity and the polarization diversity.

Spatial diversity is firstly introduced in mobile communication systems. Each cell is serviced by one transmit antenna and two receive antennas. All the antennas used are vertically-polarized. The spacing of the two receiving antennas is about ten wavelengths apart. Using two receiving antennas improves the availability of the uplink signals as the propagation paths to the two receive antennas are statistically independent. Therefore, the reliability of the communication system is improved. However, spatial diversity requires a large platform to mount the antennas, thus increasing the cost, weight, and wind load.

Polarization diversity combines pairs of radiators with orthogonal polarizations into one antenna for both transmitting and receiving. The two complementary polarizations for receiving can avoid polarization mismatch and signal fading. ±45° polarization has been used by convention in mobile communication systems. Instead of using three antennas for spatial diversity, only one antenna is used for polarization diversity, which minimizes the cell site deployment time and costs.

1.1.5 Antenna Bands

The major frequency bands allocated to mobile radio services worldwide are shown in

Table 1.1 [1]. The upcoming fifth generation of cellular mobile communications (5G) will use frequency spectrum in the existing 4G frequency range (from 0.6 GHz to 6 GHz) and also in the millimeter wave bands (from 24 GHz to 86 GHz).

Table 1.1 Frequency Bands, Short References, and Services

Frequency bands (MHz)	Short references	Services
824-890	850 MHz	
870 (880)-960	960 MHz	GSM, CDMA, 3G
698-960	Low bands	
1710-1880	1800 MHz	3G, 4G
1850-1990	1900 MHz	GSM, CDMA, 3G, 4G
1990-2170	2100 MHz	
1710-2690	High bands	4G

1.1.6 Specifications of Cellular BSAs

The commonly used industry specifications of 4G cellular base station antennas include characteristics listed below. In most cases, compromises are necessary to satisfy all the competing requirements.

- Frequency bands: 690 – 960 MHz, and 1710 – 2690 MHz
- 3-dB Azimuth beamwidth: 60° - 70° (for 120° cell)
- Elevation beamwidth: 6° - 10°
- Polarization: ±45° polarization
- Adjustable elevation tilt: 0- 10° (15°)
- Front to back ratio: > 25 dB
- Cross polarization discrimination: > 30 dB
- Beam squint: < 5°
- Other practical limitations from tower weight and wind load limits such as antenna size, shape, height, appearance, etc.

1.2 Motivation and Contribution

1.2.1 Motivation

The environmental demands and the rising costs of acquiring new sites for base stations along with the need for increased capacity of mobile networks have led to ever more

stringent requirements on BSAs. Antennas that can support different communication standards and increase system capacity are in high demand. To that end, multi-band antennas and multi-beam antennas have been the main streams in BSA designs. Although theoretical study and practical design of BSAs have been greatly developed, there are still some challenges that exist for BSAs to fulfill industrial requirements.

Firstly, BSA elements are expected to have high performance characteristics such as wide bandwidth, high port isolation, high cross-polarization discrimination, beamwidth consistency and little beam squint. Simple and compact antenna structures are desired to enhance robustness, reduce fabrication complexity, and facilitate system integration. Techniques to improve bandwidth impedance matching, stabilizing radiation patterns, and minimizing beam squints are needed. Antenna configurations to facilitate system integration should be investigated.

Secondly, in multi-band antenna arrays, antennas for different bands usually are interleaved to save space, and share a common ground plane and radome. The proximity of antennas for different bands leads to strong cross-band interference. It dramatically deteriorates radiation performances and stability of the antenna system and has been a long-existing issue for the evolution of antenna systems. Solutions to suppress cross-band scattering is of critical importance to guarantee the co-existence of antennas in different bands, especially for the deployment of the future 5G system.

Thirdly, for multi-beam antenna arrays, the challenges are placed on broadening the arrays' operating bandwidth, controlling the side lobe and grating lobe levels and stabilizing coverage of the formed beams. More concentrations should be focused on improving wideband beam-forming networks and designing suitable array elements.

1.2.2 Original Contribution

This work aims to tackle the challenges discussed above and provide new approaches for the development of BSAs. Major contributions are summarized as follows.

The first contribution is the improvement of the BSA elements. Three antenna configurations have been thoroughly studied, including square-dipole-array, cross-dipole and dual-dipole configurations. For square-dipole-array configuration, a method to minimize beam squint and stabilize radiation pattern is discussed. Circuit theory model of a wideband feed network is presented, which greatly facilitates impedance matching of antennas. For cross-dipole configuration, design guidelines of the tightly-coupled

cross-dipole antenna are presented. A method to broaden bandwidth with a compact size is investigated and verified in two antenna designs. For dual-dipole configuration, the design approach to realize fully planar and compact structures is investigated for the ease of system integration. In total, eight antenna elements are designed to verify proposed methods. All of them feature wideband radiation performances with simple and robust structures and could be readily applied in the BSA systems.

The second contribution is the development of novel choking techniques to minimize cross-band interference in multi-band BSA arrays. Three different choking configurations are proposed. Their working principle, together with their capability of suppressing scattering, are investigated. These techniques have been implemented in the dual-band antenna array environment to verify their performances. Experimental results show that the realized two dual-band arrays have cross-band scattering suppressed and desired stable radiation patterns achieved. Those techniques for suppressing cross-band scattering guarantee the co-existence of antennas for different services and greatly facilitate the evolution of communication standards.

The third contribution is the improvement of wideband multi-beam antenna arrays to increase system capacity with a wide coverage area. A wideband three-beam beam-forming network to cover the entire LTE band with flexible beamwidth is presented. New design solutions of key components in the beam-forming networks including wideband quadrature couplers, phase shifters and power dividers are investigated. Cross-dipole antenna with a very compact configuration and stable radiation performances is designed as the array element. Two three-beam antenna arrays are realized with required beamwidth and crossover level. The proposed design can increase system capacity by producing multiple beams in free space, which can be used in a wide range of multi-beam LTE base stations.

1.3 Thesis Outline

Chapter 1 introduces the background of cellular base station antennas by clarifying the key concepts and commonly used industrial specifications. Research motivation and contribution are presented.

Chapter 2 reviews the state-of-the-art techniques associated with base station antennas, including the design of dual-polarized antenna elements, the design of multi-band antenna arrays, and the development of Butler matrix beam-forming networks.

Chapters 3 to 5 focus on the development of wideband dual-polarized antenna elements with improved performance characteristics. Three configurations are discussed in these chapters, including the square-dipole-array, the cross-dipole, and the dual-dipole configurations.

Chapter 3 presents the design techniques of the square-dipole-array configuration. A thorough analysis of the method to stabilize radiation patterns and reduce beam squint is carried out. The antenna bandwidth is enhanced with the help of matching networks based on the ladder-type filter. Two square-dipole-array antennas are presented with consistent wideband radiation performances.

Chapter 4 describes the theory and optimization of the cross-dipole configuration. Firstly, based on a simplified tightly-coupled cross-dipole configuration, the working mechanism and design procedures of the cross-dipole antenna are analyzed. Secondly, a method of enhancing bandwidth with a compact antenna size is presented and verified in two antenna designs.

Chapter 5 discusses the planarization of wideband dual-polarized antenna elements in the form of dual-dipole configuration and its further integration. The design procedure of the planarized dual-polarized antennas is described. The planarized structure facilitates system integration with more space available. As a demonstration, a compact dual-circularly-polarized antenna is realized by integrating the designed dual-linearly-polarized antenna with a coupler.

Chapter 6 presents the development of multi-band antenna arrays. Cross-band scattering, as a long existing issue, is the main focus in this chapter. Firstly, the scattering problem in the dual-band antenna arrays is presented and discussed. Following that, three different types of choking techniques are proposed to suppress scattering. Their working principle and the capability of suppressing scattering are discussed. Later on, they are implemented in two dual-band antenna arrays to verify their performances. Simulation and measurement results demonstrate that the cross-band scattering is suppressed with the proposed techniques, and the realized arrays are capable of producing stable radiation patterns across required wide bands.

Chapter 7 focuses on the realization of multi-beam antenna arrays for the LTE application. It firstly describes design techniques of wideband three-way beam-forming network including quadrature couplers, phase shifters, and power dividers. Then a wideband dual-polarized antenna element with a very compact size and consistent

radiation performances is presented and used as array elements. Verified by experiments, the arrays achieved by implementing the designed beam-forming network and antenna elements have a good matching capability and stable beam-forming performance across the whole LTE band.

Chapter 8 concludes the thesis by summarizing the achievements and limitations of the work. Future work and plans to further develop this research topic are also discussed.

Chapter 2: Literature Review

2.1 Dual-Polarized Antenna Elements

Base station antennas for current 2G/3G/4G platforms are designed to provide dual polarizations of ±45° to enhance the system capacity and combat the multipath propagation effects. To provide full coverage of a geographic area, usually, three arrays are employed to have an omnidirectional pattern in the horizontal plane and a narrow beam in the vertical plane. The antenna elements used in the arrays are required to be able to maintain stable radiation performance in the target band. Commonly used industry specifications for the elements are:

- Reflection coefficient: less than -15 dB in the target frequency band
- Polarization: ±45° linear-polarization
- HPBW in the horizontal cut: 65°±5°
- Cross polarization discrimination (XPD): more than 20 dB at boresight; more than 10 dB within ±60° coverage in the horizontal cut.
- Front-to-back ratio (FBR): more than 20 dB
- Port isolation: more than 25 dB

Current wireless cellular communication systems employ several frequency bands for 2G/3G/4G applications, including GSM700 (698-793 MHz), GSM850 (824-894 MHz), GSM900 (880-960 MHz), DCS (1.71-1.88 GHz), PCS (1.85-1.99 GHz), UMTS (1.92-2.17 GHz), LTE2300 (2.3-2.4 GHz), and LTE2500 (2.5-2.69 GHz). Base station antenna arrays that can cover all of these bands are preferred since they can be used in multiple applications. In practice, to guarantee a good radiation performance, a lower band from 698 to 960 MHz (31.6%) and a higher band from 1710 to 2690 MHz (44.5%) are covered separately by two different antenna arrays. It is still a great challenge for the array covering the higher band to meet all of the specifications.

There are many antennas developed these years targeting at the cellular base station applications. They can roughly divided into six types: patch antennas [4]-[12], cross-dipole antennas [13]-[29], magneto-electric dipoles (ME-dipole) [30]-[37], square-dipole-array antennas [38]-[40], slot antennas [41]-[50], dual-dipole antennas [51]-[55]. Different configurations have different features and abilities to meet the standard

requirements. Among them, the cross-dipoles and the square dipole arrays are the two most promising solutions and have gained significant popularity in the industry.

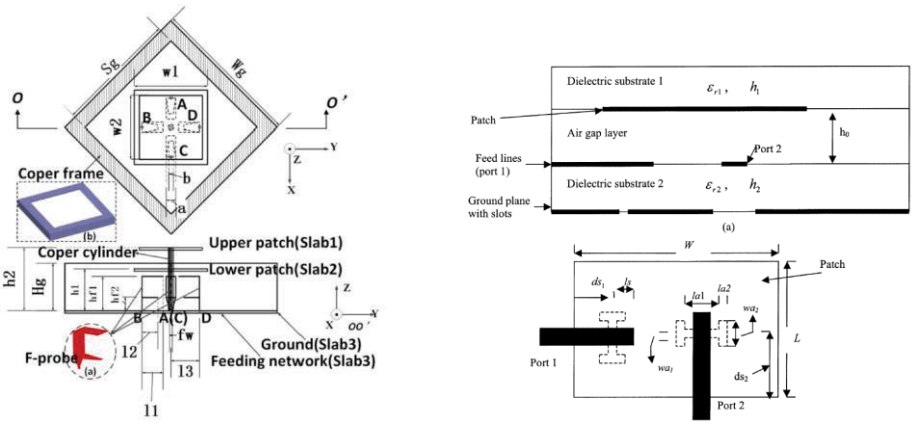

(a) (b)

Figure 2.1 Configurations of dual-polarized patch antennas reported in the literatures (a) [8], and (b) [10].

The **patch antenna** is a popular printed resonant antenna for wireless communications. It features low-profile, ease of fabrication and integration with circuit elements, and conformal nature, but is hard to well operate in a wide band. The bandwidth can be increased by using thick and low permittivity substrates, introducing parasitic patches, aperture coupling fed structure, and different probe feed structures [1]. Different feed techniques can be combined to realize a wider bandwidth. The size of the patch antennas can be reduced by using shorting walls or shorting pins [1]. Following those guidelines, wideband dual-polarized patch antennas are designed in [4]-[12]. In [4]-[8], patch antennas were fed by various types of probes: meandering probe [4], hook-shaped probe [5], wideband triangle probe [6], L-probe and meandering probe [7], and F-probe [8]. A wide bandwidth of 112% is achieved in [6], but the matching capability is limited to VSWR< 2. By further using the stacked patch as shown in Figure 2.1(a), a bandwidth of 45% with VSWR < 1.5 is realized in [8]. Patch antennas with aperture-coupled feed structure are proposed in [9]-[12], and the basic configuration is shown in Figure 2.1(b). Those antennas have relatively wide bandwidths of more than 20% with high isolations, but the bandwidth they achieve is not enough for the cellular base station applications. Moreover, the wideband patch antennas usually have a large size or high profile, which limited their use in the base station applications.

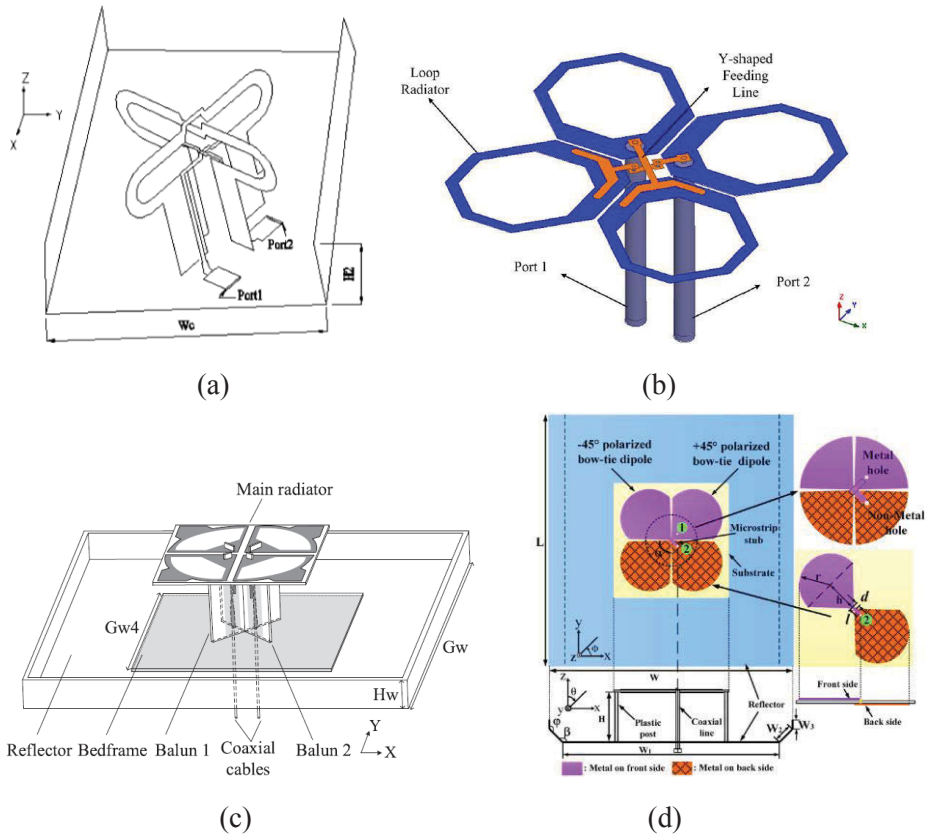

Figure 2.2 Configurations of dual-polarized cross-dipole antennas reported in the literatures (a) [13], (b) [15], (c) [16], and (d) [17].

Cross-dipole antennas are one of the most promising solutions to meet all the industry standard. A dual-polarized cross-dipole antenna consists of a pair of sub-dipoles oriented perpendicular to each other. By exciting either one of the two sub-dipoles, different polarizations can be obtained. Figure 2.2 illustrates some cross-dipole configurations reported in the literature [13]-[29]. Primitive cross-dipoles have their two sub-dipoles "isolated" from each other [13], [14], as shown in Figure 2.2(a). These "isolated" configurations can only achieve a limited bandwidth of less than 30%. It does not come close to covering the higher-band bandwidth requirement of 44.5%. More recently, cross-dipoles that have their sub-dipoles closely spaced and tightly coupled to each other are developed [15]-[21], as shown in Figures 2.2(b) to 2.2(d). With the help of the strong mutual coupling between the two sub-dipoles, both sub-dipoles can be activated when only one of them is excited. This behavior leads to a significant improvement of the impedance bandwidths. For example, all the reported antennas shown in Figures 2.2(b) to 2.2(d) [15]-[17] have their bandwidths more than 44.5% with reflection coefficients < -15 dB. Many configurations have been designed to continue improving the performance

of cross-dipoles. In [22] and [23], the bandwidth enhancement is realized by adopting multi-mode radiators, and bandwidths of 51.0% and 54.5% are achieved respectively. Wider bandwidth of more than 63% is achieved by loading parasitic elements in [24] and [25]. The antenna's aperture can be minimized by loading a parasitic radiator and a director [26], and the antenna's profile can be reduced by adopting an artificial magnetic conductor (AMC) reflector [27]. Thorough theoretical analysis of enhancing cross-polarization discrimination (XPD) for cross-dipoles is carried out in [28] and [29]. Realistic antenna models are developed based on the theoretic analysis, and both achieved XPD more than 20 dB at the boresight, and more than 10 dB within ±60° coverage of the main lobe in the horizontal plane.

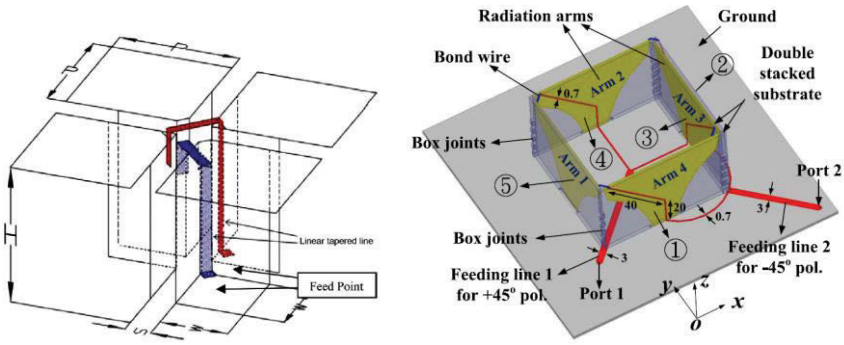

(a) (b)

Figure 2.3 Configurations of dual-polarized ME-dipole antennas reported in the literatures (a) [31], and (b) [34].

The **ME-dipole** is the combination of a vertically oriented quarter-wave shorted patch representing a magnetic dipole and a horizontally placed electric dipole. It can achieve relatively stable radiation pattern and low back radiation by compensating radiation patterns of the electric dipole and the magnetic dipole [30]. ME-dipoles have been developed recently for base station applications in [31]-[37]. In [31], two ME-dipoles are cross placed with each other to realize ±45°-polarized radiation, as shown in Figure 2.3(a). A bandwidth of 65.9% with reflection coefficients < -10 dB is achieved with very stable radiation patterns. In [32], the antenna profile is reduced to 0.15 λ_0 with dielectric loading, but the bandwidth reported is only 24.9%. The bandwidth of the ME-dipole is enhanced to 48% and 56% with VSWR<1.5 in [33] and [34] by optimizing radiators and arrangements of the feed network, as shown in Figure 2.3(b). A differential-fed scheme was adopted for ME-dipoles to have higher isolation level [35], and reconfigurable ME-

dipoles are reported to simplify the feed structure while maintaining polarization diversity [36], [37].

Square-dipole–array antennas [38]-[40] are configured as four connected electric dipoles arranged in a square loop, as shown in Figure 2.4. For each polarization, all four electric dipoles are excited simultaneously and contribute to the radiation. Beam consistency has been achieved in the reported work [38] and [39] with horizontal HPBW varies within 65° ± 5°, but the bandwidths are limited (< 30%). This structure has the potential to fulfill the specifications of the base station antenna element, but it needs further investigation.

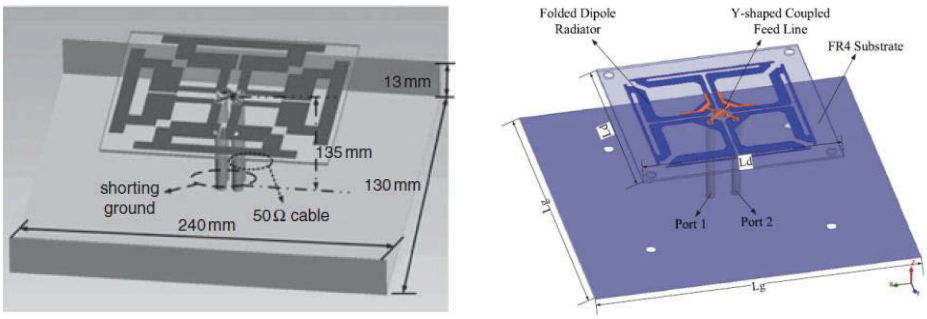

(a) (b)

Figure 2.4 Configurations of dual-polarized square-dipole-array antennas reported in the literatures (a) [38], and (b) [39].

Dual-polarized **slot antennas** are achieved by exciting slots with orthogonal feeds [41]-[50]. They are backed by cavities [41]-[46], or reflectors [47]-[50] for unidirectional radiation. Different configurations of slots are utilized: annular slots [40]-[43], Y-shaped slot [44], cross-slots [45]-[50]. For the annular ring slots, orthogonal microstrip feedlines are utilized to excite dual polarizations [41]-[43]. Pairs of grounded strips and center-located pillars are introduced to improve cross-polarization level and enhance port isolation in [42], [43], as shown in Figure 2.5(a). More than 30 dB port isolation levels and more than 30 dB XPD levels are achieved, but only less than 10% bandwidths are reported with annular slot antennas. With a Y-shaped slot shown in Figure 2.5(b), the bandwidth can be enhanced to 14.2%, but port isolation is only 15 dB [44]. Cross-slot antennas shown in Figure 2.5(c) can further enhance the bandwidth while maintaining the high port isolations [45]-[50]. Simple cross-slot antennas fed by differential feeds [45], and U-shaped microstrip lines [48] can achieve bandwidths of 19%, and 34%, respectively. By adding shorting pillars, the bandwidth for the U-shaped-line fed cross-

slot antenna is enhanced to 68% [49]. Stepped cross-slot antenna [50] and dual-slot antenna [46] are also investigated, and both proved to have a wideband property with high isolation and XPD level. The slot antennas usually have a large size, compared with other types of antennas, which limits their use in the base station applications.

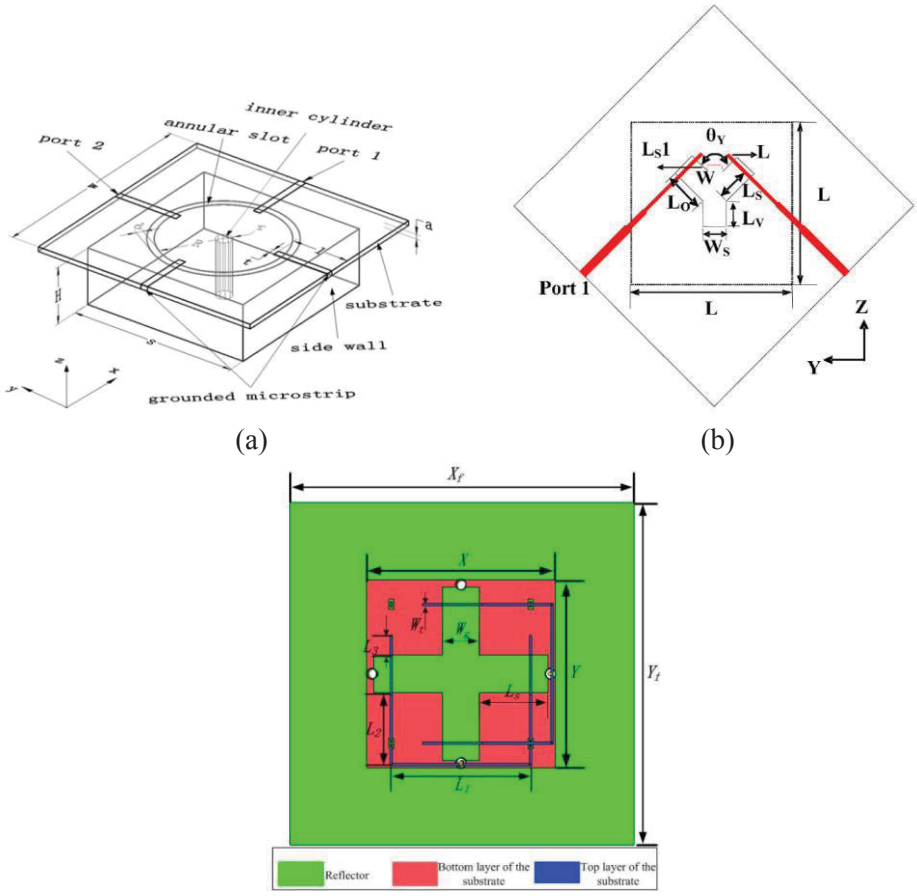

Figure 2.5 Configurations of dual-polarized slot antennas reported in the literatures (a) [42], (b) [44], and (c) [49].

Dual-dipole antennas are usually formed by four dipole elements placed with square arrangement upon a reflector [51]-[55], as shown in Figure 2.6(a). Different from the square-dipole-array configuration, which excites four dipoles simultaneously for one polarization, the dual-dipole antenna excites one pair of parallel elements for one polarization. The four dipoles can either have separate feed networks [51], or two feed networks for two polarizations [52]-[55]. The antenna configuration reported in [51] has been widely used for low-band elements in dual-band antenna arrays. The feed networks for the four dipoles are separated in the four sides. Each pair of feed networks is fed by a

two-way power divider. The space in the middle can have the high-band element integrated into. The detail of the dual-band array will be discussed in Section 2.2. Antennas like the one shown in [51] usually cover bandwidth of more than 37%. The dual-dipole antennas with planar configurations are reported in [52]-[55]. In [52], the antenna has its feed network printed on the same substrate with the radiating dipoles, as shown in Figure 2.6(b). However, only a single polarization was reported with such a configuration. The required dual-polarization was realized by placing two orthogonal-polarized antennas side-by-side. Improved planar configurations with four dipoles integrated are reported in [53] and [54], as shown in Figure 2.6(c). All of the antennas in [52]-[54] can cover 1.71 GHz to 2.69 GHz with reflection coefficients < -15 dB. To minimize the radiator size of the dual-dipole antenna, a shared-dipole configuration is proposed in [55], as shown in Figure 2.6(d). Different from the traditional dual-dipole antenna, which has four dipoles with eight arms, the shared-dipole antenna only has four arms shared for two orthogonal polarizations. The wideband impedance matching and the stable radiation performances are maintained, while the overall size of the radiator is reduced by 50%.

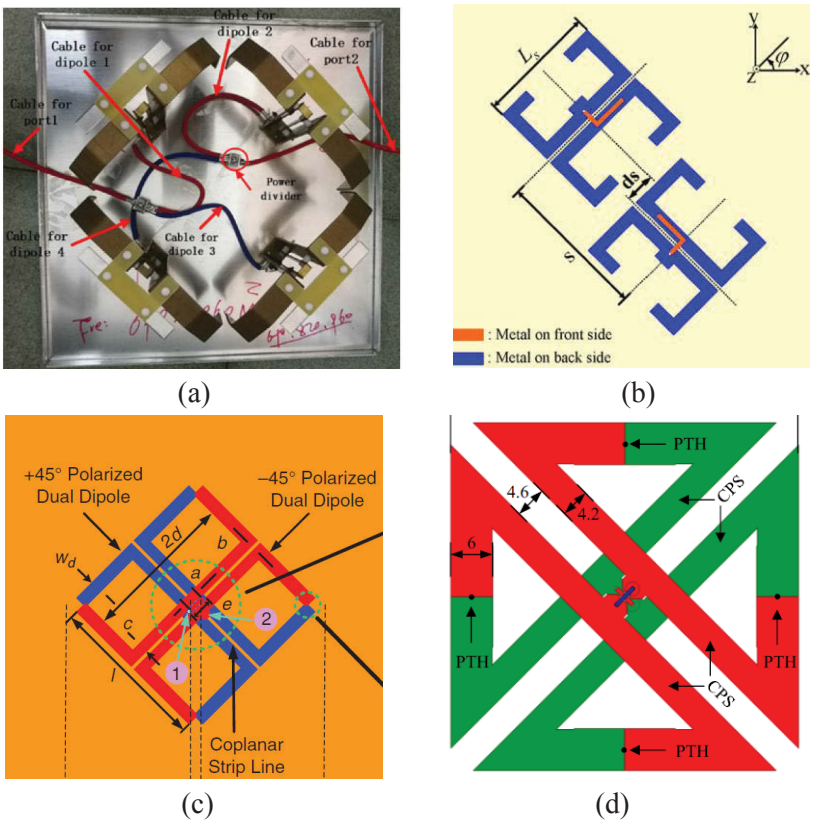

Figure 2.6 Configurations of dual-dipole antennas reported in the literatures (a) [51], (b) [52], (c) [53], and (d) [54].

2.2 Multi-Band Antenna Arrays

The exponential growth of data traffic and demand for mobility have driven an unprecedented expansion of the mobile communications industry for over two decades. As mobile communication standards evolve from generation to generation, and now rapidly move towards 5G, multi-band antenna arrays are in urgent need to simultaneously support different standards. Currently, the most commonly used frequency bands for mobile communication systems are the low band (LB) from 698 MHz to 960 MHz, and the high band (HB) from 1.7 GHz to 2.7 GHz.

There are two types of dual-band arrays, one of them is the array formed by dual-band antenna elements. The dual-band elements cover low and high bands are designed in [55]-[58]. In [56], the dual-band element is formed by two strip dipoles of different lengths are connected through a parallel stripline. In [57], the dual-band element comprises a V-slot loaded triangular shaped dipole for lower frequency and two trapezoidal dipoles for upper frequency, as shown in Figure 2.7(a). It covers LB from 680 MHz to 1100 MHz, and HB from 1.58 GHz to 2.62 GHz. The dual-band elements in [56] and [57] can only radiate single polarization, which cannot fulfill the requirements for the base station antenna. A dual-polarized dual-band element is proposed in [58], using cross-dipole with swastika-shaped configuration, as shown in Figure 2.7(b). This antenna can fully cover the LB and HB with reflection coefficients less than -10 dB and port isolation more than 26 dB. The array formed by the dual-band elements reduces the numbers of antenna units and minimizes the visual installation area. However, the desired performances in both bands for the dual-band arrays is more difficult to achieve than it is for a single-band array, and additional polarization decoupling arrangement will be needed. Also, these antennas are unable to adjust the down-tilt angles in LB and HB independently.

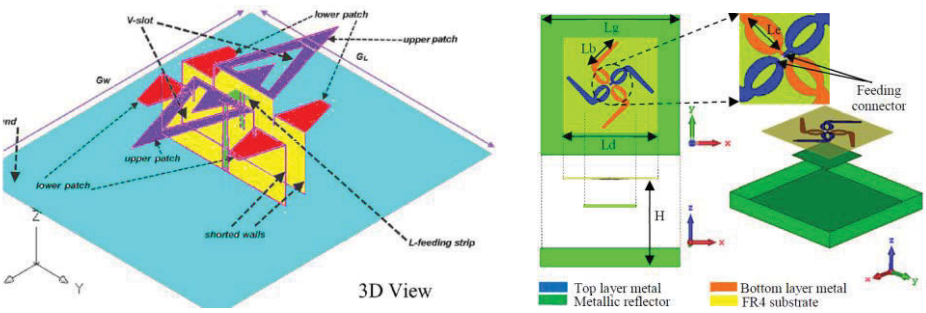

(a) (b)

Figure 2.7 Configurations of dual-band antenna elements reported in the literatures (a) [57], and (b) [58].

The other type of dual-band array consists of individual subarrays operating at different bands. The elements in the subarrays can be either type of dual-polarized elements discussed in Section 2.1. There are three popular arrangement schemes of subarrays: up-and-down scheme, embedded scheme, and side-by-side scheme, as shown in Figure 2.8.

In the up-and-down scheme as shown in Figure 2.8(a), the LB array and HB array are mounted on a long reflection plate and are placed up and down. This scheme minimizes the interference between the LB and HB array, thus reducing the antenna's design cycle. However, the length of the array is the sum of the length of the two subarrays, so it occupies a large installation area.

In the embedded scheme as shown in Figure 2.8(b), every second HB element is embedded in a physically larger LB element. This configuration is guaranteed as the HB frequencies are almost one octave above the LB frequencies, so the HB element is almost half the size of the LB element, and the spacing of HB elements is half that of the LB elements. By sharing the same area for the LB and HB arrays, the occupied space of the dual-band array is similar to the single-band array, which improves space efficiency and saves space rental costs. However, this scheme increases the design difficulty as elements operating at different bands are closely spaced, and are very likely to have strong mutual coupling between each other. Therefore, adjusting for the isolation and the radiation pattern is essential. Many dual-band arrays with the embedded scheme are designed in [59]-[68]. In those arrays, the LB elements are annular ring antenna [59], ME-dipole [60], dual-dipole antennas [61]-[67], and patch antenna [68], and the HB elements are cross-dipoles [59], [61]-[66], [68], ME-dipole [60], and dual-dipole antenna [67]. Different shapes of metal baffles and walls are added to stabilize radiation patterns and improve isolation between LB and HB elements. Among those antennas, the one in [63] covers the required two bands with reflection coefficients less than -15 dB. The isolations between different polarizations in each band are above 27.5 dB. The patterns are stable in both bands, but the HPBW in the high band is wider than required. In [67], by utilizing patch antennas as LB elements, a low-profile dual-band array is achieved. The array has a large front-to-back ratio and high isolations in both bands, but the radiation patterns need to be further stabilized.

In the side-by-side schemes shown in Figures 2.8(c) and (d), the LB and HB columns are parallel placed on a reflection plate [69], [70]-[72]. The problem encountered with side-by-side scheme shown in Figure 2.8(c) is that each array operates in an

unsymmetrical environment where the reflector extends farther on one side of the column than it does on the other side, so the resultant radiation pattern in the horizontal plane (*zx*-plane) is unsymmetrical and the beam maximum may squint off-axis. The configuration with one LB column and two HB columns shown in Figure 2.8(d) is commonly used nowadays [69]. This configuration provides MIMO capability in the HB and LB in a minimum width package. The problem arising from interleaving the elements is that because of the proximity of the HB and LB elements, and due to the electrically large dimension of the LB element in the HB, the LB element becomes a scatterer in the HB, and its presence destroys the HB radiation pattern to a great extent.

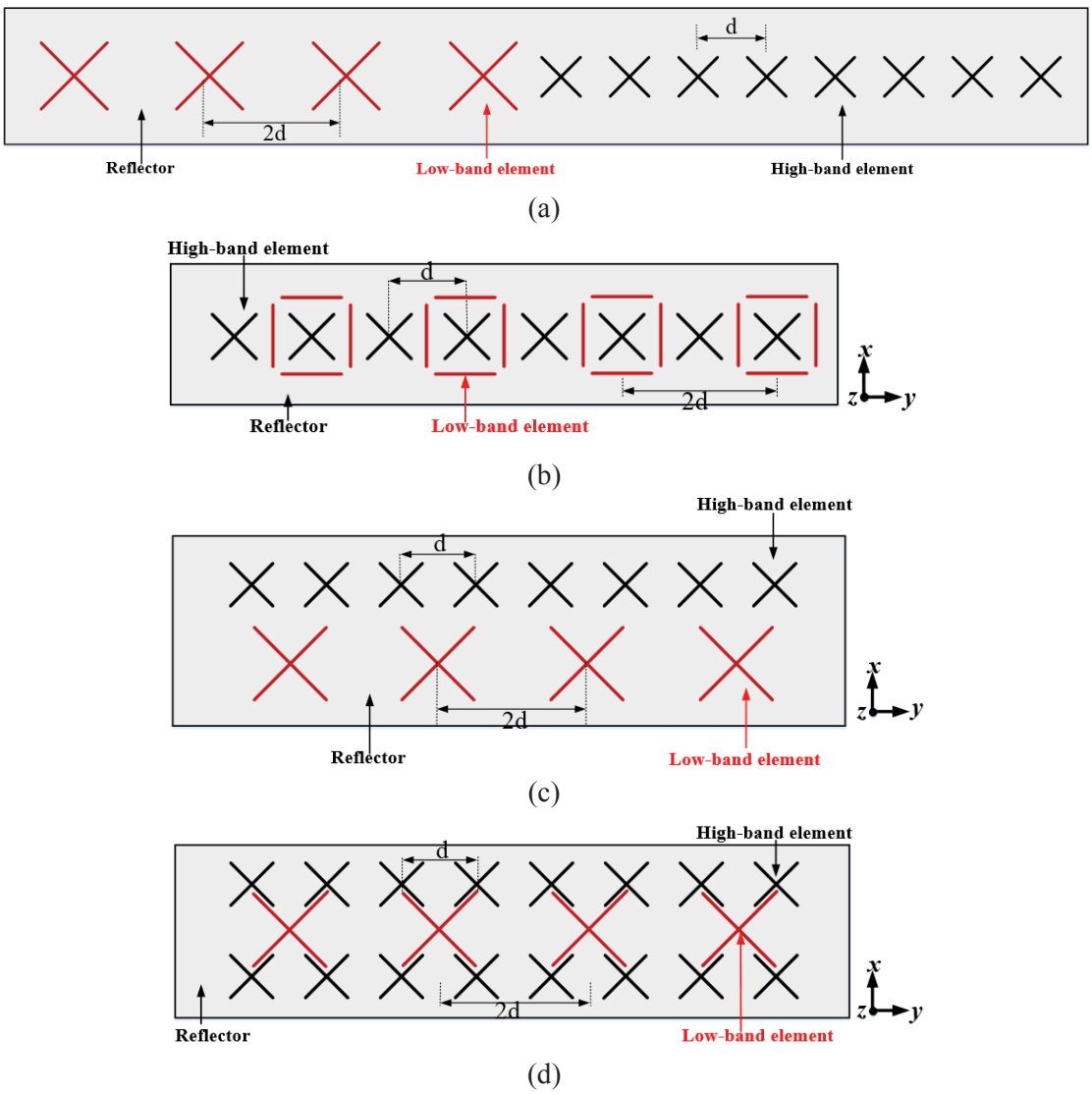

Figure 2.8 Different base station antenna array schemes: (a) Up-and-down scheme, (b) embedded scheme, and interleaved schemes with (c) one HB columns and one LB column and (d) two HB columns and one LB column.

For closely spaced elements operating at different bands, the mutual coupling between them is noticeable. To improve the cross-band isolation, the traditional method is to adopt decoupling networks for the LB and HB columns [73]-[75]. Recently, filtennas are proposed as an alternative and a more straightforward way to suppress mutual coupling [66], [70]-[72]. The filtennas are designed to have high in-band radiation efficiency and out-of-band radiation rejection levels. In [70] and [71], the filtennas are realized by stacked patch antenna with shorting pins and E-slots, and band notch dipoles, respectively. Filtennas operating at band 1710-1880 MHz, and 1920-2170 MHz are designed and placed side-by-side. Cross-band isolation of above 35 dB and 28 dB are achieved, respectively. In [72], a dual-band dual-polarized array utilizing stacked patch filtennas is presented. The LB and HB filtennas operate at 3G (1710-2170 MHz) and long-term evolution (2490-2690 MHz), respectively. A compact array size with a high cross-band isolation of above 20 dB is obtained. In [66], an embedded dual-band dual-polarized antenna array is presented for sub-6 GHz base station application. By placing C-shaped filtering stub close to LB feedlines, and adding L-shaped filtering stub to HB feedlines, elements with filtering properties are realized. The cross-band isolation is improved about 15 dB in both bands after using filtering stubs.

2.3 Butler Matrix Beam-Forming Networks

Increasingly crowded data traffic is a major issue in today's mobile wireless communication systems. The data capacity can be improved by splitting cells and covering them by narrow-beam antennas. However, having many antennas mounted in a tower increasing the installation cost, tower load and wind load. Multi-beam antenna array serves as a good solution to increase system capacity without adding the number of antennas. It splits the wide main beam into narrower beams to meet the need of large data capacity.

The multi-beam antenna array is formed by array elements and beam-forming networks, as illustrated in Figure 2.9. The beam-forming network is in charge of generating different amplitude and phase distributions at the output ports for different beams. Promising beam-forming performance is guaranteed by co-optimizing the elements and the networks. Typical beam-forming networks include Butler matrix, Blass matrix and Nolen matrix, among which Butler matrix [76] is the most commonly used one with its simple structure and low-loss nature.

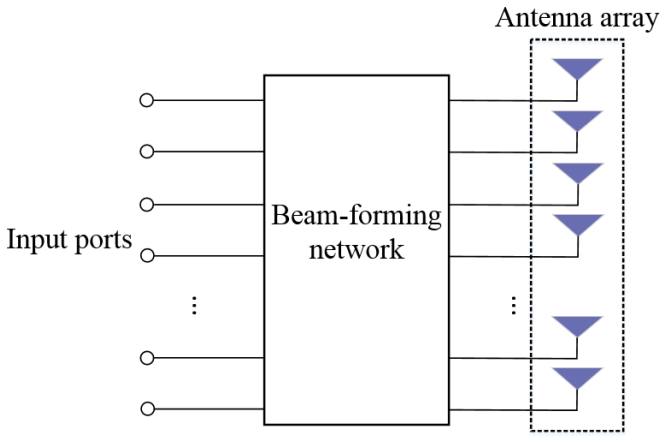

Figure 2.9 Schematic for the beam-forming arrays.

A Butler matrix is an N × N network formed by quadrature couplers and phase shifters. It generates uniform amplitude and linear phase distribution at its output ports. An n-way Butler matrix can achieve incremental phase difference of a multiple of 360/n at the output ports depending on which input port is excited. By alternatively selecting the input excitation, main beam direct at different angles can be chosen. The scattering matrix of a Butler matrix can describe its function:

$$[S_r] = \begin{bmatrix} S_{(M+1)1} & \cdots & S_{(M+1)M} \\ \vdots & \ddots & \vdots \\ S_{(M+N)1} & \cdots & S_{(M+N)M} \end{bmatrix} \tag{2.1}$$

If $[S_r][S_r]^{*T} = [I]$, where $[S_r]^{*T}$ is the conjugate transpose matrix of $[S_r]$, then

$$[S] = \begin{bmatrix} 0 & [S_r]^T \\ [S_r] & 0 \end{bmatrix} \tag{2.2}$$

Here M and N can be arbitrary positive integers. When $M = N = 2^n$, the matrix of $[S]$ can represent the scattering matrix of a $2^n \times 2^n$ Butler matrix.

Printed circuit boards (PCB) are firstly adopted to realize traditional Butler matrices with their low cost, ease of fabrication and integration properties. PCB structures have multiple realizations including microstrip lines [77], strip lines [78], slot lines, coplanar waveguide (CPW) [79], suspended strip lines, etc. The operating bandwidths of these Butler matrices are subjected to the bandwidths of the individual components within the structure, such as couplers. These Butler matrices are mainly targeted at narrowband width, single band range and no miniaturization considered. Figure 2.10 shows some typical design prototypes on PCB technology using microstrip lines, striplines and CPW.

As the narrow bandwidth of traditional Butler matrix cannot meet special requirements of wireless systems, research has been focused on the bandwidth broadening of the Butler matrices [80]-[84]. In [80], multi-section coupled-line was used in directional coupler designs to achieve more than 100% bandwidth. Multi-layer structures were investigated and applied in wideband Butler matrix designs in [81] and [82], where strong coupling was easy to realize for wide band range coverage. The substrate integrated waveguide (SIW) was utilized in a wideband Butler matrix design [83] with around 25% bandwidth. Broadside slot-coupled structure used in [84] was proved to have perfect matching and isolation across an extremely wide band range, which is very attractive in wideband Butler matrix design. Though these designs can achieve wide bandwidth, such kind of multilayer structures may have high cost and difficulty in the fabrication process and integration capabilities. Table 2.1 shows the comparison of some key parameters among the works mentioned above.

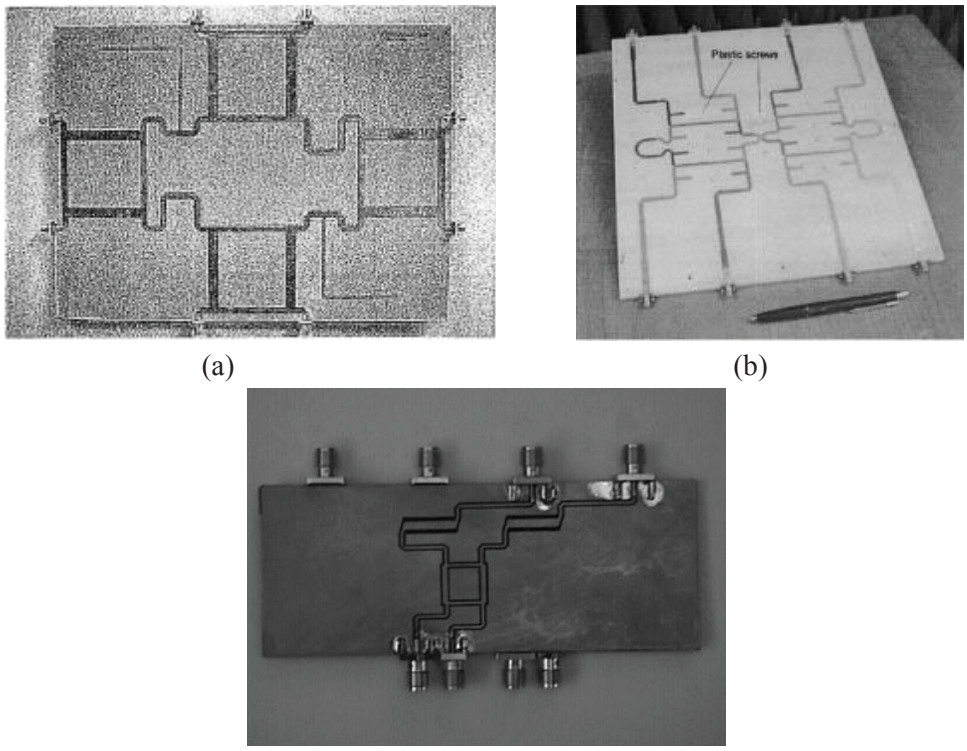

(a) (b)

(c)

Figure 2.10 Butler matrix designs using microstrip lines [77], striplines [78] and CPW [79].

Dual-band Butler matrices have also been studied to satisfy specific requirements of the communication systems [85]-[89]. In [85]-[87], dual-band couplers, crossovers and phase shifters were designed and applied in a 4×4 Butler matrix. This method is the most

straight-forward, but it suffers from high difficulty in building dual-band passive devices. In [88], four diplexers were cascaded with a traditional 4×4 Butler matrix to realize dual-band performance, with the drawback of bulky size and high losses. A modified dual-band butler matrix was proposed in [89] to realize N-independent beams pointing at N-different directions at a higher frequency and N-independent beams pointing at N/2 different directions at a lower frequency and having two orthogonal polarizations.

Table 2.1 Comparison of Wideband Butler Matrices

Ref.	Amplitude imbalance (dB)	Phase error(°)	Transmission S-parameter (dB)	Band range (GHz)	Bandwidth
[79]	3	25	11	5-6.5	26%
[80]	3	8	8.5	1-5	133%
[81]	1.6	5	7.5	1.6-3.2	66%
[82]	5	14	10	3.1-10.6	109%
[83]	2	10	7.5	11-14	24%
[84]	1.2	4.5	9.5	3.1-10.6	109%

To make the design more compact, some miniaturization techniques have been presented. The size miniaturization of Butler matrices can be realized using proper substrate or special materials to build planar structures [90], [91], and using particular transmission line structures reduce circuit areas [92]-[95]. Artificial transmission line [92], composite right/left-handed transmission line [93], swap-port coupler [94], and lumped-element network [95] have been adopted with great size reduction capability in realizing Butler matrices.

Traditional uniform Butler matrices usually include 2^n input ports and 2^n output ports. In many cases, for cell sectorization, it is more economical to choose the required number of beams based on the coverage requirements. M × N beam-forming networks are sometimes more desirable where the number of beams is not constrained to 2^n. Some non-uniform beam-forming networks have been described such as in [96]-[98]; however, relatively narrowband is achieved in [96], [97], and none of them has been applied with antennas to test their performances.

Chapter 3: Square-Dipole-Array Antennas

3.1 Introduction

The square-dipole-array configuration is formed by four connected electric dipoles arranged in a square loop. The four electric dipoles are excited simultaneously for each polarization, and ±45° polarizations are achieved by utilizing two different feed networks. Beam consistency has been achieved with HPBW variation less than 10°, but the bandwidth is limited (< 30%) in the reported works [38]-[40]. Moreover, there has been no report on the working mechanism of such antennas. Without the insight of how it works, it would be difficult to improve the performance of square-dipole-array antennas.

In this section, two square dipole array antennas comprising four folded dipoles and four simple dipoles respectively are presented. Theoretical analysis is carried out based on the current distribution to obtain insight and to provide qualitative explanations to the performances of the antennas. Guideline of designing feed networks for dipole elements are presented, which greatly facilitates the matching process of antennas. Simulated and measured results show that the two antennas have their performance characteristics meet all the specifications of 4G base station antenna elements.

3.2 Square-Folded-Dipole-Array Antenna

3.2.1 Antenna Configuration

The configuration of the antenna element is shown in Figure 3.1. It consists of four folded dipole radiators, two microstrip feed structures, and a flat square metallic plate as a reflector. The four folded dipoles are printed on a substrate and are closely arranged in the shape of an octagon. The folded dipole arms are fed by parallel lines to four points forming a square at the center of the board. They are excited by two feed structures in the diagonal directions to realize the ±45° polarizations. When one polarization is excited, all four folded dipoles are used and are excited in two pairs of series connected dipoles. The two feed structures are mounted between the radiator and the reflector. The details of the feed structure are discussed in Section 3.3.3. The distance between the radiator and the reflector is 27 mm, which is 0.20λ at 2.2 GHz. All the substrates employed in Figure 3.1 are FR4 substrate with a dielectric constant of 4.3 and loss tangent of 0.02. The thicknesses of the substrate for the radiator and feed structures are 0.5 mm and 1.0 mm,

respectively. The optimized parameters of the radiator are listed in Table 3.1.

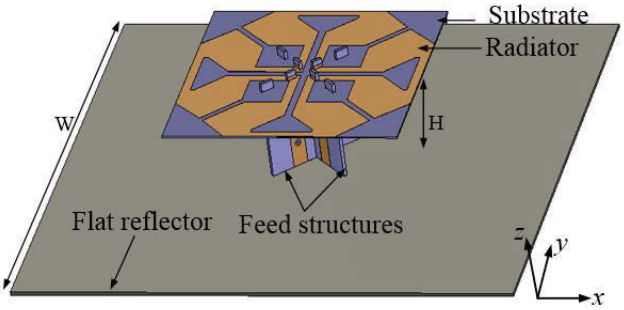

(a)

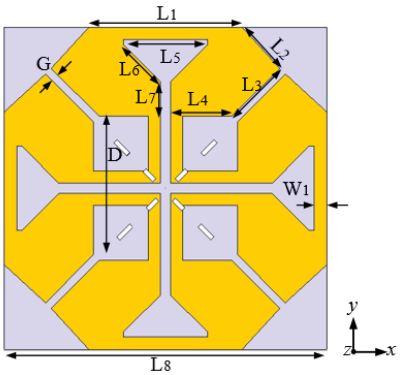

(b)

Figure 3.1 (a) Perspective view of the proposed antenna, and (b) top view of the aperture.

Table 3.1 Optimized Parameters of the Radiator

Parameter	Value	Parameter	Value	Parameter	Value
W	200.00	H	27.00	L1	33.48
L2	12.73	L3	14.76	L4	14.22
L5	18.36	L6	11.39	L7	7.56
L8	70.38	G	0.64	W1	2.70
D	31.50				

3.2.2 Working Principle

3.2.2.1 Half-Power Beamwidth

To understand the working principle of the proposed antenna, we examined the current distribution on four folded dipoles arranged in an octagon, as shown in Figure 3.2(a). The parallel conductor transmission lines carry principally balanced currents and make a minor contribution to the radiation pattern; therefore they are not considered in the analysis. All the four dipoles are excited simultaneously to realize the ±45° polarizations. Figure 3.2(a) shows the ideal excitation method to achieve the −45° polarization as an

illustration, where four 50-Ohm discrete ports are added across the edge of the four folded dipoles, and all the four ports are excited simultaneously. The arrows represent the direction of the excitations. The resultant current distribution at 2.2 GHz, in this case, is shown in Figure 3.2(b). It is clear that dipoles I and II radiate horizontal polarization (HP) while dipoles III and IV radiate vertical polarization (VP). We can separate these two components and calculate their beams in the horizontal plane (*zx*-plane). The finite ground plane has different and quite significant effects on the HP and VP beamwidths. To separate the variation caused by the element from the variation caused by the width of the ground plane, we first examine the case of an infinite ground plane.

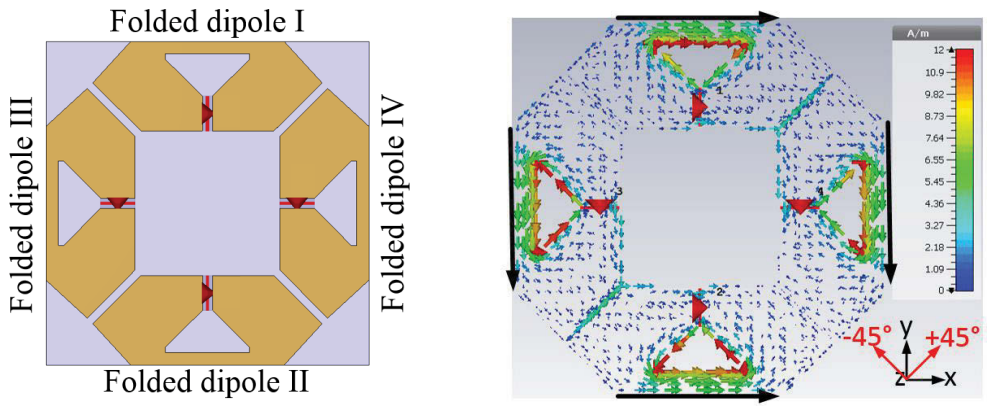

(a) (b)

Figure 3.2 (a) Configuration of the radiator without feed network, and (b) the current distribution on the radiator at 2.2 GHz.

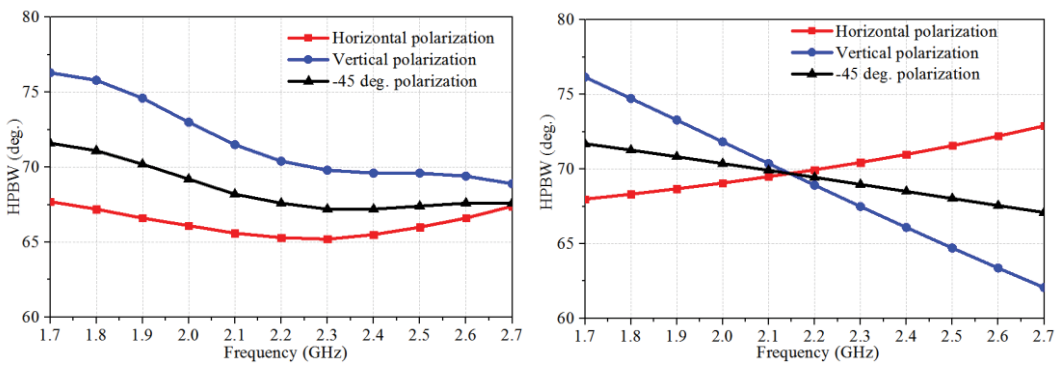

(a) (b)

Figure 3.3 (a) The simulated and (b) the calculated HPBW variations of HP, VP, −45°-polarized patterns of the element in the horizontal plane with an infinite ground plane.

The simulated variations of VP and HP HPBWs with frequency are shown in Figure 3.3(a) for the case of an infinite ground plane. It is seen that the variation of the HPBWs

of the −45° co-polar combination is less than 5° across the band. To understand the factors influencing this variation, we compared this plot with the HPBW variations of four simple linear dipoles with sinusoidal current distributions, as shown in Figure 3.3(b). The substitute linear dipoles are aligned with the centers of the actual folded dipoles.

The factors affecting the beams in the horizontal plane are:

- Horizontal polarization

a) Dipole pattern

$$f_{hd} = [\cos(k\frac{l}{2}\cos\alpha) - \cos(k\frac{l}{2})] \ / \sin\alpha \tag{3.1}$$

where l is the effective length of the dipole, $k = 2\pi/\lambda$ is the wave factor, and α is the azimuth angle in the horizontal plane.

b) Height above the ground plane

$$f_{gp} = \sin(kH\cos\alpha)/\sin(kH) \tag{3.2}$$

where H is the height of the dipoles above the ground plane. This is calculated based on the pattern of a source and its image in an infinite ground plane.

- Vertical polarization

a) Pattern of pair of vertical dipoles in the horizontal plane

$$f_{vd} = \cos(k\frac{s}{2}\sin\alpha) \tag{3.3}$$

where s is the horizontal spacing of the dipoles.

b) Height above ground plane

$$f_{gp} = \sin(kH\cos\alpha)/\sin(kH) \tag{3.4}$$

The HP and VP beams in the horizontal plane are given by $f_{hd} \times f_{gp}$ and $f_{vd} \times f_{gp}$, respectively. The HPBWs of these patterns along with the HPBWs of the −45° co-polar combination of the orthogonal polarizations are plotted in Figure 3.3(b). The parameters used in this calculation were height $H = 27\ mm$ (actual value), dipole length $L = 51.5\ mm$ (end to end length of the folded dipole), and dipole spacing $s = 52.4\ mm$ (spacing of centerlines of the folded dipoles). The agreement with the simulation results of Figure 3.3(a) is quite close in values, although the curvature is not predicted by the elementary model. This discrepancy must be attributed to the variation of the current distribution with frequency on the wide folded dipoles. Both plots show a relatively stable

−45° co-polar HPBW with a total variation of approximately 5° across the band.

As discussed above, dipole length (*L*), dipole separation distance (*D*), and antenna height (*H*) have noticeable effects on the radiation patterns. Here we remark that infinite ground plane was considered in (3.1) to (3.4); however, the finite reflector size (*W*) in the practical application has great influence on the radiation pattern as well. The effects of *D*, *H*, and *W* on the HPBWs are illustrated in Figure 3.4. Note that the influence of dipole dimensions is not considered as it is a dominant parameter for impedance matching.

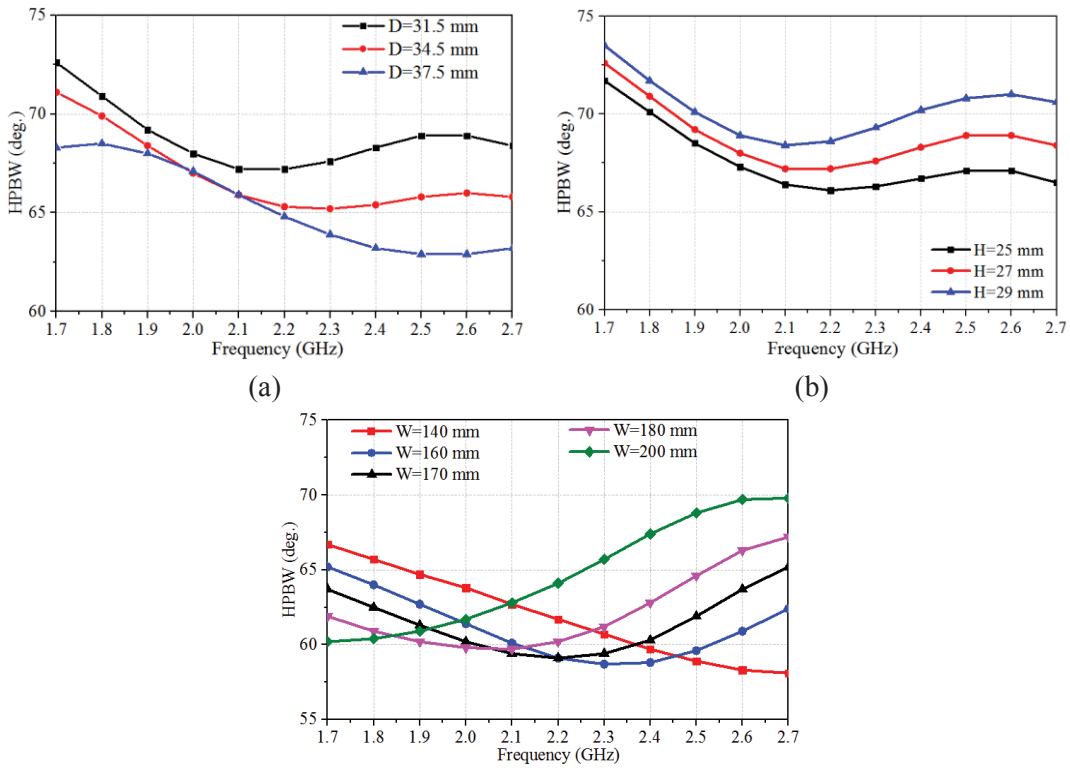

Figure 3.4 The variation of co-polar HPBWs across the band with (a) different distance D between the folded dipole elements, (b) different antenna height H, and (c) different widths W of ground plane.

As shown in Figure 3.4(a) and (b), the HPBW gets narrower with an increasing distance between the folded dipoles (*D*) or with a decreasing antenna height (*H*). The pattern variations attributed to these two parameters are moderate and can be used for fine tuning. As observed in Figure 3.4(c), while there is a significant variation in HPBWs caused by the width of the ground plane, selection of an optimum width of the ground plane about 170 mm again results in a total variation in HPBW of about 5°. The HPBWs of the VP, HP, and −45° co-polar combination of the orthogonal polarizations for this optimum

configuration are shown in Figure 3.5.

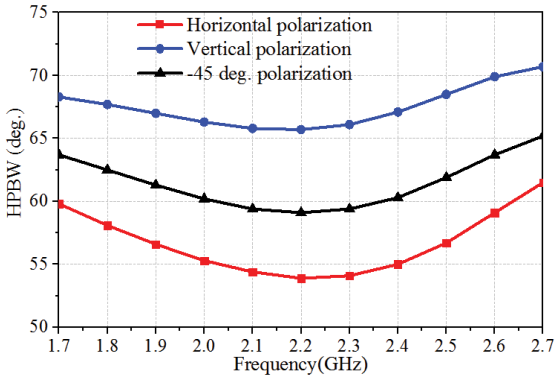

Figure 3.5 The HP, VP and co-polar HPBWs of the antenna element placed on a ground plane of width 170 mm.

3.2.2.2 Beam Squint

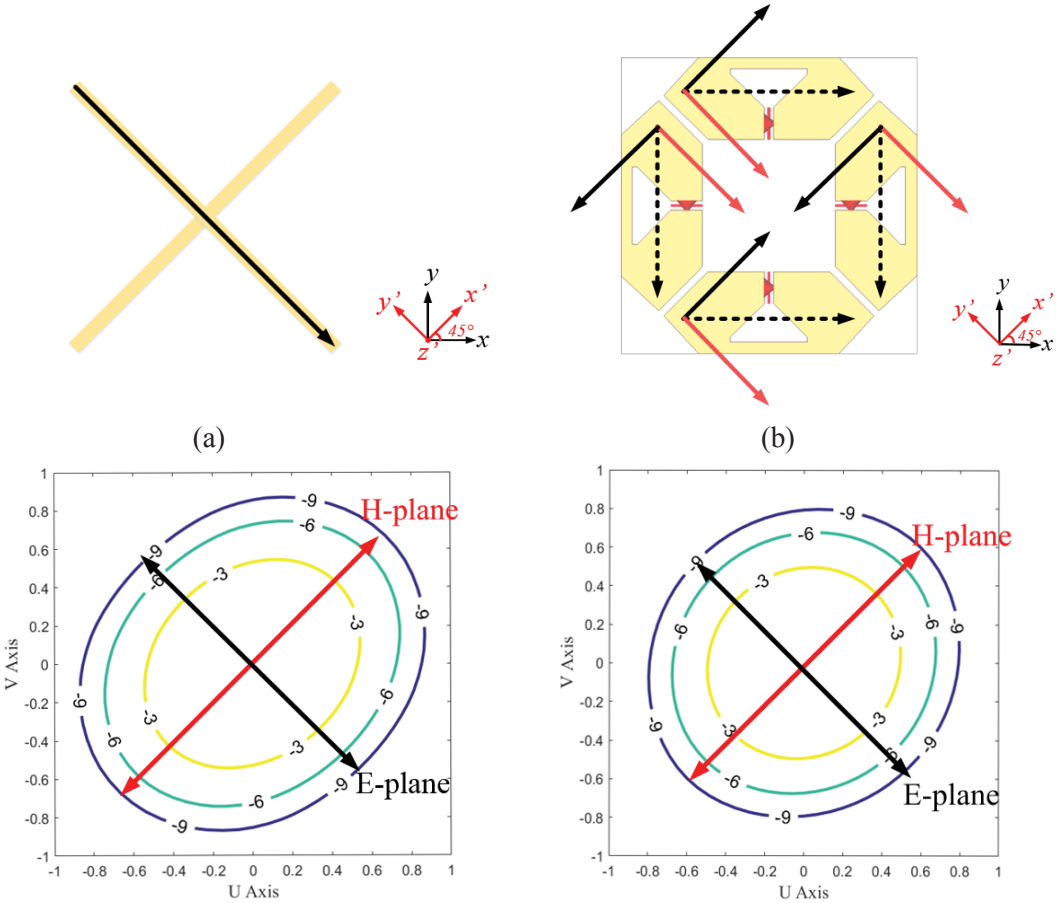

Figure 3.6 Current distribution illustration of (a) a cross-dipole, and (b) the four folded dipole elements; contour plot of beam of (c) a cross-dipole, and (d) the four folded dipole elements in u-v coordinates.

A characteristic of slant polarized arrays is that they show squint when the beam is tilted away from the horizontal plane if the E- and H-plane beamwidths of the radiating patterns are unequal. The long axis of the intrinsically elliptical pattern of a conventional 45° inclined dipole element is aligned 45° away from the y-axis, which destroys the symmetry to the y-axis. Therefore, with a down-tilt angle, the peak of the cut of interest no longer stays at the mechanical boresight. To alleviate the beam squint problem, the solution is to make the intrinsically elliptical pattern as circular as possible. To evaluate the severity of the beam squint, a factor is defined as $n = \mathrm{HPBW}(+45°)/\ \mathrm{HPBW}(-45°)$, which represents the ratio of HPBW in the +45° plane to that in the −45° plane. The closer the value n to 1, the less the squint will be. Here we remark that beam squint of an antenna element is approximately equal to that of the array employing the antenna elements.

To eliminate the beam squint, the E- and H- plane patterns of the element need to be equal in beamwidth. With a pair of crossed dipoles shown in Figure 3.6(a), when −45° polarization is excited, a line current is induced along y'-axis. This leads to a narrow E-plane pattern and a broad H-plane pattern, as shown in Figure 3.6(c). Widening the induced currents along x'-axis can help to achieve similar radiation patterns in the two planes. In the element described here, the current of a single dipole is replaced by the currents in all four dipoles, and the current distribution is illustrated in Figure 3.6(b). The extent of the currents along x'-axis is broadened, making the H-plane patterns narrower while maintaining the E-plane pattern almost unchanged, as shown in Figure 3.6(d). For the cross-dipole model, $n = 1.29$ at its resonant frequency. For the element described in this paper, n varies from 1.09 to 1.20 across the entire targeted band, demonstrating its ability to suppress beam squint.

3.2.3 Feed Network

In order to excite the four dipoles simultaneously for each polarization, the configuration in Figure 3.7(a) is used. Parallel conductor transmission lines connect each folded dipole to the feed points AB and CD as shown in the diagram. If a signal is fed in across AB, it is applied to a series connection of the impedances of dipole I and dipole IV each seen through the length of transmission line. Connected in parallel with this combination is the series connection of dipoles II and III each seen through the length of transmission line. Each dipole has the same impedance Z which is transformed to Z' through the lengths of parallel conductor line. Across the feed points AB (or CD) we see two impedances of $2Z'$ in parallel. The impedance seen at AB or CD is therefore Z'.

Matching the input impedance at AB is therefore equivalent to matching the input impedance of each folded dipole with the associated section of transmission line. Therefore, firstly we need to optimize each folded dipole to get readily matched input impedance while maintaining the desired radiation performance.

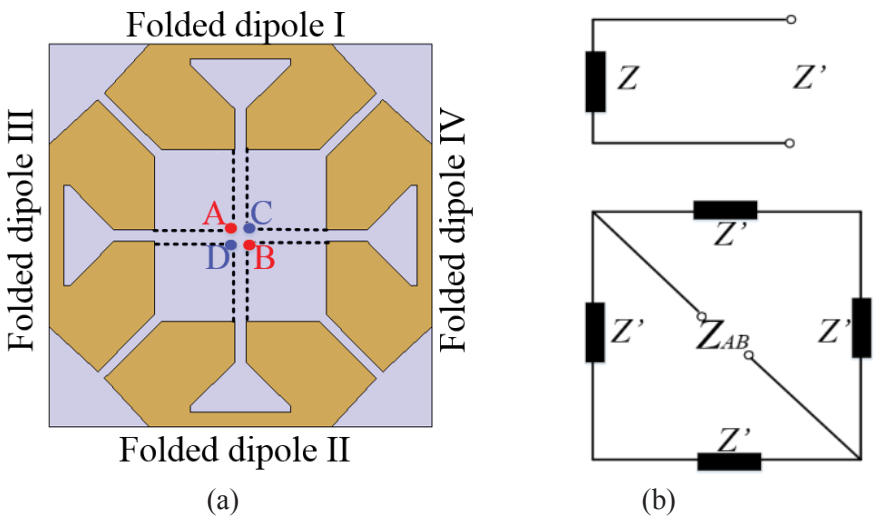

Figure 3.7 (a) Feed method, and (b) the equivalent circuit model of the impedance.

There are four factors that have significant influences on the input impedance: gap width between the folded dipoles (*G*), antenna height (*H*), outer perimeter (*OP*) of the folded dipoles where $OP=L_1+2\times L_2+2\times L_3+2\times L_4$, and inner perimeter (*IP*) of the folded dipoles where $IP=L_5+2\times L_6+2\times L_7$. The variation of the input impedance of the folded dipole elements (*Z*) with different parameter values was studied and shown in Figure 3.8. As shown in Figure 3.8(a), when the folded dipoles are closely arranged with a small gap, there is a 'fish' pattern indicating a double resonance; but with a wider gap, the resonance disappears. It suggests that the coupling between the folded dipoles plays an important role in the impedance matching. In this work, we choose *G*=0.64 mm to get the double resonance. Figure 3.8(b) shows that the 'fish' pattern is smaller with a larger *H*, which indicates a smaller variation of the resistance and reactance across the band, making it easier to be matched. However, a low-profile structure is preferred to reduce the mutual coupling between elements when the antenna is applied in an array. Therefore, *H*=27 mm was chosen as a compromise. Figure 3.8(c) and (d) shows the input impedance with different outer and inner perimeters of the folded dipole. Note that when we changed these two parameters, all the related parameters (L_1 to L_7) were scaling up or down together to keep the shape unchanged. It is observed that by changing the outer perimeter, the

resonance moves to a higher or lower frequency. The inner perimeter only influences the impedance near the starting frequency point (1.7 GHz) while the impedance near the ending frequency point (2.7 GHz) remains stable.

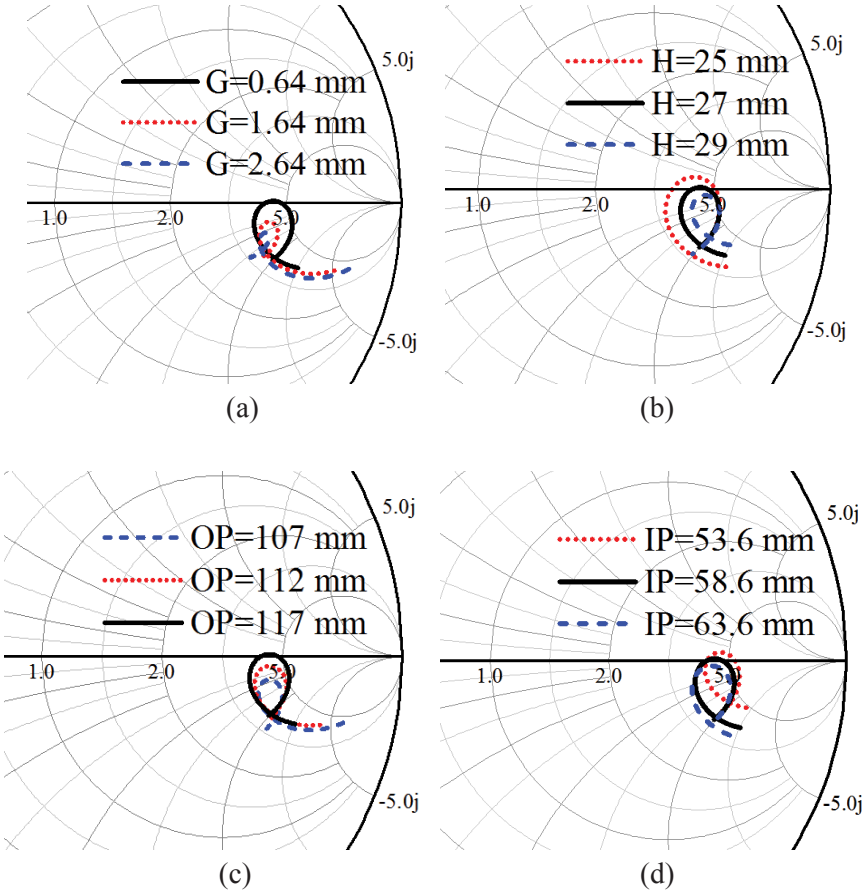

Figure 3.8 Input impedance of the folded dipole elements (Z) on the Z-Smith for parameters (a) D, (b) H, (c) OP, (d) IP.

After optimizing the dimension of the folded dipoles and connecting them using parallel conductor transmission lines to the feed points AB and CD, two feed structures are connected to AB and CD to excite the ±45°-polarized radiation separately. In developing the matching circuit, the transmission lines are considered as circuit elements, and the interaction with the dipole fields is neglected.

The locus of the impedance of the optimized folded dipoles Z on the Smith chart is shown as solid black line in Figure 3.8. It shows the characteristic 'fish' pattern indicating a double resonance slightly below the real axis and with a resistive component of approximately 230 Ohms. The task of matching this to 50 Ohms is relatively simple and can be notionally achieved with a wide band two-section transformer that transforms the

230 Ohms to 50 Ohms with some minor reactive corrections.

Figure 3.9 shows a circuit representation of the elements involved in the matching. The two-section transformer (line transformer I and II) is formed by transmission lines TL_M, LL, and TL. The balun consisting of a short line (SL), an open line (OL), and a 1:1 transformer is relatively wideband and does not contribute very much to the matching, however, its components were included in the optimization. The 1:1 transformer is a circuit artifice for connecting the impedance of the OL in series with the impedance of the parallel connection of LL and SL. The optimized parameter values of the circuit elements and the resultant calculated reflection coefficient are shown in Figure 3.10. An excellent matching result was obtained with $|S_{11}| < -15$ dB from 1.62 GHz to 2.8 GHz.

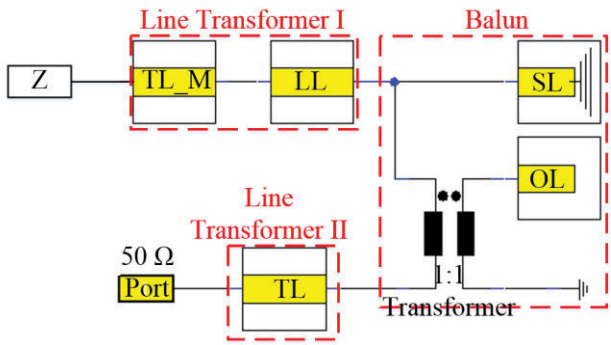

Figure 3.9 Configuration of the matching circuit.

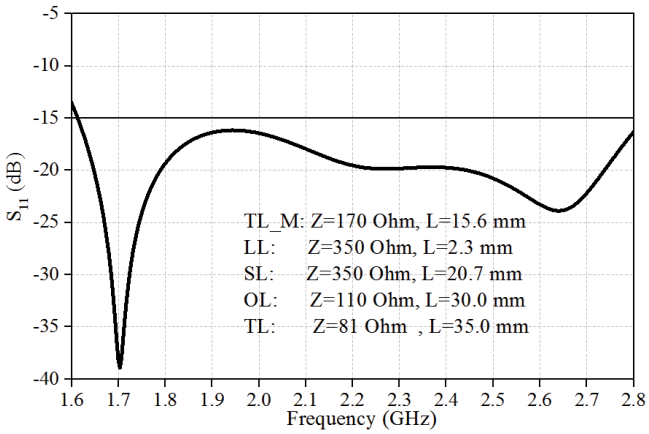

Figure 3.10 Calculated $|S_{11}|$ of the matching circuit model.

To provide insights into how this matching circuit works, the input impedance on Z-Smith Chart with different parts of the matching circuit added are shown in Figure 3.11. Figure 3.11(a) shows the input impedance of the optimized folded dipoles, which has a double resonance. By adding the line transformer I, a third resonance is introduced, and

the high resistance of the folded dipole is reduced to some extent, as shown in Figure 3.11(b). The balun consisting of SL and OL has a minor effect on the impedance, as shown in Figure 3.11(c), but they are essential to provide balance feeding. Finally, by employing line transformer II, the input impedance is transformed to around 50 Ohms with a four resonator match, as shown in Figure 3.11(d). With this matching circuit, excellent matching (VSWR<1.5) can be realized across the required band.

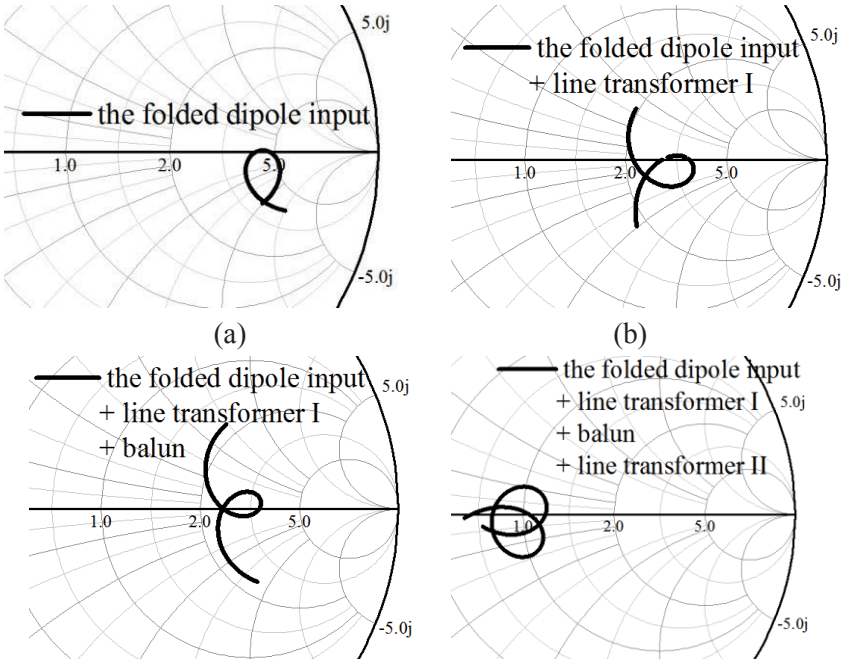

Figure 3.11 The impedance of (a) the folded dipole input, (b) the folded dipole input and the line transformer I, (c) the folded dipole input, line transformer I, and balun, (d) the folded dipole input, the line transformer I, balun, and line transformer II on the Smith chart from 1.60GHz to 2.80 GHz.

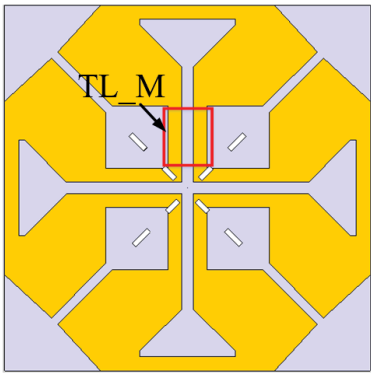

(a)

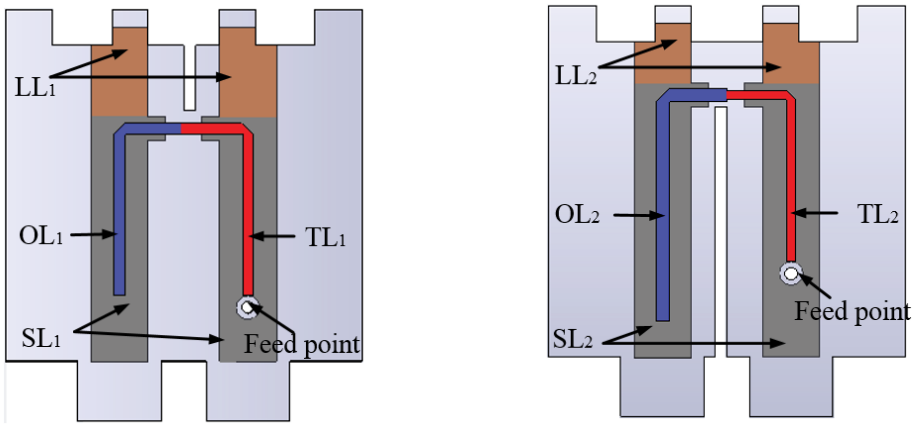

(b) (c)

Figure 3.12 Realization of the matching circuit. (a) Top view of antenna aperture, and perspective views of the feed network for (b) +45° polarization, and (c) −45° polarization.

Table 3.2 Optimized Parameters for the Physical Implementation of the Matching Network

Elements	Line length (mm)	Line width (mm)	Gap width(mm)
TL_M	14.7	2.7	2.1
LL_1	6.5	4.8	6.0
SL_1	20.5	4.8	6.0
TL_1	18.5	0.9	-
OL_1	18.4	1.0	-
LL_2	4.5	4.8	6.0
SL_2	22.5	4.8	6.0
TL_2	18.6	0.8	-
OL_2	23.3	1.1	-

The implementation of the matching circuit using microstrip technology is shown in Figure 3.12. The line TL_M is the parallel conductor line from the folded dipole to the connection points at the center of the PCB. The line LL is a parallel conductor line on the balun board. The component TL and OL are microstrip lines on the balun board. Note that the lines TL_M, LL, and SL are balanced twin conductor lines whereas lines OL and TL are unbalanced microstrip lines. The TL and OL are printed on the front layer, whereas LL and SL are printed on the back layer of the substrate. The parameters for these lines are calculated based on the optimized parameters of the corresponding circuit elements. Minor adjustments were made to the layout to optimize the performance with allowance for parasitic discrepancies and the effects of interaction of the circuit components with the dipole fields. Note that the two feed structures are slightly different to avoid

interference between the cross-over conductors. The optimized parameters are all listed in Table 3.2.

3.2.4 Experimental Results

The prototype with a 200×200 mm^2 ground plane was fabricated and tested, as shown in Figure 3.13. Figure 3.13(b) illustrates the details of the feed structure. The cables are directly inserted to the feed points with the outer conductor soldered on SL, and the inner conductor soldered on TL, as shown in Figure 3.13(b).

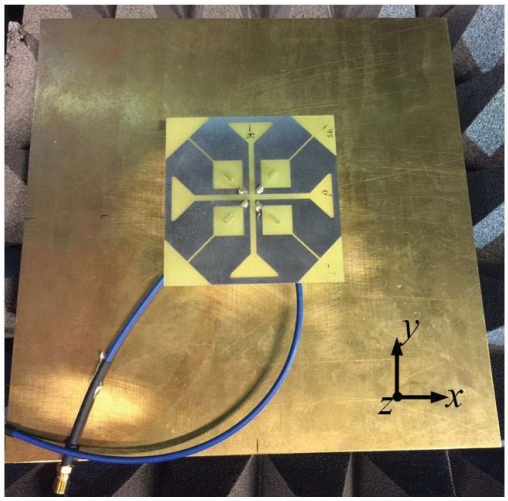

(a)

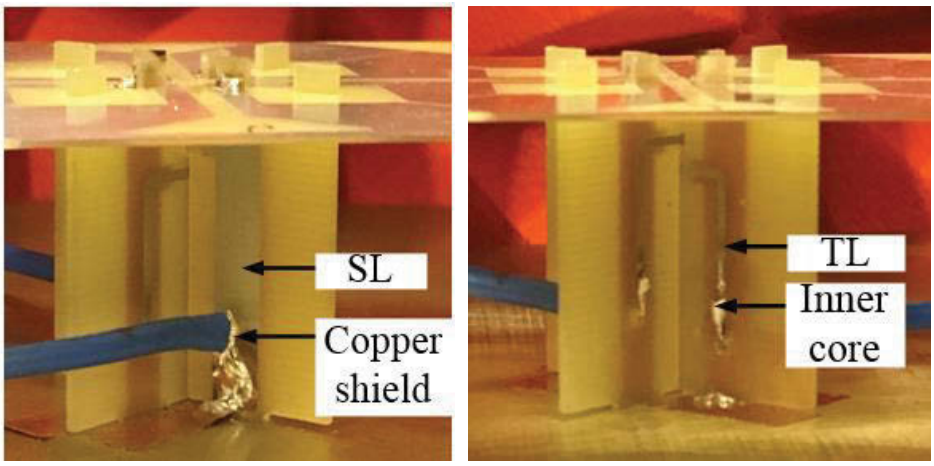

(b)

Figure 3.13 (a) Front view, and (b) side view of the prototype of the proposed antenna.

Figure 3.14 plots the simulated and measured S-parameters of the two ports. The measured bandwidth for $|S_{11}|/|S_{22}|\leq-15$ dB is 46.4% from 1.69 GHz to 2.71 GHz, which covers the required bandwidth from 1.71 to 2.69 GHz for base station application. The simulated port-to-port isolation is more than 35 dB, and the measured result is around 30

dB over the entire operating frequency band.

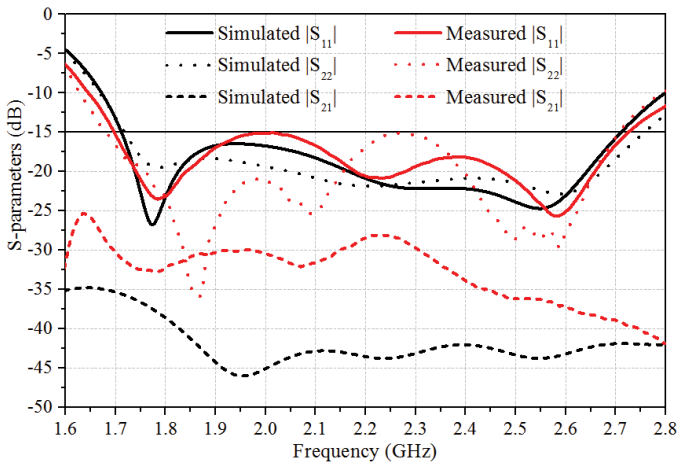

Figure 3.14 Simulated and measured S-parameters.

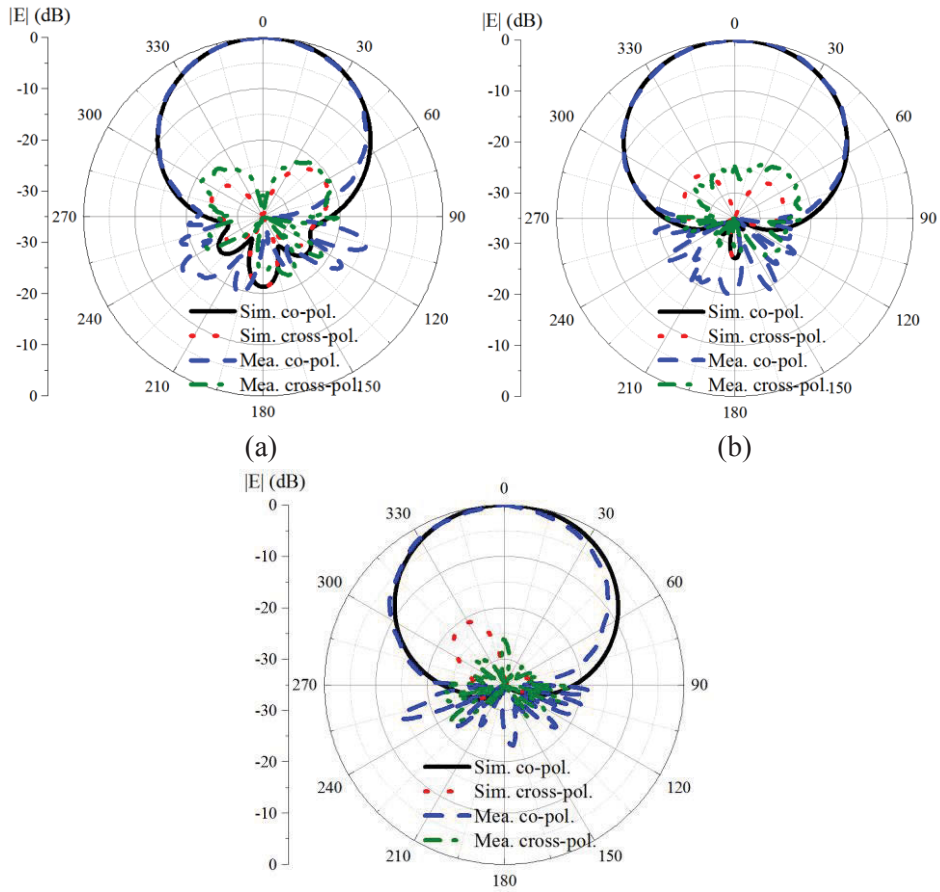

Figure 3.15 Simulated and measured radiation patterns in the horizontal plane at (a) 1.7 GHz, (b) 2.2 GHz, and (c) 2.7 GHz.

The simulated and measured radiation patterns at 1.7, 2.2, and 2.7 GHz in the *zx*-plane

are shown in Figure 3.15. Only the results of +45° polarization are shown here as the antenna is symmetrically arranged and the radiation patterns of the two polarizations are very similar. The simulated and measured patterns agree well. The measured XPD is more than 25 dB at the main lobe in the horizontal plane. The simulated and the measured front-to-back ratio is more than 22 dB and 20 dB, respectively.

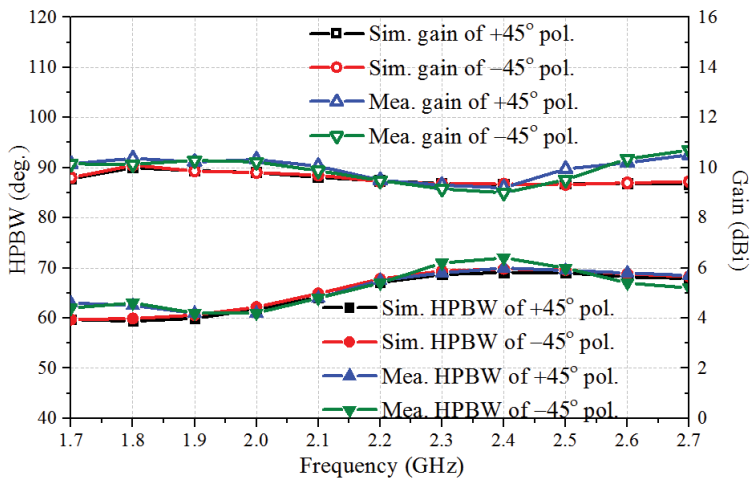

Figure 3.16 Simulated and measured HPBWs and gains.

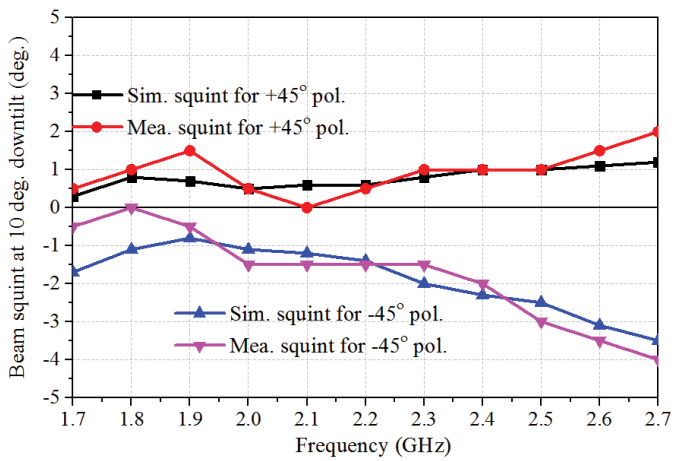

Figure 3.17 Simulated and measured beam squint at 10° down-tilt.

Figure 3.16 shows the simulated and measured HPBWs of the antenna for both the two polarizations. The simulated HPBWs are 64.5°±5.0° for both two polarizations, and the measured HPBWs are 65.5°±4.5° and 66.5°±5.5° for the +45° and −45° polarization patterns, respectively. The measured results demonstrate that this antenna has very stable radiation patterns across a wide bandwidth. Less beamwidth variation (±3°) is predicted with a ground plane width of 170 mm. The simulated and measured gains are also shown

in Figure 3.16. The simulated gain varies from 9.3 dBi to 10.1 dBi, and the measured gain varies from 9.0 dBi to 10.7 dBi within the targeted bandwidth. The radiation efficiency is above 80% across the operating frequency band. The beam squint results are shown in Figure 3.17. At 10° down-tilt, the simulated and measured beam squints are all less than 4°.

3.3 Simplified Square-Dipole-Array Antenna

3.3.1 Antenna Configuration

In this section, we present a simplified square-dipole-array antenna using conventional dipoles. The antenna configuration is as shown in Figure 3.18(a). Similar to the antenna element in Section 3.2, it consists of four dipoles, two microstrip baluns, and a square metallic plate as the reflector. The two baluns are perpendicular to each other and are located between the radiator and the reflector.

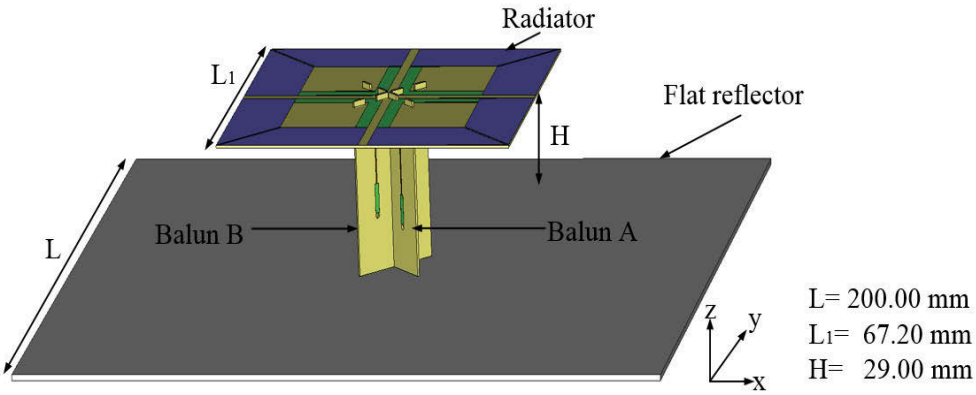

(a)

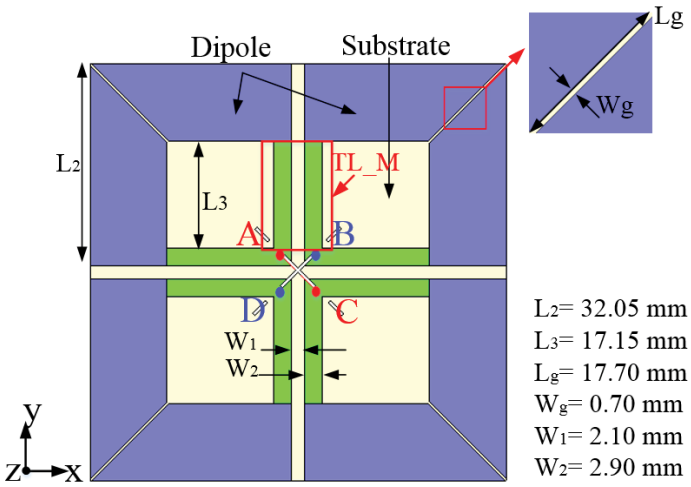

(b)

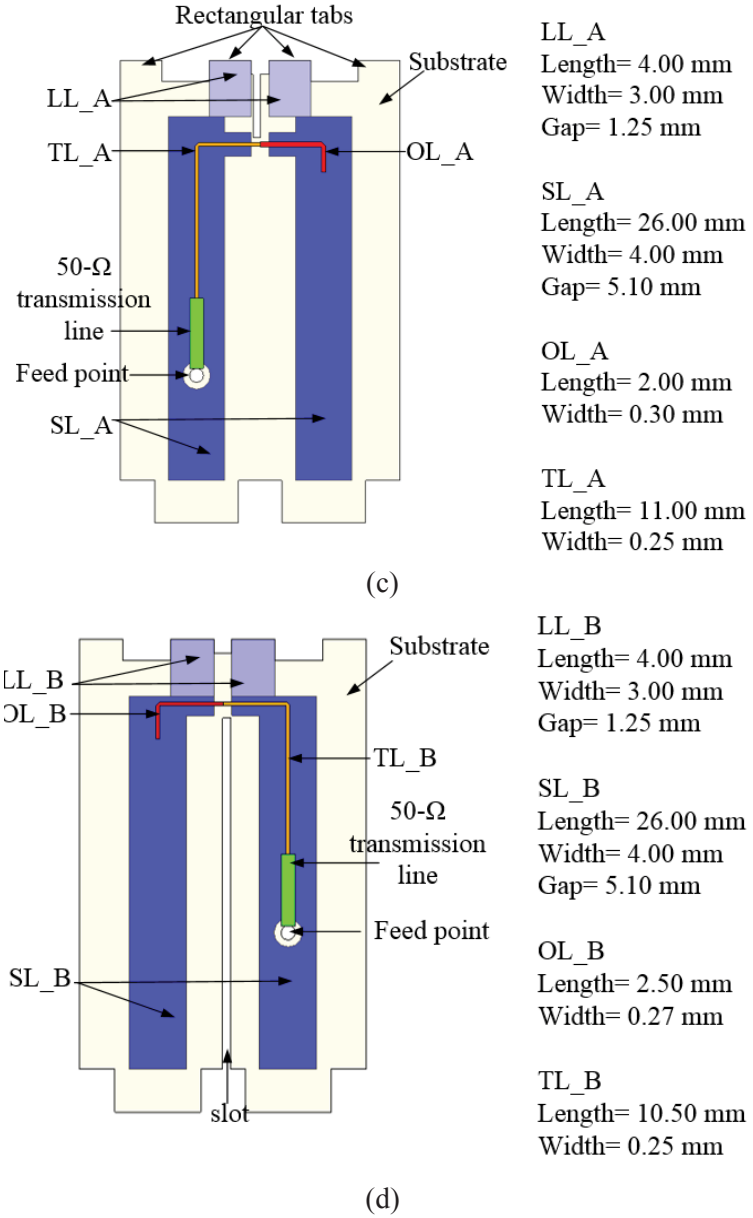

Figure 3.18 Antenna configuration: (a) perspective view; (b) top view; (c) detached view of balun A; (d) detached view of balun B.

Figure 3.18(b) gives a detailed view of the radiator. The four dipoles are printed on a substrate and arranged in a square. Gaps with width W_g and length L_g separate adjacent dipoles. The dipoles are fed through parallel coupled lines (TL_M) so that they are excited together. Two baluns denoted by A and B are employed to provide balance feeds at AC and BD to excite orthogonal polarizations. The baluns have the configurations shown in Figure 3.18(c) and (d). Each balun consists of a link line (LL), a transmission line (TL), an open line (OL), and a short line (SL). In addition, a segment of 50 Ω microstrip line is added at the end of the TL and connected to a 50 Ω coaxial cable at the feed point. LL

and SL are located on the rear side of the balun board, while OL, TL, and 50 Ω microstrip lines are located on the front side of the balun board. The slots and rectangle tabs on the baluns are designed for antenna assembly. All the substrates shown in Figure 3.18 are FR4 substrate with a dielectric constant of 4.3 and a thickness of 0.5 mm. Figure 3.18 also lists all the optimized dimension values of the antenna. The *zx*-plane and *yz*-plane are referred to as the horizontal and vertical planes, respectively.

3.3.2 Analysis and Optimization

The design of the element commences with the four simple dipoles arranged in a square without the feed networks. Here, the length of the dipoles is fixed at 66.2 mm, which is approximately $\lambda_0/2$ (λ_0 is the wavelength at the center frequency 2.2 GHz in free space). To achieve ±45° slant polarizations, the four dipoles are connected as shown in Figure 3.19(a). By placing a differential voltage across A′C′ or B′D′, −45°- or +45°-polarized radiation is generated. Figure 3.19(a) illustrates the current directions in the −45° polarization case. The dipoles are at a height of 29 mm (0.21 λ_0) above the reflector. This height has been selected as the minimum that results in the required bandwidth. A minimum height also results in reduced coupling between adjacent elements in array applications. In the early stage of design, the four dipoles are connected via ideal parallel lines in the analysis as shown in Figure 3.19(a) and 3.19(b). Later, the parallel lines are replaced by physical lines.

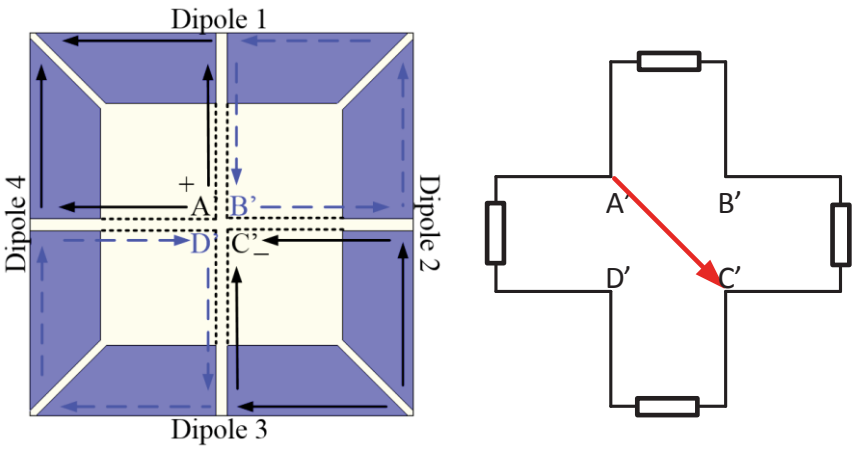

(a) (b)

Figure 3.19 (a) Schematic current distribution and (b) equivalent circuit model of the concentrically arrange dipoles without feed network.

Parameter sweeps of the gap size *(W_g, L_g)* are conducted to show how the coupling

between dipole arms affects the impedance. Figure 3.20 and Figure 3.21 show the real and imaginary parts of $Z_{A'C'}$, respectively, with different W_g and L_g. It is noted in Figure 3.20 that the input impedance of the proposed model without gaps (W_g=0) is significantly different from that of the models with gaps (W_g>0). For the case without gaps, the model is a conventional cross-dipole employing two dipoles. In this case, both the real and imaginary parts of the input impedance vary significantly in the designed band, making the antenna hard to match. By introducing the gaps between dipoles, the variations of the real and imaginary parts are greatly reduced, which makes it easier to match the antenna with a designed feed network. Increasing W_g or L_g can flatten the variation of the reactance with frequency and reduce the resistance within the required band. With the overall goal of obtaining both a stable resistance and reactance, optimum values W_g =0.7 mm and L_g =17.7 mm were chosen in the model.

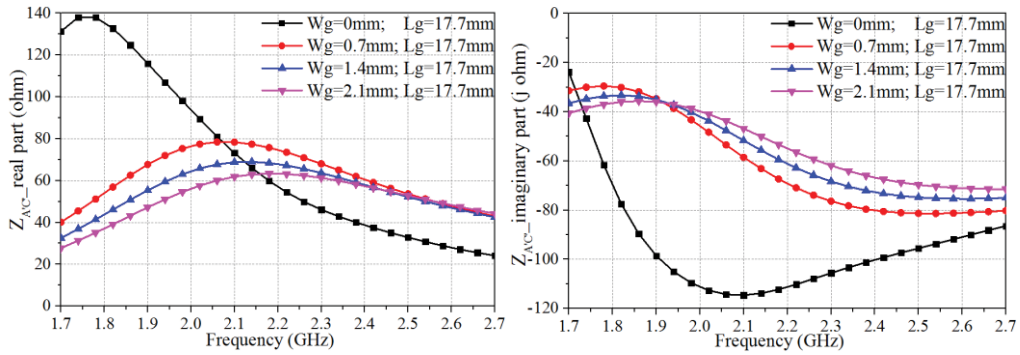

(a) (b)

Figure 3.20 Variation of the (a) real and (b) imaginary parts of the antenna input impedance with different W_g.

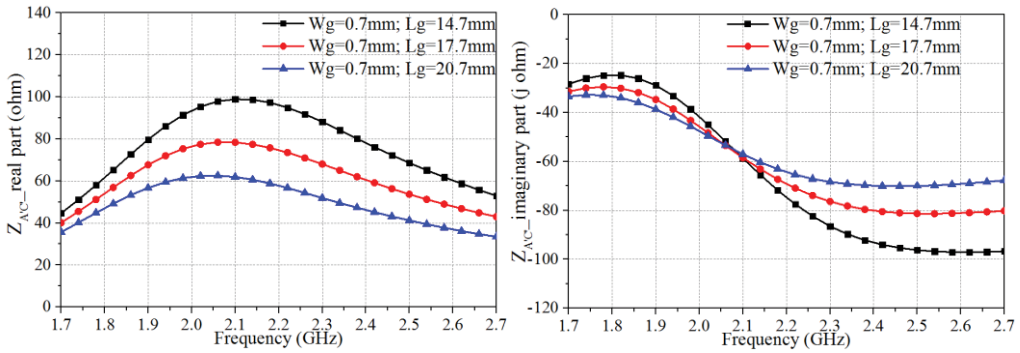

(a) (b)

Figure 3.21 Variation of the (a) real and (b) imaginary parts of the antenna input impedance with different L_g.

With the optimized slot size, the combined radiation pattern of the four electric dipoles produces a stable HPBW and a low cross-polarization level within the required band as shown in Figure 3.22. To be specific, the variation of HPBWs is less than 7°, and the cross-polarization level is less than −23 dB within the main lobe. Moreover, the gaps between the dipoles also provide additional flexibility in the design of the antenna. For example, lumped elements or chokes can be used to load the antenna and allow tuning of the antenna's performance or to achieve reconfigurability with switches.

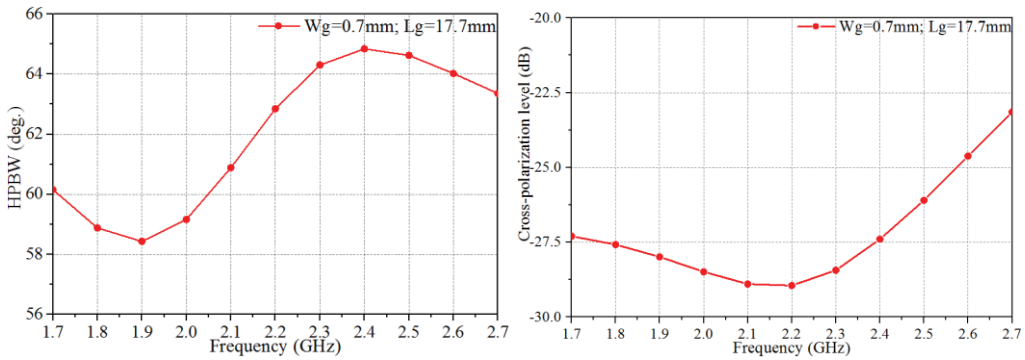

(a) (b)

Figure 3.22 Simulated (a) HPBW (b) cross-polarization level within main lobe with optimized gap size.

After the optimization of the radiators, the same configuration of the feed network as Section 3.2.3 was used to match the antenna. Figure 3.23 shows the equivalent circuit of a feed network for one polarization and its physical realization using microstrip lines. The feed network consists of three line transformers TL_M, LL, and TL to tune the radiators' impedance and a balun formed by OL and SL to provide balance feeding. These circuit components shown in the equivalent circuit are ideal transmission lines. Overall optimization of the matching circuit was conducted based on a circuit theory model. The achieved reflection coefficient with optimized circuit elements is shown in Figure 3.24. Based on the optimized parameters of the circuit model with ideal transmission lines, a 3D model was developed in CST full-wave simulation environment. As there are some discrepancies between the ideal circuit theory model and physical microstrip model, final tuning of the physical model was undertaken to obtain the desired matching result using CST Microwave Studio.

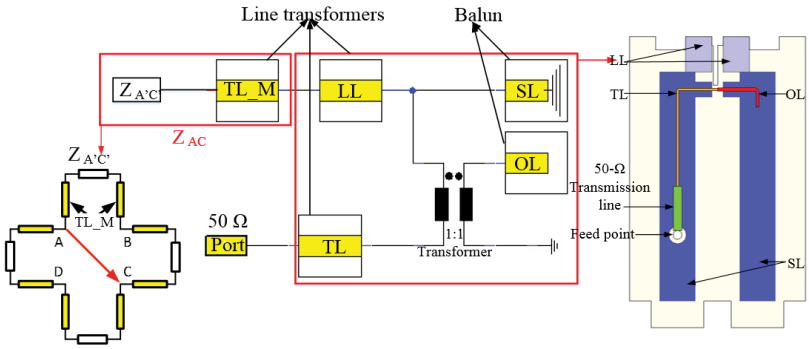

Figure 3.23 Equivalent circuit and the physical implementation of the antenna feed network. (Optimized values for circuit elements: TL_M: 250 Ω, 8.3 mm; LL: 100 Ω, 6.6 mm; SL: 416.7 Ω, 50.7 mm; OL: 113.6 Ω, 20.5 mm; TL: 91.77 Ω, 23.2 mm.)

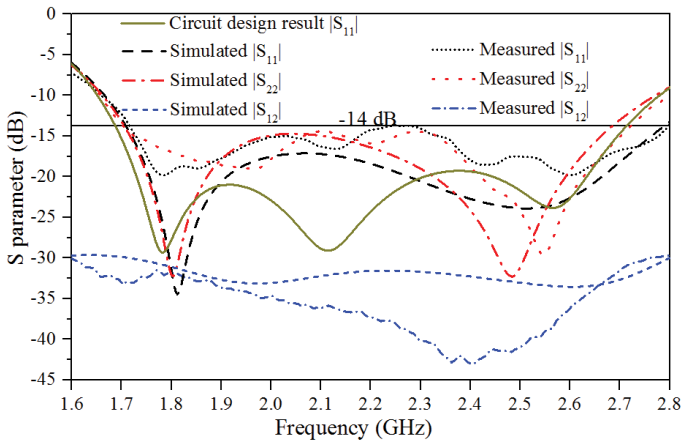

Figure 3.24 The calculated, simulated and measured S-parameters of the antenna.

3.3.3 Experimental Results

To verify the performance of the element, a prototype of the single element was fabricated and tested, as shown in Figure 3.25. Figure 3.24 also plots the simulated and measured S-parameters of the two ports. Within the target band (1.71 GHz to 2.69 GHz), the measured reflection coefficients are all less than −14 dB. The port-to-port isolations of the simulation and measurement results are all more than 30 dB over the entire operating frequency band. The simulated and measured radiation patterns at 1.7, 2.2 and 2.7 GHz in the horizontal plane are shown in Figure 3.26. As the radiators are symmetrically arranged, the radiation patterns of the two polarizations are very similar. Therefore, only the results given here are when port 1 is excited. The simulated and measured patterns agree well with each other. The measured cross-polarization level is less than −25 dB at the boresight. Figure 3.27 shows the simulated and measured HPBW and gain of the dipole antenna for both the two polarizations. The simulated HPBW is

64.6°±3.8° and 64.9°±3.7° for port 1 and port 2, respectively. The measured HPBW is 64.0°±4.5° and 65.3°±4.2° for port 1 and port 2, respectively. The measured gain varies from 8.8 dBi to 10.1 dBi for port 1, and from 8.6 dBi to 9.9 dBi for port 2. The measured results demonstrate that this element achieves a stable radiation pattern over the cellular band without shaping of the reflector or use of walls.

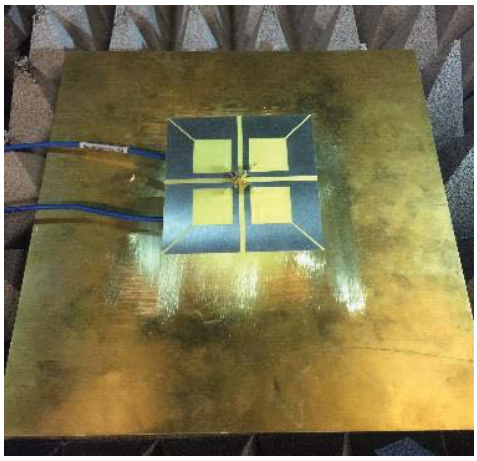

Figure 3.25 Prototype of the antenna.

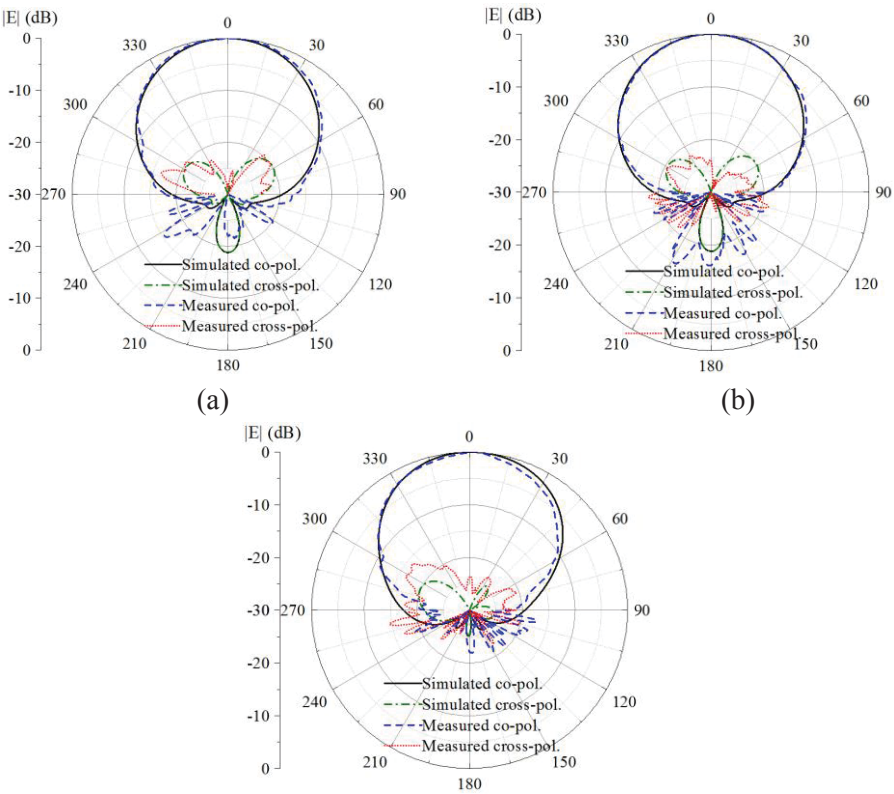

Figure 3.26 Simulated and measured radiation patterns. (a) 1.7 GHz, (b) 2.2 GHz, and (c) 2.7 GHz.

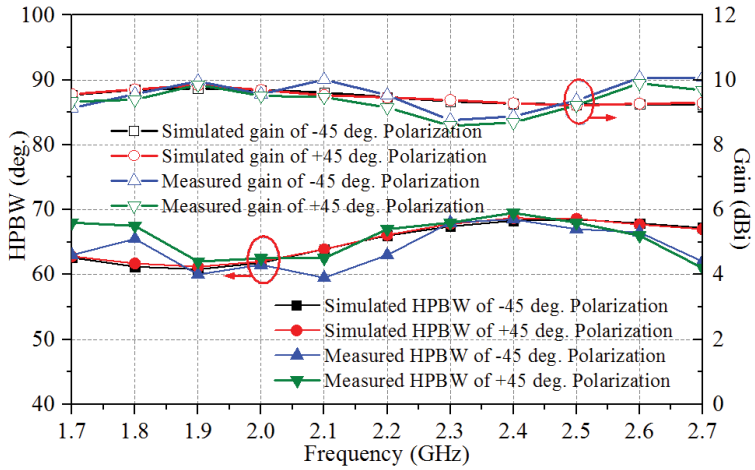

Figure 3.27 Simulated and measured HPBW and gain.

3.4 Comparison

Table 3.3 Comparison of Antenna Performances

Type	Ref	Radiator side length (λ_0)	Ant. height (λ_0)	BW (%)	Isol-ation (dB)	HPBW (°)	Shaped reflect-or	Gain (dBi)	XPD (dB)	Squint (°)
Cross dipole antenna	[16]	0.45	0.23	48	> 22	62.0± 4.0	Yes	8.2± NG	19	NG
	[15]	0.41	0.25	45	> 25	68.0± 2.0	Yes	8.2± 0.6	NG	NG
	[23]	0.39	0.27	54.5	>28.5	66.2± 3.7	Yes	8.5± 0.9	NG	NG
Square-dipole-array antenna	[38]	0.49	0.23	23.7	> 30	65.3± 1.2	Yes	9.7± 0.2	23.5	NG
	[39]	0.42	0.23	27.8	> 25	65.0± 5.0	No	8.0± NG	16	NG
	Ant I	0.51	0.20	46.4	> 28	66.5± 5.5	No	9.8± 0.9	25	< 4
	Ant II	0.49	0.21	44.5	> 30	64.5± 5.0	No	9.4± 0.8	25	NG

* Ant I is the square-folded-dipole-array antenna presented in Section 3.2; Ant II is the simplified square-dipole-array antenna presented in Section 3.3.

A detailed comparison between the designed two square-dipole-array antenna elements and other types of base station antenna elements reported in recently published literature is provided in Table 3.3. It can be seen from the table that, using well-designed square-

dipole-array structures, the antenna elements can achieve comparable performances to that of cross-dipole, but it does not need additional modifications on the ground plane, thus being more suitable to be used in a base station antenna array. Compared with other square-dipole-array elements, the bandwidth of the antenna is almost doubled in our work. Moreover, reduced beam squint is less than 4° is achieved in the work described in Section 3.2. The profiles of the two antennas are relatively low ($0.20\lambda_0$ and $0.21\lambda_0$), which helps to reduce mutual coupling when elements are used in antenna arrays. The comparison demonstrates that the designed two antenna elements are competitive candidates for base station applications.

3.5 Summary

In this section, the square-dipole-array configuration for wideband dual-polarized radiation is investigated. Method of stabilizing radiation pattern and reducing beam squint is analyzed. Theoretical explanation of the working mechanism of the square-dipole-array radiator and design guidelines of wideband matching networks are presented, which greatly facilitate the improvement of performance characteristics of this configuration. Two square-dipole-array antenna elements are designed comprising four folded dipoles and four simple dipoles respectively. Simulated and measured results demonstrate that the two antennas all achieve excellent radiation performance including low cross polarization, stable radiation patterns, and reduced beam squint across a wide well-matched band. Moreover, the elements have simple and low-profile structures and require no walls or other external beam shaping techniques, thus being ideal for use in antenna array systems.

The circuit theory model of the wideband matching network presented in this chapter provides valuable guidance for the general feed network design of current and future BSA elements. It has been used in optimizing antenna feed networks in the next several chapters.

Chapter 4: Cross-Dipole Antennas

4.1 Introduction

Over decades, the cross-dipole antenna has been one of the most promising antennas to meet the industry standard for base station elements. The antenna is constructed as a pair of sub-dipoles oriented perpendicular to each other and backed by a reflector. By exciting either one of the two sub-dipoles, different polarizations can be obtained. Primitive cross-dipoles have the two sub-dipoles "isolated" from each other. The bandwidths they achieve are limited (less than 25%). To broaden the bandwidth, many tightly-coupled cross-dipoles have been designed. The sub-dipoles are closely spaced to introduce mutual coupling between each other. The resultant bandwidth could be enhanced to more than 45%. Although it is known that the coupling between the sub-dipoles in the tightly-coupled cross-dipoles can increase the impedance bandwidth, the fundamental understanding of its working principle is still superficial. Moreover, there is no clear methodology available currently to guide the optimization of the coupling to achieve the best performance.

Recently, some improved cross-dipole antenna elements have been presented to further broaden the bandwidth of cross-dipoles. In those configurations, parasitic elements such as strips, disks, or loops are introduced near the radiators. The bandwidth can be enhanced to more than 60%, but with a sacrifice of the radiators' size or antennas' height. Therefore, it is still a big challenge to broaden bandwidth while maintaining a compact size for the cross-dipole antennas.

In this chapter, the two issues mentioned above related to the development of cross-dipole antennas are addressed. Section 4.2 presents a deep understanding and the design guideline of tightly-coupled cross-dipole antennas. A simplified cross-dipole antenna is designed to verify the theoretical analysis. Section 4.3 focuses on a novel bandwidth enhancement technique for cross-dipole antennas. By applying the technique, the bandwidth of an isolated cross-dipole element (ICD) and a tightly-coupled cross-dipole (TCCD) element are enhanced to 46% and 63%, respectively, with a very compact size.

4.2 Simplified Tightly-Coupled Cross-Dipole Antenna

4.2.1 Model Description

The analysis in this work is based on a cross-dipole antenna with a simplified configuration as shown in Figure 4.1(a). It consists of two identical sub-dipoles placed perpendicular to each other. Square-looped dipole arms are used in order to have a larger aperture to get more bandwidth and gain. The traces constructing the square-looped arms have length *L* and width *W*. The square-looped arms are placed close to each other and separated by a small distance *s*. This choice enables the strong coupling between the elements. The dipoles are printed on a Rogers 4530B substrate whose relative permittivity and permeability are, respectively, 3.55 and 1.0; loss tangent is 0.0027; and thickness is 1.524 mm. The driven dipole is shown in Figure 4.1(b). The other dipole is a parasitic element. The traces between the square loops have a 0.3 mm width.

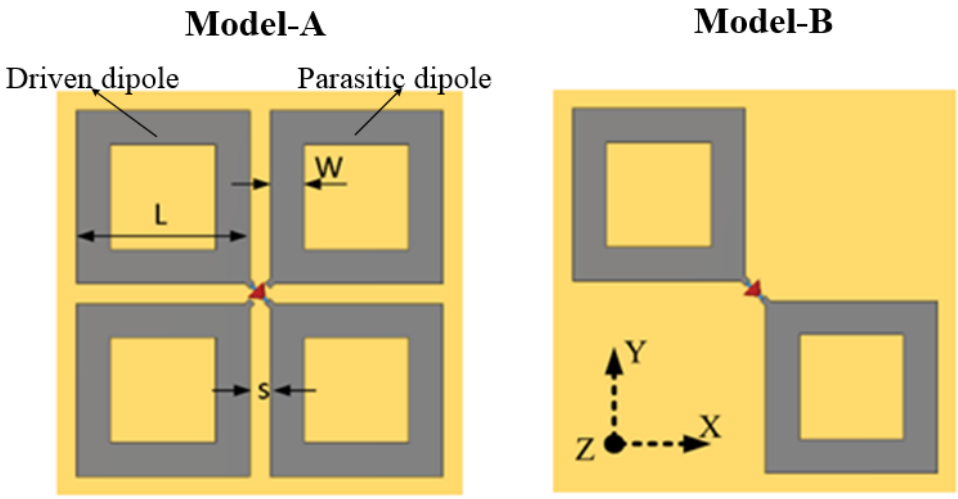

(a) (b)

Figure 4.1 Cross-dipole geometry. (a) Model-A: tightly-coupled cross-dipoles consisting of a driven dipole and a parasitic dipole. (b) Model-B: driven dipole only.

The analysis is conducted within the frequency band from 1.7 to 2.7 GHz, which covers the base station operational band from 1.71 to 2.69 GHz. The data used for the theoretical analysis are obtained from a simulation model which does not include the presence of the matching circuit and balun. The matching circuit and balun are only used to facilitate impedance matching and a balanced feed. This model choice simplifies the computational effort; it is very reasonable because the matching circuit will be shielded by the balun in

reality and a well-designed balun only has minor currents on its outer surface. Consequently, the latter will have only a very minor effect on the radiation performance. The theoretical model thus leads to an optimized cross-dipole structure that provides a satisfactory assessment of the radiation performance and impedance bandwidth. The balun and matching circuit are then added back into the optimized theoretical design, and the cross-dipole system is re-optimized to achieve impedance in the target band.

4.2.2 Coupling Analysis

By exciting the driven dipole shown in Figure 4.1(b), the parasitic dipole included in Figure 4.1(a) can also be activated because of the coupling between them. To determine how the coupling changes the overall performance, the driven dipole was simulated by itself. The differences between the results of these two models were then obtained. The model with and without the parasitic dipole is denoted as Model-A and Model-B, respectively. The traces in Model-A and Model-B had the same dimensions (L = 25.5 mm, W = 6.0 mm, s = 3.0 mm). Their dipole elements were placed above a square reflector at a vertical distance of h = 32 mm. The size of this square reflector was 160 × 160 mm^2. These design parameter values were selected to facilitate having the resulting idealized cross dipole system work properly in the target band.

4.2.2.1 Impedance

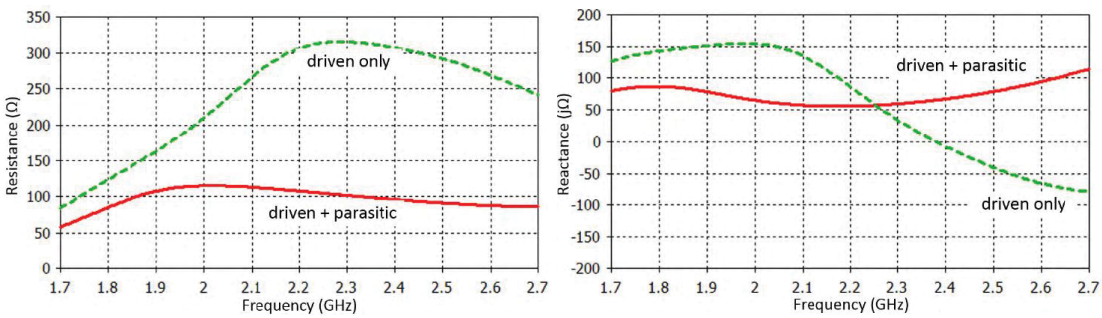

(a) (b)

Figure 4.2 Variations of the impedance of Model-A and Model-B in the target band. (a) Resistance. (b) Reactance.

Figure 4.2(a) and (b) shows the variations of the resistance and reactance, respectively, of Model-A and Model-B across the design frequency band. It is observed that the fluctuations in both the resistance and the reactance are smaller with the presence of the parasitic dipole. This behavior indicates that the parasitic dipole alleviates the impedance variation of the driven dipole, making it easier to match the system to a real source within

the design band. The bandwidth is also enhanced with the parasitic dipole because it leads to a larger size of the radiating structure.

4.2.2.2 Radiation Performance

Comparisons of the main radiation performance indices of interest are listed in Table 4.1. It is clear that the coupling between the driven and parasitic dipoles offers a higher directivity, a narrower HPBW, and a higher XPD within ±60° of the *z*-axis in the horizontal plane cut (*zx*-plane). To have a better understanding of what causes these enhancements, the current distributions within the apertures of both models are depicted in Figures 4.3(a) and (b). It is observed that the driven dipole exhibits the standard behavior with or without the coupling, i.e., the peaks of the current distributions occur near the excitation source, and the valleys are located at the ends of the dipole arms. On the other hand, the parasitic dipole has a different current distribution since it is excited by the capacitive coupling between the parallel branches of the two sub-dipoles.

Table 4.1 Comparison of the Radiation Performance of Model-A and Model-B

	Model-A: driven + parasitic dipoles	Model-B: driven dipole only
Directivity (dB)	8.6 – 9.3	8.5 – 9.0
HPBW (deg.)	63 – 69	65 – 75
XPD @ 0° (dB)	> 50	> 50
XPD @ 60° (dB)	9 – 11	7 – 11

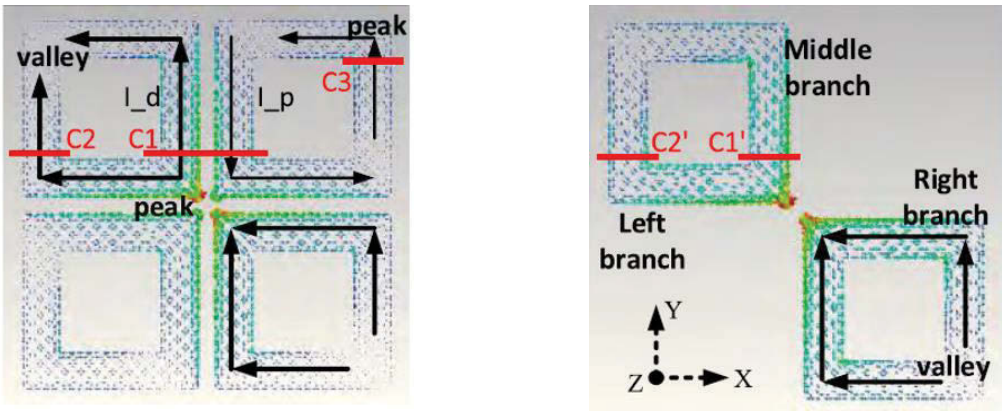

(a) (b)

Figure 4.3 Current distributions on the traces of the models. (a) Model-A. (b) Model-B.

The currents were monitored on several branches of the dipoles and as a pair of adjacent branches. One observed feature was that the induced current *I_p* and the driven current *I_d* are out of phase. This phenomenon is interesting since a reverse current should

theoretically reduce the directivity, but the realized directivity is even higher. In order to explain this dichotomy, the trace current monitors: C1, C2, C3, C1' and C2', were located as shown in Figure 4.3. They are placed near the peaks of the current distributions on the individual branches. Due to the diagonal symmetry of the aperture, the current distributions on the *x*- and *y*-aligned branches are identical. Therefore, only the *y*-aligned currents were monitored and analyzed. Moreover, the *y*-aligned currents on the left-, middle-, and right branches work together to produce field contributions analogous to a 3-element dipole array. This aspect facilitated explaining the results. The magnitudes and phases of the currents within the entire frequency band were obtained.

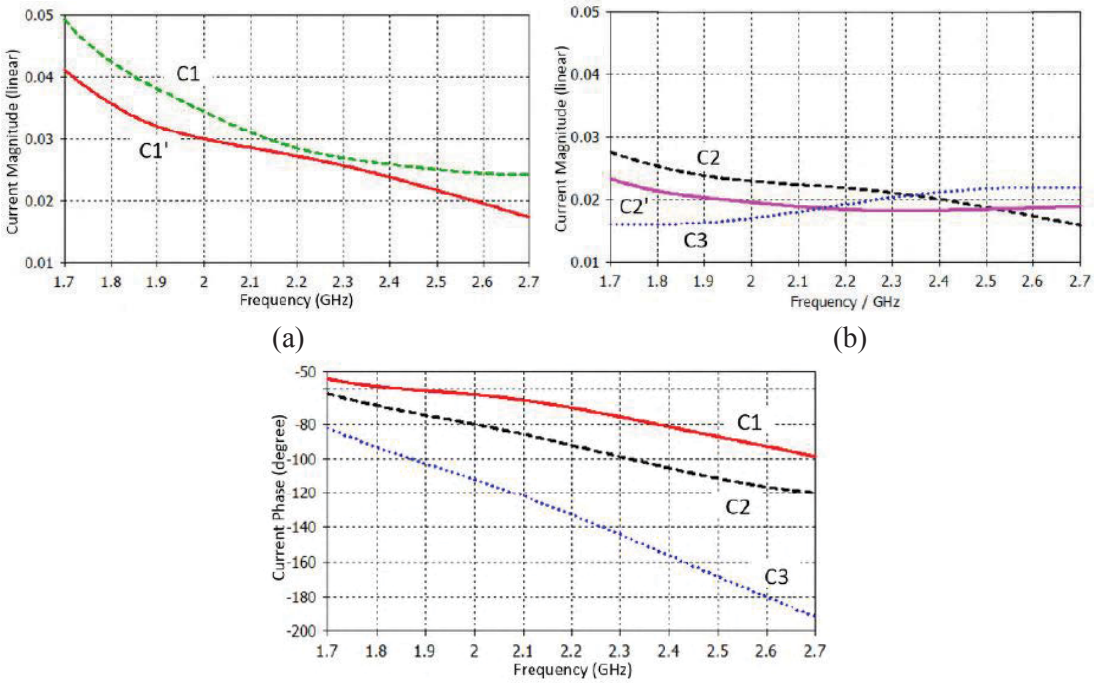

Figure 4.4 Simulated currents. (a) Current magnitudes on the middle branches of Model-A and Model-B. (b) Current magnitudes on the side branches of Model-A and Model-B. (c) Current phases on three different branches of Model-A.

The current magnitudes on the middle branches of the two models at C1 and C1' are compared in Figure 4.4(a). Their values on the left branches at C2, C2' and those on the right branch at C3 are compared in Figure 4.4(b). First, notice that the magnitudes of the total current (I_d - I_p) on the middle branch with or without the coupling are at the same level (i.e., $C1 \approx C1'$). Although the coupling introduces a reverse current I_p on the parasitic dipole, an increase of the current density on the driven dipole I_d compensates

for it. Hence, there is no reduction in the directivity. Second, notice that the currents on the left-most branch of the driven dipole with or without the coupling also remain at a similar level (i.e., $C2 \approx C2'$). Third, notice that there is additional current (C3) induced on the top right branch of the parasitic element and it has a magnitude comparable to the driven current on the left branch (i.e., C3 is comparable with C2). Finally, the phases of the currents on the left-, middle-, and right-branches of Model-A are plotted in Figure 4.4(c). The phase differences between these currents are < 90° within the entire band. Therefore, the contributions to the radiated field from the three *y*-aligned currents add coherently on boresight. The outcome is the fact that a higher directivity and a narrower HPBW are obtained from this cross-dipole system.

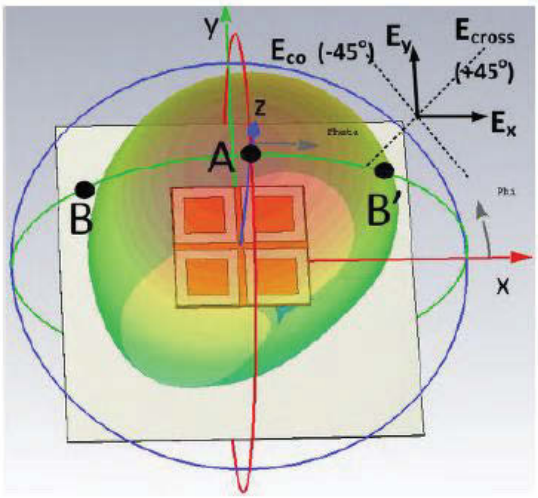

Figure 4.5 3D radiation pattern of the proposed tightly-coupled cross-dipole.

The XPD is another crucial factor used to assess the radiation performance of a base station antenna. In order to achieve a higher XPD in base station designs, one must start by investigating what contributes to it. Grasping the impact of this performance factor can be confusing because one usually looks at the ±45° polarization vector in the *zx*-plane cut ($\phi = 0°$) rather than in the $\phi = 45°$ cut. To examine its meaning, consider the electric field that is generated by the cross-dipole antenna as shown in Figure 4.5. The far-field *x*- and *y*- components can be expressed as:

$$\hat{x} \cdot \vec{E} = E_x e^{j\phi_x}, \ \hat{y} \cdot \vec{E} = E_y e^{j\phi_y} \tag{4.1}$$

which is commensurate with the presence of the already identified *x*- and *y*-aligned currents in Figure 4.3(a). Then the co- and cross-polarized field vectors in the $\phi = 45°$

cut planes take the form:

$$E_{co} = \cos\frac{\pi}{4}E_x e^{j\phi_x} + \cos\frac{\pi}{4}E_y e^{j\phi_y}$$
$$E_{cross} = \cos\frac{\pi}{4}E_x e^{j\phi_x} - \cos\frac{\pi}{4}E_y e^{j\phi_y} \tag{4.2}$$

The XPD is the ratio of the co- and cross-pol magnitudes:

$$XPD = \left|\frac{E_{co}}{E_{cross}}\right| = \sqrt{\frac{E_x^2 + E_y^2 + 2E_xE_y\cos(\phi_x - \phi_y)}{E_x^2 + E_y^2 - 2E_xE_y\cos(\phi_x - \phi_y)}} = \sqrt{\frac{1+M}{1-M}} \tag{4.3}$$

where

$$M = \frac{2E_xE_y\cos(\phi_x - \phi_y)}{E_x^2 + E_y^2} \tag{4.4}$$

Note that if one observes the fields at a point infinitely far away from the antenna aperture, both E_x and E_y components arrive at essentially the same time, which means $\phi_x = \phi_y$. Therefore, the term M can be written to a very good approximation as

$$M = \frac{2E_xE_y}{E_x^2 + E_y^2} = \frac{2}{\frac{E_x}{E_y} + \frac{E_y}{E_x}} \tag{4.5}$$

Then to connect the XPD value to the field components most naturally generated by the currents on the antenna elements, we define

$$N = \frac{E_x}{E_y} \tag{4.6}$$

as the cross polarization discrimination factor between the *x*- and *y*-polarized far-field components. Then the actual XPD factor can be expressed as

$$XPD = \left|\frac{N+1}{N-1}\right| \tag{4.7}$$

Consequently, it is now clear that in order to obtain a larger XPD as required for base station applications, N should be as close to 1 as possible. In other words, we have to optimize the antenna to maintain the difference between the magnitudes of the generated *x*- and *y*- polarized radiation to be as small as possible in the *zx*-plane cut across the entire operational band.

Figure 4.6 compares the *x*- and *y*-polarized radiation patterns generated with Model-A and Model-B in the *zx*-plane cut. A strictly diagonal, symmetric structure relative to the

boresight direction would ensure that $E_x = E_y$ and, hence, would produce an infinitely high XPD @0°. As shown, this is true for both models. However, the symmetry in a real environment is difficult to ensure, and the ratio of the field components may deteriorate some from unity, resulting in a lower XPD.

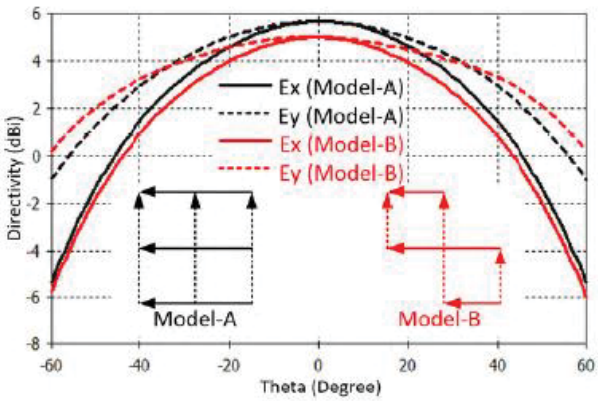

Figure 4.6 Comparison of *x*- and *y*-aligned radiation patterns of Model-A and Model-B.

Note that this symmetry generally no longer exists at the edges of the coverage directions, i.e., when $\theta \approx \pm 60°$. As illustrated in Figure 4.6, although both E_x and E_y are getting smaller as θ varies from 0 to ±60°, E_x decreases faster than E_y. This behavior is more noticeable for the non-symmetric Model-B. Although the *x*- and *y*-aligned currents are nearly the same, the asymmetry of the overall structure causes the patterns in the E-plane (horizontal cut, *zx*-plane) and H-plane (vertical cut, *yz*-plane) to be different. In contrast, the more symmetric Model-A, in which the parasitic sub-dipole is excited by the mutual coupling effects, leads to more stable E- and H-plane patterns and a larger XPD across the entire coverage range.

4.2.3 Design Methodology

To more closely tie the design parameters to its performance characteristics, we have developed an analytical array model of the tightly-coupled cross-dipole antenna. This model and a parameter study based on it provide further insights into how the system achieves low VSWR, stable HPBW, and high XPD across the coverage range and the operational bandwidth.

4.2.3.1 Array Model

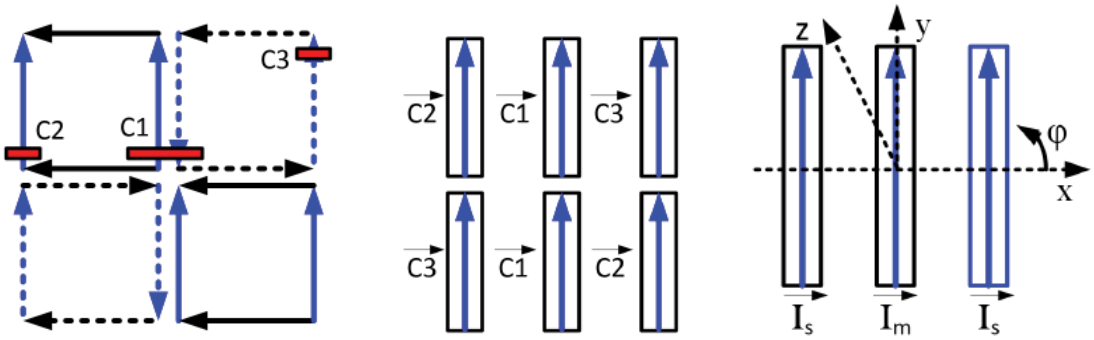

(a) (b) (c)

Figure 4.7 Representation of the current distributions. (a) Schematic for the tightly-coupled cross-dipole antenna. (b) Equivalent six-element dipole array for model-A. (c) Reduced, equivalent three-element dipole array model.

Figure 4.7(a) presents a schematic of the current distributions on the cross-dipole aperture. The solid and dashed arrows denote the directly-excited currents and the induced parasitic currents, respectively. To develop the array model, only the *y*-aligned currents are considered. An analogous model can be developed in the same manner for the *x*-aligned currents.

The three current monitors C1, C2, and C3 identified previously, monitor the magnitudes and phases at the peaks of their distributions. Due to the observed symmetries, there are only three unique current vectors on the aperture:

$$\begin{aligned} \overrightarrow{C1} &= C1e^{j\phi_1}, \\ \overrightarrow{C2} &= C2e^{j\phi_2}, \\ \overrightarrow{C3} &= C3e^{j\phi_3}, \end{aligned} \tag{4.8}$$

They are identified in Figure 4.7(b). Although these three current vectors have different magnitudes and phases, they all have similar quarter-period quasi-sinusoidal magnitude distributions and small phase differences < 90° as long as the size of the cross-dipole system is reasonable (i.e., the side length of the aperture is near a half-wavelength). Therefore, we can merge the current vectors on the six branches of the model depicted in Figure 4.7(b) into the three dipole current vectors shown in Figure 4.7(c).

Next, because the detected currents on the outside branches of the three-element array are the same, the currents on their equivalent dipoles will be denoted by the vector $\overrightarrow{I_s}$. The current on the equivalent center dipole is then denoted by the vector $\overrightarrow{I_m}$. From the

Model-A simulation data, it is found that the currents $\overrightarrow{I_s}$ and $\overrightarrow{I_m}$ have identical half-period quasi-sinusoidal current directions, to be denoted as $\overrightarrow{I_0}$. Thus, they can be represented as

$$\overrightarrow{I_s} = \overrightarrow{I_0}(C3e^{j\phi_3} + C2e^{j\phi_2})/2,$$
$$\overrightarrow{I_m} = \overrightarrow{I_0}C1e^{j\phi_1}, \tag{4.9}$$

where $\overrightarrow{I_s}$ is the combination of the branch currents C2 and C3, as depicted in Figure 4.7.

The radiation pattern generated by these three *y*-polarized current elements can be represented as

$$F_y(\theta,\phi) = AF(\theta,\phi) \times f_0(\theta,\phi) \tag{4.10}$$

where $AF(\theta,\phi)$ is the three-element array factor, and $f_0(\theta,\phi)$ is the radiation pattern of a dipole element. The corresponding radiation pattern, $F_x(\theta,\phi)$, that is generated by the analogous *x*-oriented three-element dipole array model has the same form. Consequently, it can be related to $F_y(\theta,\phi)$ by simple rotation, i.e., as:

$$F_x(\theta,\phi) = F_y(\theta,\phi + 90°) \tag{4.11}$$

Therefore, combining the fields radiated by both the *x*- and *y*-aligned currents, the total radiation pattern is:

$$F(\theta,\phi) = F_x(\theta,\phi) + F_y(\theta,\phi) = F_y(\theta,\phi + 90°)+F_y(\theta,\phi) \tag{4.12}$$

The *zx*-cut of this radiation pattern is

$$\begin{aligned} F(\theta,\phi = 0) &= F_y(\theta,\phi = 0) + F_y(\theta,\phi = 90°) \\ &= AF(\theta,\phi = 0) \times f_0(\theta,\phi = 0) \\ &\quad +AF(\theta,\phi = 90°) \times f_0(\theta,\phi = 90°) \\ &= AF(\theta,\phi = 0) \times f_H(\theta) + AF(\theta,\phi = 90°) \times f_E(\theta) \end{aligned} \tag{4.13}$$

where $f_H(\theta)$ and $f_E(\theta)$ represent the H- and E-plane patterns of the dipole oriented along $\overrightarrow{I_0}$. Because the *y*-aligned currents are spaced along the *x*-axis, the array factor along the *y*-axis is identically equal to 1.0, i.e.,

$$AF(\theta,\phi = 90°) \equiv 1 \tag{4.14}$$

Therefore, the cross-dipole's radiation pattern in the *zx*-cut (4.13) can be rewritten as

$$F(\theta,\phi)|_{\phi=0} = AF_H(\theta,\phi = 0) \times f_H(\theta) + f_E(\theta) \tag{4.15}$$

where AF_H is the three-dipole element array factor in the dipole's H-plane. The first and second terms in this expression represent the contributions from the *x*- and *y*-aligned

dipole currents, respectively.

From Eq. (6), one then has

$$N = AF_H \times f_H / f_E \tag{4.16}$$

and the XPD factor from Eq. (7) becomes:

$$XPD(\theta) = \left|\frac{N(\theta)+1}{N(\theta)-1}\right| = \left|\frac{f_E(\theta) + AF_H(\theta) f_H(\theta)}{f_E(\theta) - AF_H(\theta) f_H(\theta)}\right| \tag{4.17}$$

Therefore, it is concluded that the radiation performance characteristics, XPD and HPBW, are determined simply with the array factor $AF_H(\theta)$ and the dipole's E- and H-plane patterns, $f_E(\theta)$ and $f_H(\theta)$. Consequently, when the physical dimensions of the cross-dipole antenna are being optimized, one is equivalently manipulating the array factor and the radiation patterns of the array elements.

From equation (9) and Figure 4.7(c), the three-element dipole array factor is calculated as:

$$\begin{aligned} AF(\theta) &= \left|\sum_{n=1}^{3} W_n e^{-jk\cdot r_n}\right| \\ &= \left|A_s I_0 e^{j\phi_s} e^{jk(-d)\cos(\theta)} + A_s I_0 e^{j\phi_m} e^{j0} + A_s I_0 e^{j\phi_s} e^{\mathrm{jkdcos}(\theta)}\right| \\ &= I_0 \left|2A_s \cos(kd\cos\theta)\, e^{j(\Delta\phi)} + A_m\right| \end{aligned} \tag{4.18}$$

where $k = 2\pi/\lambda$, $\Delta\phi = \phi_s - \phi_m$, and d is the separation distance between the dipole elements. The array factor is thus calculated straightforwardly once the magnitudes and phases of the currents are obtained from the monitors C1, C2, and C3.

Figures. 4.8(a) and (b) show the E- and H-plane radiation patterns, $f_E(\theta)$ and $f_H(\theta)$, respectively, of a straight half-wavelength dipole placed a quarter-wavelength above a ground plane and oriented parallel to it for several source frequencies. To eliminate the effect of the ground plane's size, it is set to be infinitely large. It is observed from these two sub-figures that a typical dipole placed above a reflector has its H-plane pattern getting wider and its E-plane pattern being relatively stable as the frequency increases. Figure 4.8(c) plots the array factor patterns of Model-A alone in free space. Figure 4.8(d) plots the corresponding cross-dipole array patterns calculated from (4.15) at the same frequencies. These composite patterns are very stable across the target band. It is clear that along with the stable E-plane patterns, the array factor variations with frequency nicely compensate for the variations in the H-plane patterns, resulting in very stable

overall patterns.

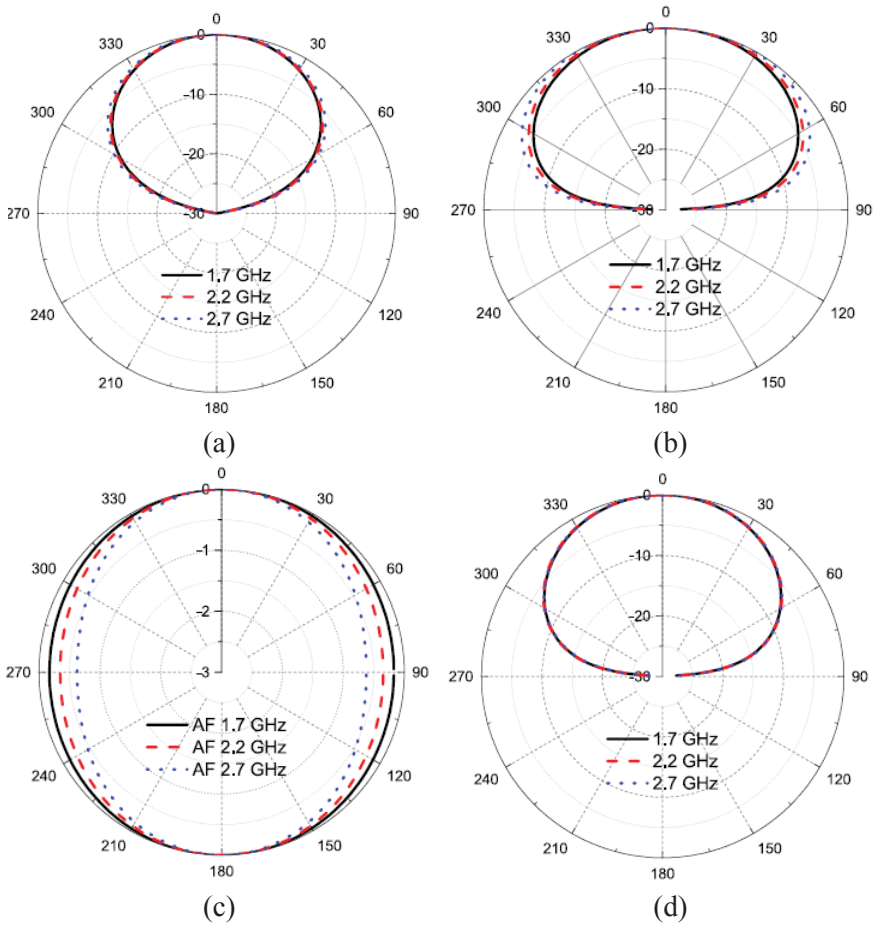

Figure 4.8 Simulated radiation patterns. (a) E-plane pattern and (b) H-plane pattern of a single half-wavelength dipole placed a quarter-wavelength above an infinite ground plane and oriented parallel to it. (c) Three-element array factor pattern alone. (d) Model-A-based cross-dipole radiation pattern.

4.2.3.2. Parameter Analysis

The array model analysis theoretically demonstrated why a stable radiation pattern can be realized across a wide band with a cross-dipole configuration. Because only the E- and H-plane patterns of the equivalent dipole elements and the H-plane array factor determining the overall pattern, there are methods available to engineer these key factors. These include:

- E-plane pattern of a dipole above a reflector $f_E(\theta)$:

  Dipole length; distance away from the reflector; reflector size.

- H-plane pattern of a dipole above a reflector $f_H(\theta)$:

Distance away from the reflector; reflector size.

- H-plane array factor $AF_H(\theta)$:

  Shape of the array element, which changes the amplitude and phase distributions on it (e.g., adding a slot/stub to or bending it can result in a different array factor); separation distance between the array element.

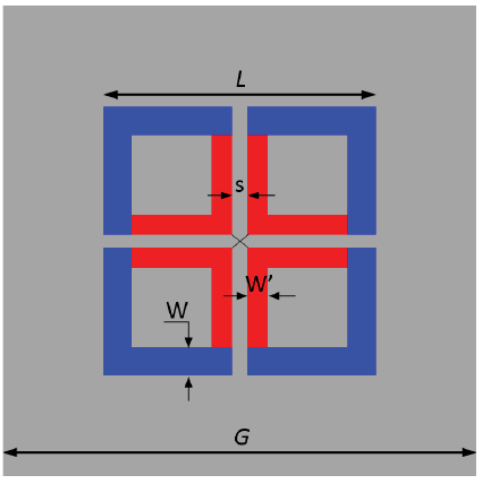

Figure 4.9 Revised and simplified cross-dipole configuration.

Table 4.2 Optimized Dimensions of the Simplified Cross-dipole Antenna

Parameters	Values (mm)	Description
L	60.0	Aperture length
W	5.5	Width of the outside branches
W'	4.0	Width of inside branches
s	5.4	Distance between inside arms
h	33.0	Antenna height
G	160.0	Reflector's length

These methods are used to optimize the design of the simplified, practical cross-dipole model illustrated in Figure 4.9. The adjustable parameters are the aperture length L, outside branch width W (black branches), inside branch width W' (grey branches), gap width s, antenna height h, and ground plane reflector size G. It is noted that any of these parameters and any of their combinations can affect the radiation patterns. Furthermore, some of these parameters are also critical for impedance matching. To obtain a cross-dipole system that meets all of the design specifications, it is very helpful to know how each parameter impacts the overall performance. A variety of parameter sweeps were investigated. During each sweep, only one of these design parameters was allowed to vary

and the others were fixed to the values listed in Table 4.2. These tabulated dimensions are their optimized values, which were obtained with an exhaustive set of simulations, and are the ones used for the fabrication of the prototype antenna.

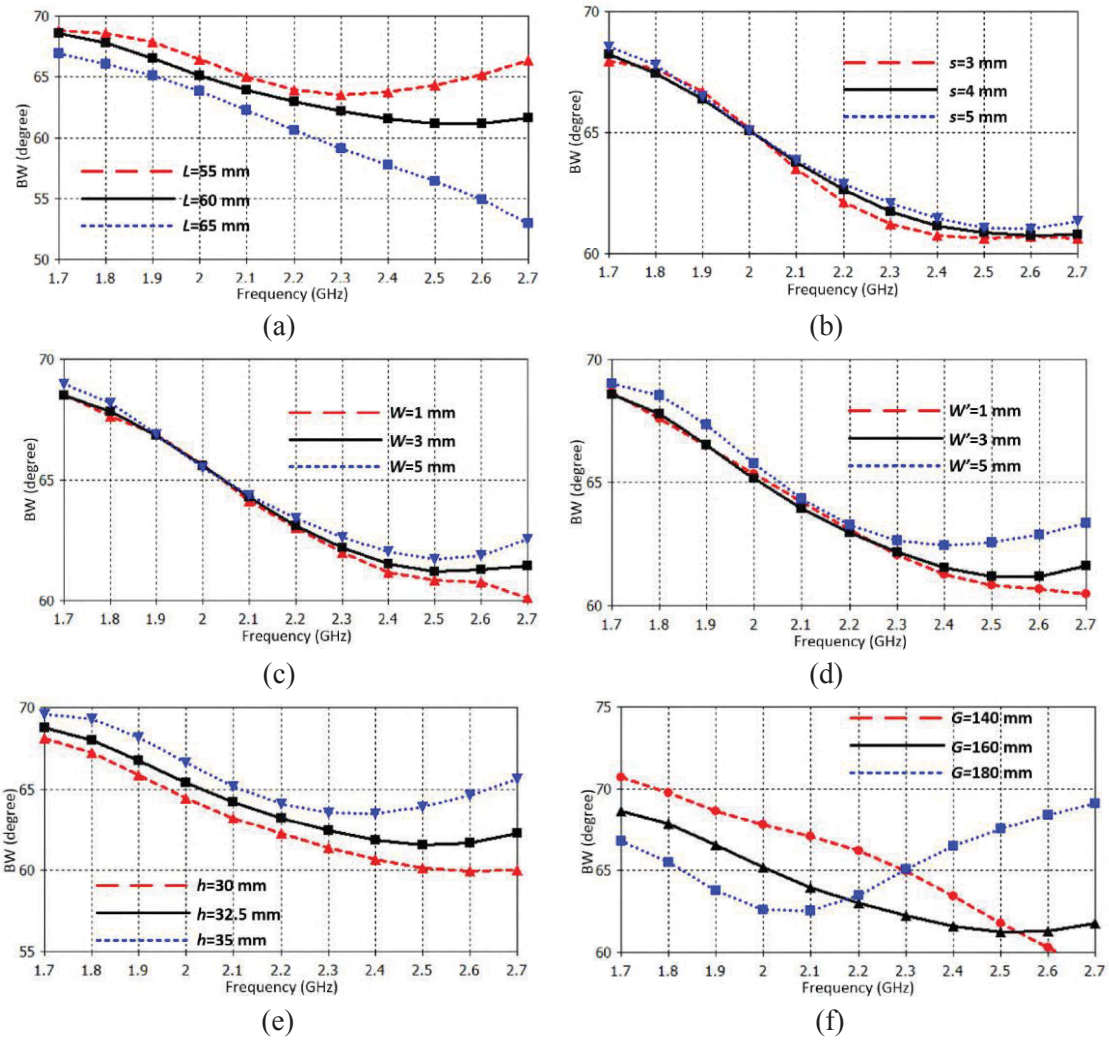

Figure 4.10 HPBW plotted on the Z-Smith diagram for the parameters: (a) L, (b) s, (c) W, (d) W', (e) h, and (f) G.

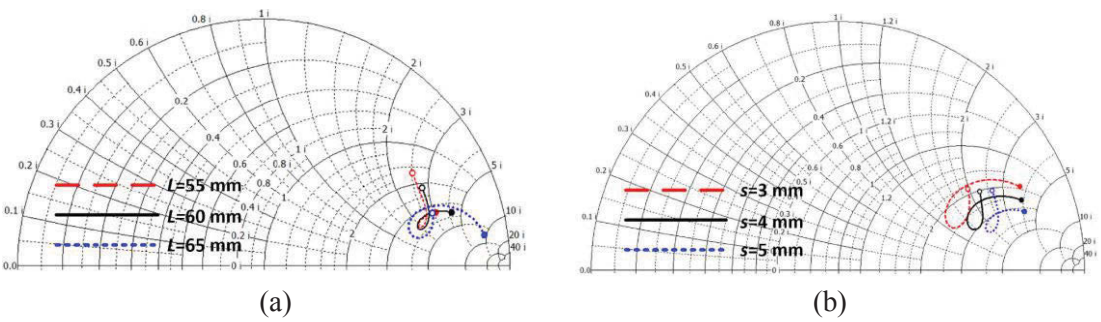

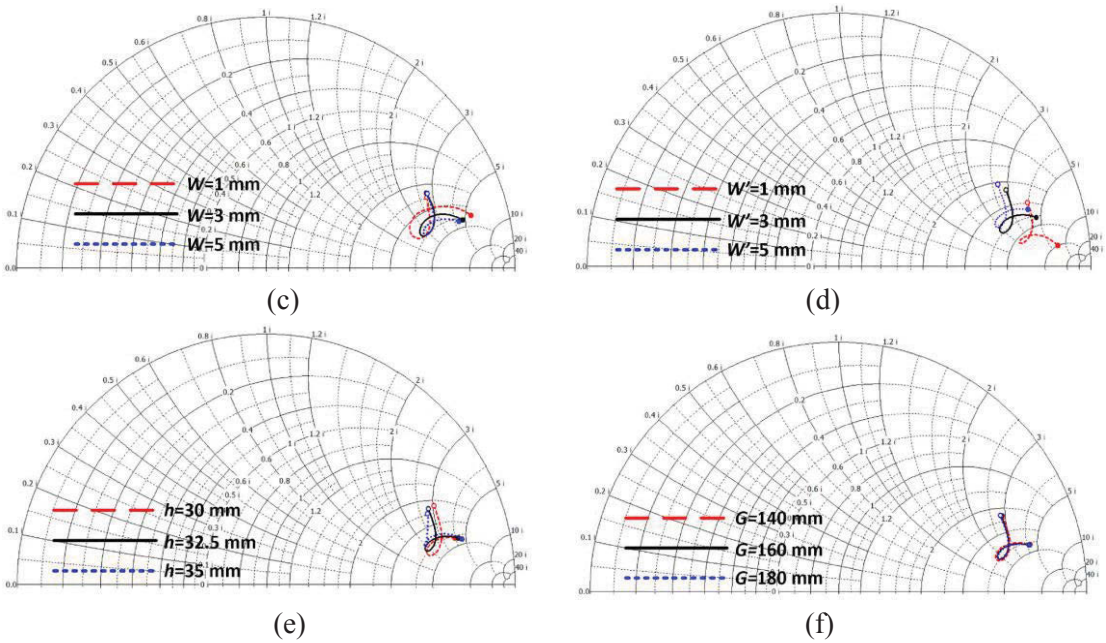

Figure 4.11 Input impedance plotted on the Z-Smith diagram for the parameters: (a) L, (b) s, (c) W, (d) W', (e) h, and (f) G.

Figures 4.10 and 4.11 illustrate how each design parameter affects the HPBW and the input impedance of the cross-dipole system. Only the HPBW results are presented in Figure 4.10 since it is a key coverage parameter and whatever impacts it will also affect the other radiation performance characteristics such as the XPD and gain. The input impedance results given in Figure 4.11 are obtained for the cross-dipole elements placed above the reflector, but with no feed network being present.

As shown in Figure 4.10(a), the HPBW varies significantly with the aperture length L. This is attributed to the fact that L is closely related to the array factor $AF_H(\theta)$ as $L/2$ is the separation distance between the array elements. A larger L results in a more directive $AF_H(\theta)$, and thus a narrower HPBW. At the same time, L is also a key parameter for tuning the input impedance as shown in Figure 4.11(a). Figures 4.10 (e) and (f) show that the HPBW also changes with the antenna height h and the ground plane reflector size G. These larger variations are associated with the fact that h and G critically impact the dipole radiation patterns $f_E(\theta)$ and $f_H(\theta)$. However, they do not affect the couplings that occur between the elements in the aperture. Consequently, they do not affect the array factor $AF_H(\theta)$. Moreover, as long as they are changed in reasonable ranges, they do not affect much to the input impedance. This feature is illustrated in Figures 4.11(e) and (f).

As shown in Figures 4.10(b), (c), and (d), the remaining parameters: s, W, and W' only

demonstrate minor abilities to aid in the tuning of the HPBW. This fact is easy to understand since the radiation pattern of a dipole is much more closely related to its length rather than to its widths. On the other hand, optimizing those widths and the coupling distance between the dipole branches is critical for realizing good impedance matching. The parameter sweep results shown in Figures 4.11(b), (c), and (d) prove the fact that these parameters have a definite impact on the input impedance tuning.

4.2.3.3. Discussion

The presented analysis and results demonstrate that the tightly-coupled cross-dipole configuration addressed in this work can be decomposed into two arrays, an *x*-aligned and a *y*-aligned 3-element dipole array placed above a ground plane reflector. The radiation pattern was determined to be given by two factors: the E- and H-plane patterns of the dipole element and its ground plane image, and the bare H-plane array factor. Because with increasing frequency the patterns associated with the dipole (pattern widens) and array factor (pattern narrows) have compensating effects, high pattern and, hence, high XPD consistency can be achieved across the entire operational band.

The imaging effects, of course, can be controlled by the reflector's size G and the distance h between dipole elements and reflector. They have a significant effect on the radiation pattern but only a minor effect on the input impedance. The array factor is a much more important factor for the radiation performance, especially for the XPD. However, as shown in Figure 4.9, it is not easy to adjust the array factor because of competing effects. Changing L can change the array factor, but it also affects the impedance matching. A more appropriate and practical method to change the array factor is to introduce parasitic elements. Equivalently, this introduces more array elements, resulting in an array factor that can be engineered.

Based on the identified features of the equivalent dipole array model, the following design procedure is advocated:

- First, the design dimensions L, h, and G should be determined to yield a satisfactory radiation performance. We have employed the commercial software environment CST Microwave Studio for these simulation parameter studies. The antenna height h and reflector size G are expected to be as small as possible to guarantee a compact structure. Parasitic elements should be considered to better shape the beam if necessary.
- Second, the design parameters s, W, and W' should be optimized to facilitate

good input impedance matching. To determine whether the realized cross-dipoles can be matched in the target band, one can export the simulated S1p file representing the input impedance. One can then connect it with an idealized matching circuit in the MWS circuit simulator as shown in Figure 4.12(c) to optimize the system. This matching method, as described in Section 3.2.3, is an optimal way to match the dipole antennas to the feed network and readily leads to a printed circuit board (PCB) implementation. Subsequently, a physical matching circuit can be designed from the resulting optimized circuit theory model.

- Finally, if needed, minor overall adjustments can be made to the overall design to achieve excellent impedance matching performance.

4.2.4 Antenna Design

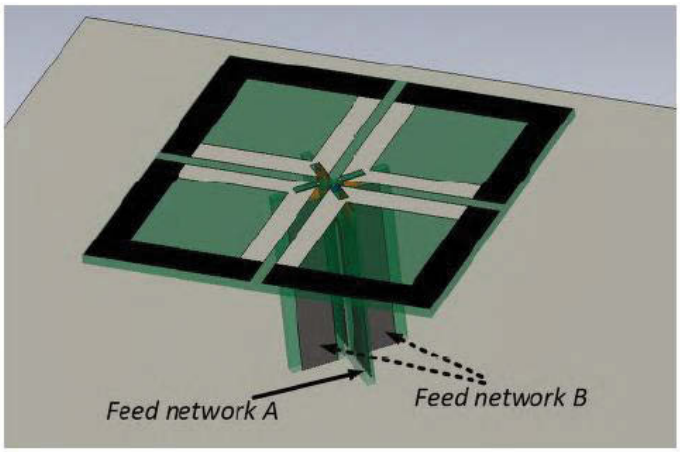

(a)

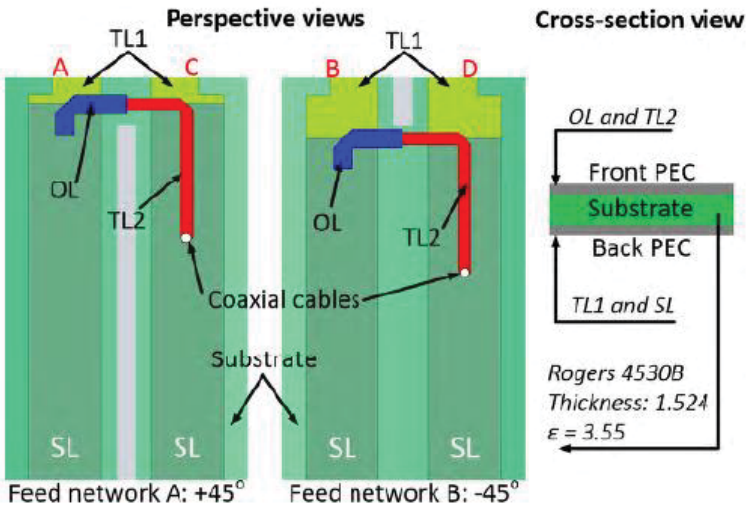

(b)

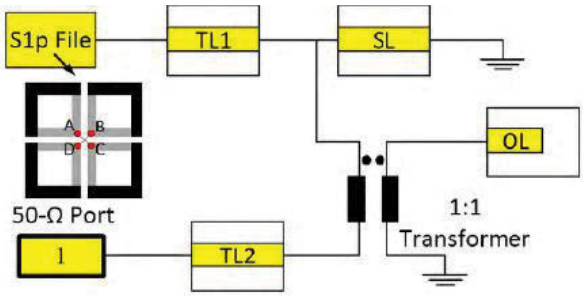

(c)

Figure 4.12 Optimized simplified cross-dipole antenna. (a) Perspective view. (b) Details of the two feed networks implemented using PCBs. (c) Circuit theory model of the matching circuit.

It was desired to fabricate and test a prototype of our simplified cross-dipole antenna. Following our design procedure, the basic structure and its radiation performance were obtained. A matching circuit was then designed to facilitate its realization. Then, the combined antenna and matching circuit was optimized together to achieve the final prototype design.

4.2.4.1. Matching

The ideal cross-dipole structure shown in Figure 4.9 together with the ground plane reflector were firstly optimized numerically to have a good radiation performance. As noted for the idealized system, the structure was designed to be printed on a Rogers 4530B substrate. The optimized dimensions of the structure are those listed in Table 4.2. The next step was to design the matching network.

As shown in Figure 4.12(a), two feed networks, one for each sub-dipole, are placed perpendicular with each other and to the cross-dipole aperture. A matching circuit was implemented using microstrip technology. Two feed networks were designed to excite the two polarization states; they are depicted in Figure 4.12(b). Note that TL_2 and OL are conventional microstrip lines. They are designed on the front conducting layer. The lines TL_1 and SL are realized as coupled lines printed on the back conducting layer. They not only part of a balun to provide a balanced feed, but they also act as the ground planes for the microstrip lines TL_2 and OL. This implementation results in a compact structure. The coaxial cables of the 50 Ω source are connected to the ends of TL_2.

As shown in Figure 4.12(c), the S1p file representing the input impedance between points A and C (or points B and D) was extracted from the full-wave simulation software CST Microwave Studio. It was connected with the depicted ideal matching circuit in the MWS circuit simulator. The matching circuit consists of two segments of transmission

lines TL_1 and TL_2, a short circuit transmission line SL, and an open circuit transmission line OL. Together with the cross-dipole itself, the matching circuit acts like a ladder-type filter. By optimizing the parameters of the transmission lines, excellent matching was achieved. The optimized dimension values of the feed networks are listed in Table 4.3.

Table 4.3 Optimized Dimensions of the Two Feed Networks

Parameter	Feed A	Feed B	Description
W_SL	6.0	6.0	Width of the SL
L_SL	30.7	28.0	Length of the SL
W_TL1	6.0	6.0	Width of the TL_1
L_TL1	2.4	5.1	Length of the TL_1
W_TL2	6.0	6.0	Width of the TL_2
L_TL2	15.0	15.0	Length of the TL_2
W_OL	6.0	6.0	Width of the OL
L_OL	1.5	1.5	Length of the OL
g	4.0	4.0	Separation distance between SL

4.2.4.2. Experimental Results

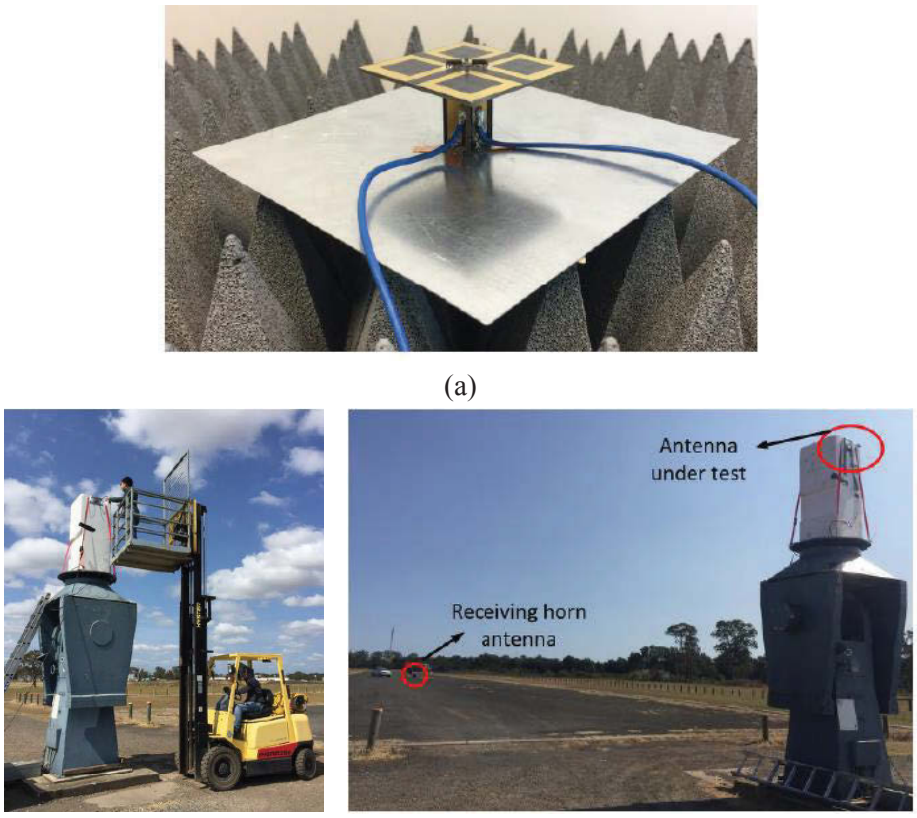

(a)

(b) (c)

Figure 4.13 Photos of the antenna and measurement system. (a) Fabricated and assembled antenna prototype. (b) Mounting the antenna. (c) Antenna under test (AUT).

The antenna was fabricated and tested. Figure 4.13 shows the pictures of the antenna prototype and the test arrangement. The performance characteristics of the antenna were measured with an outdoor antenna range owned by Vecta Pty Ltd, located in Castle Hill, Sydney, Australia.

Plots of the simulated and measured reflection coefficients at the two ports as functions of the source frequency are shown in Figure 4.14. The achieved impedance bandwidth with reflection coefficients less than -15 dB is 1.1 GHz from 1.7 GHz to 2.8 GHz, which is even wider than the target bandwidth.

The co- and cross-polarized radiation patterns of the -45°-polarized cross-dipole at 1.7, 2.2, and 2.7 GHz are shown in Figures 4.15(a), (b), and (c), respectively. The radiation patterns of the +45°-polarized cross-dipole are not given since those results are essentially the same. Figure 4.16 illustrates the simulated and measured HPBWs of the two polarization states. They share a similar pattern, but a noticeable discrepancy at higher frequencies is observed. It is attributed mainly to the antenna fabrication and assembling errors. Despite this, the achieved HPBWs are quite stable and can meet the general industrial requirements. According to the measured results, the XPD at the boresight is > 20 dB and the lowest XPD level within the main beam (-60° < θ < 60°) is > 8 dB. The measured XPD levels are lower than the simulated results. According to the engineer associated with Vecta's outdoor antenna range, the observed higher measured cross polarization levels are due to the imperfect ground plane (earth). The measured front-to-back ratio (FBR) is > 20 dB across this band. The measured realized gain varies from 7.3 to 8.2 dBi, which agrees very well with the simulated values. The corresponding simulated radiation efficiency values are above 81% across the entire band.

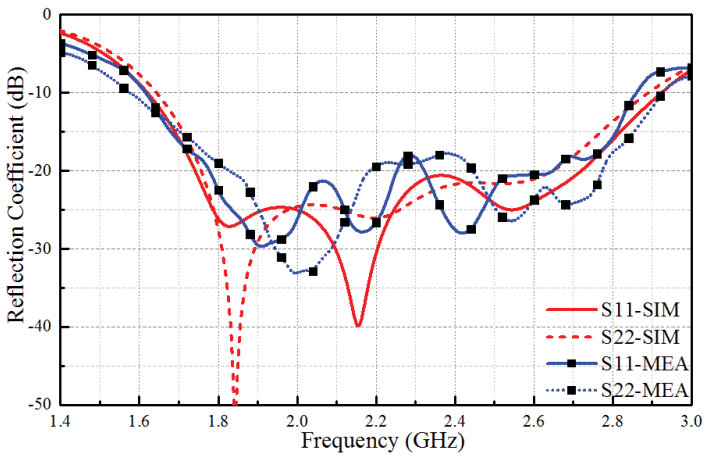

Figure 4.14 Simulated and measured reflection coefficients of the two ports.

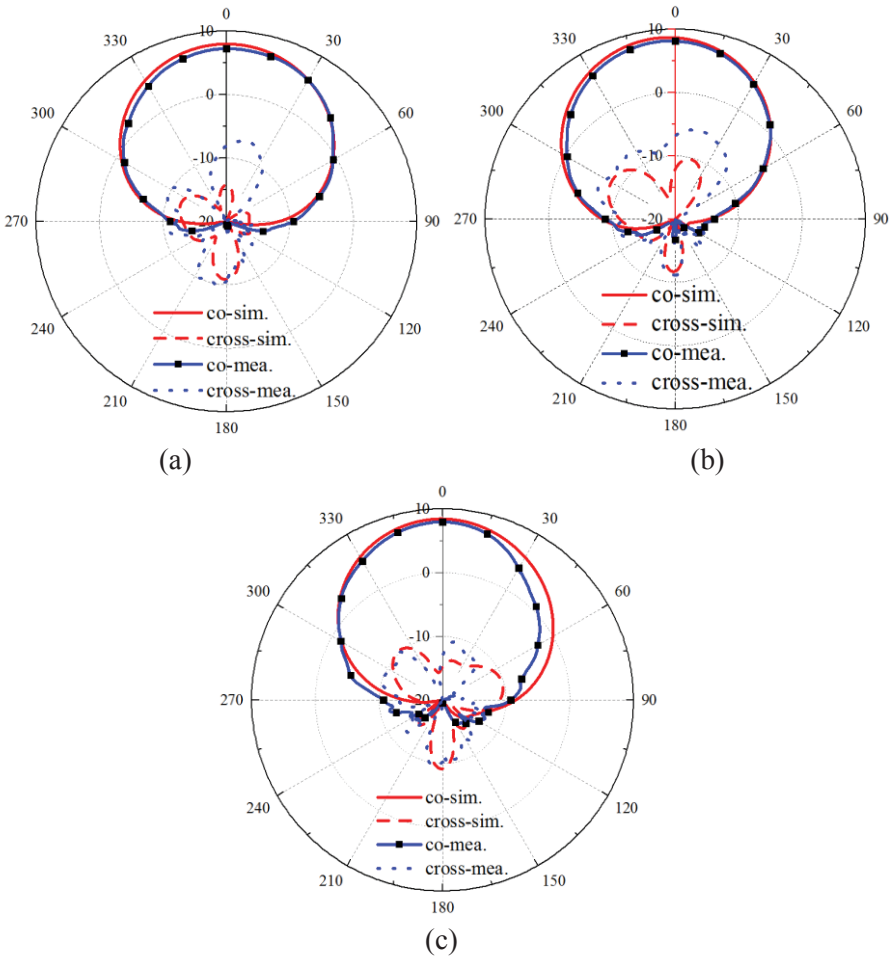

Figure 4.15 Simulated and measured co- and cross-polarization radiation patterns at (a) 1.7, (b) 2.2, and (c) 2.7 GHz.

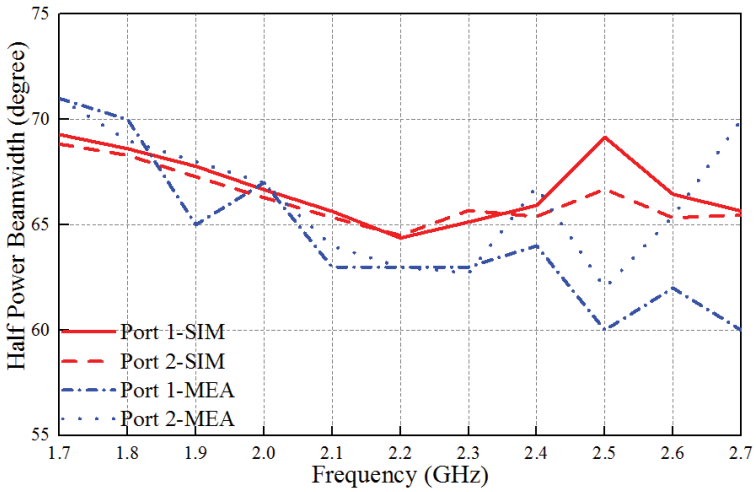

Figure 4.16 Simulated and measured HPBW for the two polarizations across the target band.

4.3 Bandwidth Enhancement of Cross-Dipole Antennas

In this section, a method to broaden bandwidth for dual-polarized cross-dipole antennas is presented. Based on the traditional cross-dipole configuration, an additional loop is attached to sub-dipoles and links four dipole arms together. The new configuration of the radiator has improved impedance properties and has the potential to be matched across a wider band. Two antennas based on isolated cross-dipole element and tightly-coupled cross-dipole element have been presented to verify the method.

4.3.1 Antenna I: Loop-Connected Isolated Cross-Dipole Element

4.3.1.1 Radiator Description

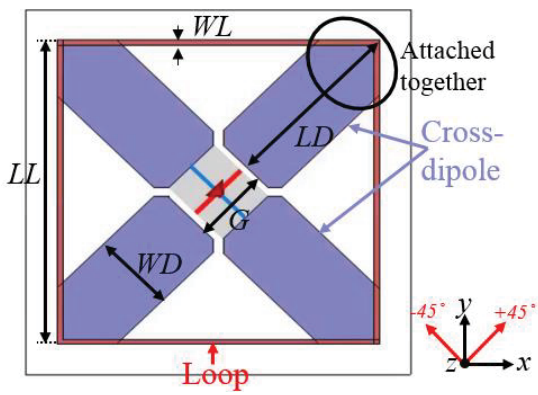

Figure 4.17 Configuration of the radiator of the loop-loaded isolated cross-dipole.

The radiator of the loop-connected isolated cross-dipole is shown in Figure 4.17. To illustrate the configuration clearly, the cross-dipole and loop are marked in different colors. They are printed on the same side of the substrate and attached together at four corners. When exciting each dipole, +45° or -45°-polarized radiation is obtained. The excitation for -45°-polarized radiation is shown in Figure 4.17. The substrate has a dielectric constant of 4.4, loss tangent of 0.0025, and a thickness of 1.0 mm. The radiator is placed above a flat metal reflector with a distance of 32 mm.

4.3.1.2 Analysis of the Radiator

To explain the working mechanism of the loop-loaded isolated cross-dipole, the procedure of designing the radiator is shown in Figure 4.18(a). In those models, a discrete port is used to excite the -45˚-aligned dipoles. The input impedances at the ports are plotted in Fig. 4.18(b) from 1.65 GHz to 2.75 GHz.

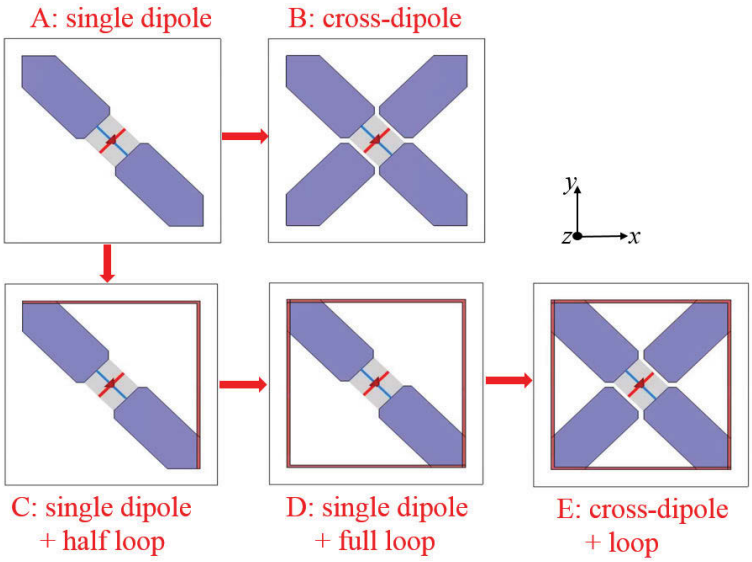

(a)

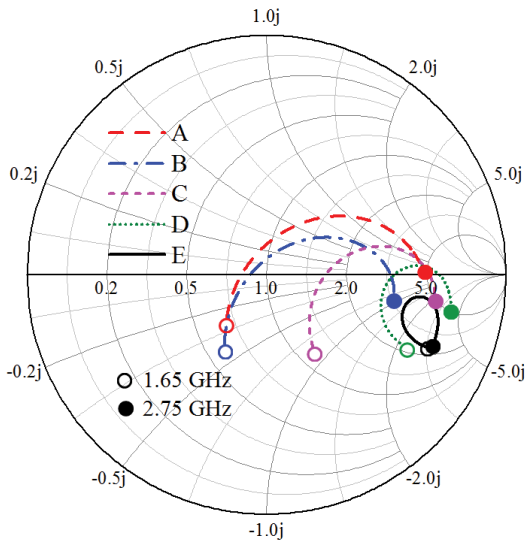

(b)

Figure 4.18 (a) Design procedure of the loop-connected radiator. (b) Impedance of radiators at different steps from 1.65 GHz to 2.75 GHz in Smith Chart.

For traditional cross-dipole, two sub-dipoles are placed perpendicular to each other, shown as Model B. The impedance variation from Model A to Model B is not obvious. The impedance of cross-dipole has slightly smaller resistance and larger capacitance than that of a single dipole as limited amount of coupling between the two sub-dipoles exists in this case. For this cross-dipole radiator, the reactance fluctuates around 0 across the band, but the resistance varies greatly from 33.4Ω to 153.2 Ω. It is hard to be matched to 50Ω across the entire band.

In this design, a loop is added to connect the dipole arms. Starting from Model A which is a single dipole, half of the loop is added and attached to the dipole arms, shown as

Model C. As shown in the impedance plot, the resistance of the radiator is increased and have less variation across the targeted band. It is because an irregular folded dipole with unbalanced driven arm and parasitic arm is formed. Folded dipoles in theory have higher impedance than dipoles [98]. Following that, the other half of the loop is added, and the radiator is evolved to Model D, which can be seen as a folded dipole with two parasitic arms. More parasitic branches offer higher impedance step-up ratio for the folded dipole [99], therefore, the resistance of Model D continues to increase and has less variation. Finally, the other dipole is added, forming Model E. Similar to the transformation from Model A to Model B, by adding another dipole, the resistance at high frequencies is slightly decreased, and the capacitance is slightly increased across the band. The radiator now has a resistance varies from 114.4Ω to 233.0Ω, with a reactance around -100jΩ. The impedance variation of Model E is smaller than Model B, which facilitates the impedance matching.

To examine the bandwidth potential of the models B and E, they are both fed by an optimized matching circuit shown in Figure 4.19(a), which is a practical feed network for dipoles as described in Section 3.2.3. The optimized matching results for models B and E are shown in Figure 4.19(b). For model B, the matching capability is only $|S_{11}|< -10$ dB across the band from 1.7 GHz to 2.7 GHz, whereas for model E, the matching capability is improved to $|S_{11}|< -15$ dB across the band.

The current distribution on the radiator when excite -45°-polarized radiation at 2.2 GHz is shown in Figure 4.20. It is clear that there are three current paths contribute to the radiation: the currents on the driven dipole arms, and on the two half loops which are the parasitic arms. As the configuration of the radiator is symmetrical, the radiator also performs in the same way when the +45°-aligned dipole is excited.

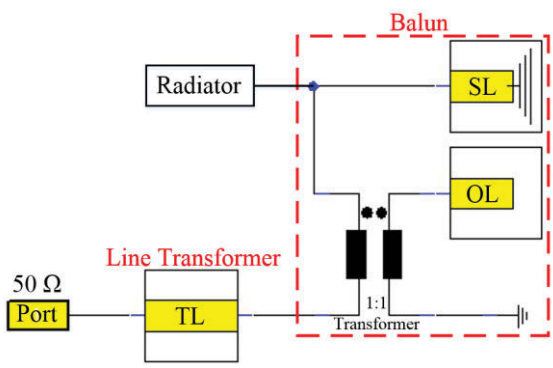

(a)

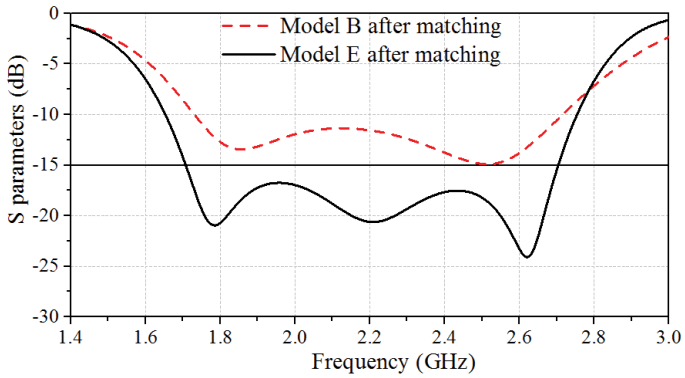

Circuit for Model B:
TL: 64.88 ohm; 26.77 mm
OCL: 91.89 ohm; 38.88 mm
SCL: 142.33 ohm; 43.53 mm

Circuit for Model E:
TL: 99.80 ohm; 34.76 mm
OCL: 184.77 ohm; 44.89 mm
SCL: 500.00 ohm, 34.80 mm

(b)

Figure 4.19 (a) Circuit model of a practical feed network for dipole, (b) matching results for Models B and E.

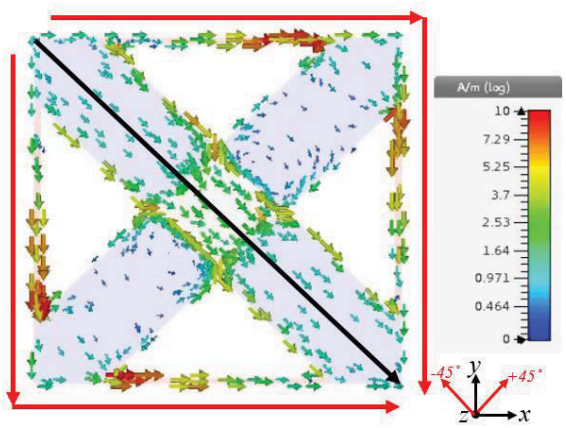

Figure 4.20 Current distribution at 2.2 GHz on the loop-loaded isolated cross-dipole radiator.

There are five important parameters for tuning the radiator's impedance: the length and width of the dipole arm denoted as LD and WD, the length and width of the loop denoted as LL and WL, and the gap width between dipole arms G, as marked in Figure 4.17. Their influences on the radiator's impedance are studied, and the comparison plots are shown in Figure 4.21. As shown in Figure 4.21(a), LD is mainly in charge of the operating band. Larger LD has a lower frequency response. Figures 4.21(b)-(e) shows that WD, LL, WL, and G have more impact on the impedance. Figure 4.21(b) shows that the impedance of the radiator with a larger WD has a lower resistance value. Figures 4.21(c) and (d) show that shorter LL or wider WL both result in a higher resistance value. It agrees well with the folded dipole theory that a wider parasitic arm results in a larger impedance step-up ratio. As shown in Figure 4.21(e), increasing G decreases capacitance value as it reduces

coupling between the two sub-dipoles. The optimized radiator dimensions are LD = 27.5 mm, WD = 12 mm, LL= 46.67 mm, and G = 11 mm, and impedance curve is shown as the black solid curve in Figure 4.18(b).

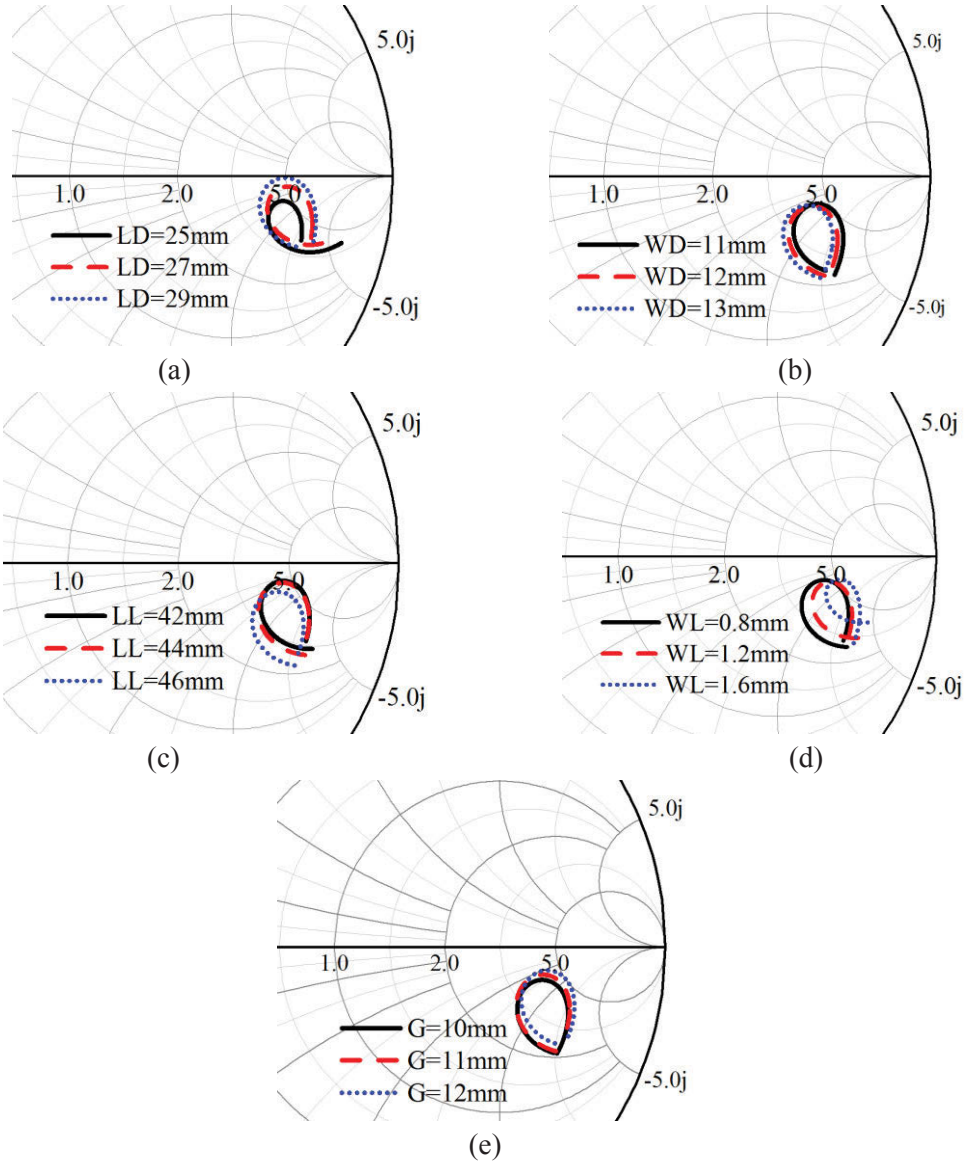

Figure 4.21 Impedance of the radiator from 1.7 GHz to 2.7 GHz with different values of (a) LD, (b) WD, (c) LL, (d) WL, and (e) G.

4.3.1.3 Experimental Results

The optimized radiator is fed by traditional baluns designed following the guideline in section 3.2.3. They provide balanced feeds to the dipoles and transform the dipole's impedance from around 170Ω to 50Ω with minor reactance correction. The configurations of the two baluns, together with the final configuration of the antenna are

shown in Figure 4.22. The feed lines are arranged in slightly different positions to avoid overlapping with each other. The final parameters of the feed networks are marked in the figures.

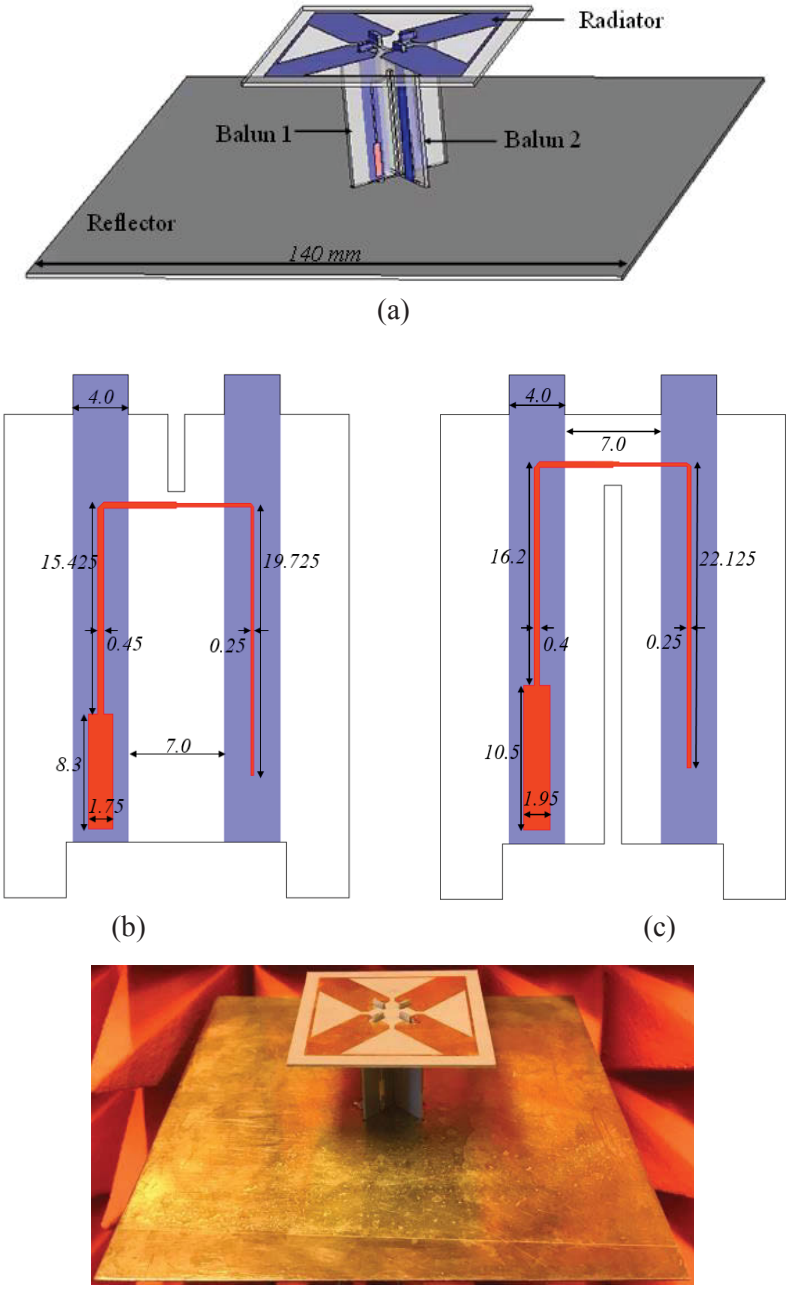

Figure 4.22 (a) Perspective view of the antenna I. Plots of (b) balun 1, and (c) balun 2. (d) Fabricated prototype of the antenna I.

The antenna has been fabricated and tested. The fabricated prototype is shown in Figure

4.22(d). The S-parameters of the antenna are shown in Figure 4.23. Both the simulated and measured results demonstrate that the antenna has a bandwidth of 46.7% from 1.69 GHz to 2.72 GHz with reflection coefficients less than -15 dB. Across the band, the measured port isolation is above 35 dB. The radiation patterns in the horizontal plane (*zx*-plane) are shown in Figure 4.24. The measured results agree well with the simulated ones, and the patterns are very symmetrical and stable across the wide band. For the cross polarization discrimination (XPD), the simulated results are > 22.5 dB at boresight, and > 9 dB within ±60˚ coverage, whereas the measured results are > 19 dB at boresight, and > 10 dB within ±60˚ coverage. The simulated and measured HPBW and gain results are shown in Figure 4.25. With a flat metal reflector, the antenna has very stable radiation patterns with horizontal HPBW of 68.7˚ ± 2.5˚ for the two polarizations. The realized gain is 8.6 ± 0.9 dBi.

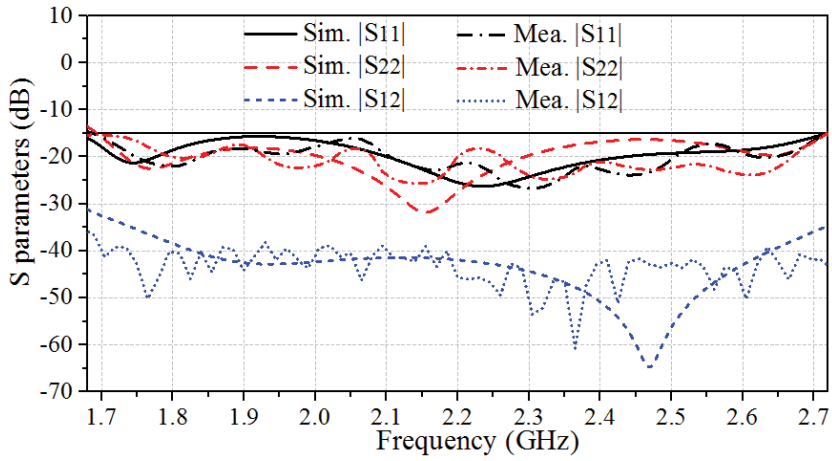

Figure 4.23 Simulated and measured S-parameters of antenna I.

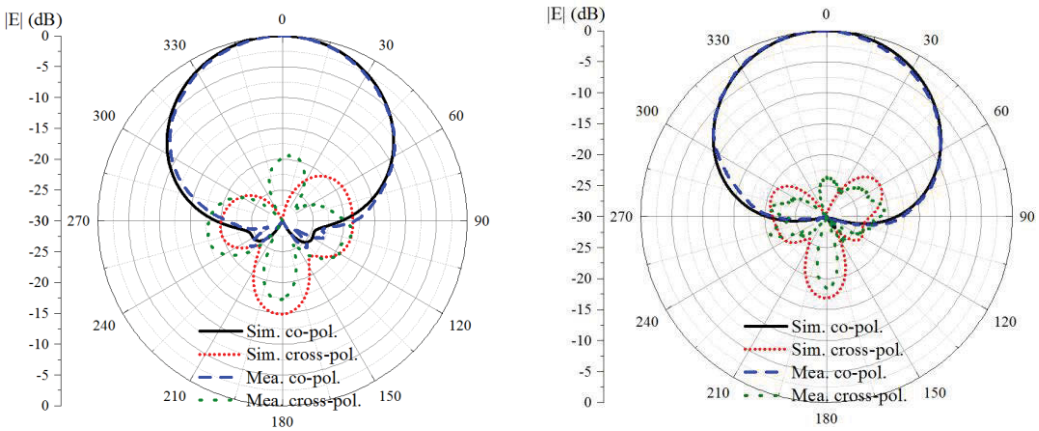

(a) (b)

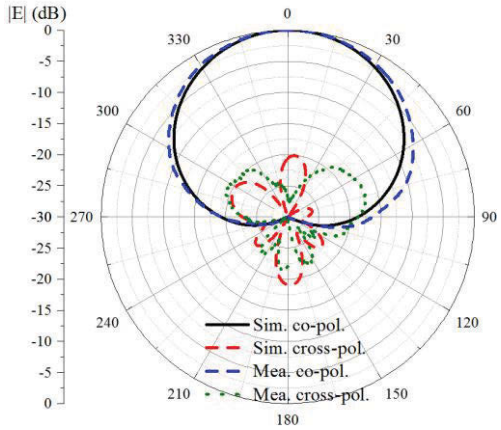

(c)

Figure 4.24 Horizontal radiation patterns of +45°-polarized radiation of antenna I at (a) 1.7 GHz, (b) 2.2 GHz, and (c) 2.7 GHz.

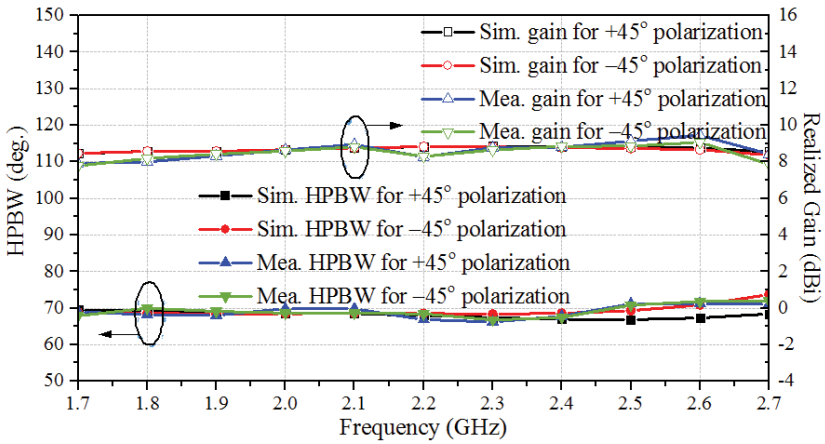

Figure 4.25 Simulated and measured HPBW and realized gain of the antenna I.

4.3.2 Antenna II: Loop-Connected Tightly-Coupled Cross-Dipole Element

4.3.2.1 Configuration and Analysis of Antenna II

TCCD has a wide bandwidth around 45% with the help of the strong coupling between the two dipoles. Inspired by the design of antenna I, it is worth investigating whether adding a loop can further broaden the bandwidth for TCCD. Therefore, a similar loop-connecting configuration is applied for the TCCD to examine its performance, as shown in Figure 4.26. Different from the radiator of antenna I, the TCCD and the loop in this case are placed on different layers of substrate and connected with each other using via holes at the four corners of the loop. This different-layer arrangement is made because

the TCCD arms are fat, and the loop will be mostly overlapped with the arms if they are placed on the same layer. The substrate used in this case has a dielectric constant of 3.48 and a thickness of 0.76 mm. The radiator is mounted above a flat reflector with a distance of 34 mm.

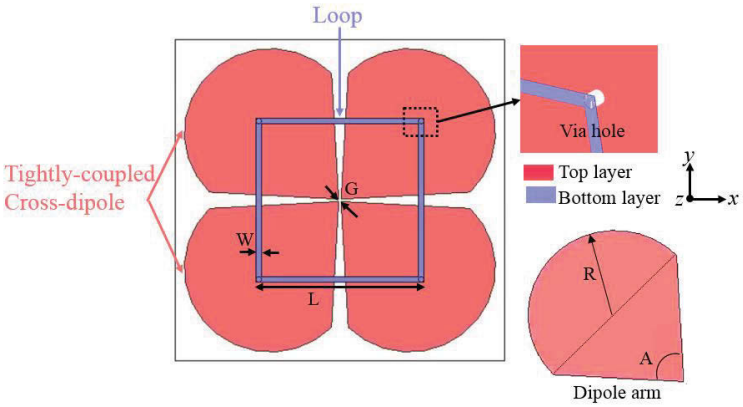

Figure 4.26 Radiator of loop-loaded tightly-coupled cross-dipoles. (R = 14.4 mm, A = 83.6°, L= 28 mm, W= 0.8 mm, and G = 0.56 mm)

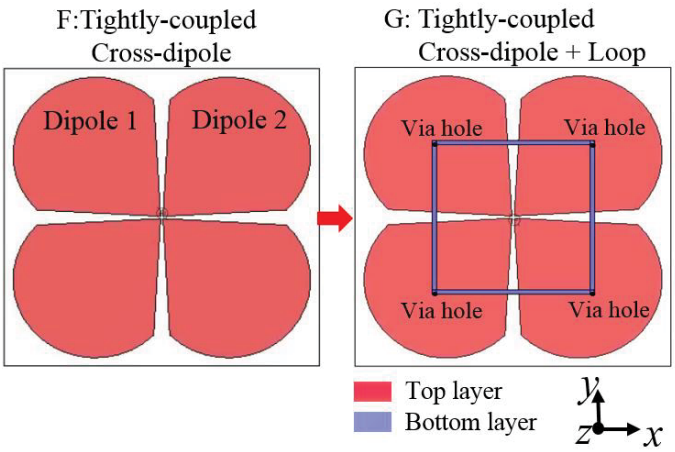

(a)

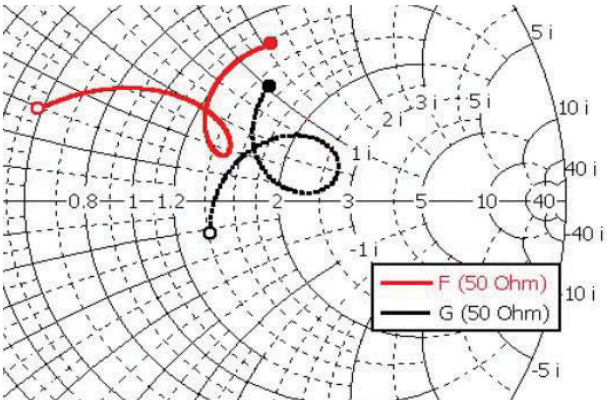

(b)

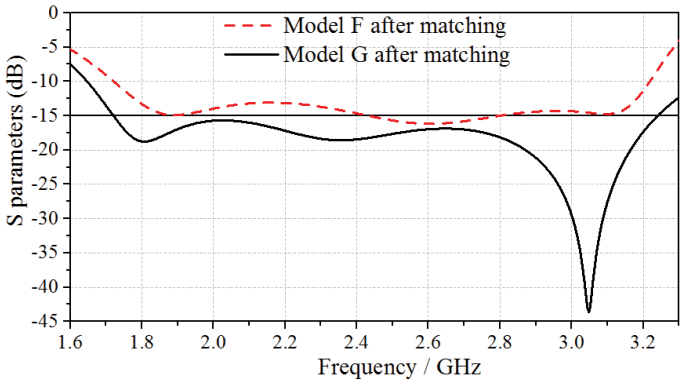

Circuit for Model F:
TL: 57.27 ohm; 13.16 mm
OCL: 41.67 ohm; 31.32 mm
SCL: 200.00 ohm; 43.02 mm

Circuit for Model G:
TL: 73.07 ohm; 32.12 mm
OCL: 71.43 ohm; 29.50 mm
SCL: 200.00 ohm, 34.10 mm

(c)

Figure 4.27 (a) Design procedure of radiator. (b) Impedance of radiators at different steps from 1.7 GHz to 3.2 GHz in Smith Chart. (c) Matching results for Models F and G using circuit in Figure 4.19(a).

To show the effect of the attached loop on the impedance variation, the impedances of the TCCD before and after attaching the loop are compared. The radiator models and the corresponding impedances are shown in Figure 4.27. Model F and G show the configuration of TCCD without and with loop attached, respectively. Similar to the previous case, Model G with the loaded loop has higher impedance level and less impedance variation across the band than Model F. The matching capabilities of the two models using the balun circuit shown in Figure 4.19(a) are examined, and the optimized results are shown in Figure 4.27(c). Model G has better matching results than Model F, demonstrating the bandwidth enhancement capability of the attached loop.

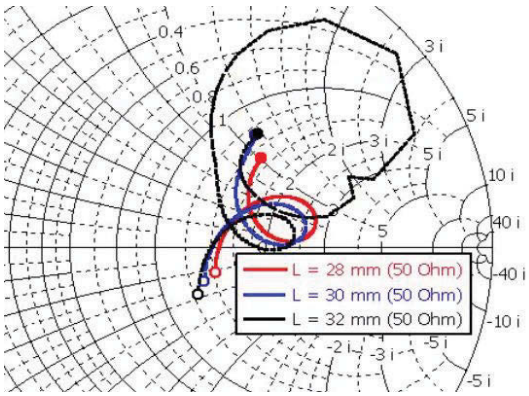

Figure 4.28 Influence of length of loop *L* to the radiator's impedance.

As a detailed parameter study has been carried out in 4.3.1.2, in this case, parameters' influences on the impedance are not presented. One thing needs to be noticed is that in this case, L cannot be too large, otherwise the large overlapping area of loop and dipole arms will results in undesired resonance, as shown in "L = 32 mm" case in Figure 4.28.

4.3.2.2 Experimental Results

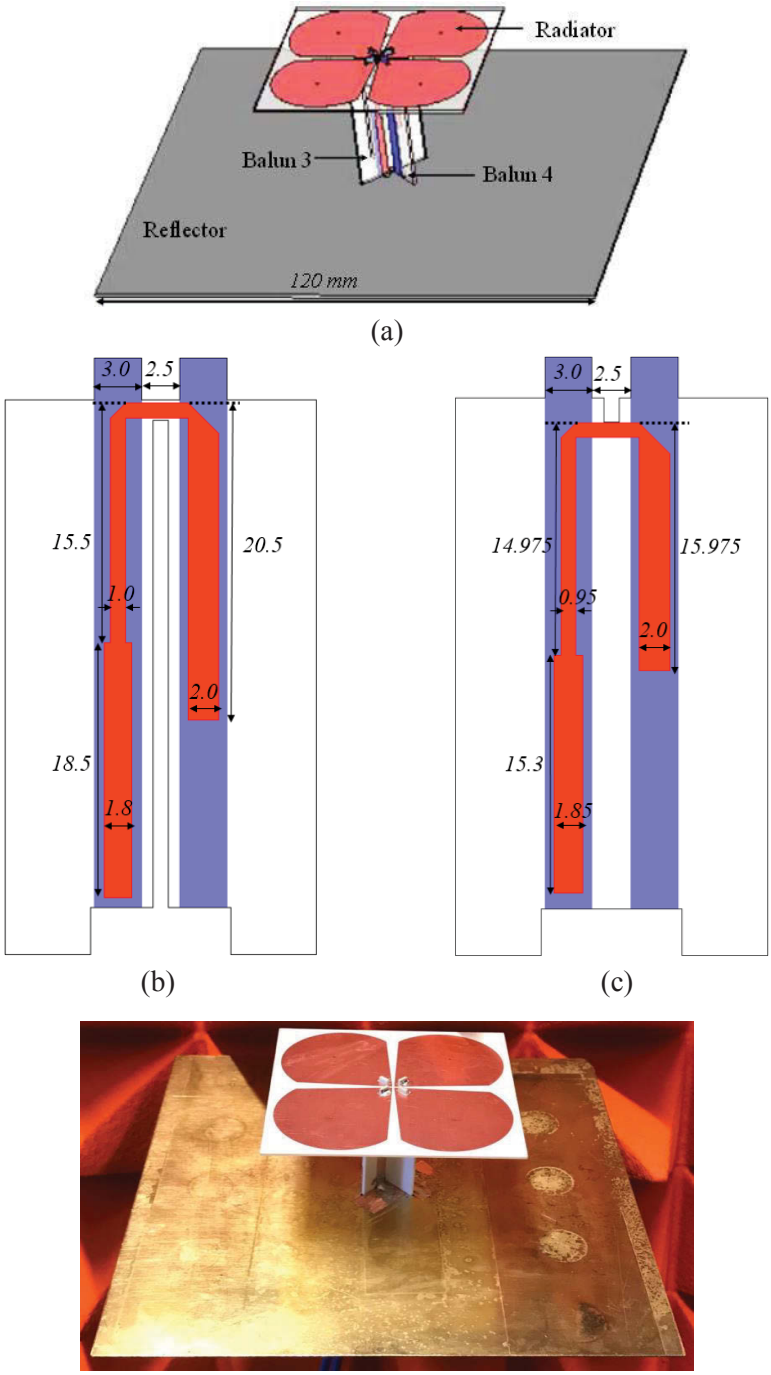

Figure 4.29 (a) Perspective view of the antenna II. Plots of (b) balun 3, and (c) balun 4. (d) Fabricated prototype of the antenna II.

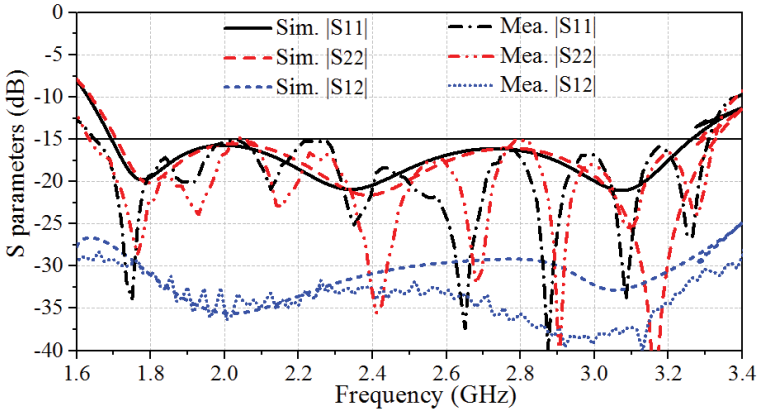

Figure 4.30 S-parameters of loop-loaded tightly-coupled cross-dipole.

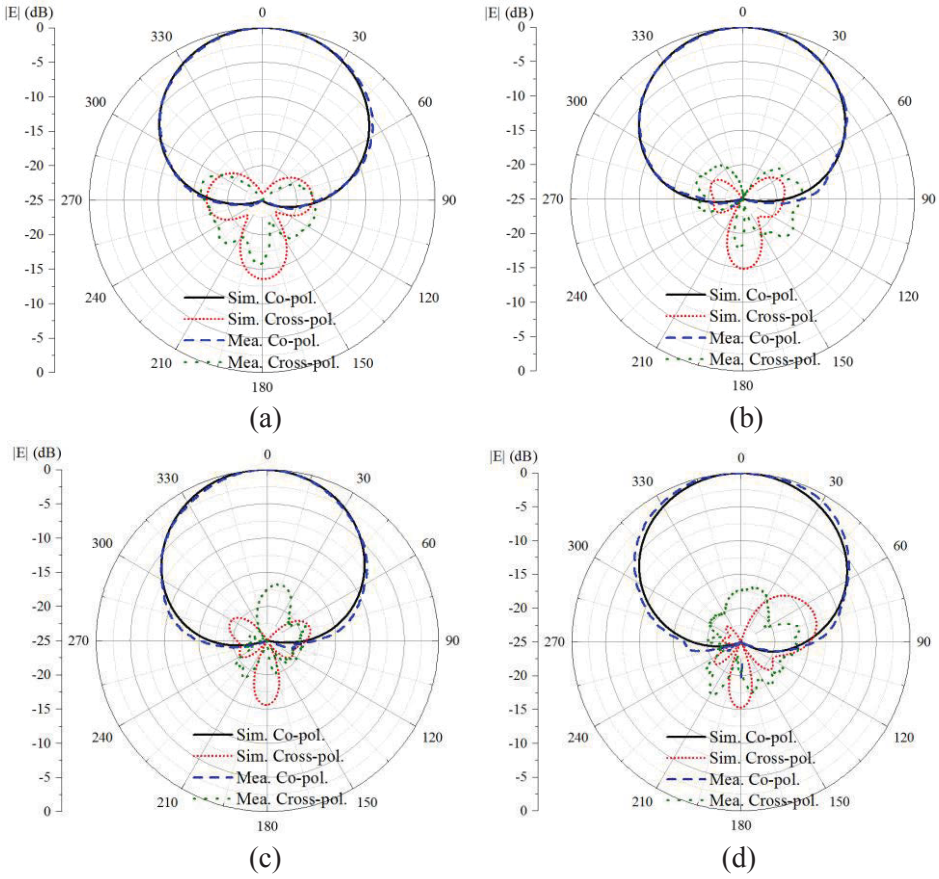

Figure 4.31 Radiation patterns of the loop-loaded tightly-coupled cross-dipole at (a) 1.7 GHz, (b) 2.2 GHz, (c) 2.7 GHz, and (d) 3.2 GHz.

Similar to antenna I, two baluns are designed to match the radiator. The configurations of the antenna with two baluns and optimized parameters are shown in Figure 4.29. The antenna is also fabricated and tested, as shown in Figure 4.29(d). The simulated and measured S-parameters of the antenna are shown in in Figure 4.30. The antenna has a measured bandwidth of 66.7% from 1.65 GHz to 3.30 GHz with reflection coefficients

for the two ports < -15 dB. Across the band, the port isolation is > 28 dB. The simulated and measured radiation patterns are shown in Figure 4.31. The patterns are very symmetrical and stable. The measured XPD is > 17 dB at boresight. The HPBW and gain results are shown in Figure 4.32. The simulated and measured HPBWs of the radiation patterns vary within 78.0° ± 6.5°, and 76.1° ± 8.5° respectively for the two polarized radiation across the operating band. The realized gain is 7.9 ± 1.0 dBi.

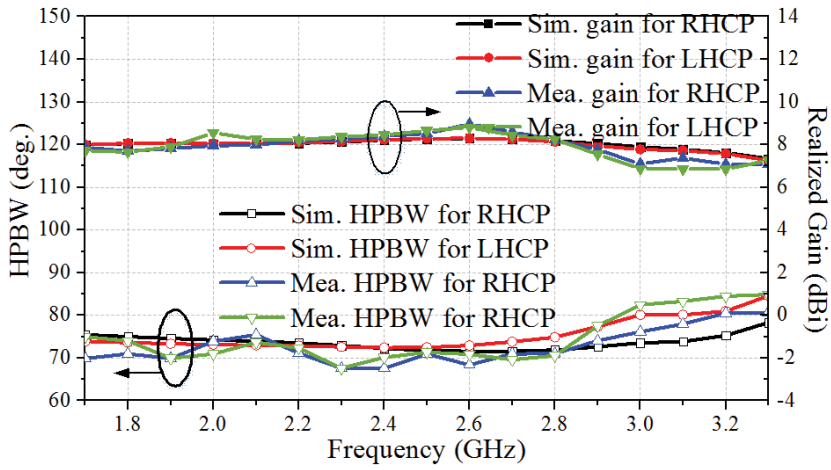

Figure 4.32 (a) HPBW, and (b) gain of the loop-loaded tightly-coupled cross-dipole.

4.3.3 Comparison

Table 4.4 Comparison of Antennas' Performances

Ref.	Configuration	Size (*λ_0^2)	Height (*λ_0)	BW	Isolation (dB)
[13]	ICD	0.33*0.33	0.31	23.7%	25
[14]	ICD	-	0.29	25.6%	30
[16]	TCCD	0.45*0.45	0.23	48%	22
[17]	TCCD	0.42*0.42	0.26	45%	30
[24]	TCCD+parasitic elements	0.93*0.93	0.38	64%	30
		0.48*0.48	0.39	63%	30
[25]	TCCD+parasitic elements	0.46*0.46	0.35	67%	30
This work	Ant I: ICD+loop	0.34*0.34	0.23	46.4%	30
	Ant II: TCCD+loop	0.42*0.42	0.28	63%	28

The two designed antennas are compared with state-of-the-art cross-dipole antennas, as listed in Table 4.4. For antenna I which is the loop-connected ICD, it has a much wider bandwidth than other ICDs by 20%. It has comparable performances with traditional

TCCDs, but with a reduced size and profile. For antenna II which is the TCCD with an attached loop, the bandwidth is broader than traditional TCCDs by 15% while maintaining a similar size. Compared with antennas in [24] and [25] which are TCCDs with parasitic elements, antenna II has comparable bandwidth with reduced size and profile. It can be concluded that connecting loops to cross-dipoles can effectively enhance bandwidth with a compact volume. Therefore, this technique can be used to broaden the bandwidth and/or reduce the size and profile of dual-polarized cross-dipoles.

4.4 Summary

This chapter aims at investigating the working mechanism and improving the performance characteristics of cross-dipole antennas. Firstly, the TCCD configuration is analyzed. A deep insight into how this type of antenna works was given by decomposing the cross-dipole into two equivalent dipole arrays. By observing and studying the current distributions on the simplified model, it was found that the radiation performance of the system is determined by the patterns of the dipole arrays in the presence of the ground plane reflector and their array factor pattern. The interaction between these two factors makes the cross-dipole system achieve wideband stable radiation performance, which is a requirement for commercial base station applications. A design strategy of the cross-dipole antennas based on a simplified dipole array model was introduced. An optimized cross-dipole system was synthesized following this design strategy. Simulated and measured results demonstrate that the antenna prototype has low reflection coefficients less than -15 dB and consistent radiation performance across a wide band of 44.5%.

Secondly, a new technique is presented to broaden the bandwidth of the cross-dipole antenna with a compact size. The method relies on improving impedance characteristics of radiators by connecting dipole arms together with a loop. As a demonstration, two antennas are designed based on an ICD and a TCCD. By attaching loops to the dipole arms, the matching capability of radiators is greatly improved. The bandwidths of the modified ICD antenna and the modified TCCD antenna are enhanced to 46.4% and 63.0% respectively without increasing antenna sizes. Other performance characteristics such as port isolation, XPD, radiation pattern are not affected by modifying the radiator. Simulated and measured results show that radiation performances of the two antennas are stable across entire operating bands. With their wideband performances and simple and compact structures, the two antennas serve as good candidates in BSA array application.

Chapter 5: Dual-Dipole Antennas

5.1 Introduction

Polarization diversity is a critical solution to minimize the multipath fading in a rich scattering environment. To that end, dual-linearly-polarized (dual-LP) antennas, especially ±45°-polarized antennas, and dual-circularly-polarized (dual-CP) antennas have been widely used in communication systems. Wide bandwidth and stable radiation performances are desired for these antennas to support reliable high-data-rate communications. Simple antenna configurations are preferred to reduce fabrication complexity and facilitate system integration.

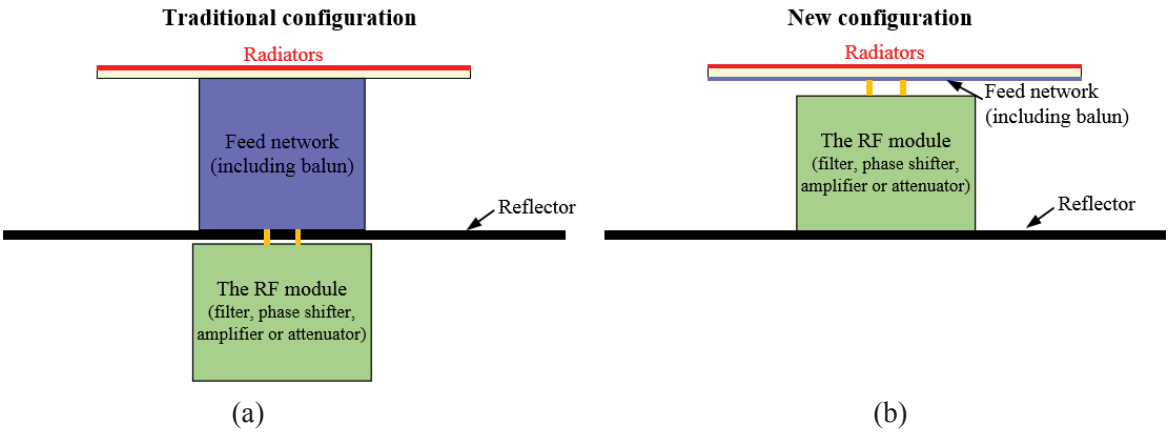

(a) (b)

Figure 5.1 (a) Traditional, and (b) new configurations of communication systems consisting antennas and RF modules.

Many wideband dual-LP antennas have been realized using dipole radiators, such as in cross-dipole antennas and square-dipole-array antennas. These designs usually have three main parts: dipole radiators, baluns, and reflectors. Balun, as an essential component to provide balanced feeding for dipoles, is always placed between the radiator and the reflector, occupying a large space. However, this space can be saved for system integration by replacing bulky and vertically placed baluns with planar ones, as illustrated in Figure 5.1. Some planar dual-LP antennas have been designed in [52], [53]. In [52], the feed network is printed on the same substrate with the radiating dipoles. However, only one polarization was achieved with this configuration. In [53], an improved planar structure is realized using 180° hybrid coupler to provide differential feeds for dipoles, but the coupler inevitably adds design complexity. Integrating baluns in a planar structure

to realize dual-LP radiation has not been considered in the literature so far.

Compared with wideband dual-LP antennas, wideband dual-CP antennas are more difficult to achieve, due to further bandwidth limitation by axial ratio (AR) performance. Recently, wideband dual-CP radiation have drawn ongoing attention by using patch antennas [100], [101], waveguide antennas [102]-[104], and frequency-independent antennas [105], [106]. However, most of the reported dual-CP antennas only have an operating bandwidth of less than 20% [101]-[104]. Wider bandwidth can be obtained using frequency-independent antennas such as log-periodic antenna [105] and sinuous antenna [106], which, however, suffer from complicated design and fabrication process, and require relatively large space.

In this section, we present two forms of planarized dual-LP antennas by integrating baluns on the same substrate as dipole radiators. The circuit of the balun-included feed network is designed to facilitate the impedance matching within a restricted space. The planarized antennas both achieved stable radiation performance across a wide operating band. The planarized structure designed facilitates system integration as RF components can be integrated into the space saved between the radiators and reflector. In this way, the integrated system is not only more compact, but can also reduce the installation complexity and cost. As a demonstration, the designed planarized dual-LP antenna has been integrated with a coupler to realize dual-circularly-polarized (dual-CP) radiation. Efforts have been made to minimize the coupler's effect on the radiation performance, and the attained dual-CP antenna achieved desired wideband and stable radiation performance with a compact size.

5.2 Working Mechanism of the Dual-Dipole Radiators

The design of the planarized dual-LP antennas was commenced from arranging the position of radiators to get desired ±45° polarized radiation with stable patterns. As shown in Figure 5.2(a), four dipoles are arranged in a square and are printed on the same substrate. The substrate is mounted above a flat square metal reflector. By simultaneously exciting dipoles 1 and 2, or dipoles 3 and 4, −45°- or +45°-polarized radiations can be realized. The stable radiation patterns are realized by exciting separated dipoles, as suggested in Section 3.2.2.

Figure 5.2(b) shows the current distribution on the four dipoles at 2.2 GHz when dipoles 1 and 2 are excited to achieve −45°-polarized radiation as an example. A small amount

of currents is observed on parasitic dipoles (dipoles 3 and 4) since they are placed in perpendicular with the excited dipoles (dipoles 1 and 2). Besides, the induced currents on the two arms of the parasitic dipoles are out of phase, thus having little contribution to the radiation pattern. Therefore, a low cross-polarization level can be guaranteed.

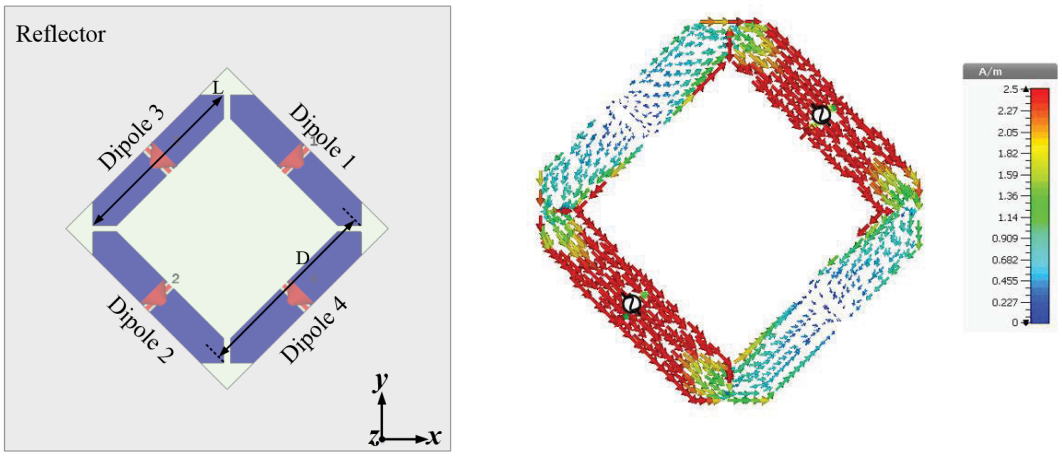

(a) (b)

Figure 5.2 (a) Configurations of the radiators; and (b) the simulated current distribution when excite dipole 1 and 2.

To illustrate the mechanism of realizing stable radiation patterns using two slant-positioned dipoles, the mathematical calculation is presented. The factors that contribute to the radiation beams in the horizontal plane are:

- Dipole pattern

$$f_d = \left[\cos\left(k\frac{L}{2}\frac{\sin\alpha}{\sqrt{2}}\right) - \cos\left(k\frac{L}{2}\right)\right] / \sqrt{1 - \left(\frac{\sin\alpha}{\sqrt{2}}\right)^2} \tag{5.1}$$

where $k = \frac{2\pi}{\lambda}$ is the wave number, L is the length of the dipole, and α is the azimuth angle in the horizontal plane.

- Array factor of the two elements

$$AF = \cos(k\frac{D}{2}\frac{\sin\alpha}{\sqrt{2}}) \tag{5.2}$$

where D is the separation distance between two dipoles.

- Ground plane effect (image effect)

$$f_{gp} = \sin(k\,H\cos\alpha) \tag{5.3}$$

where H is the height of dipoles above the ground plane.

The generated pattern in the horizontal plane by the two dipoles can be calculated using $f_d \times AF \times f_{gp}$, whereas for a single slant dipole is calculated using $f_d \times f_{gp}$. The HPBWs of the calculated patterns from a pair of dipoles and from a single slant dipole are plotted in Figure 5.3 for comparison. The parameters used in this calculation are actual values of the antenna in section 5.4, which are *L*=50.8 mm, *D*=51.64 mm, and *H*=35mm. Figure 5.3 also includes the simulated results of the proposed structure above an infinite ground plane. As observed from the figure, the HPBW varies significantly across a wide band for a single dipole, but is much more stable for a pair of dipoles. Moreover, the HPBW obtained from the full-wave simulation of the real antenna model agree quite well with the result calculated from the two dipoles' mathematic model. This indicates that the parasitic dipoles have a minor contribution to the radiations and the proposed antenna can be simplified to a dual-dipole array in future research. The HPBWs of the proposed structure with an infinite ground plane varies within a small range of 80.1°±3.5° across a wide band from 1.5 GHz to 3.0 GHz. This demonstrates that this simplified two-dipole array configuration features stable radiation patterns as desired.

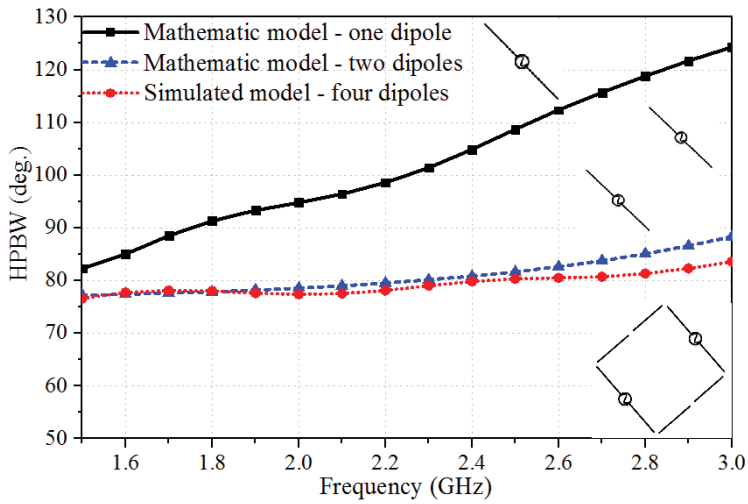

Figure 5.3 Comparison of the calculated HPBWs from the mathematic models of the one dipole and two dipoles configurations, and the simulated HPBWs of the actual antenna with four dipoles.

5.3 Three-Layer Planarized Dual-Dipole Antenna

5.3.1 Antenna Configuration

The configuration of the planar dual-polarized antenna is shown in Figure 5.4. It

consists of two substrate layers and three metallic layers stacked together. The radiators shown in Section 5.2 are located on the middle metallic layer and two feed networks are positioned on the top and bottom metallic layers. Each feed network excites two dipoles simultaneously for one polarization. The stacked layers with radiators and feed networks are placed above a ground plane with a distance of 35 mm and are supported by four plastic posts. The substrate used in this work is Rogers 4350B with a dielectric constant of 3.48 and a thickness of 1.524 mm. The optimized parameters of the radiator shown in Figure 5.4 are L=53.5 mm, w=9.5 mm, D=45.0 mm, G=3.0 mm.

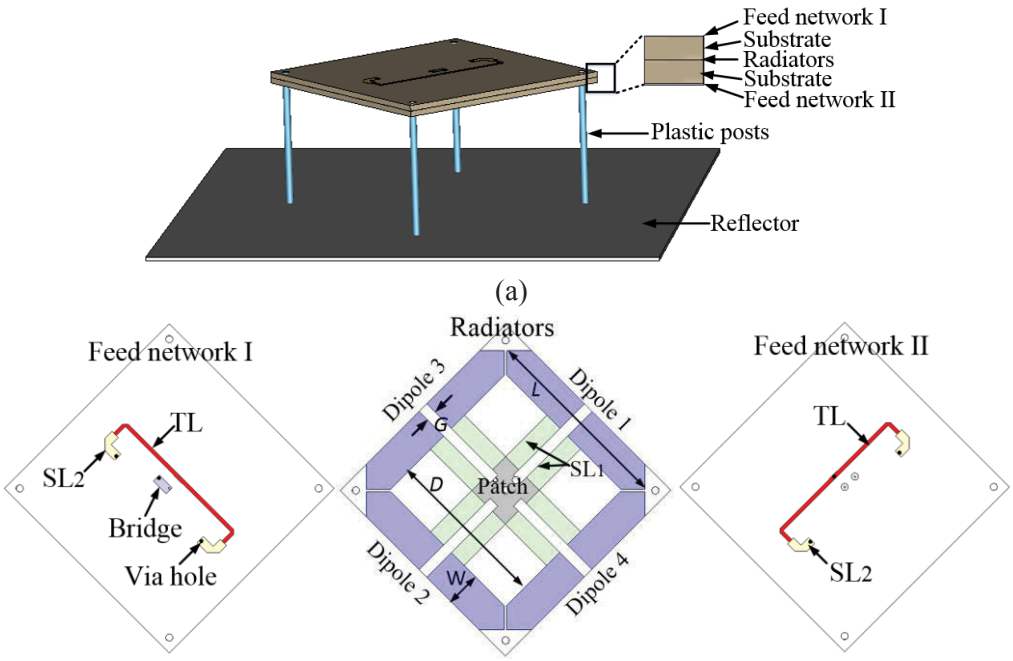

Figure 5.4 Antenna configuration: (a) Perspective view; Top views of the (b) top, (c) middle, and (d) bottom metallic layers.

5.3.2 Feed Network

The feed networks of the proposed antenna need to excite a pair of dipoles simultaneously while providing good impedance matching. Figure 5.5 shows the circuit representation of the proposed feed network. Since the dipoles are identical and have the same input impedance Z, the feed network is a duplication of the matching circuit for one dipole. As shown in Figure 5.5, the input impedance of each dipole is firstly transformed to nearly 100 Ω (Z_1', Z_2') by an impedance matching circuit, and then connected in parallel to match to a standard 50-Ω coaxial cable. The impedance matching circuit for each

dipole consists of one transmission line TL and two short lines SL_1 and SL_2. The matching result with the optimized matching circuit is shown in Figure 5.6.

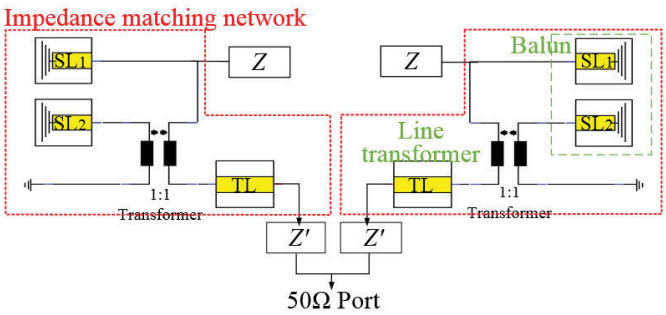

Figure 5.5 Circuit representation of the feed network.

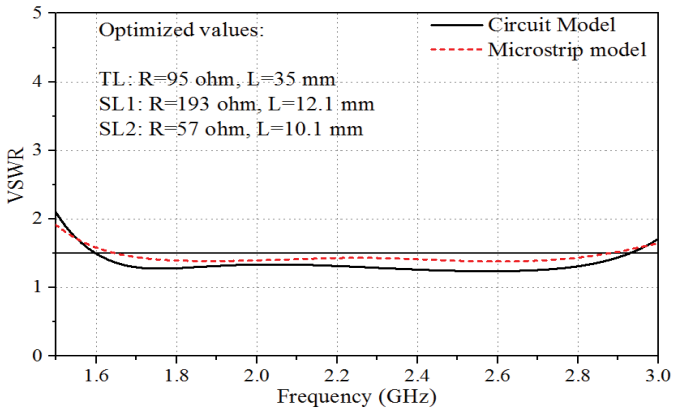

Figure 5.6 SWR results of the circuit model and physical model.

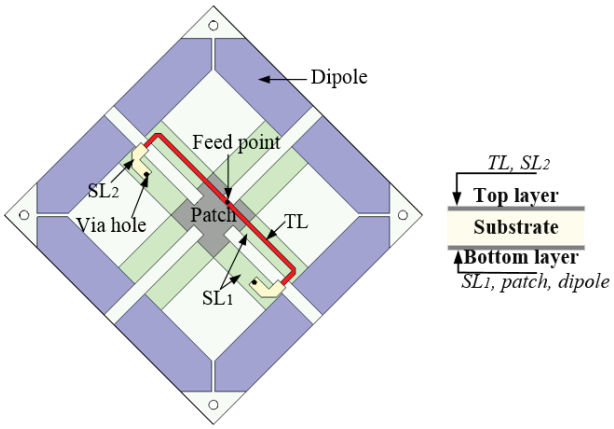

Figure 5.7 Physical realization model.

The feed network was implemented using the microstrip structure, as shown in Figure 5.7, where only the feed network for dipoles 3 and 4 is shown for clarity. The SL_1s are realized by coupled lines connecting the dipoles to a rectangular patch located at the

center of the board. The dipoles, SL_1s, and the shorting patch are all located on the same layer. The SL_1s with the shorting patch also act as the ground for TL and SL_2, which are realized by the microstrip lines printed on a different layer. SL_2 is connected to SL_1 at its end by a via hole. The parameters of SL_1, SL_2 and TL are calculated based on the optimized results in the matching circuit. Proper tuning of the microstrip lines was conducted, and their parameters are also listed in Table 5.1. The SWR result of the physical realization model is also shown in Figure 5.6, which agrees well the circuit design results, realizing a bandwidth of 54.8% from 1.64 GHz to 2.88 GHz with SWR<1.5.

Table 5.1 Optimized Parameters of the Matching Elements.

Elements	Line length (mm)	Line width (mm)	Gap width (mm)
TL	24.5	1.1	-
SL_1	18.0	5.0	3.0
SL_2	5.8	2.4	-

For the realization of the dual-polarized planar antenna, we put the two feed networks for the two polarizations in different layers, as shown in Figure 5.4. The antenna is fed by 50-Ω coaxial cables, where the inner conductor connected to the feed lines at the top and bottom layer, and the outer conductor connected to the patch at the middle layer. In order to place the coaxial cables at the bottom of the structure, a small piece of metal is printed on the top side to connect the inner conductor of the coaxial cable and the feed lines at the bottom layer together. Eight holes are drilled on the two layers of the substrate for the assembly the antenna.

5.3.3 Experimental Results

The proposed antenna was fabricated and tested. Figure 5.8 presents the prototype of the antenna. The simulated and measured S-parameters and the matching result based on circuit theory model are shown in Figure 5.9. The measured results agree well with the simulated one. According to the measured results, $|S_{11}|/|S_{22}|$ are < -10 dB across a wide bandwidth of 66.6% from 1.5 GHz to 3.0 GHz. The port-to-port isolations are > 29 dB over this band. The radiation patterns in the horizontal plane at 1.7 GHz, 2.2 GHz, and 2.7 GHz are shown in Figure 5.10. The cross polarization discrimination is > 21 dB at the boresight. The simulated and measured HPBW and gain are shown in Figure 5.11. The HPBWs are maintained within 67°±7° and the cross polarization discriminations (XPDs) are > 22 dB at boresight for both the two polarizations. Moreover, the measured gains are

from 7.3 dBi to 9.2 dBi across the band.

Figure 5.8 Prototype of the three-layer planarized dual-LP antenna.

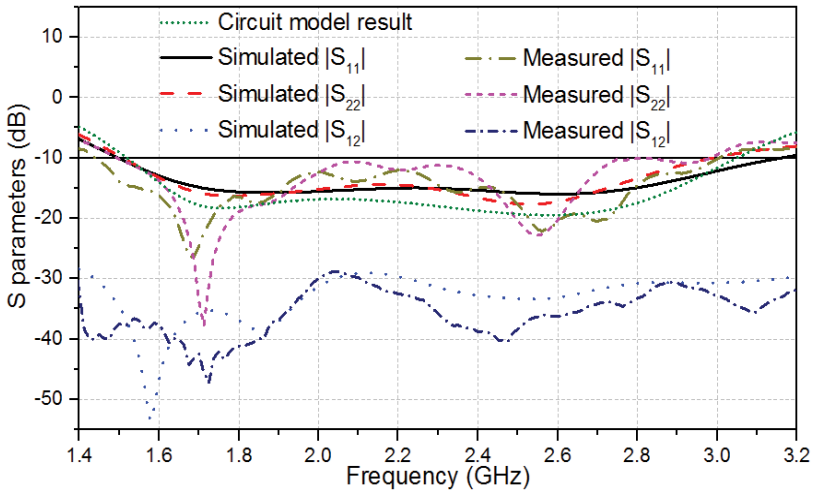

Figure 5.9 Circuit matching results, and the simulated and measured S parameters.

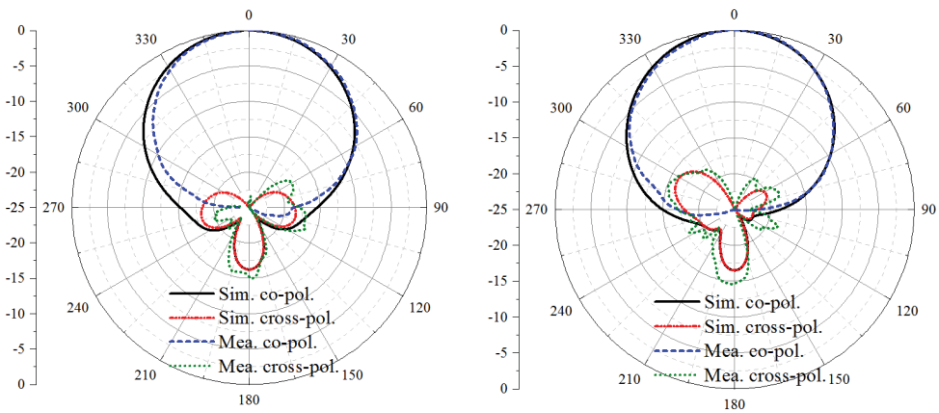

(a) (b)

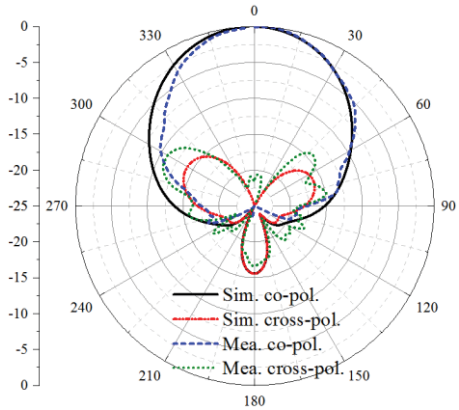

(c)

Figure 5.10 Simulated and measured radiation patterns. (a) 1.7 GHz, (b) 2.2 GHz, (c) 2.7 GHz.

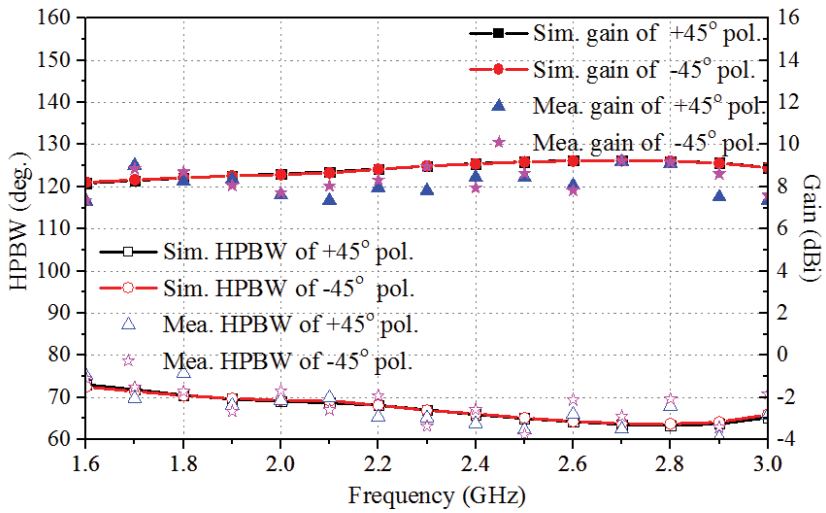

Figure 5.11 Simulated and measured HPBWs and gains.

5.4 Two-layer Planarized Dual-Dipole Antenna

5.4.1 Antenna Configuration

The configuration of the planar ±45° dual-LP antenna is shown in Figure 5.12. In this case, the feed network for the two polarizations is arranged on the same layer of the substrate to ease fabrication and assembling process. An 'air bridge' is used to avoid intersection between the two feed networks. The substrate used in this work is Rogers 4350B with a dielectric constant of 3.48 and a thickness of 1.524 mm. The antenna is placed above a reflector with a distance of 35 mm. The optimized parameters for the radiator are L = 50.8 mm, W_d = 9.24 mm, D = 42.4 mm, G_d = 0.59 mm, G = 1 mm.

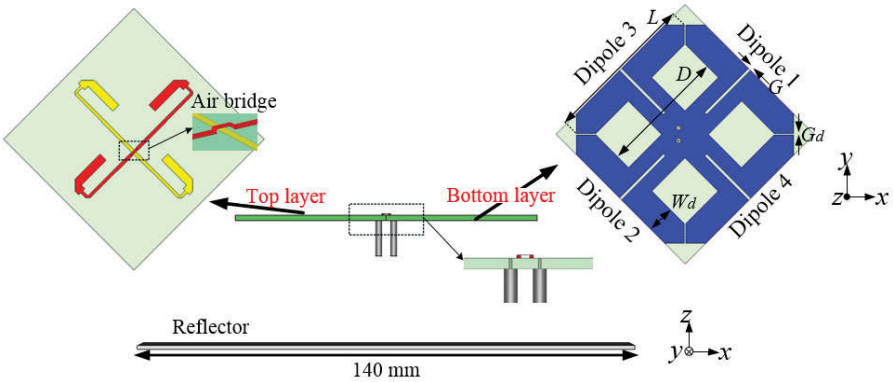

Figure 5.12 Configuration of the wideband ±45°-polarized antenna.

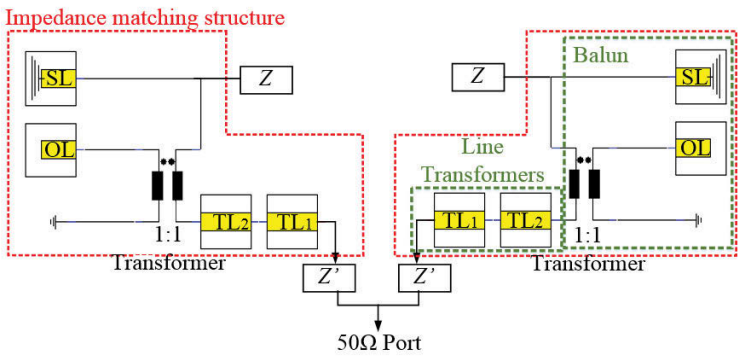

(a)

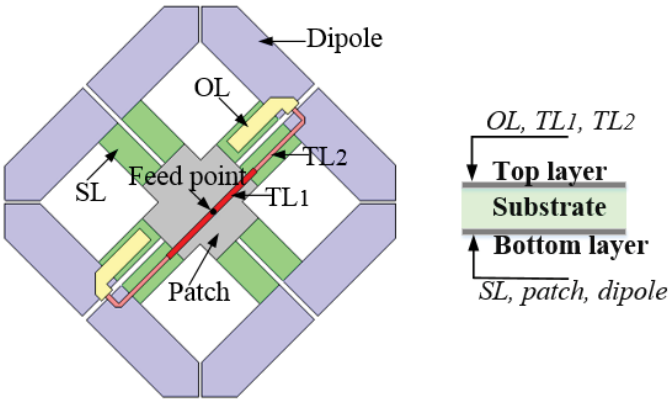

(b)

Figure 5.13 (a) Equivalent circuit, and (b) physical realization of the feed network.

Figure 5.13(a) and 5.13(b) shows the equivalent circuit model and the physical realization of the feed network. It is similar to the feed network presented in Section 5.3.2, thus is not explained in detail here. The optimized values of the circuit elements and the resultant impedance matching result are shown in Figure 5.14. The antenna is well matched to reflection coefficients < -10 dB from 1.55 GHz to 3.12 GHz. The optimized parameters for the realized microstrip feed network are listed in Table 5.2. The reflection

coefficient after applying the feed network is also shown in Figure 5.14. It agrees well with the result of the circuit model, and the antenna is well-matched across a bandwidth of 63.7% from 1.55 GHz to 3.0 GHz.

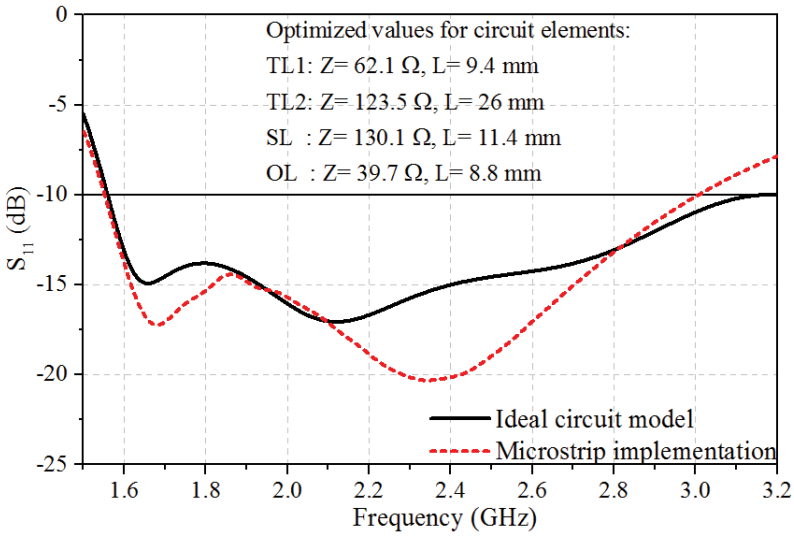

Figure 5.14 Simulated reflection coefficients of the antenna with ideal circuit feed network and its physical realization.

Table 5.2 Optimized Parameters of the Matching Elements

Elements	Line length	Line width	Gap width
TL1	11.44 mm	1.1 mm	-
TL2	15.10 mm	0.9 mm	-
OL	13.10 mm	2.9 mm	-
SL	11.50 mm	5.0 mm	1.0 mm

5.4.2 Experimental Results

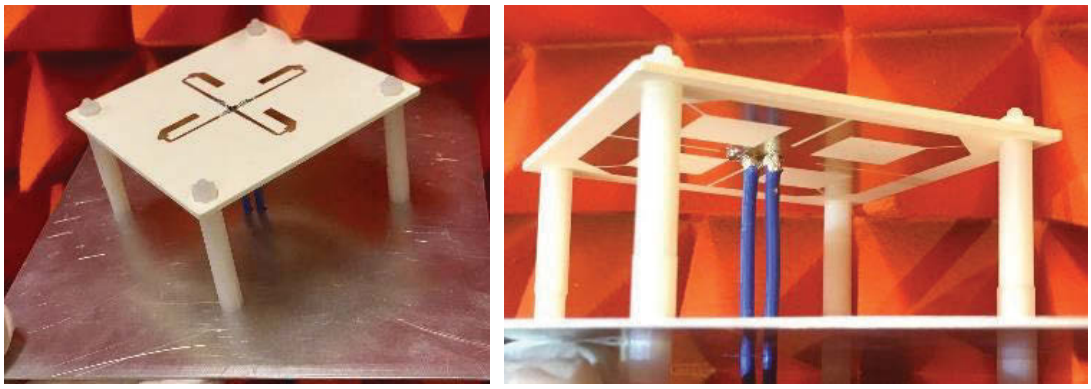

Figure 5.15 Prototype of the dual-linearly polarized antenna.

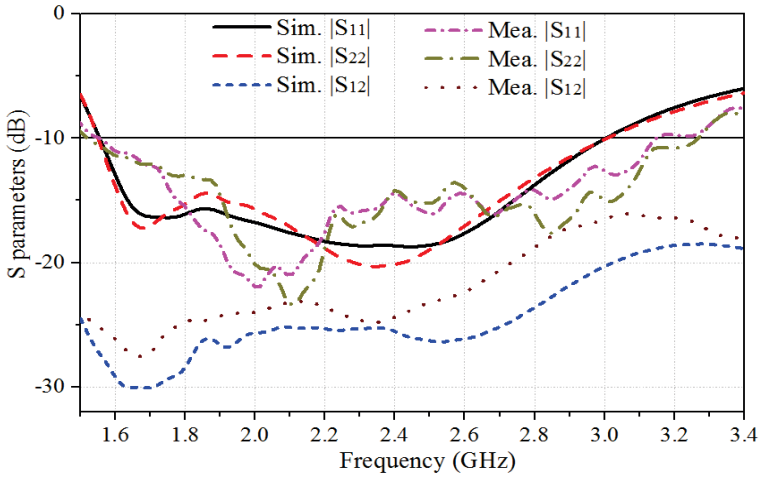

Figure 5.16 Simulated and measured S parameters.

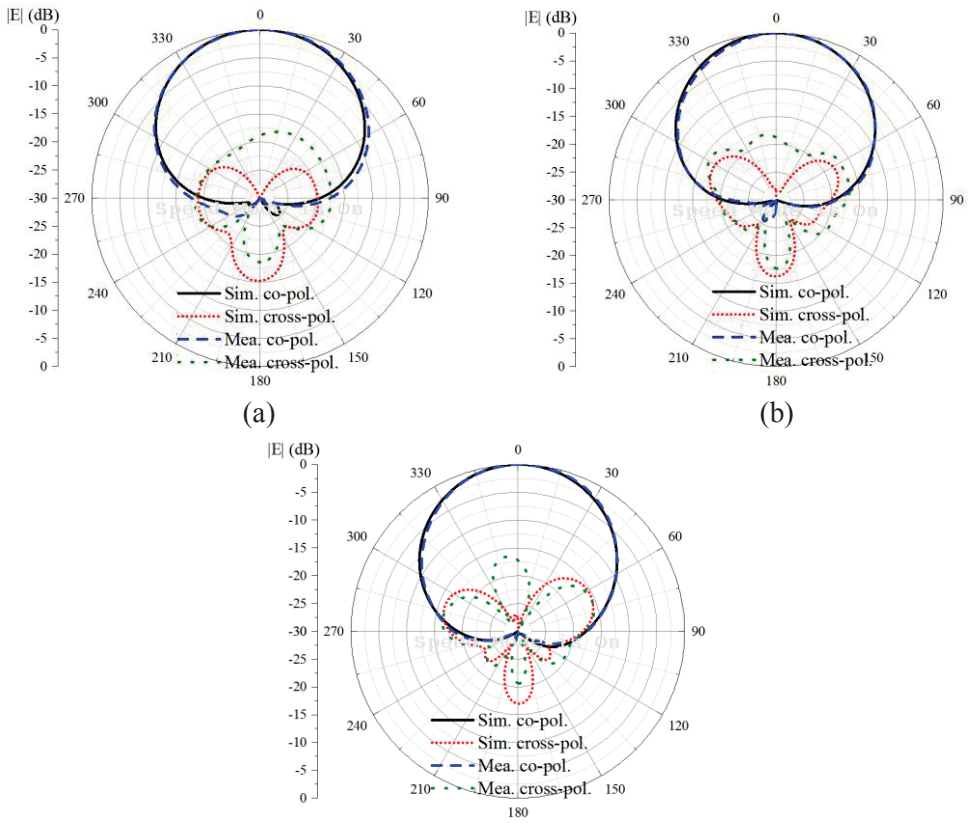

Figure 5.17 Simulated and measured radiation patterns. (a) 1.7 GHz, (b) 2.2 GHz, and (c) 2.7 GHz.

A prototype of the proposed antenna was fabricated and tested, as shown in Figure 5.15. Plastic posts are used to support the antenna. The simulated and measured S-parameters of the two ports are shown in Figure 5.16. The simulated bandwidths with reflection coefficients less than −10 dB is 63.7% from 1.55 GHz to 3.0 GHz, while the measured

bandwidth is slightly wider, which is 68% from 1.55 GHz to 3.15 GHz. This difference can be caused to the losses in the cables and substrate, and also the fabrication and measurement error. Across this wide band, the port-to-port isolation is more than 17 dB. The simulated and measured radiation patterns at 1.7 GHz, 2.2 GHz, and 2.7 GHz are given in Figure 5.17. Due to the symmetry in the antenna configuration, the radiation patterns for the two polarizations are very similar, therefore, only the +45°-polarized patterns are presented here. As observed in Figure 5.17, the measured results agree well with the simulated ones. The measured cross-polarization discrimination is more than 16 dB. Figure 5.18 shows the simulated and measured HPBWs and gains. The measured HPBWs agree well with the simulated results and vary within 67.5°±6.5° for both the two polarizations across this wide band. The simulated gain varies from 8.0 dBi to 9.3 dBi, whereas the measured gain varies from 6.5 dBi to 8.7 dBi. The discrepancy between the simulated and measured gain is mainly attributed to the losses from coaxial cables and SMA connectors.

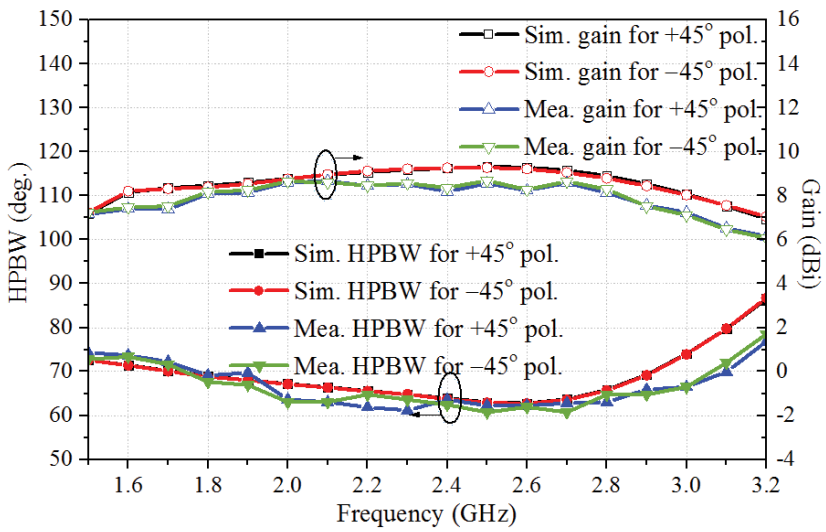

Figure 5.18 Simulated and measured HPBWs and gains.

5.5 The Integration of Planarized Dual-Dipole Antennas

The planarized structures presented in Sections 5.3 and 5.4 can greatly facilitate system integration as RF components can be integrated into the space saved between the radiators and reflector for different purposes. In this way, the integrated system is not only more compact but can also reduce the installation complexity and cost. As a demonstration, in this section, the designed planarized dual-LP antenna in Section 5.4 is integrated with a

coupler to realize dual-circularly-polarized (dual-CP) radiation.

5.5.1 Configuration of the Wideband Coupler

By creating +90° and −90° phase differences while maintaining equal magnitude between two input ports of an orthogonal dual-LP antenna, dual-circular polarization can be realized. In this work, a quadrature coupler is utilized to provide the required ±90° phase differences.

The wideband quadrature coupler was designed using a three-section microstrip branch-line structure. The circuit configuration and the layout of the microstrip realization of the coupler are shown in Figure 5.19. When Port 1 or Port 2 is excited, the output signals at Port 3 and Port 4 have a 90° or −90° phase difference, respectively, with equal magnitudes. The substrate used in this work is Rogers RO3003 with a thickness of 1.52 mm, a dielectric constant of 3.0, and a loss tangent of 0.001. The length of each branch-line is fixed as quarter-wavelength at the center frequency. The coupler optimization was firstly conducted in circuit simulation with the model shown in Figure 5.19(a), then it was implemented using microstrip lines, as shown in Figure 5.19(b). Finally, overall adjustments were made based on the full-wave simulation results in CST Microwave Studio. The optimized dimensions for the microstrip lines are listed in Table 5.3.

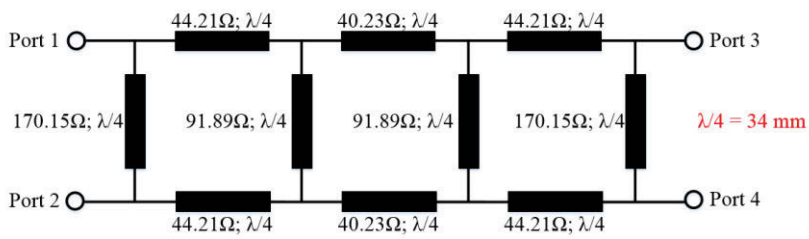

(a)

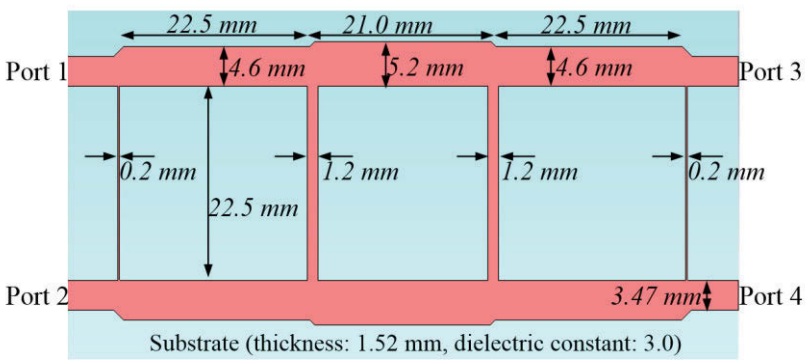

(b)

Figure 5.19 (a) Circuit design and (b) the printed circuit board realization of the wideband coupler.

Table 5.3 Optimized Parameters for Coupler

Parameters	VALUE	Parameters	Value
Lc1	22.5 mm	Lc2	21.0 mm
Lc3	22.5 mm	Wc1	4.6 mm
Wc2	5.2 mm	Wc3	0.2 mm
Wc4	1.2 mm	Wc5	3.47 mm

Figure 5.20 illustrates the full-wave simulation results of the three-section branch-line coupler when Port 1 is excited. As shown in Figure 5.20(a), both the coupler's reflection coefficient $|S_{11}|$ and port isolation $|S_{21}|$ are less than −15 dB across a very wide band from 1.42 GHz to 3.0 GHz. The magnitudes of the two outputs are depicted in Figure 5.20(b). It is observed that across the band from 1.56 GHz to 2.84 GHz, the maximum amplitude imbalance between two output ports is less than 1.5 dB. As shown in Figure 5.20(c), across that band, the phase difference between the two outputs is around 90° with only 2° deviations. When Port 2 is excited and Port 1 is terminated, all the performances are very similar except that the phase difference between Ports 3 and 4 is −90°. Therefore, the results when Port 2 is excited are not repeated here.

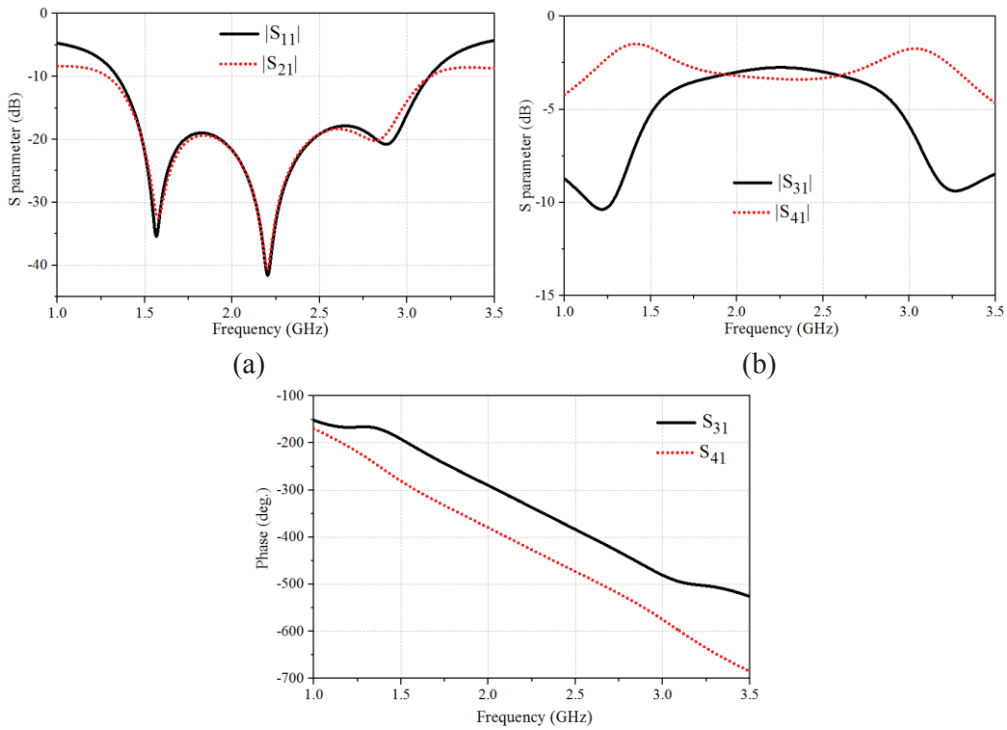

Figure 5.20 Simulated (a) magnitude of S_{11} and S_{21}, (b) magnitude of S_{31} and S_{41}, and (c) phases of S_{31} and S_{41} of the wideband coupler.

5.5.2 Configuration of the Integrated Dual-CP Antenna

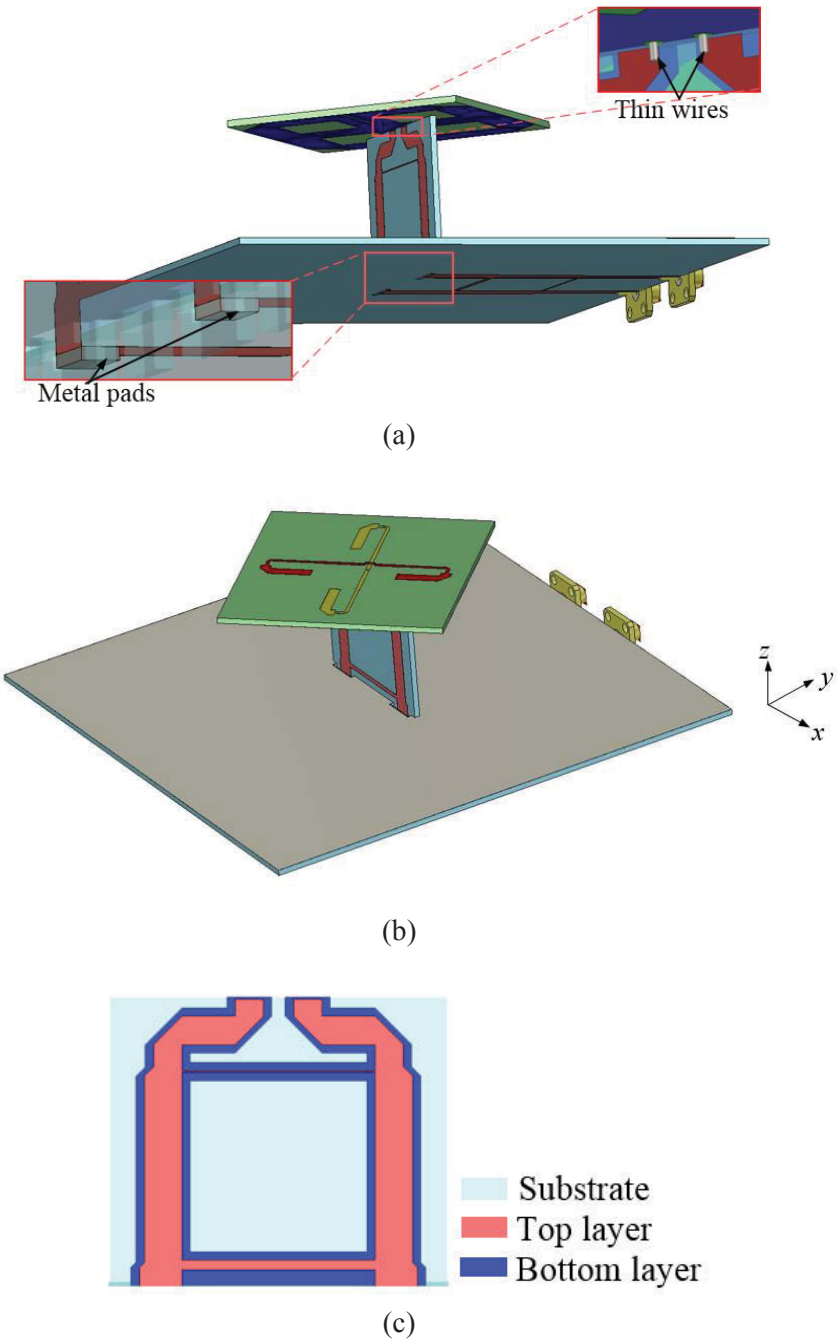

Figure 5.21 Configuration of the wideband dual-circularly-polarized antenna: (a) high-angle perspective view, (b) low-angle perspective view, and (c) detail view of the vertical coupler.

The wideband coupler is then integrated with the designed dual-LP antenna to realize desired dual-CP radiation. Although the coupler has a large dimension, it can be bent to optimally fit in the space saved by the planar-configured dual-LP antenna, as shown in Figure 5.21. Part of the coupler is placed between the antenna aperture and the reflector,

providing mechanical support. The other part of the coupler is located on the other sides of the reflector. After being integrated with the bent coupler, the reflector becomes a printed circuit board with one side all covered with metal functioning as the reflector and the other side printed with microstrip lines.

For the vertical part of the coupler, instead of using a traditional ground fully covered by metal, a defected ground is adopted, as shown in Figure 5.21(c). Most of the metal of the ground is removed except the metal at the back of microstrip lines, making the ground appear as a zoomed-out coupler. The reason for modifying the ground is to minimize its negative effect on the antenna's AR performance. Figure 5.22 shows the current distribution and the resultant AR performance with the traditional and defected grounds, respectively. As shown in Figure 5.22(a), a considerable amount of currents are distributed in the edges and middle of the traditional ground, which significantly deteriorates the AR performance shown in Figure 5.22(c). By adopting the defected ground, the currents concentrate on the back of the microstrip line, as shown in Figure 5.22(b), thereby introducing minimal deterioration to AR. With the defected ground, AR is maintained < 2 dB from 1.4 GHz to 2.75 GHz.

The connections between the antenna aperture, the vertical part of the coupler, and the reflector are carefully designed. On the upper part, the ground of the coupler is directly attached to the middle patch on the radiator layer, and the microstrip lines are connected with the feed lines on the top layer using thin wires. On the lower part, the reflector is etched with some slots to insert the vertical coupler in. Additional metal pads are utilized to ensure a good connection between the microstrip lines on the vertical and horizontal parts of the coupler.

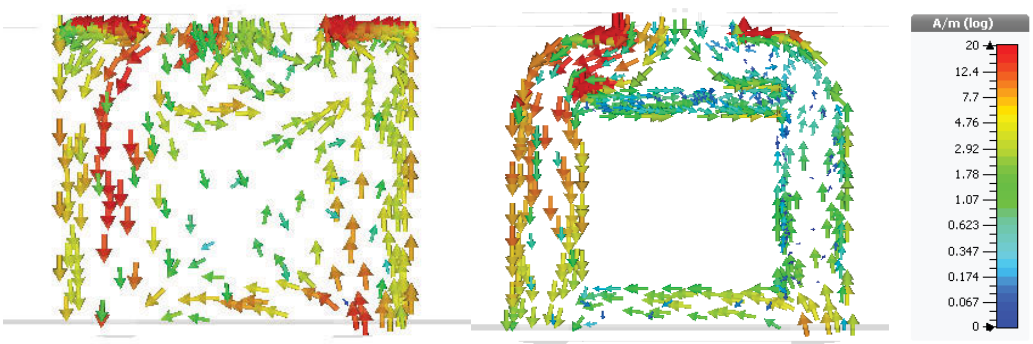

(a) (b)

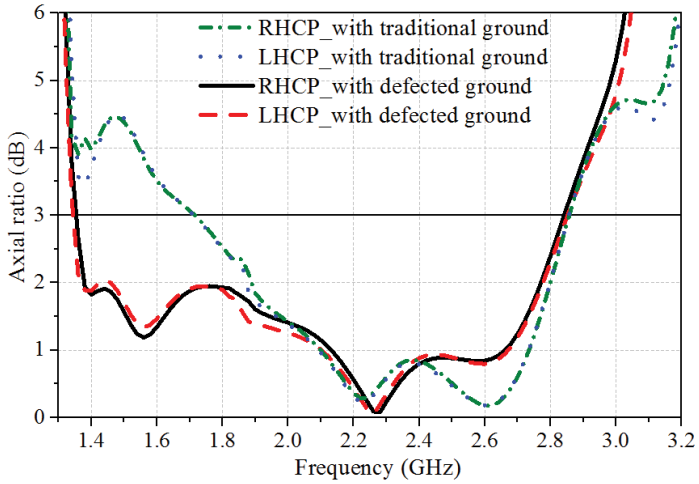

(c)

Figure 5.22 Current distribution on the coupler with (a) a traditional ground plane and (b) a defected ground plane, and (c) the resultant AR for the two cases.

5.5.3 Experimental Results

(a) (b)

(c)

Figure 5.23 Prototype of the dual-circularly polarized antenna: (a) top view, (b) side view, and (c) perspective view.

The dual-CP antenna is also fabricated and tested, as shown in Figure 5.23. When ports 1 or 2 is excited, left-handed circular polarization (LHCP) or right-handed circular polarization (RHCP) radiation is obtained.

The simulated and measured reflection coefficients and AR results of the two circular polarizations are shown in Figures 5.24 and 5.25. The simulated and measured 10-dB impedance bandwidth for the two ports are 79.7% and 81%, respectively. The measured 3-dB AR bandwidth is 80% from 1.3 GHz to 3.04 GHz.

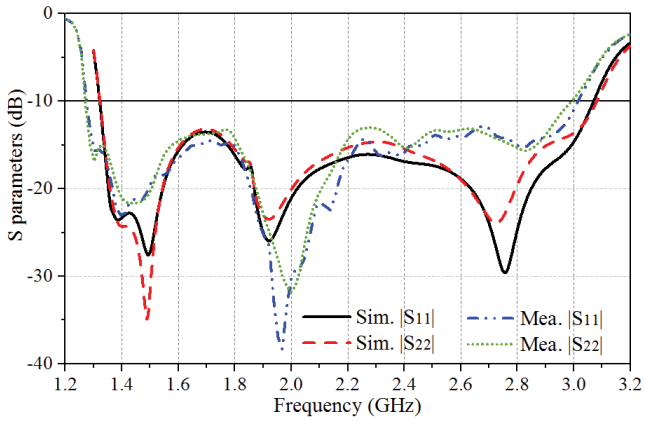

Figure 5.24 Simulated and measured reflection coefficients of the dual-circularly-polarized antenna.

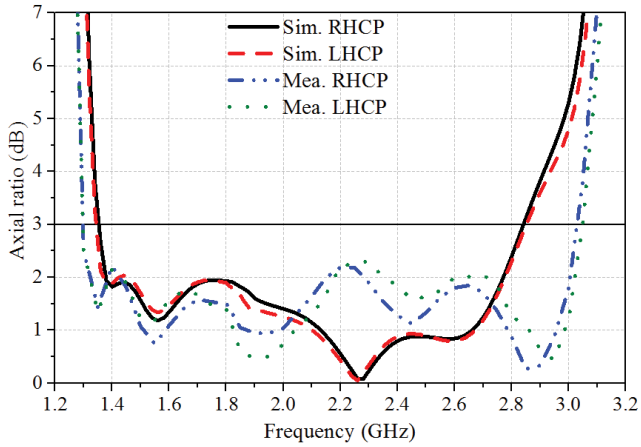

Figure 5.25 Simulated and measured axial ratio of the dual-circularly-polarized antenna.

The radiation patterns for RHCP at 1.5 GHz, 2.2 GHz and 3.0 GHz are shown in Figure 5.26. As the radiation patterns for LHCP are very similar to those of the RHCP, they are not shown here for brevity. The measured patterns agree well with the simulated ones, and both demonstrate good broadside CP radiations. The HPBW and gain results for the two polarizations are shown in Figure 5.27. The gain is very stable across most of the

operation band, with a peak of 9.3 dBi at 2.7 GHz. The overlapped bandwidth of −10-dB reflection coefficient, 3-dB AR, and 3-dBi gain variation is 66.7% from 1.50 GHz to 3.0 GHz. Across this wide band, the radiation pattern is very stable with the horizontal HPBW varies within 67.5°±5°.

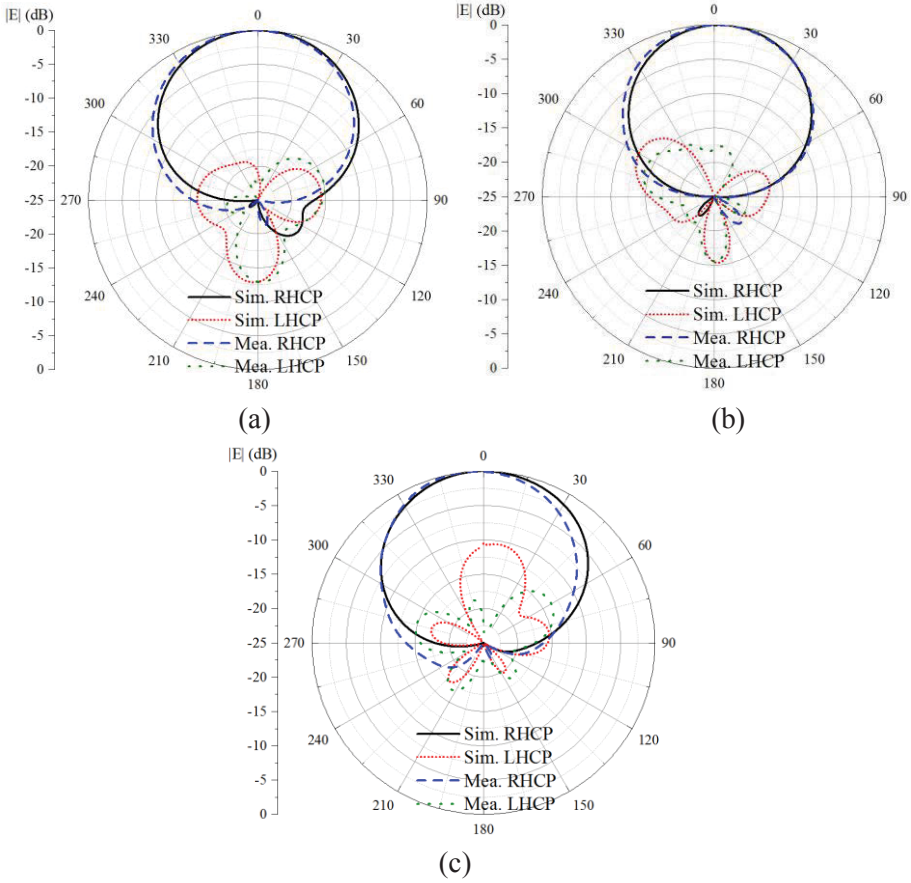

Figure 5.26 Simulated and measured radiation patterns of LHCP at (a) 1.5 GHz, (b) 2.2 GHz, and (c) 3.0 GHz.

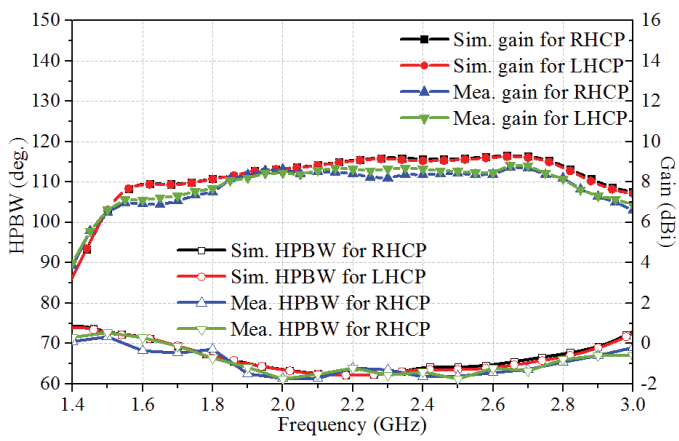

Figure 5.27 Simulated and measured HPBWs and Gains of the dual-circularly-polarized antenna.

Table 5.4 lists the comparison of this work and previous published wideband dual-CP antenna elements. It shows that this antenna has a wideband and high-gain performance with a relatively compact size.

Table 5.4 Comparison of Dual-CP Antennas' Performance

Ref.	Antenna size (λ^3)	Bandwidth*	Maximum gain (dBi)
[101]	0.76*0.76*0.22	13.0%	4.9
[104]	5.44*2.69*0.54	11.8%	10.3
[106]	1.17*1.17*1.75	85.7%	7.5
This work	0.95*0.95*0.26	80%	9.3

* The criteria for the operating band is reflection coefficients < -10 dB and AR< 3 dB.

5.6 Summary

This chapter presents the design and integration of the planarized dual-dipole antennas. For the first time, baluns are integrated on the same substrate with dual-LP radiators to achieve a fully planar configuration. The circuit model of feed network including balun is proposed to facilitate the impedance matching within a restricted space. Two planarized dual-dipole antennas are designed with simple and compact structures. Simulated and measured results show that the antennas have stable radiation performances across wide operating bands. To demonstrate the advantage of planarized configuration in antenna integration, a dual-CP antenna is realized by integrating a wideband coupler into the space between the radiators and reflector of the planar dual-LP antenna. Physical modifications of the coupler were made to realize a compact structure and improve the axial ratio while maintaining desired performances. The dual-CP antenna has a wide well-matched bandwidth and stable radiation performance with a very compact structure. The proposed planarized design of dual-LP antennas and the integrated dual-CP antenna serves as good candidates and offers a direction for future integrated antenna systems.

Chapter 6: Multi-Band Base Station Antenna Arrays

6.1 Introduction

The exponential growth of data traffic and demand for mobility have driven an unprecedented expansion of the mobile communications industry for over two decades. As mobile communication standards evolve from generation to generation, and now rapidly move towards 5G, multi-band antenna arrays are in urgent need to simultaneously support different standards. The arrays for different bands usually share a common ground plane and radome, and elements of different bands are often interleaved to save space. However, there is a penalty for the proximity of the elements in the form of distortion of radiation pattern due to scattering of the signals of one band by the antenna elements operating in another band. Since LB antenna elements are typically larger than HB ones, suppression of the scattering of HB signals from LB elements can significantly improve the system performance.

In this section, we present novel methods to suppress scattering in multi-band antenna arrays using choking techniques. Firstly, the scattering problem in the dual-band antenna arrays is presented and discussed. Following that, three different types of choking techniques are proposed and analyzed. To verify their performances, they are implemented in the LB antenna elements in dual-band antenna arrays. Two dual-band base station antenna arrays targeting at 3G and 4G applications, and 4G and 5G applications, respectively are designed. Simulated and measured results demonstrate that the cross-band scattering in the dual-band array is reduced, and the arrays are capable of producing stable radiation patterns across required wide bands.

6.2 Statement of Cross-band Scattering Problem

A section of interleaved dual-band BSA array shown in Figure 6.1 is simulated to demonstrate the scattering problem. The complete BSA array consists of array sections repeated in the y-direction. In this array, a strip-shaped cross-dipole is used as the unaltered LB element, and square-shaped cross-dipoles are used as the HB elements. Baluns are used to provide balanced feeding and impedance matching for these elements. The LB element is located midway between the four HB elements in two columns. The two HB columns form two HB sub-arrays, and they are fed from independent wideband

phase-shifters which for modeling purposes are represented as power dividers, as shown in Figure 6.1(b). HB elements with the same polarization in one column are excited simultaneously. The LB element is fed separately at the inputs to the two baluns. The parameters for the array arrangement are marked in Figure 6.1. Those parameters were chosen for good MIMO performance while keeping the array compact. The S-parameters for the LB and HB elements when alone are shown in Figure 6.2. The LB element operates from 0.82 GHz to 0.98 GHz, and the HB element operates from 1.70 GHz to 2.30 GHz.

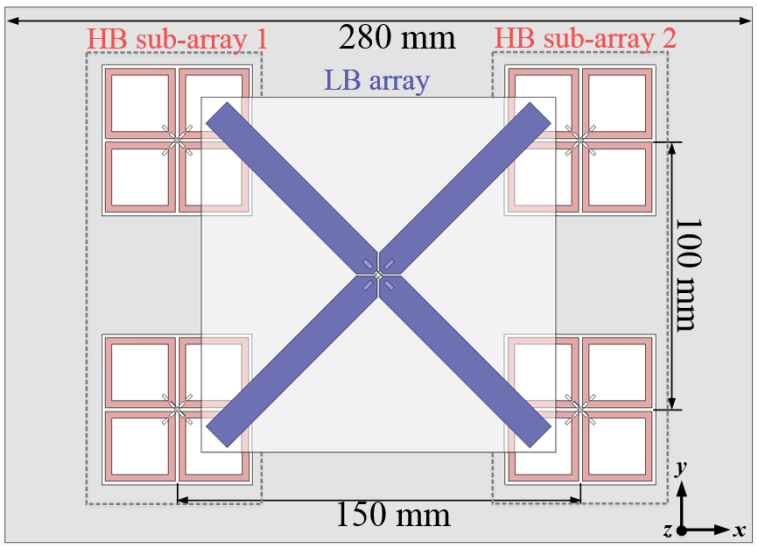

(a)

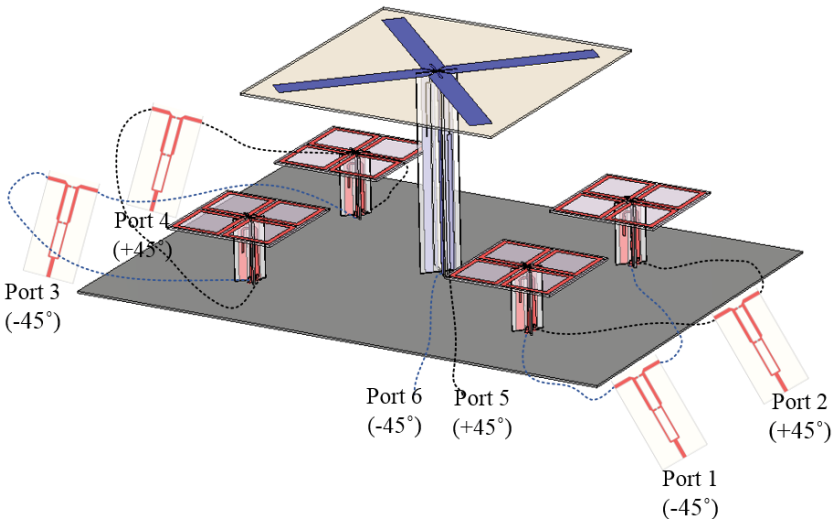

(b)

Figure 6.1 Configuration of the interleaved BSA array section: (a) top view, and (b) perspective view.

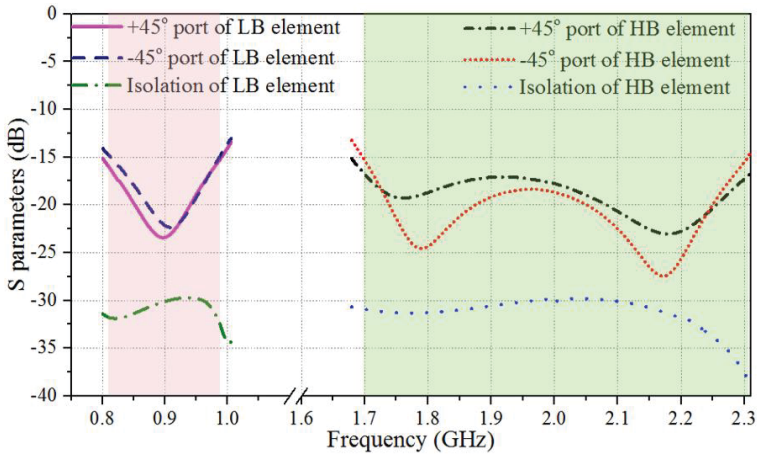

Figure 6.2 Simulated S-parameters for the LB and HB antennas when working alone.

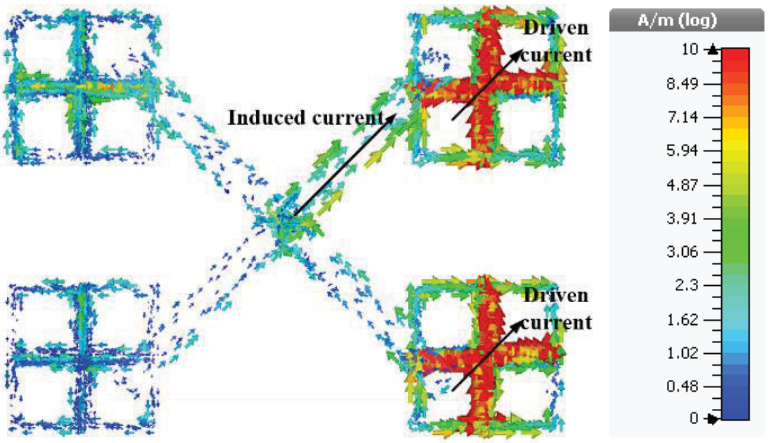

Figure 6.3 Current distribution on the array section when HB array on the right column is excited.

It is apparent from Figure 6.1(a) that the LB element overlaps the HB elements. The close spacing between LB and HB elements causes scattering of HB signal by the LB element. The simulated current distribution in the array with unaltered LB element at 1.7 GHz is shown in Figure 6.3. Most of the induced current on the LB arms has the same direction as the HB driven current. These currents re-radiate, resulting in a deteriorated HB radiation pattern. The radiation patterns in the horizontal plane (*zx*-plane) with and without the LB element are shown in Figure 6.4 at 1.7 GHz, 1.8 GHz and 1.9 GHz. Without the LB element, the HB array has a symmetrical pattern with the main beam pointing at boresight. After the LB element is added, the HB radiation pattern deteriorates, i.e. the main beam splits or shifts away from boresight. In the worst case, the main lobe direction of the pattern is tilted to 19°, as shown in Figure 6.4(a). The distorted radiation patterns obtained after adding the LB element cannot provide required coverage, and lead

to signal loss in particular areas. This is generally unacceptable by cellular operators. It is therefore very desirable to find a method of suppressing the scattering and restoring the pattern in such multi-band BSAs.

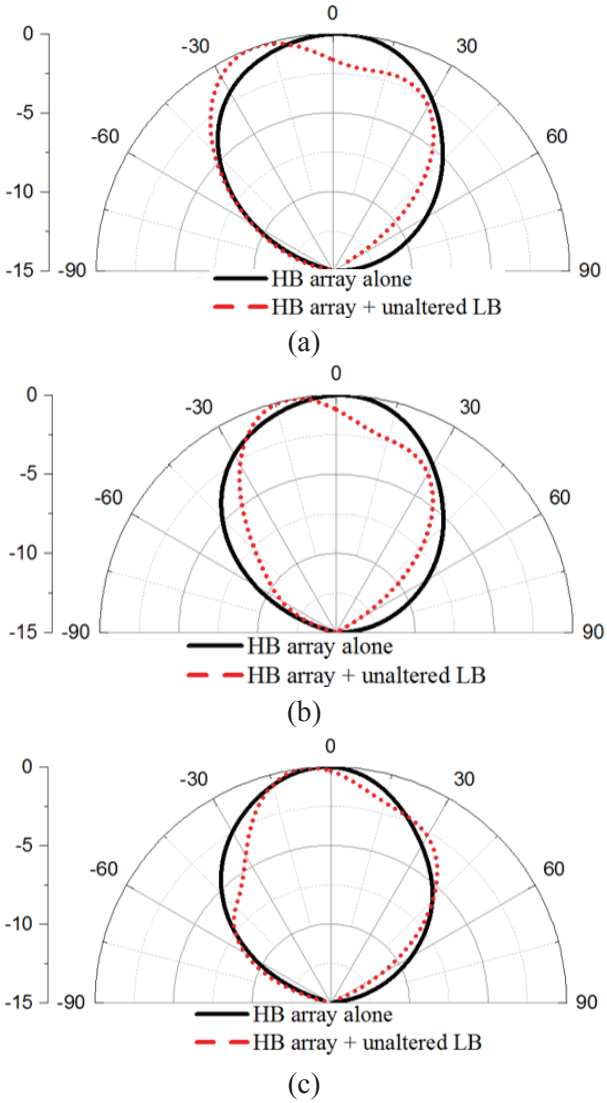

Figure 6.4 Horizontal radiation patterns of the HB array i) without, and ii) with the unaltered LB element at (a) 1.7 GHz, (b) 1.8 GHz, and (c) 1.9 GHz.

6.3 Choking Techniques to Suppress Cross-Band Scattering

To minimize the scattering caused by the LB element, one effective way is to suppress the induced HB currents on the LB arms. In this work, this is achieved by introducing chokes periodically along LB dipole arms, or as LB dipole arms to block the HB currents but affect LB currents as little as possible. An illustration of choke-inserted LB radiator is shown in Figure 6.5. These chokes should present an open circuit at the high band and

a short circuit at the low band. Similar concept has been adopted to realize multi-band trap antenna [107], [108]. The theoretical analysis of chokes is detailed in the following. Note that in the analysis, the suppressed high band is around 3.5 GHz. Different suppressed bands for different applications can be tuned by optimizing parameters of chokes.

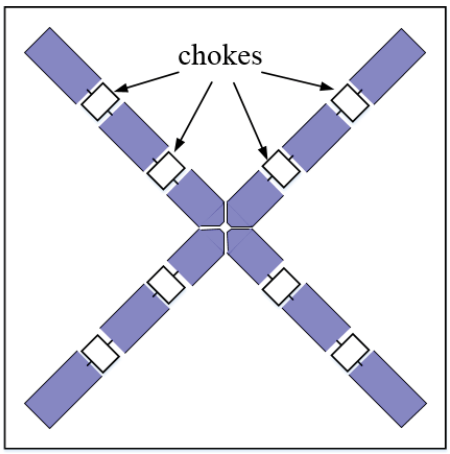

Figure 6.5 One example of the choked radiator.

6.3.1 Choke 1: The Spirals

The first choking structure investigated is the spiral, as shown in Figure 6.6. Similar to the helix coil, each cell of the spiral can be represented as a parallel LC circuit. It presents an open circuit at its resonant point, where the impedance at both ends tends to infinity, and the current at that point cannot be effectively induced. In the frequency bands much lower than the resonant point, the spiral has a lower inductive impedance and a higher shunt capacitive impedance. It therefore introduces a small inductance compared with the corresponding cylindrical conductor, and only has minimal effect on the LB radiation and impedance. Therefore, utilizing its intrinsic property, the spiral structure can be used as a LB radiator to suppress the unwanted HB induced currents while maintaining the radiating currents in the low band.

There are three important parameters to tune its resonant frequency point: distance between adjacent turns g, the inner diameter of spiral d, and the width of strip w. The thickness of the strip here is set as 0.5 mm. The influences of these parameters on the resonant frequency point are examined in the simulation. As shown in Figure 6.6(b), the spiral is illuminated by a plane wave with E-field along the axis of the spiral, and currents induced on it are monitored. One turn of the spiral is placed in a boundary box which has

a periodic boundary in the *x*-direction, and open-space boundary in the *y*- and *z*-directions. The periodic boundary in the *x*-direction was set to simulate an infinitely long spiral to eliminate the effects of discontinuity. The maximum currents flowing on the spiral structure with different values of *g*, *d*, and *w* are plotted in Figure 6.7. For comparison, currents flowing on a cylinder conductor with the same diameter as the spiral are included in the figures as a reference. As shown in Figure 6.7(a), larger g moves the minimum induced current point to a higher frequency, corresponding to the resonant point of the spiral moving to a higher frequency. This is because increasing g decreases the capacitance, which raises the parallel resonant frequency. As shown in Figure 6.7(b), larger d moves the resonant point to a lower frequency, as it increases the inductance and capacitance of the spiral. The inductance increases approximately as the square of d and the capacitance linearly with d. As shown in Figure 6.7. (c), larger *w* moves the resonant point to a higher frequency, as it decreases the inductance of the spiral.

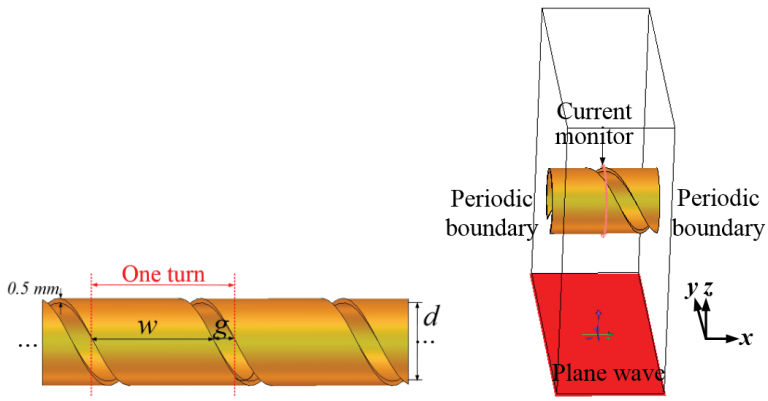

(a) (b)

Figure 6.6 (a) Configuration of spiral structure. (b) Demonstration of spiral structure illuminated by plane wave.

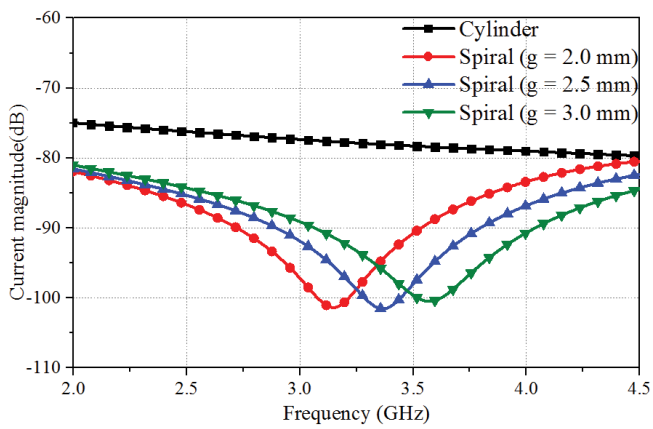

(a)

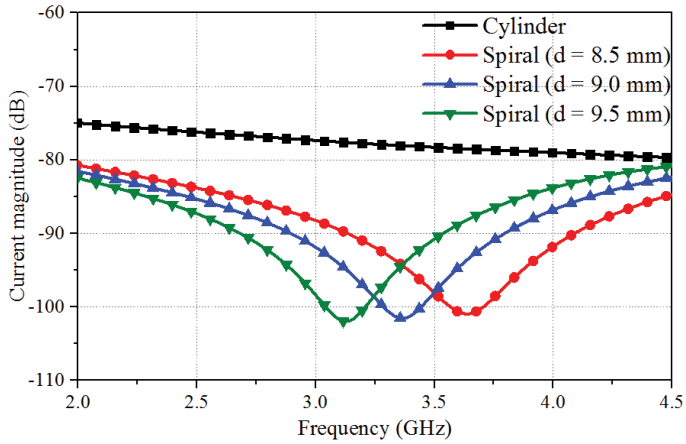

(b)

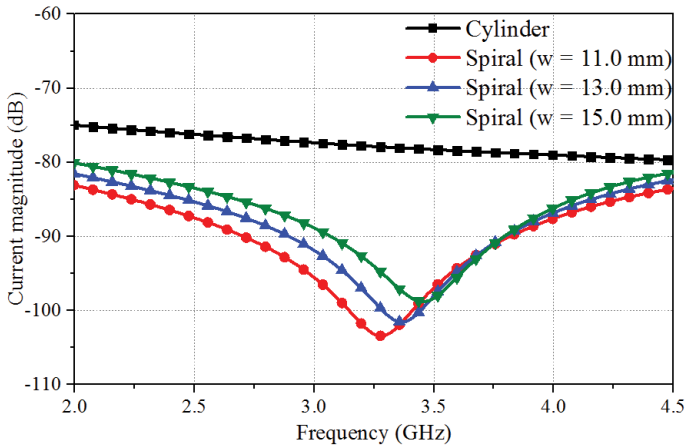

(c)

Figure 6.7 Maximum induced current on the spiral structure with different (a) gap *g*, (b) inner diameter *d*, and (c) width of strip *w*.

To assess the capability of a choke to efficiently suppress the scattering currents, we define scattering suppression bandwidth (SSBW) as the band in which Δ>10 dB, where Δ is the difference (in dB) between the currents induced on a structure with and without chokes. In this case, the structure without chokes is a cylinder. We selected several spirals with the same resonant point at 3.5 GHz but with different combinations of parameters, and monitored the induced currents on them, as shown in Figure 6.8. The current induced on the unmodified cylinder is also simulated and plotted for comparison. The difference Δ is marked in the plot. The SSBWs for spiral with different combinations of parameters are calculated and listed in Table 6.1. It shows that the spiral with a larger *g* and a smaller *w* has a wider SSBW. Similar to coils, the spiral with a larger *g* and a smaller *w* leads to a smaller capacitance and a larger inductance. Therefore, we expect that a larger L/C ratio leads to a broader SSBW for the spiral structure.

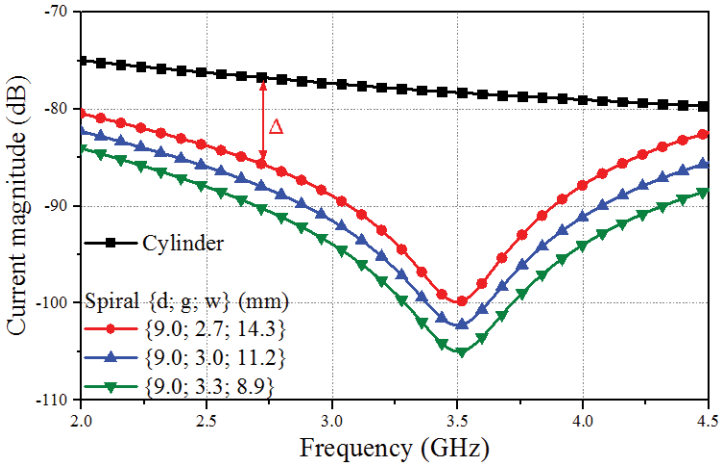

Figure 6.8 Maximum induced current on the spiral structure resonating at 3.5 GHz with different combinations of parameters.

Table 6.1 SSBW of Spiral with Different Combinations of Parameters

{ d; g; w} (mm)	SSBW
{9.0; 2.7; 14.3}	32.0%
{9.0; 3.0; 11.2}	47.5%
{9.0; 3.3; 8.9}	66.0%

6.3.2 Choke 2: The Coaxial Chokes

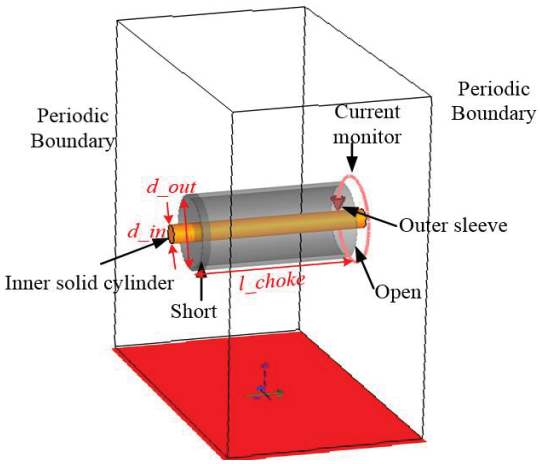

Figure 6.9 Configuration of coaxial chokes.

The second choking structure presented is the coaxial choke, as shown in Figure 6.9. A large diameter cylindrical sleeve with a length around quarter wavelength in the high band surrounds the thin inner conductor and has one end attached to it. The working principle for this structure is creating a quarter-wavelength coaxial resonator in the high band to

stop the scattering currents flowing on it. The performance of coaxial choke is also examined using plane-wave illumination in a periodical boundary condition, as shown in Figure 6.9. Three parameters determining the resonating frequency point are the length of the sleeve *l_choke*, the diameter of the sleeve *d_out*, and the diameter of the inner conductor *d_in*. The induced currents on the chokes with different parameters are monitored, and the results are plotted in Figure 6.10. The induced current on the conductor without sleeve is also plotted in Figure 6.10 for comparison. It can be observed that large *l_choke*, large *d_out*, or small *d_in* move the minimum induced current point to a lower frequency.

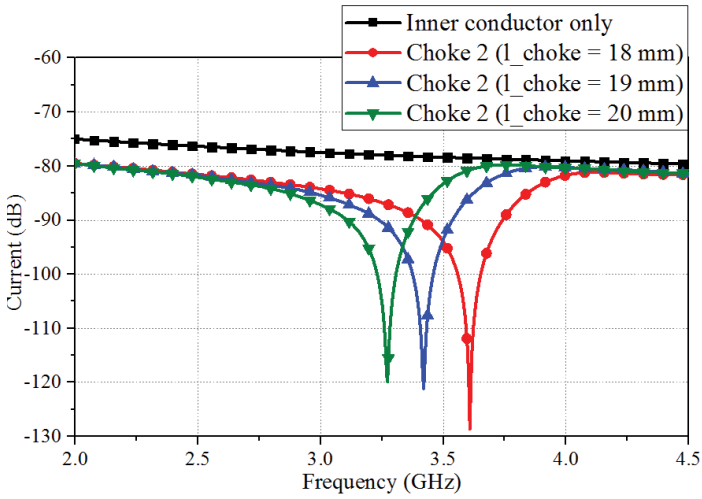

(a)

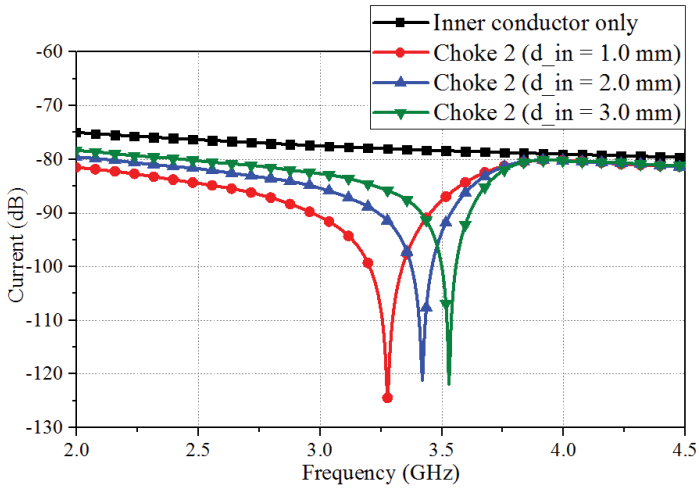

(b)

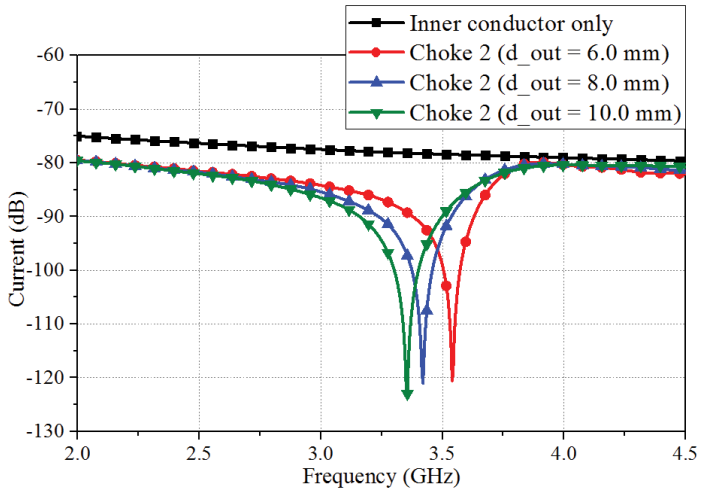

(c)

Figure 6.10 Maximum induced current on the arm with coaxial chokes with different (a) *l_choke*, (b) *d_in*, and (c) *d_out*.

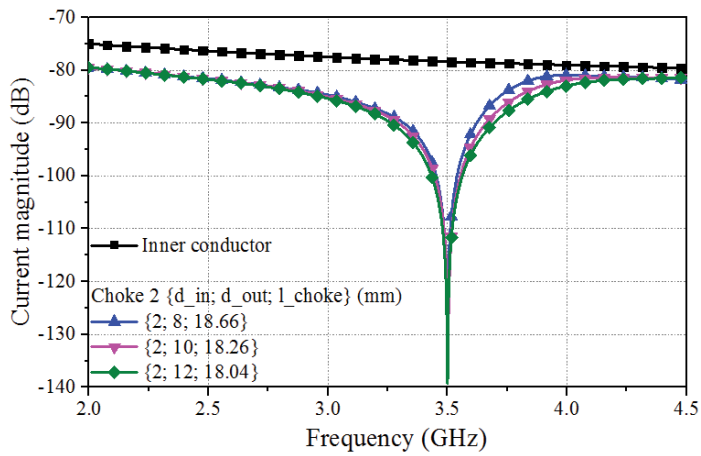

Figure 6.11 Maximum induced current on the arm with coaxial chokes with resonant point at 3.5 GHz but with different combinations of parameters.

Table 6.2 SSBW of Coaxial Chokes with Different Combinations of Parameters

{*d_in; d_out; l_choke*} (mm)	SSBW	Impedance of the coaxial (Ω)
{2; 8; 18.66}	11.8%	83.12
{2; 10; 18.26}	13.9%	96.50
{2; 12; 18.04}	16.0%	107.44

The induced currents on the coaxial chokes that have the same resonant point at 3.5 GHz but with different combinations of parameters are plotted in Figure 6.11. It is clear that different combinations of parameters have different SSBW. SSBW with different parameters is calculated and listed in Table 6.2. The characteristic impedance of the

coaxial chokes is also calculated and included in the table. A clear relationship between the choking bandwidth and the characteristic impedance of the coaxial choke is revealed, i.e., larger impedance enhances the SSBW of the coaxial choke.

6.3.3 Choke 3: The Stripline Chokes

The third choking structure analyzed here is the choke formed by conducting lines, as shown in Figure 6.12. It is constructed as a parallel LC circuit, where the inductance is provided by the thin conducting strip and the capacitance is provided by the gap in the radiators. It presents an open circuit at its resonant point, which can be utilized to suppress the HB scattering current. The suppression capability is investigated using the same method as the last two cases. The parameters that are important for the resonant point (open-circuit point) in this case are the width of the conducting line *w,* the height of the conducting line *h*, and the gap width *s*. The induced current flowing on this structure is monitored with different parameters, and the results are shown in Figure 6.13. Smaller *w* and larger *h* move the resonant point to a lower frequency as they increase the inductance. Larger *s* moves the resonant point to a higher frequency as it decreases the capacitance.

The induced currents on the choke 3 with the same resonant point but different combinations of parameters are shown in Figure 6.14. The SSBWs in different cases are listed in Table 6.3. From Figure 6.14 and Table 6.3, it can be observed that the combination with a larger *s*, or thinner *w* has a wider SSBW. As a larger *s* decreases the capacitance *C* and a thinner *w* increases the inductance *L* for the corresponding circuit model, it can be concluded that a larger *L/C* ratio enhances the scattering suppression bandwidth of the stripline choke.

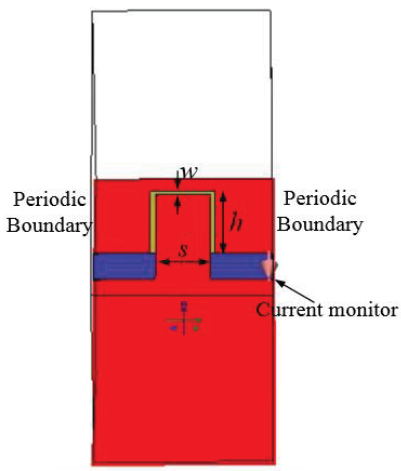

Figure 6.12 Configuration of choke 3 with conducting lines.

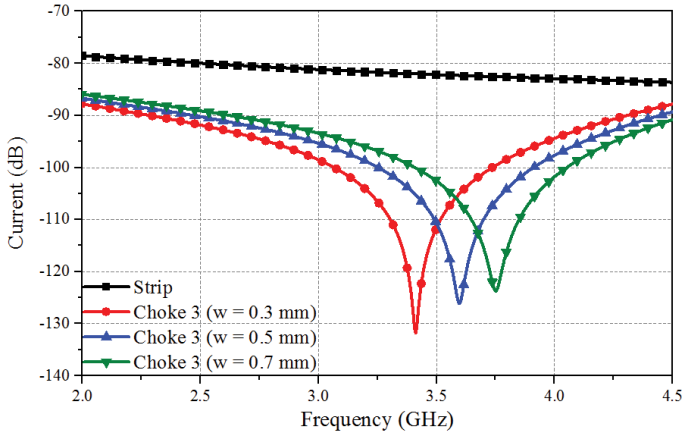

(a)

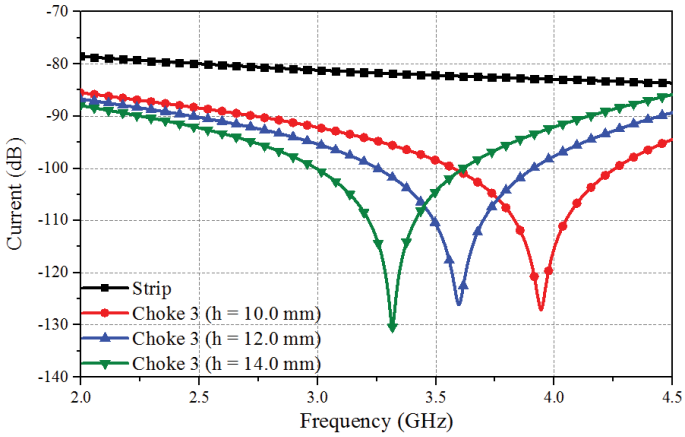

(b)

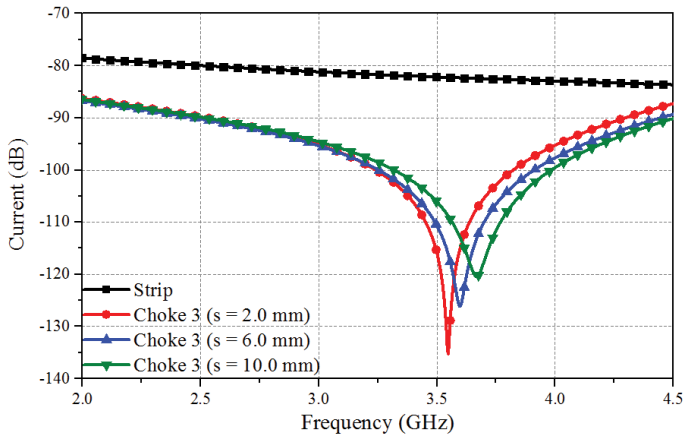

(c)

Figure 6.13 Maximum induced current on the radiator with conducting lines with different (a) *w*, (b) *h*, and (c) *s*.

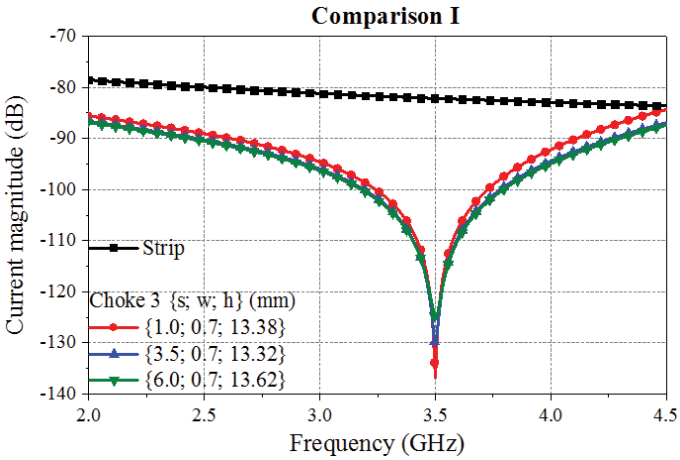

(a)

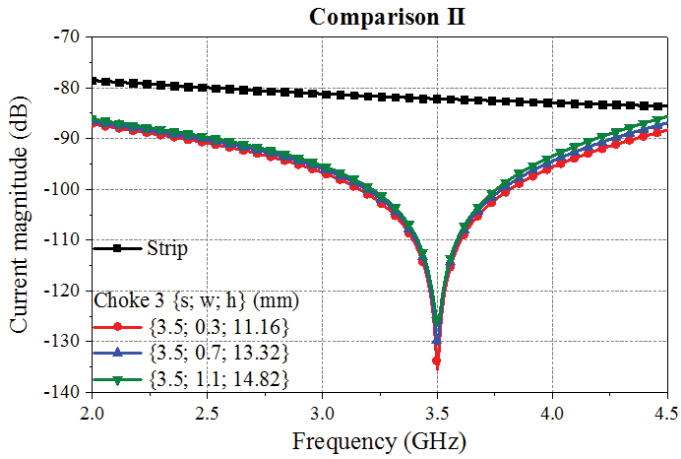

(b)

Figure 6.14 . Magnitudes of the induced currents on the arm with stripline chokes with resonant point at 3.5 GHz but with different combinations of parameters: (a) different combination of *s* and *h* when fix *w*, and (b) different combination of *w* and *h* when fix *s* (unit: mm).

Table 6.3 SSBW of Stripline Chokes with Different Parameter Combinations

	{*s, w, h*} (mm)	SSBW
Comparison I	{1.0; 0.7; 13.38}	39.7%
	{3.5; 0.7; 13.32}	49.7%
	{6.0; 0.7; 13.62}	52.7%
Comparison II	{3.5; 0.3; 11.16}	55.9%
	{3.5; 0.7; 13.32}	49.7%
	{3.5; 1.1; 14.82}	44.9%

6.3.4 Discussion

In this section, we analyzed the working principle and the scattering suppression capability of three different chokes. To study the scattering suppression capabilities, a series of chokes is illuminated by a plane wave and the induced currents on the chokes

are monitored at different frequencies. SSBW is defined based on the monitored currents as a measure of the scattering suppression capability. It is found that for the investigated chokes that act as a parallel LC circuit, a higher inductance/capacitance ratio (*L/C*) leads to a wider SSBW. When the choke is implemented by a transmission line, e.g., Choke 2, the higher *L/C* value directly translates into a higher characteristic impedance of the transmission line, which is more straightforward for designers. For the three chokes analyzed, the coaxial choke only suppresses scattering across a very narrow band, whereas the spiral and stripline chokes have wideband scattering capabilities.

6.4 Application I: Interleaved 3G and 4G Base Station Antenna Array

In this section, we target at solving the cross-scattering problem in the dual-band 3G and 4G BSA array illustrated in Section 6.2. The modified array section is shown in Figure 6.15. The LB element is located midway between the four HB elements in two columns. The array is designed to operate at low band ranging from 820 MHz to 1000 MHz and high band from 1710 MHz to 2280 MHz – which cover the operating frequencies of most mobile communication systems, including CDMA, GSM, PCS, and UMTS.

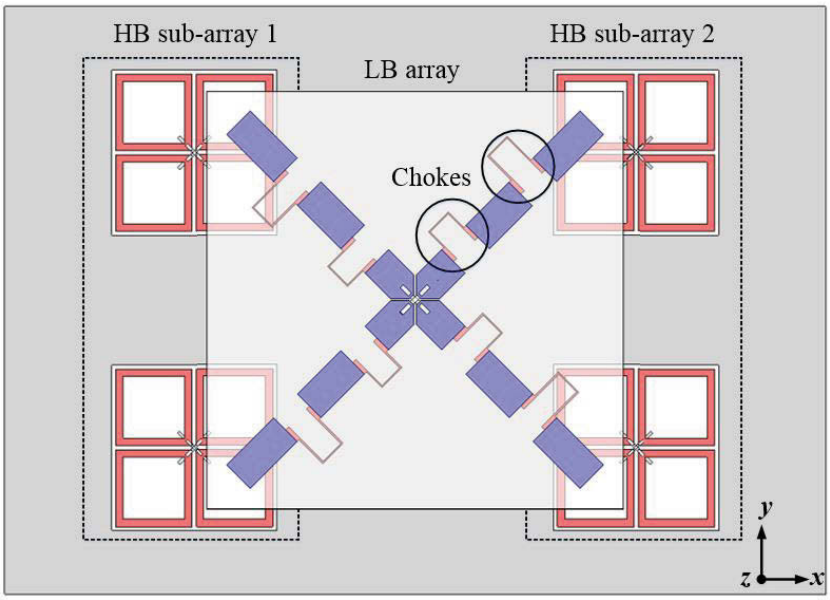

Figure 6.15 Dual-band dual-polarized base station antenna array configuration with interleaved scheme.

6.4.1 Design of Stripline-Choked LB Element

In this application, choke 3, which is the stripline choke, is utilized to suppress HB scattering. It is periodically introduced along LB dipole arms to block the HB currents but affects LB currents as little as possible, as shown in Figure 6.15. The design procedure and the performance of the choked LB antenna are detailed in the following.

6.4.1.1 Circuit Model of the Choke

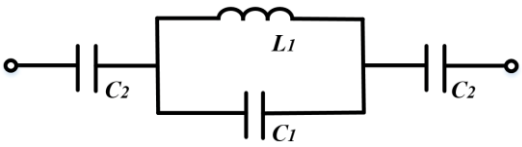

Figure 6.16 Circuit model of the choke.

The circuit model of the choke is shown in Figure 6.16. It consists of a parallel resonant at the high band comprising L_1 and C_1, and a series resonance at the low band with two additional capacitances C_2. These requirements give

$$j2\pi f_h C_1 + \frac{1}{j2\pi f_h L_1} = 0 \tag{6.5}$$

$$\frac{2}{j2\pi f_l C_2} + \frac{1}{j2\pi f_l C_1 + \frac{1}{j2\pi f_l L_1}} = 0 \tag{6.6}$$

where f_h is the open-circuit frequency point at high band, and f_l is the short-circuit frequency point at low band. The values of f_h and f_l are both known in our target application. A remaining variable can be chosen to determine values for all the components L_1, C_1 and C_2.

$$Z_c = \sqrt{\frac{L_1}{C_1}} \tag{6.7}$$

This equation sets the impedance level at which the choke operates and determines the bandwidths over which the open circuit and short circuit are effective, as discussed in Section 6.3.3. L_1, C_1, and C_2 can be found given f_h, f_l, and Z_c. By suitably choosing L_1, C_1, and C_2, we can attain the desired open-circuit and short-circuit frequency points at high and low bands, respectively.

6.4.1.2 Physical Realization of the Choke

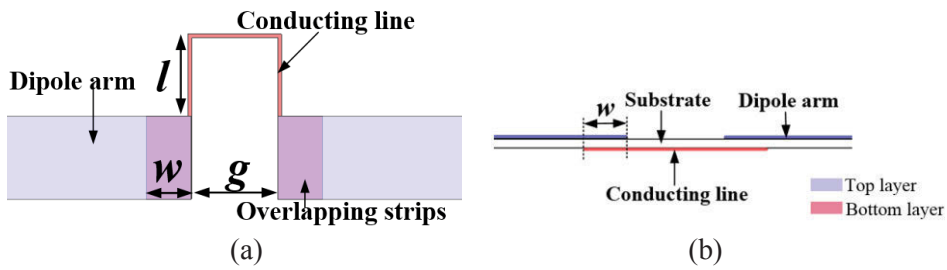

Figure 6.17 (a) Top, and (b) side view of the realized choke.

The choke circuit is realized by a conducting strip structure, as shown in Figure 6.17(a) and (b). The thin conducting strip and the capacitance across the gap in the dipole arm provide L_1 and C_1. C_2 is realized by placing the inductive lines on the bottom layer of the substrate and adding strips that overlap with dipole arms on the top layer. Therefore, the thin inductive line and gap capacitance control the open circuit at high band, and the overlapping strips control the short circuit at low band. In this way, a geometry that approximately represents the circuit in Figure 6.16 is designed. The choke is optimized following two criteria, i.e. to suppress the current at the high band and to create a pass band at the low band, which are discussed in subsection A and B, respectively. The number of the chokes to be inserted in the dipole arms is determined in the last step, which is shown in subsection C. The details of the optimization and analysis are as follows.

A. Optimization of the Choke for HB Suppression

Firstly, the choke is optimized to suppress induced current at high band around 2.0 GHz. To assess the effect of the choke suppressing scattering, it is introduced into a strip representing a section of the dipole arm with a length around $\lambda/2$ at 2.0 GHz, as shown in Figure 6.18(a). ($\lambda/2$ is the resonant length including the effects of strip width and dielectric of the substrate.) Model 1 shows the strip without modification, and Model 2 shows a gap of width *g* introduced at the center of the strip. An inductive line of a length of *2l+g* and a width of *w1* is used to bridge the cut. This inductive line and the gap capacitance are used to realize C_1 and L_1 in the choke equivalent circuit. Guided by the circuit, adjusting *g, l,* and *w1* can effectively tune the open-circuit frequency point, here we fix *w1* = 0.5 mm, and optimize *g* and *l* values.

The models are illuminated by a plane wave with E-field parallel to the length of the strip, and the maximum induced HB currents flowing on the strips are monitored. For

Model 1, there a noticeable amount of HB current induced on the strip, and the induced current has its peak at around 2.0 GHz, as shown in Figure 6.18(b). For Model 2, the maximum induced HB currents with different values of *g* and *l* are monitored. The results are plotted in Figure 6.18(b) and (c). Both figures depict that Model 2 has much less amount of HB current induced on the strips than Model 1, which presents the scattering suppression capability of the choke.

The influences of parameters *g* and *l* are studied. As shown in Figure 6.18(b), for a given *g*, increasing *l* makes the minimum induced current point appear at a lower frequency, showing that the open-circuit point is moved to a lower frequency. This is because increasing *l* increases L_l, making the f_h lower. As shown in Figure 9(c), for a given *l*, increasing *g* reduces C_l and moves the open-circuit point slightly to a higher frequency. To achieve open-circuit conditions at 2.0 GHz, different combinations of *g* and *l* can be chosen. The maximum magnitudes of current flowing on the strip with some suitable combinations are plotted in Figure 6.18(d). It shows that combination with larger *g* provides current suppression across a wider bandwidth. This is because increasing *g/w1* increases *Zc* in (6.7) and widens the bandwidth of the suppression, as discussed in Section 6.3.3.

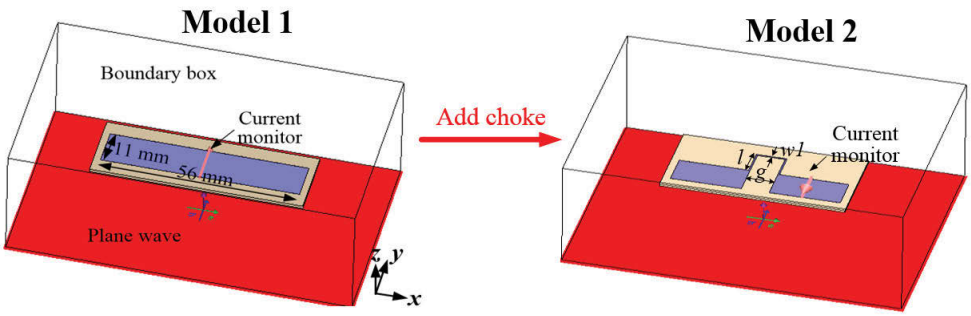

(a)

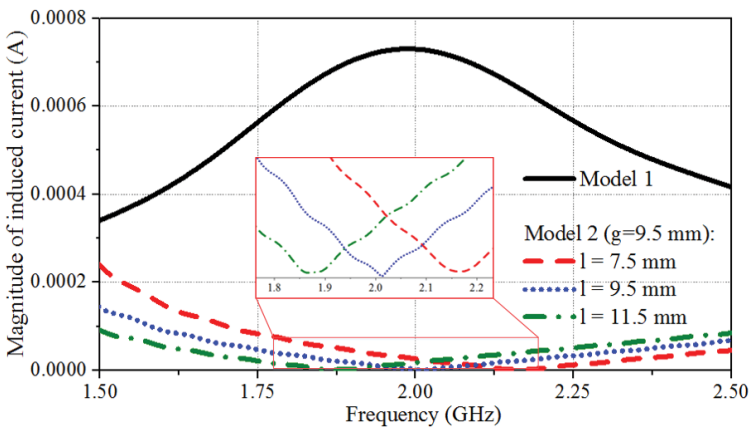

(b)

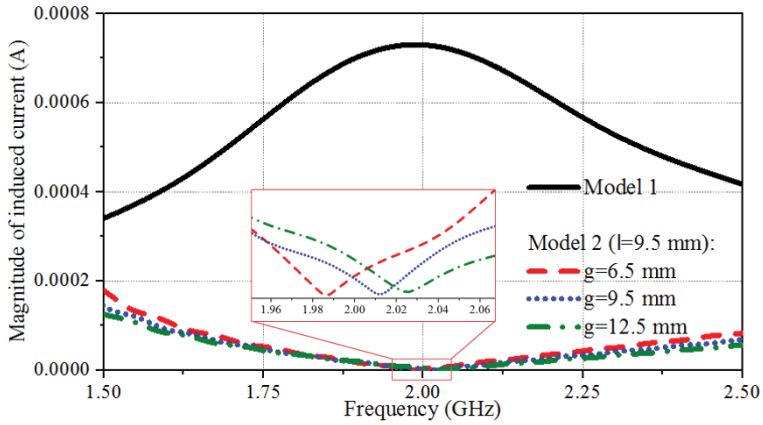

(c)

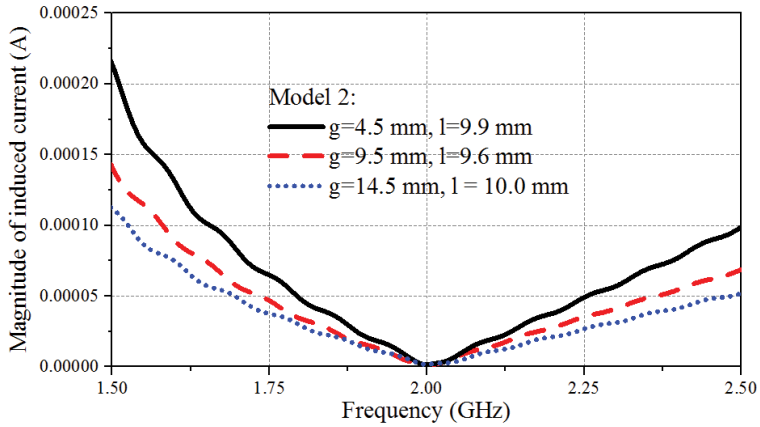

(d)

Figure 6.18 (a) Model 1: a strip with a length of around $\lambda/2$ at 2.0 GHz (middle frequency at high band) and a width of 11 mm; Model 2: the strip in Model 1 cut in the middle and bridged with an inductive line. (b) Comparison of induced HB current on the strip in Model 1, and on the strip in Model 2 with different value of l. (c) Comparison of induced HB current on the strip in Model 1, and on the strip in Model 2 with different value of g. (d) Comparison of induced HB currents on the strip in Model 2 with optimized $\{g, l\}$ values for open circuit point at 2.0 GHz.

B. Optimization of the Choke for LB Pass

After determining parameters $\{g, l\}$ having desirable scattering suppression at high band, the next step is to optimize the choke to minimize its influence at the operating low band around 0.89 GHz. In this step, a strip with a length of around $\lambda/2$ at 0.89 GHz is modeled with a choke at the center, as shown in Figure 6.19(a). The inductive line is now placed on the bottom layer of the substrate and attached to two patches overlapping the cut segments on the top layer. The overlap width w determines C_2 in the choke circuit. Adjusting it tunes the short-circuit frequency point.

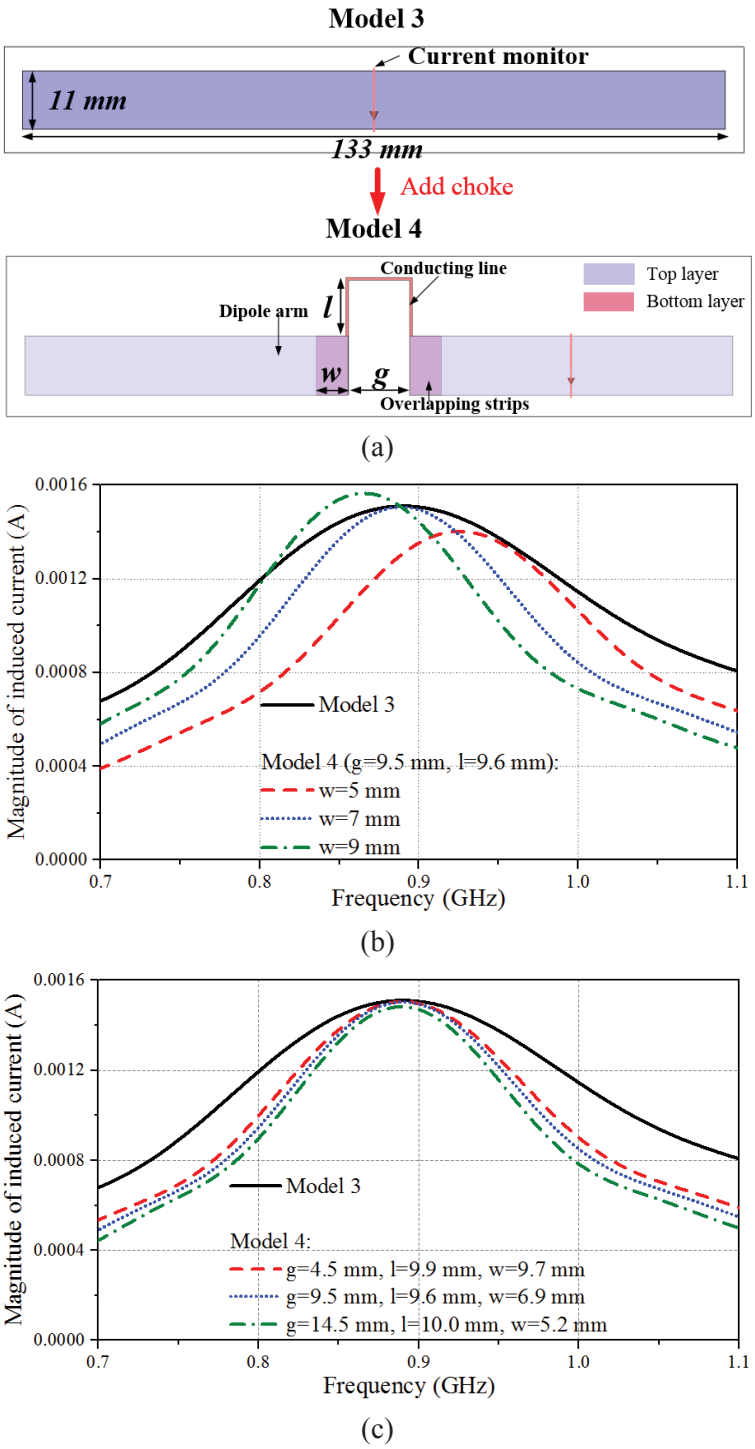

Figure 6.19 (a) Model 3: a strip with a length of around $\lambda/2$ at 0.89 GHz (middle frequency at low band) and a width of 11 mm; Model 4: the strip in Model 3 cut in the middle and bridged with a choke. (b) Comparison of induced LB current on the strip in Model 3, and on the strip in Model 4 with different values of *w*. (c) Induced LB current on the strip in Model 4 with optimized {*g, l, w*} values for open circuit point at 2.0 GHz and short circuit point at 0.89 GHz.

The models are illuminated by a plane wave at the low band, and the maximum induced

LB current is monitored. The results are shown in Figure 6.19(b). For Model 3, the induced LB current has a peak value at 0.89 GHz. As for Model 4, a similar amount of LB current is induced on the strip, but the frequency of the current maximum depends on the value of w. The frequency of the current maximum corresponds to the short-circuit point. Increasing w increases C_2 in the circuit, thus moves the short-circuit point to a lower frequency. Therefore, for a given $\{g, l\}$, larger w moves the current maximum to a lower frequency in the simulation, which is shown in Figure 19(b).

For different combinations of $\{g, l\}$ that can achieve open-circuit at 2.0 GHz, different values of w are required to achieve short-circuit point at 0.89 GHz. The induced LB current on the strip of Model 4 with the some optimized combinations of $\{g, l, w\}$ is shown in Figure 19(c). The combination with larger g has a narrower bandwidth at the low band as they require a smaller value of C_2. Therefore, the combination of $\{g, l, w\}$ needs to be selected carefully to achieve the desired pass band at the low band, and stop band at the high band.

C. Determination of the Number of Chokes Required in the LB Arms

The LB dipole arms are cut into several short segments with gaps between them, and the chokes described above are introduced into the gaps, as illustrated in Figure 6.20. It is necessary to determine the number of chokes required in a dipole arm. The choke inevitably introduces some loss to the LB antenna, i.e. the magnitude of the current on a choke is slightly smaller than that on an unmodified strip as shown in Figure 6.19(c). Therefore, unnecessary chokes should be avoided. On the other hand, using too few chokes reduces the level of current suppression at high band.

To determine the length of each segment (l_s) that assure suitably low HB currents on the segment, segments with different lengths are modelled with illumination by a plane wave with E-field parallel to the length of the segment as shown in Figure 6.21(a). The maximum induced HB current levels are monitored with results shown in Figure 6.22(b). As expected, the shorter the segment is, the lower is the induced current. Segment lengths around 20 mm offer a great reduction of the HB induced current. For the LB arms, two cuts with a gap width around 11 mm in each arm achieve that. Simulations confirm that the HB radiation pattern is almost unchanged with the cut LB arms.

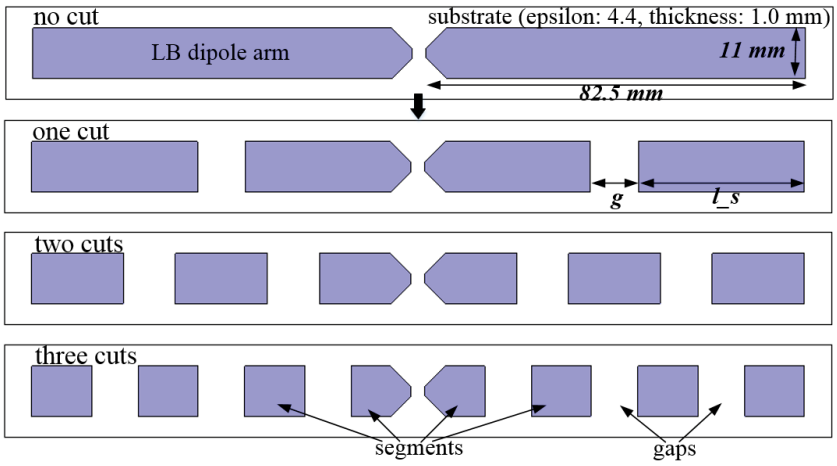

(a)

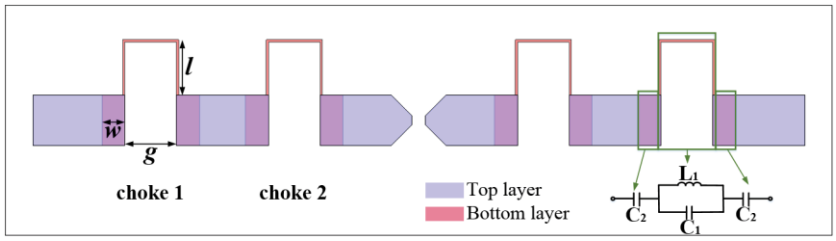

(b)

Figure 6.20 (a) The LB dipole arms with different number of cuts. (b) Top view of the LB dipole arm with chokes inserted in.

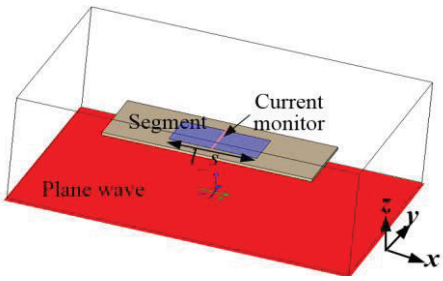

(a)

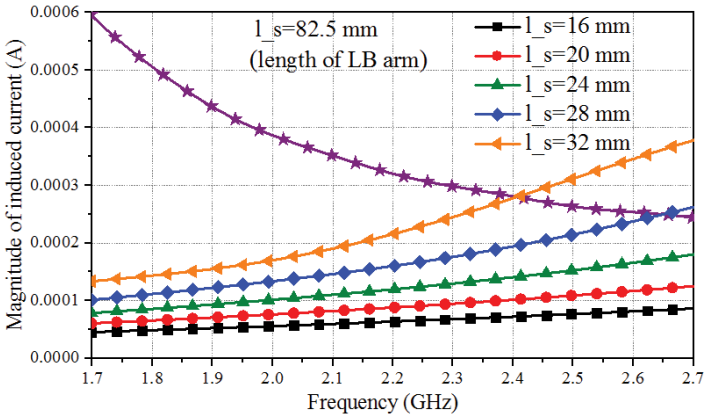

(b)

Figure 6.21 (a) Model to determine effect of segment length *l_s* in free space illuminated by HB plane wave. (b) Maximum induced HB current on the segment with different *l_s*.

6.4.1.3 Scattering Suppression of the Choked LB Radiators

The optimized choked LB radiators are shown in Figure 6.22. To achieve HB choking performance across a wide band, two chokes tuned to slightly different frequencies were chosen and introduced into the two gaps in each LB arm. The choked LB arms are still arranged in the cross-dipole configuration to realize the required dual-polarization radiation. The optimized parameters are listed in Table 6.4. The substrate for the radiator has a dielectric constant of 4.4, a loss tangent of 0.0025, and a thickness of 1.0 mm. As the size of the choke in this design is relatively large, the orientation of the chokes is arranged in an anti-clockwise direction to minimize coupling between inductors on different arms. If chokes were realized with a smaller dimension, their orientation would be of no consequence.

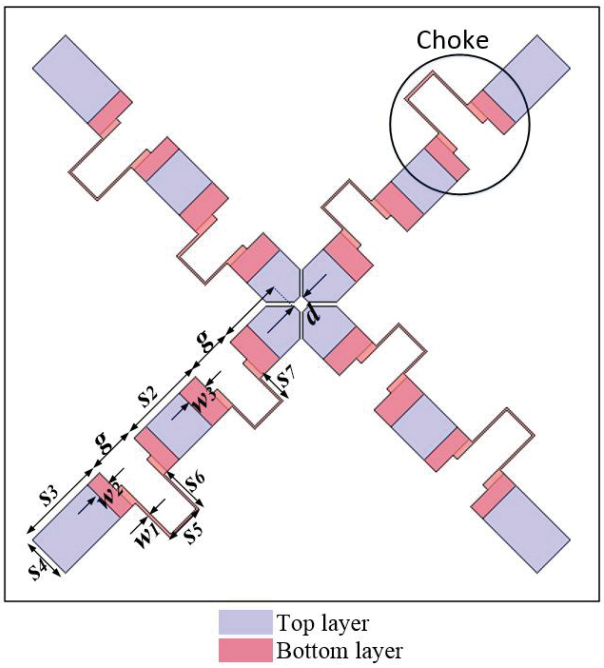

Figure 6.22 Configuration of optimized choked LB radiator.

Table 6.4 Optimized Parameters of the Choked Antenna

Parameters	Values (mm)	Parameters	Values (mm)
s1	16.75	s2	20.5
s3	22.25	s4	11
s5	9.5	s6	11
s7	7	g	11.5
d	3	w1	0.5
w2	4	w3	5.5

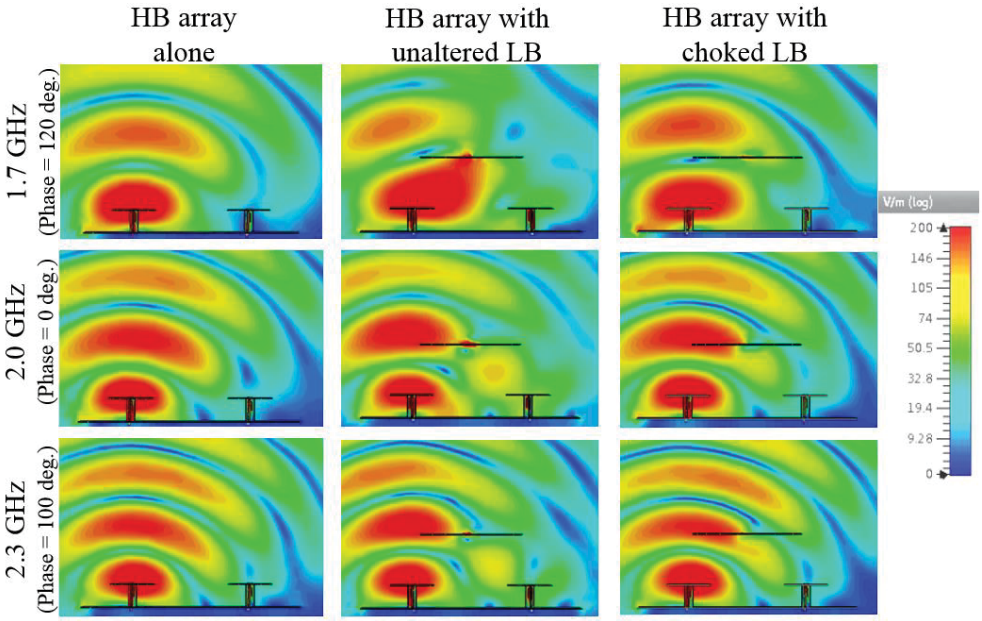

Figure 6.23 The E-field cuts in the *zx*-plane under the circumstances of i) only HB array, ii) HB array with unaltered LB radiators, and iii) HB array with choked LB radiators.

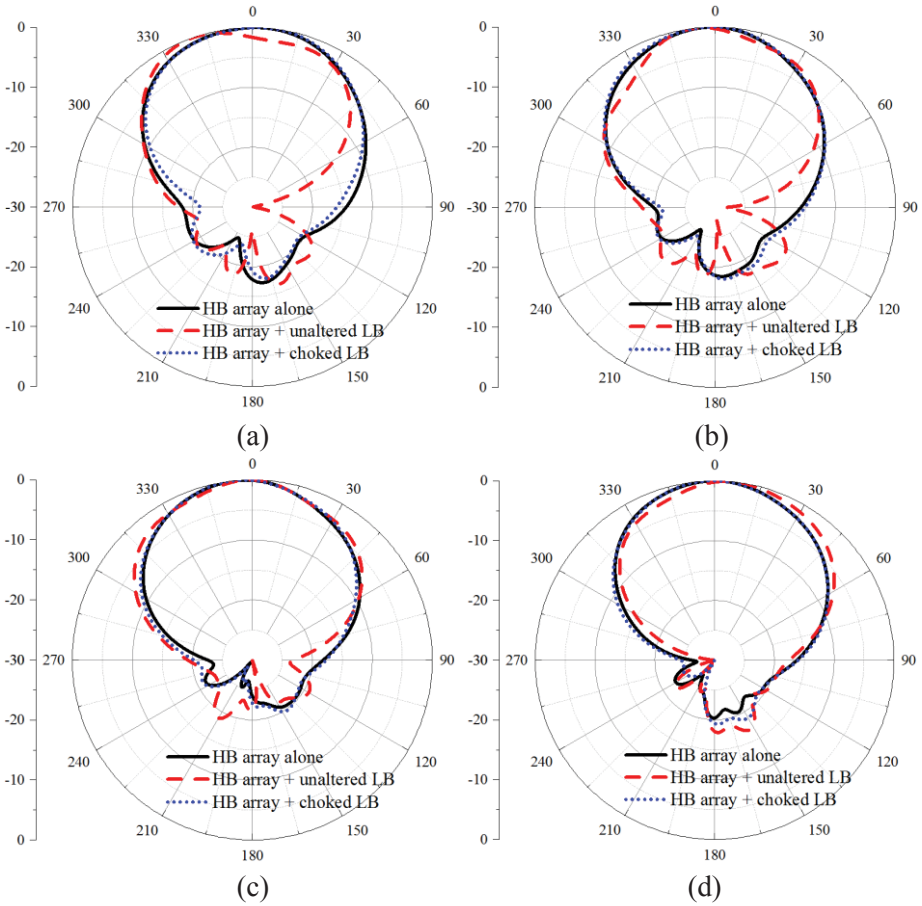

Figure 6.24 Comparison of HB radiation patterns under the circumstances of i) only HB array, ii) HB array with unalthered LB radiators, and iii) HB array with choked LB radiators at (a) 1.7 GHz, (b) 1.9 GHz, (c) 2.1 GHz, and (d) 2.3 GHz.

The optimized choked LB radiators are introduced into the dual-band antenna array as shown in Figure 6.15 to examine their effectiveness in suppressing the HB scattering. Figure 6.23 shows plots of E-field in a horizontal section through the array across the high band in the cases (i) HB array only; (ii) HB array with unaltered LB radiators; (iii) HB array with choked LB radiators. It is clear that the unaltered LB radiators block HB electric field to a large extent, especially at low frequencies. The proposed choked LB radiators have much less effect on the field than the unaltered LB radiators. The resultant horizontal HB patterns before and after adding the choked LB radiators are shown in Figure 6.24. Patterns for HB array alone are added for comparison. It is observed that the distorted HB radiation patterns in the presence of unaltered LB radiators are greatly restored by inserting chokes into the LB radiators, demonstrating the effectiveness of the chokes in reducing HB pattern distortion across the band.

6.4.1.4 Performance of the Choked LB Element

As the realized chokes are not ideal and can only approximate a short circuit over a limited range of LB frequencies, they change the impedance properties of the LB element, making the impedance matching task more difficult. Nevertheless, following the guidelines of designing the impedance matching network discussed in Section 3.2.3, a satisfactory matching result is obtained using baluns and impedance matching elements. Two specially designed baluns are orthogonally arranged to feed the two pairs of choked dipoles. The configuration of the choked LB element, together with the two baluns are shown in Figure 6.25. The detailed parameters of the baluns are listed in the Table 6.5. Figure 6.26 shows the matching results for the choked element. The antenna is matched to reflection coefficients < -14 dB from 0.82 GHz to 0.96 GHz. Compared with the unaltered LB element, the matching of the choked LB element is slightly degraded, but it is still satisfactory. The simulated radiation patterns of LB element with choked arms and unaltered arms at 0.82 GHz, 0.88 GHz, 0.92 GHz, and 0.96 GHz are shown in Figure 6.27. The patterns in the two cases are almost identical, showing that choking LB arms does not influence the radiation performance.

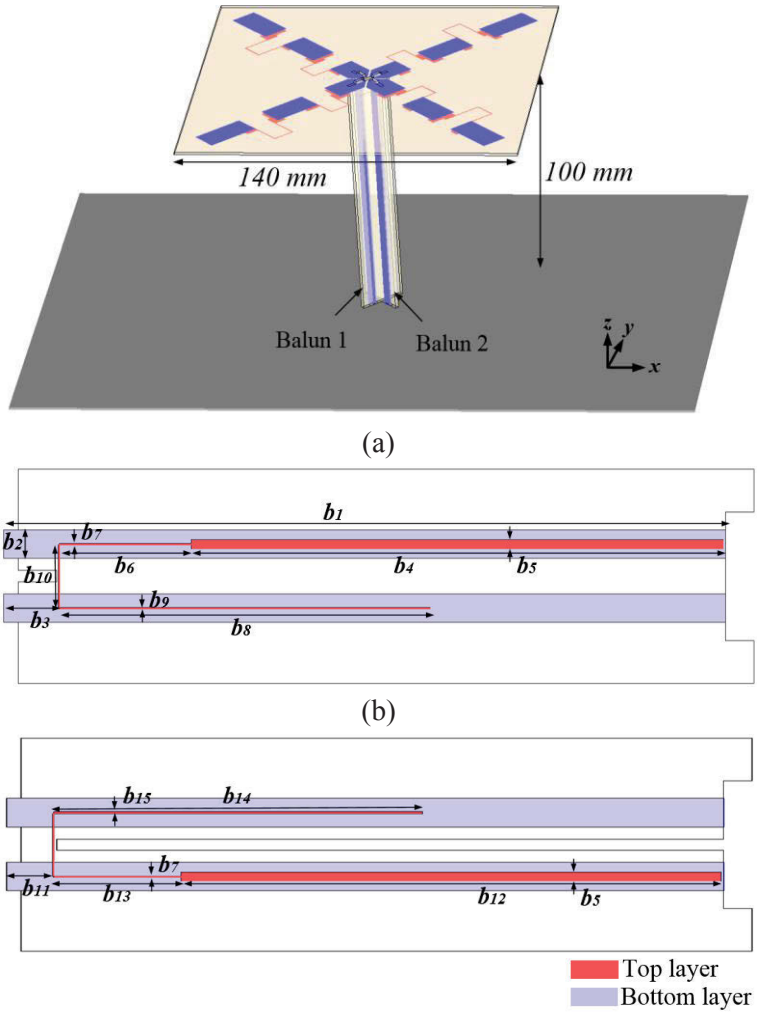

Figure 6.25 (a) Perspective view of the choked LB antenna. Configurations of (b) balun 1, and (c) balun 2. (The baluns are printed on both sides of a substrate with a dielectric constant of 4.4, a loss tangent of 0.0025, and a thickness of 1.5 mm.)

Table 6.5 Optimized Parameters of Baluns for the Choked Antenna

Parameters	Values (mm)	Parameters	Values (mm)
b1	101	*b2*	4
b3	7.6	*b4*	72.98
b5	1.4	*b6*	20
b7	0.2	*b8*	50
b9	0.2	*b10*	9
b11	6.475	*b12*	74.08
b13	20	*b14*	50
b15	0.25		

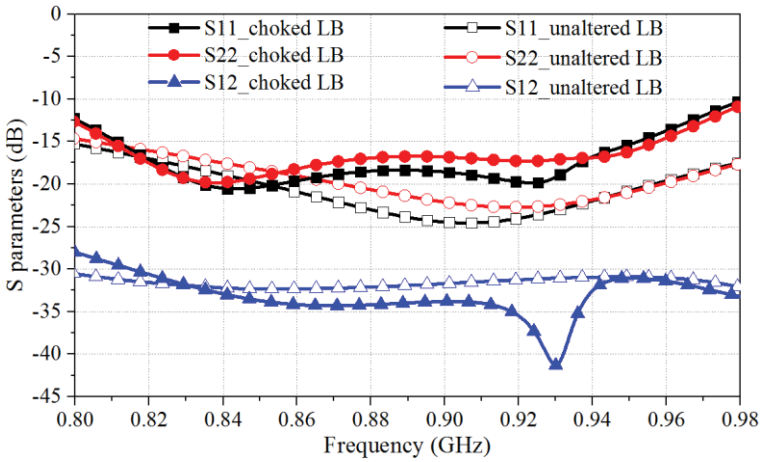

Figure 6.26 S-parameters of the choked LB element and the unaltered LB element.

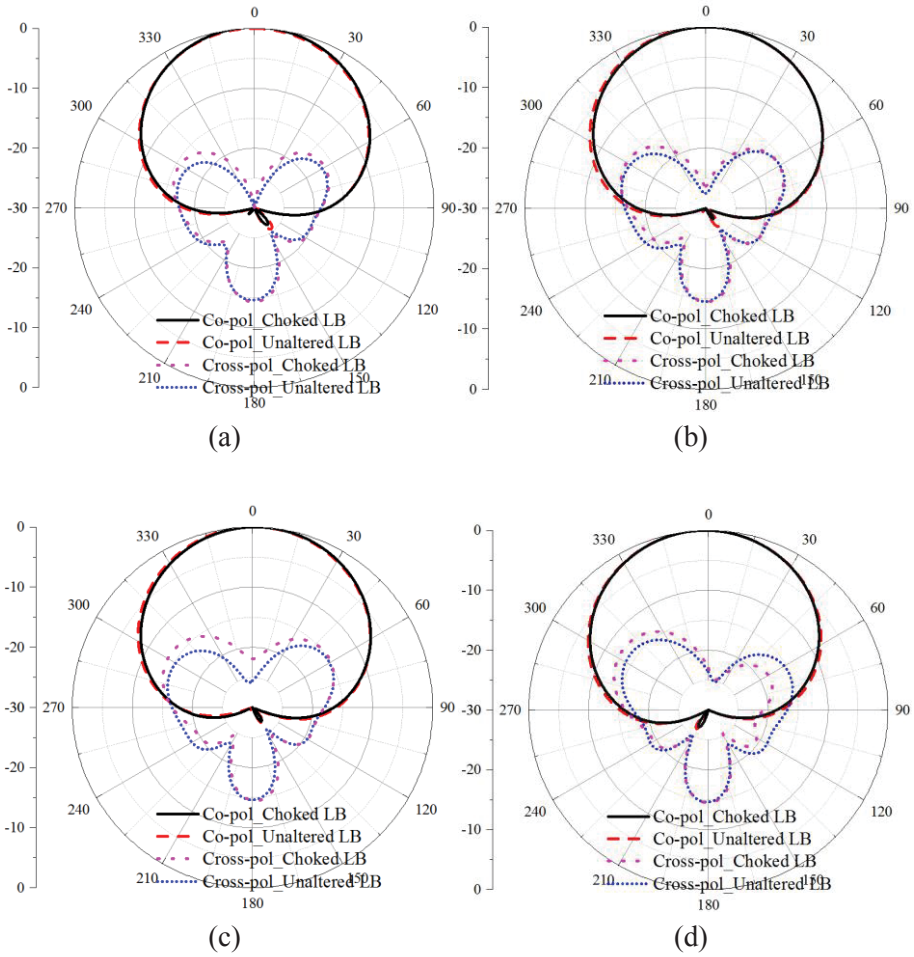

Figure 6.27 Radiation patterns of the choked LB element and the unaltered LB element at (a) 0.82 GHz, (b) 0.88 GHz, (c) 0.92 GHz, and (d) 0.96 GHz.

6.4.2 Experimental Results

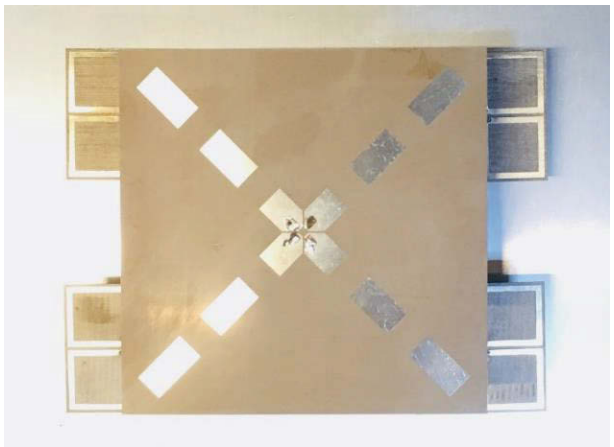

(a)

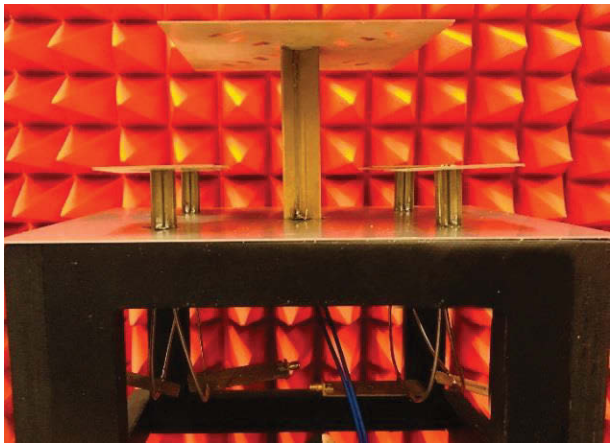

(b)

Figure 6.28 (a) Top, and (b) side views of the dual-band dual-polarized interleaved array.

The dual-band antenna array section with modified choked LB element is shown in 6.15. The prototype of the antenna array section was fabricated and tested, as shown in Figure 6.28. Figure 6.29 shows the simulated and measured reflection coefficients of the HB array. The results for the two HB arrays in the two columns are essentially the same due to the symmetric structure, so only the results for one column of the HB array are given. The HB return loss as expected is almost the same as obtained without the LB elements. Measured results agree well with the simulated ones, demonstrating good matching across a band of 28.6% from 1.71 GHz to 2.28 GHz. The radiation patterns for the ±45° polarization in one column at 1.7 GHz, 2.0 GHz, and 2.3 GHz are shown in Figure 6.30. The simulated and measured patterns agree well. The simulated and measured XPD at the boresight is more than 19 dB and more than 16 dB, respectively. Figure 6.31 shows the simulated and measured horizontal HPBW and realized gain of the

HB array. For each polarization, the measured HPBW varies within 65°±5°, which shows that the array has very stable radiation performance as required in base station applications. The simulated and measured realized gain both vary from 10 dBi to 12 dBi. All the four HB ports have efficiencies higher than 90% across the operating band. The performance of HB array with choked LB is almost the same as that of HB array only.

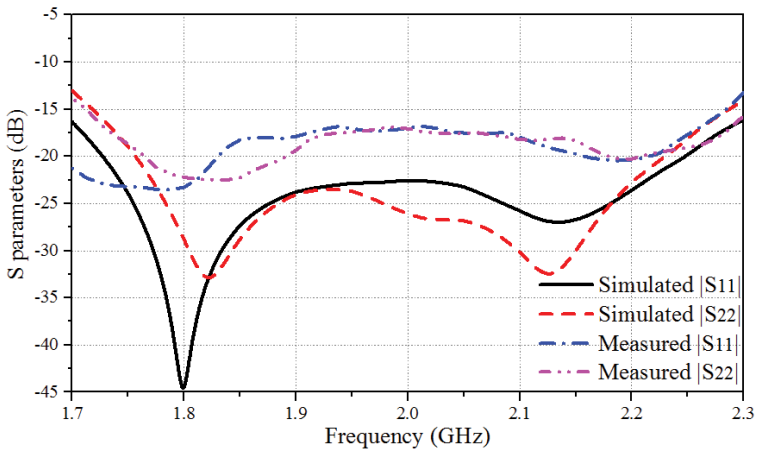

Figure 6.29 Simulated and measured reflection coefficients of the HB array.

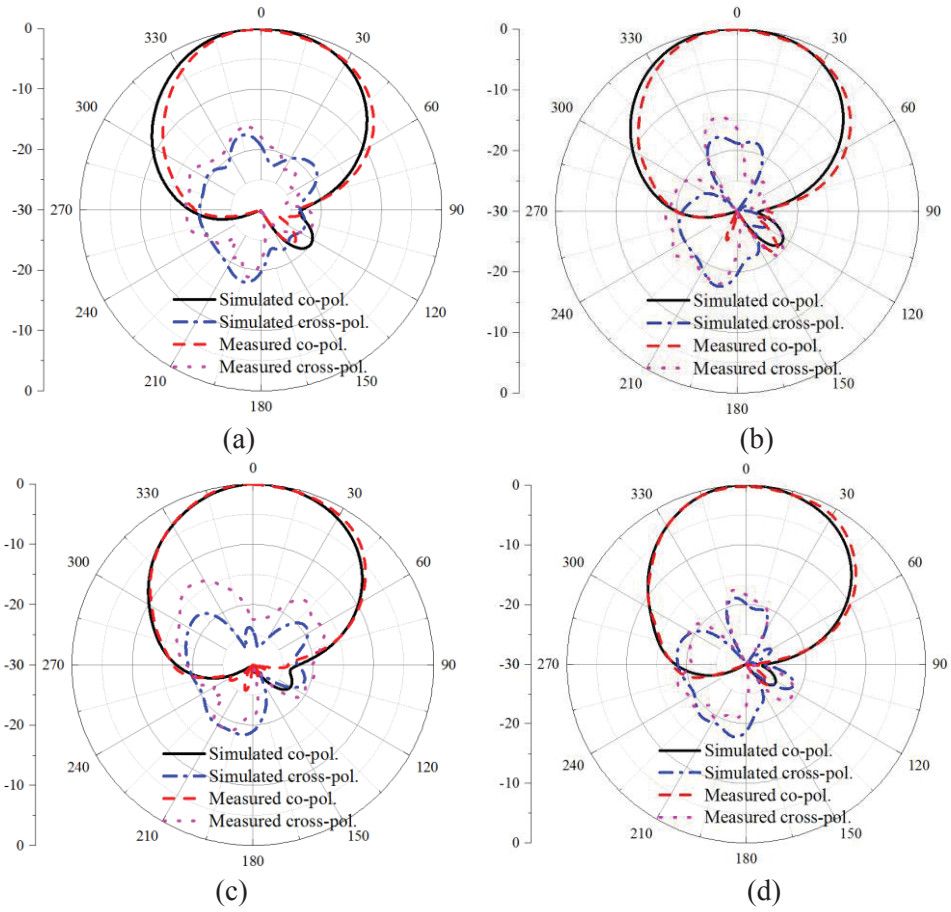

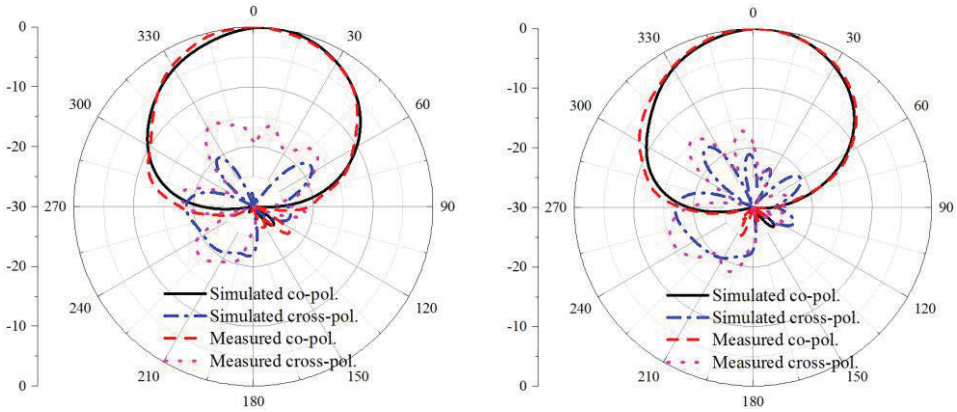

(e) (f)

Figure 6.30 Simulated and measured radiation patterns of the HB array. (a) Port 1 at 1.7 GHz. (a) Port 2 at 1.7 GHz. (c) Port 1 at 2.0 GHz. (d) Port 2 at 2.0 GHz. (e) Port 1 at 2.3GHz. (f) Port 2 at 2.3 GHz.

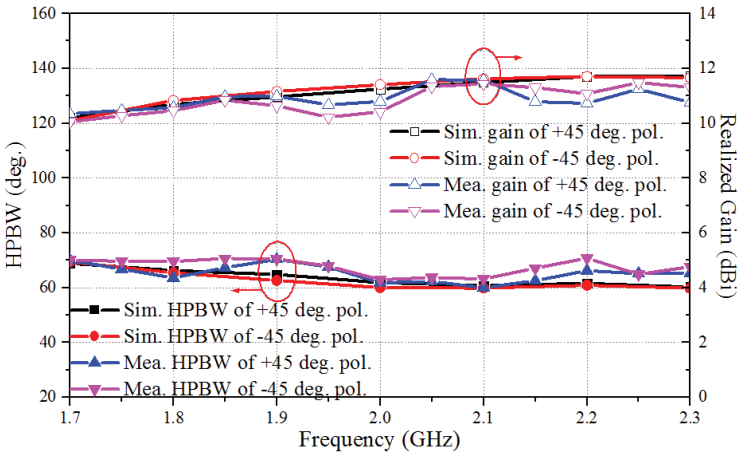

Figure 6.31 Simulated and measured horizontal HPBW and realized gain of the HB array.

The simulated and measured choked LB antenna results are shown in Figures 6.32 to 6.34. As shown in Figure 6.32, the measured bandwidth is 19.7% from 0.82 GHz to 1.0 GHz for reflection coefficients less than -10 dB. The simulated and measured horizontal radiation patterns of the choked LB antenna at 0.82 GHz, 0.88 GHz and 0.96 GHz are shown in Figure 6.33. The simulated and measured radiation patterns agree well. The measured XPD is more than 20 dB at boresight. The horizontal HPBW and realized gain are shown in Figure 6.34. The simulated and measured HPBW varies within 71.5° ± 3.5° and 69.5° ± 4°, respectively. The measured gain varies from 6.0 dBi to 7.0 dBi, which is slightly less than the simulated one. It is mainly caused by the loss of cables. The efficiencies of the LB antenna are higher than 89% across the band. Note that the presented gain results for HB and LB antennas are only for one array section. Higher gain

can be obtained by repeating the array sections in the vertical direction (*y*-direction).

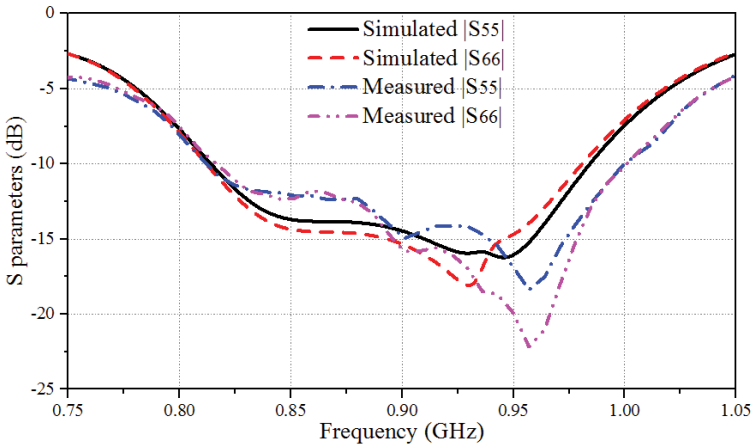

Figure 6.32 Simulated and measured S-parameters of the choked LB antenna.

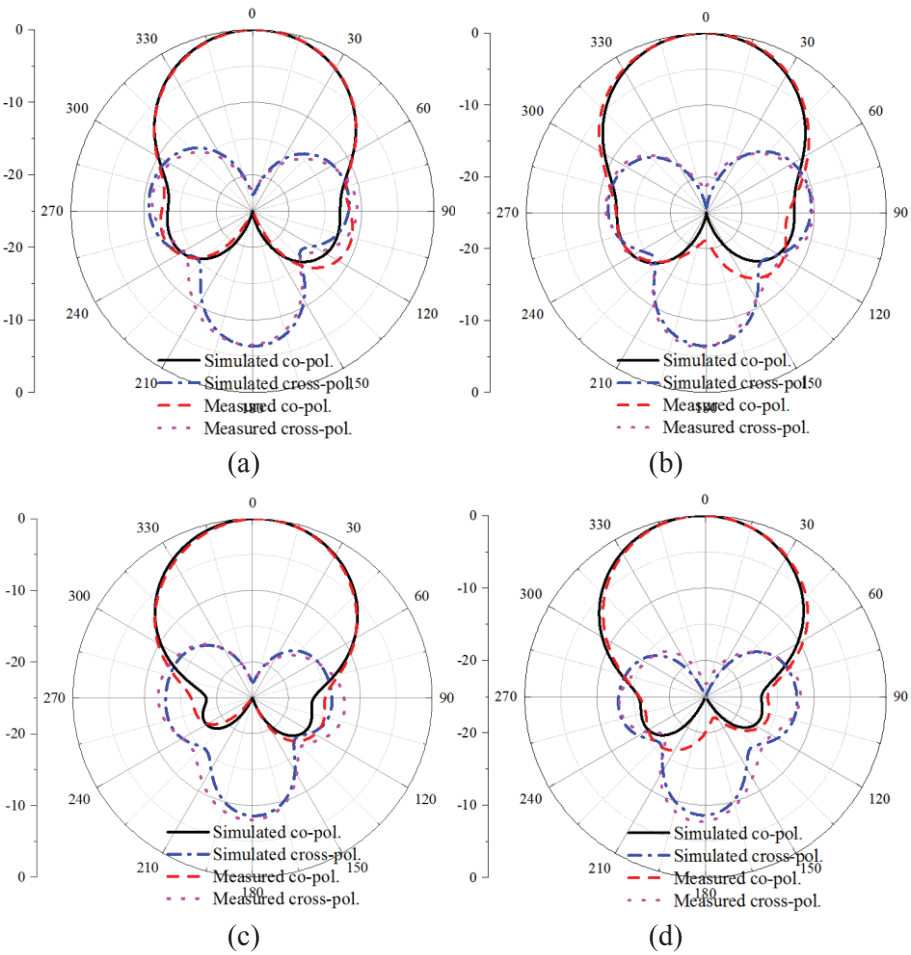

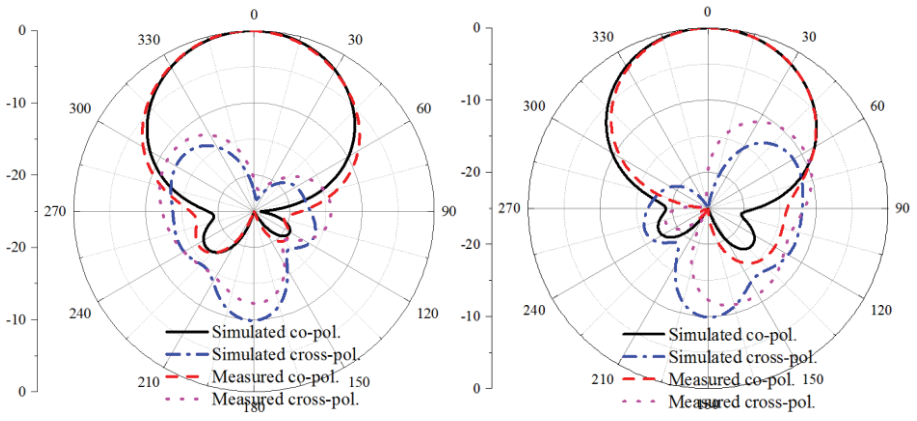

(e) (f)

Figure 6.33 Simulated and measured radiation pattern of the choked LB antenna. (a) Port 1 at 0.82 GHz. (b) Port 2 at 0.82 GHz. (c) Port 1 at 0.88 GHz. (d) Port 2 at 0.88 GHz. (e) Port 1 at 0.96 GHz. (f) Port 2 at 0.96 GHz.

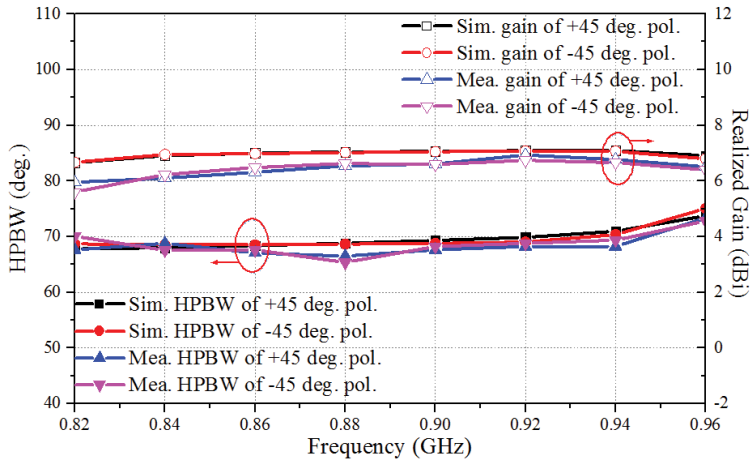

Figure 6.34 Simulated and measured HPBW and realized gain of the choked LB antenna.

6.5 Application II: Interleaved 4G and 5G Base Station Antenna Array

In application II, we consider a dual-band 4G and 5G base station antenna (BSA) array. The array configuration is also the interleaved scheme. The array is designed to operate at 4G LTE band from 1710 MHz to 2170 MHz and 5G sub-6 GHz band from 3300 MHz to 3700. The spiral choking technique is selected to construct the LB antenna. Simulated and measured results demonstrate that the HB scattering is suppressed and stable desired radiation patterns are achieved in both bands.

6.5.1 Design of Spiral LB Element

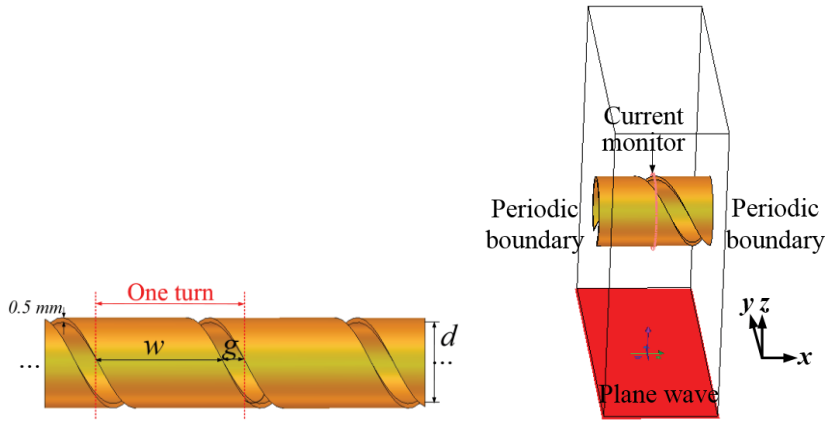

(a)

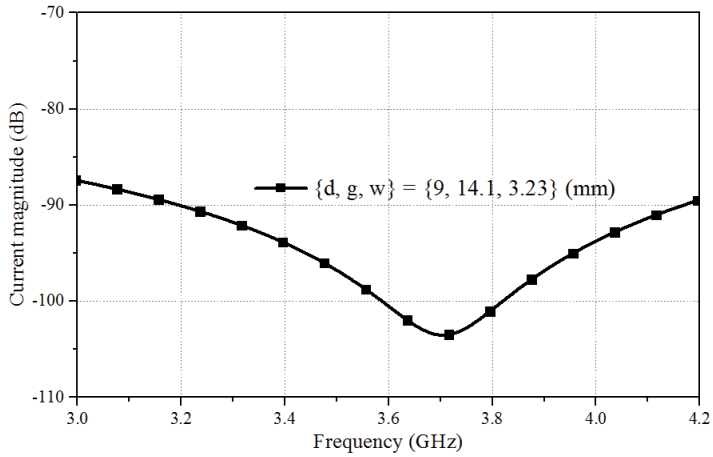

(b)

Figure 6.35 (a) Configuration of spiral structure. (b) Current suppression capability at around 3.7 GHz.

Following the study in Section 6.3.1 regarding the spiral choking technique, the parameters for the spiral are optimized to achieve the desired open-circuit point at around 3.7 GHz. The optimized parameters are *d=9 mm, w=14.1 mm,* and *g=3.23 mm*. The current suppression performance at the high band when illuminated with a plane wave is plotted in Figure 6.35.

The optimized spirals are used as LB arms in the dual-band antenna array, as shown in Figure 6.36. The arms are still arranged in the cross-dipole configuration to realize the dual-polarization performance. The E-field distribution and the radiation patterns when one of the HB sub-arrays is excited are investigated to examine the spiral's capability in suppressing the HB scattering. In this stage, only LB radiators are considered to eliminate

the influence of the feed networks.

Figure 6.37 shows plots of E-field distribution in a horizontal section through the array in the cases (i) HB array only; (ii) HB array with unaltered LB radiators; (iii) HB array with spiral LB radiators across the high band. It is clear that the unaltered LB radiators in strip form block HB electric field. The spiral LB radiators have much less effect on the field than the unaltered LB radiators across the high band. The resulting horizontal patterns in these three cases are shown in Figure 6.38 from 3.3 GHz to 3.7 GHz. The deterioration of the radiation pattern in the presence of the unaltered LB radiators has been largely eliminated using spiral LB arms, demonstrating the effectiveness of the spiral structure in reducing HB pattern distortion across the band.

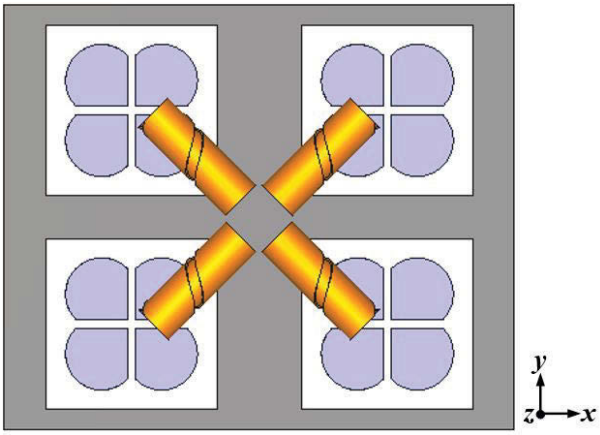

Figure 6.36 Arrangement of the interleaved dual-band array with spiral LB radiators.

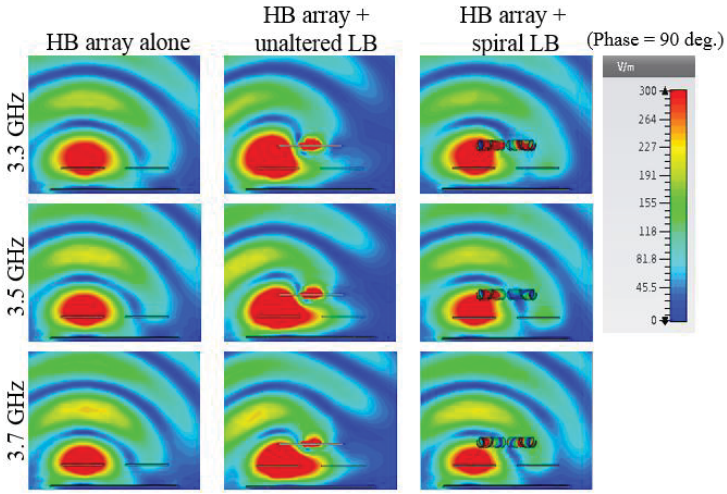

Figure 6.37 The E-field cuts in the *zx*-plane under the circumstances of i) only HB array, ii) HB array with unaltered LB radiators (dipole arm in strip form), and iii) HB array with spiral LB radiators.

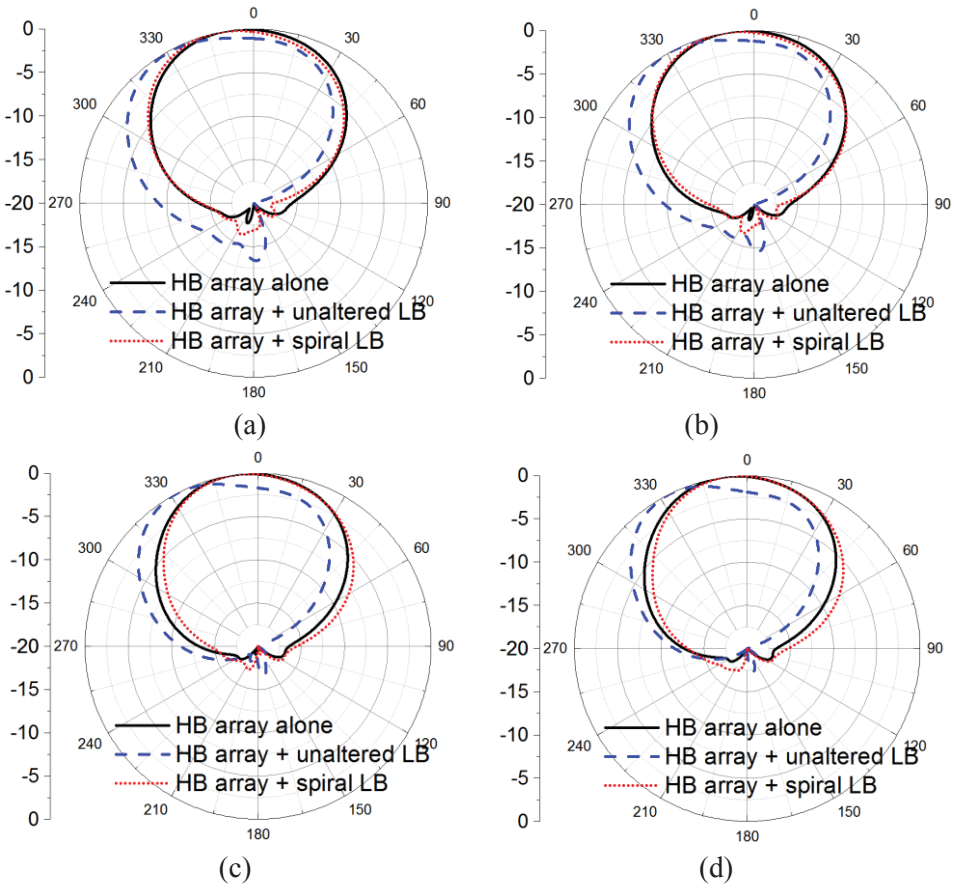

Figure 6.38 Comparison of HB radiation pattern in the horizontal plane (*zx*-plane) under the circumstances of i) only HB array, ii) HB array with unaltered LB radiators, and iii) HB array with spiral LB radiators at (a) 3.3 GHz, (b) 3.4 GHz, (c) 3.6 GHz, (d) 3.7 GHz.

After demonstrating the effectiveness of the spiral structure in suppressing the cross-band scattering, the next step is to match the spiral radiators in the low band. The baluns for the spiral-shaped LB radiators is designed following the guidelines of designing an impedance matching network given in Section 3.2.3. An excellent matching result is obtained using baluns and impedance matching elements. Two feed networks are orthogonally arranged to feed the two pairs of spiral arms. The configuration of the spiral LB antenna is shown in Figure 6.39. The detailed parameters of the baluns are included in Figure 6.39(b). Figure 6.40 shows matching results for this choked element. The antenna is matched to reflection coefficients less than -15 dB from 1.66 GHz to 2.22 GHz. The simulated radiation pattern of LB element with spiral arms and unaltered strip arms at 1.7 GHz, 1.9 GHz, and 2.2 GHz are shown in Figure 6.41. The radiation patterns are very stable across the matched band, and the cross-polarization level is less than -20 dB at the boresight. All the simulated results demonstrate that the spiral antenna can be well-

performed across the low band.

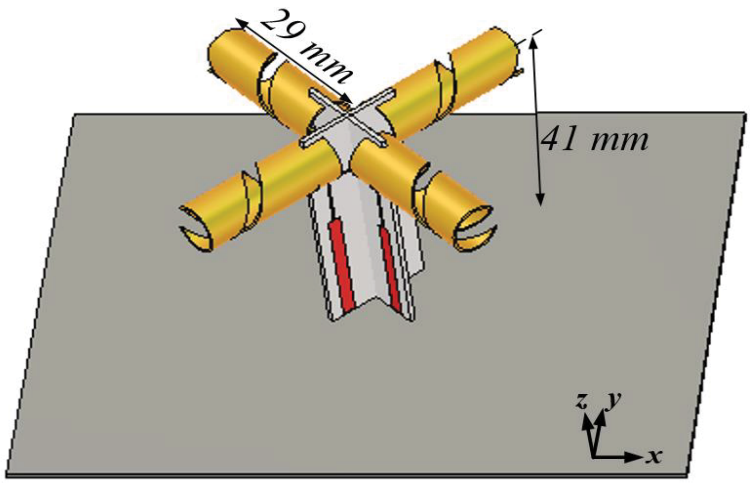

(a)

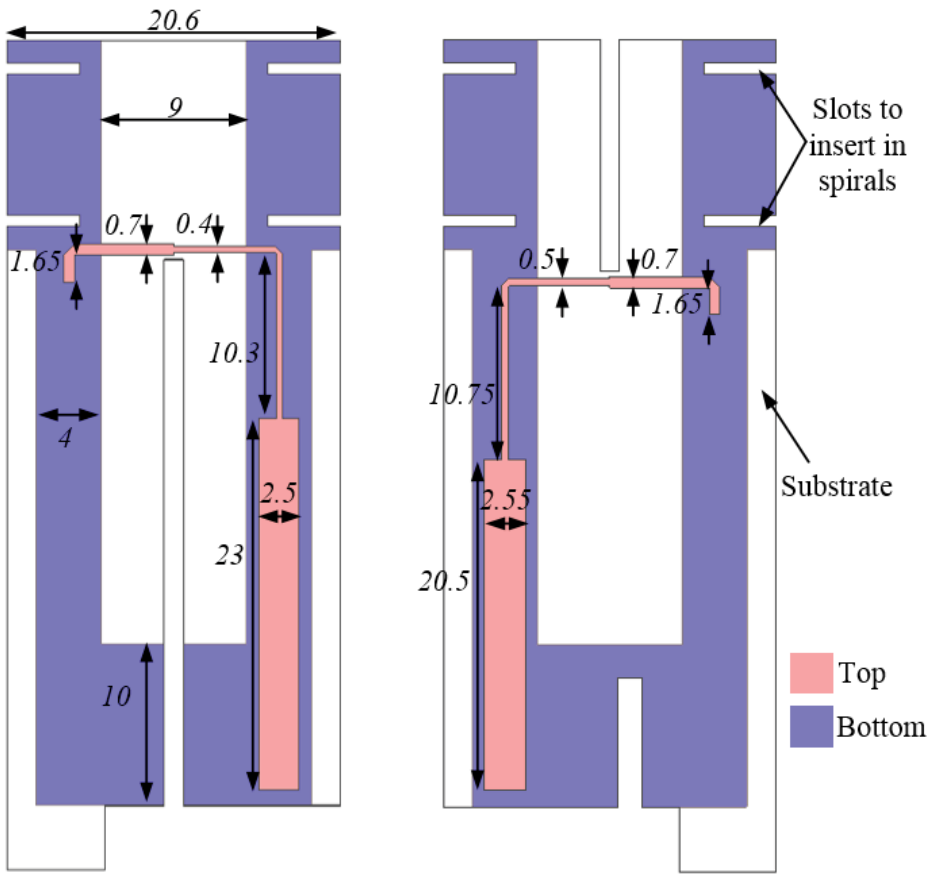

(b)

Figure 6.39 (a) Perspective view of the spiral LB antenna. (b) Configuration of two baluns for spiral LB antenna.

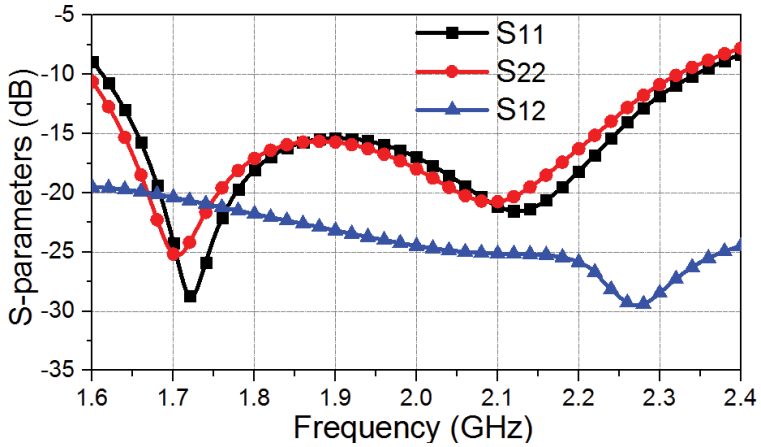

Figure 6.40 S-parameters of the spiral LB antenna.

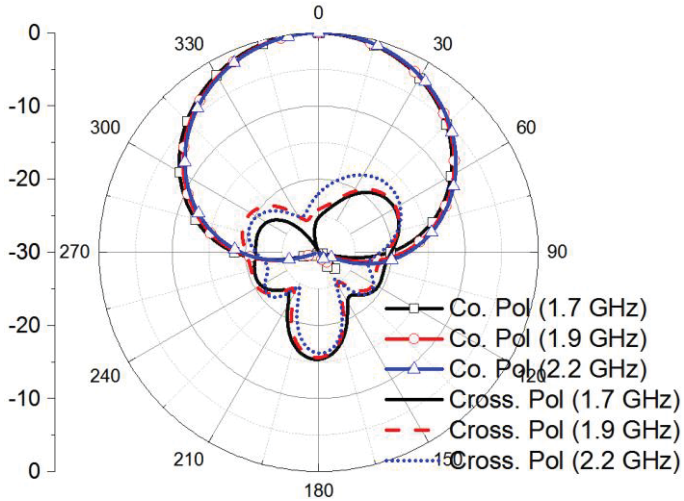

Figure 6.41 Horizontal radiation patterns of spiral LB antenna at 1.7 GHz, 1.9 GHz, and 2.2 GHz.

6.5.2 Experimental Results

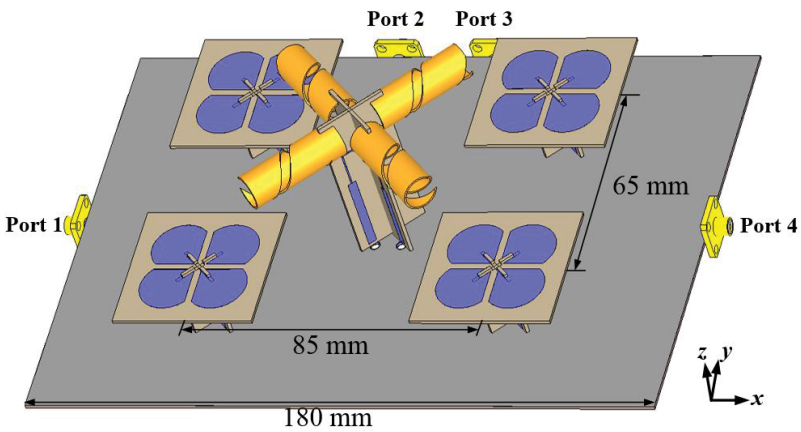

(a)

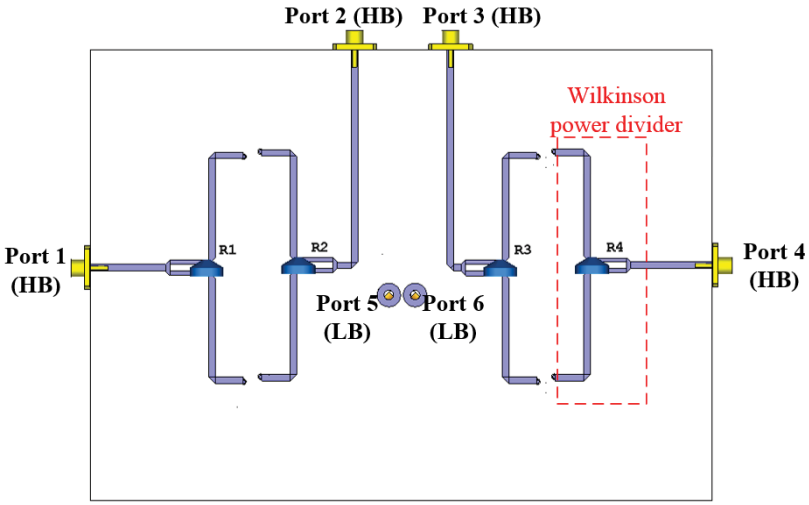

(b)

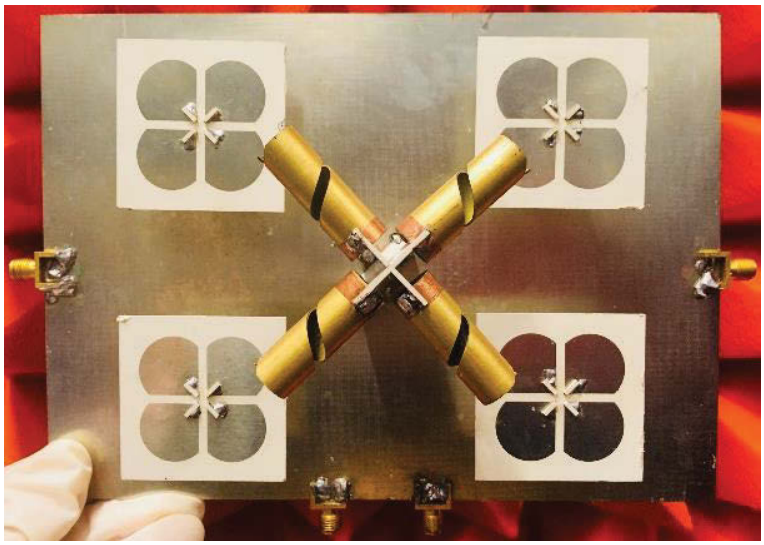

(c)

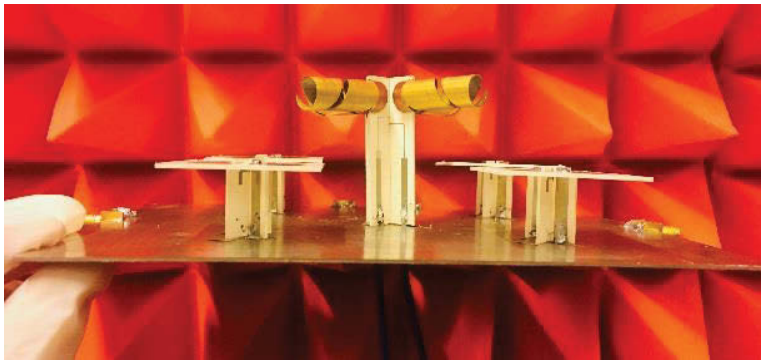

(d)

Figure 6.42 (a) Perspective view of the dual-band antenna array model. (b) View of the feed network for the dual-band antenna array. (c) Front view, and (b) side view of the fabricated antenna array prototype.

The configuration of the finalized dual-band array is shown in Figures 6.42 (a) and (b).

The distance between the two HB sub-arrays is set as 1λ to guarantee enough isolation. The HB sub-arrays are fed by power dividers printed on the back of the reflector, as shown in Figure 6.42(b). Ports 1 and 3 are in charge of +45° polarization, and Ports 2 and 4 are in charge of -45° polarization for the two HB sub-arrays. The LB element is fed directly by coaxial cables. Ports 5 and 6 excite the +45°- and -45°-polarized radiation, separately.

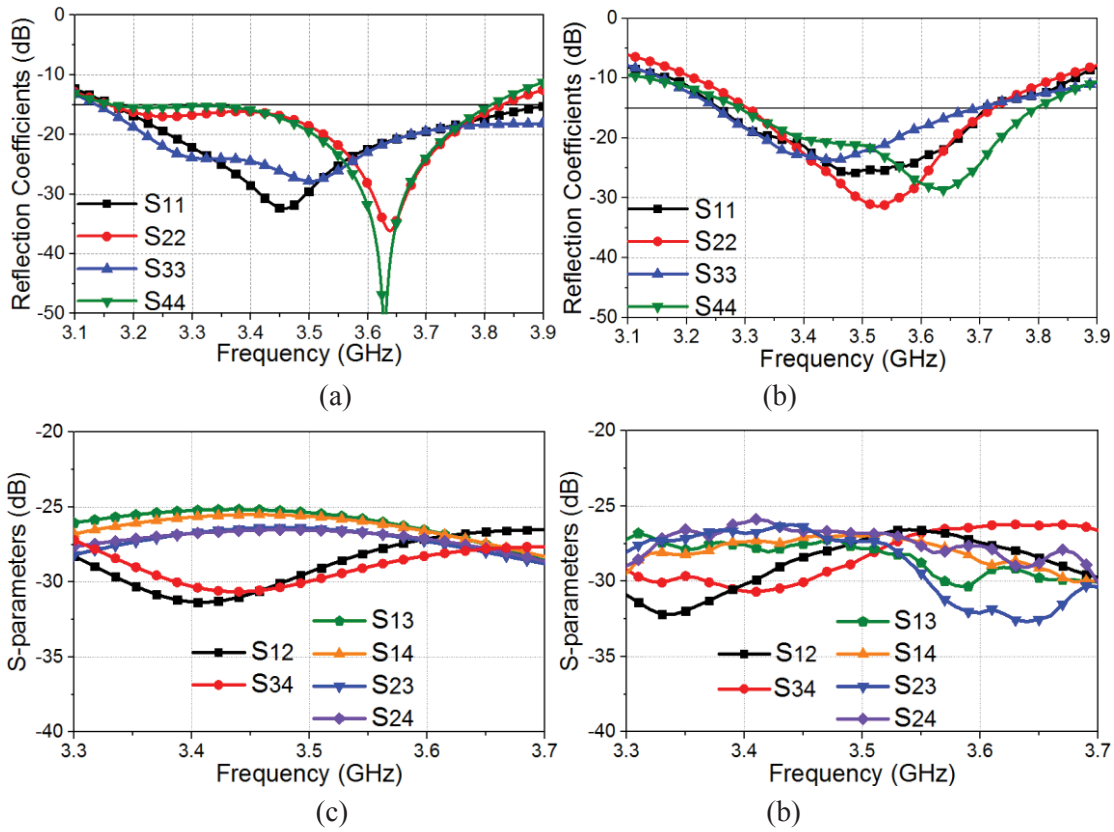

Figure 6.43 (a) Simulated and (b) measured reflection coefficients for HB ports. (c) Simulated and (d) measured isolations between HB ports.

The dual-band array is fabricated and tested, as shown in Figure 6.42(c) and (d). The simulated and measured S-parameters are shown in Figure 6.43. Figure 6.43(a) and (b) show the reflection coefficients of the four HB ports. The measured bandwidth is 11.4% from 3.3 GHz to 3.7 GHz for reflection coefficients less than -15 dB. Figure 6.43(c) and (d) show the isolations between the HB ports. It can be observed that both the simulated and measured isolations between ports in the same sub-array are more than 26 dB, and the isolations between ports in different sub-arrays are more than 25 dB. The simulated and measured radiation patterns are plotted in Figure 6.44. Both the +45°- and -45°-polarized radiation patterns for sub-array I are presented. The results for sub-array II are

almost the same as those for sub-array I due to the symmetric geometry of the array configuration, so they are not shown here. The measured patterns agree well with the simulated patterns, and both are very stable across the operating band. The simulated and measured cross-polarization level are less than -20 dB and less than -15 dB, respectively. The simulated and measured results for horizontal HPBW and gain are shown in Figure 6.45. The radiation patterns are stable with HPBW of 66.5°±3.5°. The measured gain is around 11 dBi, which is 0.5 dBi less than the simulated gain. It can be caused by the SMA terminator and cables for measurement.

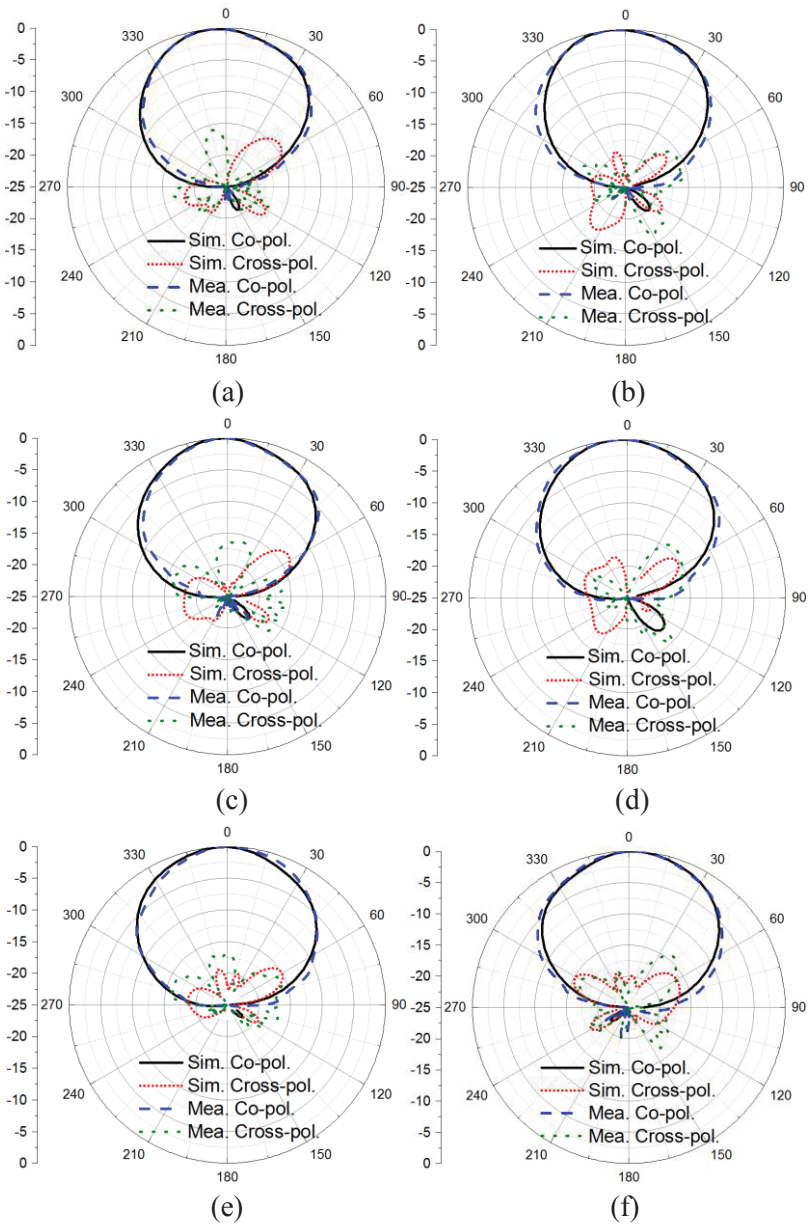

Figure 6.44 Normalized simulated and measured radiation patterns in the horizontal plane for the HB antennas. (a) Port 1 at 3.3 GHz, (b) port 2 at 3.3 GHz, (c) port 1 at 3.5 GHz, (d) port 2 at 3.5 GHz, (e) port 1 at 3.7 GHz, and (f) port 2 at 3.7 GHz.

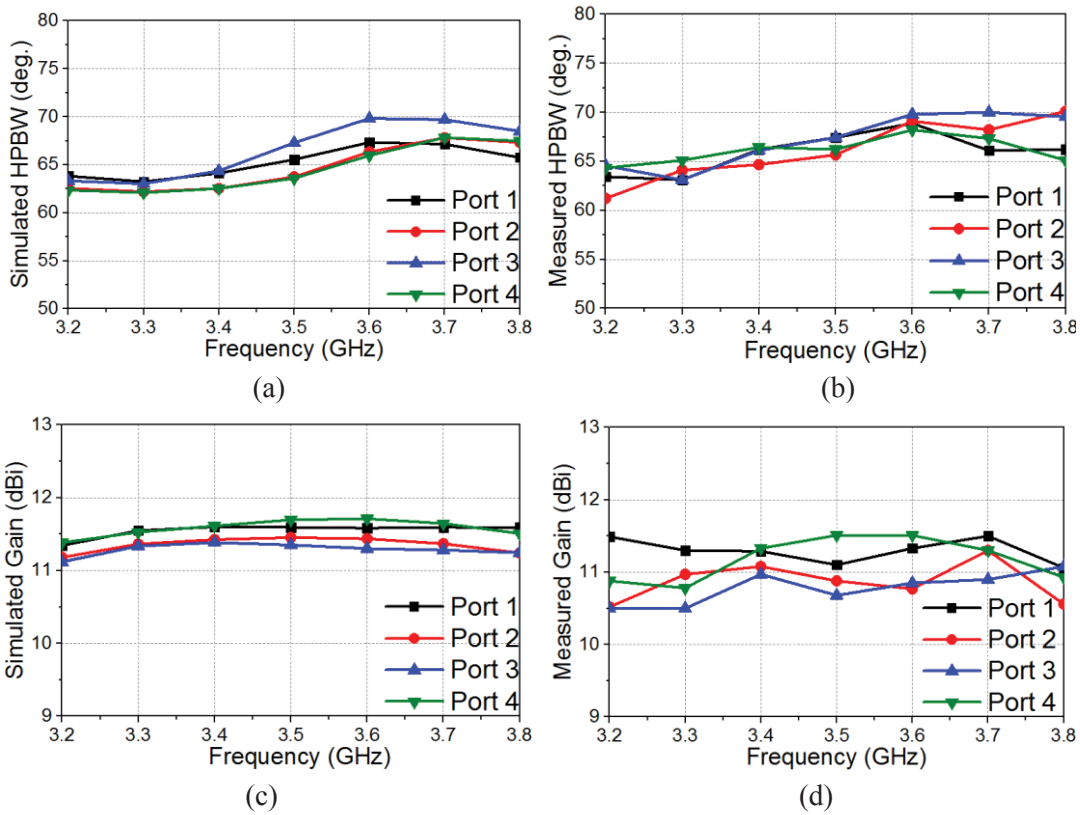

Figure 6.45 (a) Simulated and (b) measured HPBW in the horizontal plane. (c) Simulated and (d) measured gain for the HB antennas in the two columns.

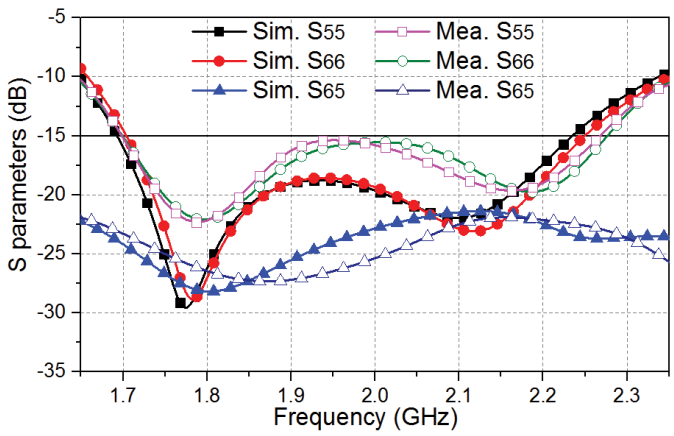

Figure 6.46 Simulated and measured S-parameters for the LB antenna.

The simulated and measured results for LB element is shown in Figures 6.46 – 6.48. Figure 6.46 plots the reflection coefficients and isolation of LB ports. The measured results agree well with the simulated results. The measured bandwidth is 28.3% from 1.7 GHz to 2.26 GHz for reflection coefficients less than -15 dB. Figure 6.47 shows the simulated and measured radiation patterns of the two polarizations. The simulated and measured patterns agree well with each other and the cross-polarization levels are less

than -17 dB across the band. The horizontal HPBW and gain of the LB element are plotted in Figure 6.48. The radiation patterns are stable with HPBW of 65°±5°. The simulated and measured gain is around 8 dBi, and 7 dBi, respectively. The difference is due to the loss of coaxial cables.

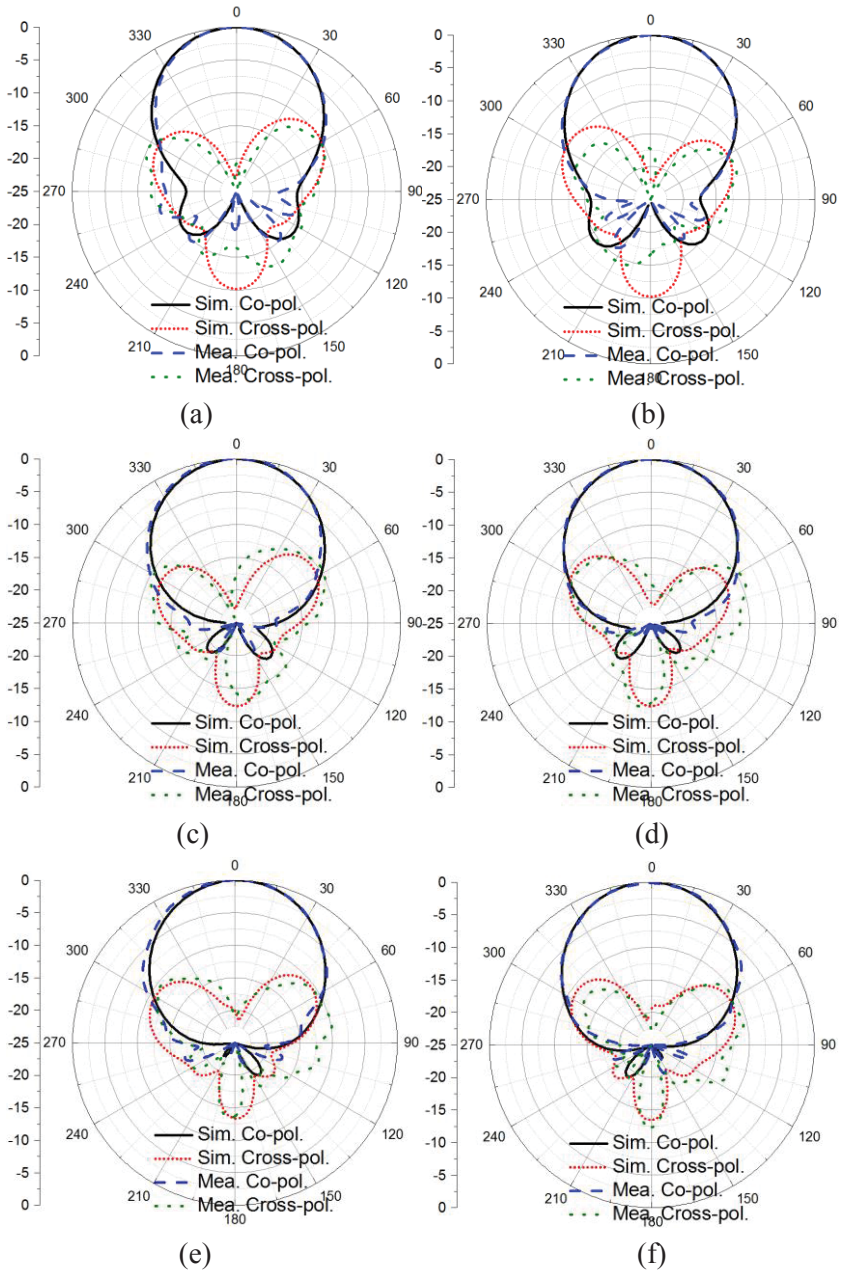

Figure 6.47 Normalized simulated and measured radiation patterns in the horizontal plane for the LB antenna. (a) Port 5 at 1.7 GHz, (b) port 6 at 1.7 GHz, (c) port 5 at 1.9 GHz, (d) port 2 at 1.9 GHz, (e) port 1 at 2.2 GHz, and (f) port 2 at 2.2GHz.

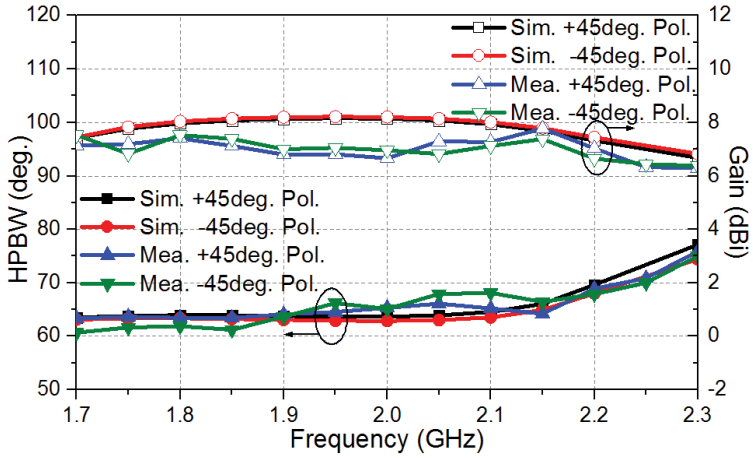

Figure 6.48 Simulated and measured HPBW and gain for the LB antenna.

6.6 Summary

In this section, we focus on solving the cross-band scattering problem in multi-band antenna arrays. To start with, deterioration of radiation pattern caused by the scattering between antennas operating at different bands is examined. To suppress cross-band scattering and restore radiation pattern, a method is proposed by modifying LB radiators with chokes to reduce HB scattering current on the LB arms. These chokes should present an open circuit at the high band and a short circuit at the low band. Three different choking configurations are proposed and analyzed. Their working principle, together with their capability of suppressing scattering, are investigated. To verify their performances, they are implemented in LB radiators in dual-band antenna arrays. Two dual-band base station antenna arrays targeting at 3G and 4G applications, and 4G and 5G applications, respectively, are designed. Simulated and measured results both demonstrate that choking the LB element largely suppresses cross-band scattering and restores radiation pattern. The realized arrays have stable radiation patterns in both well-matched high and low bands with compact sizes. Similar choking methods can be adopted to solve the cross-band scattering issue in other multi-band antenna systems.

Chapter 7: Multi-Beam Base Station Antenna Arrays

7.1 Introduction

Crowded data traffic is a major issue to tackle in the current wireless communication systems. Sectors can be split and covered by narrow-beam antennas to satisfy the demand of high capacity. However, having many antennas mounted in a tower increasing the installation cost, tower load and wind load. Multi-beam antenna serves as a good solution to increase system capacity without adding the number of antennas. It splits the wide main beam into precisely-spaced narrower beams to meet the need of large data capacity.

In LTE base stations, arrays with multiple vertical columns of dual polarization elements are arranged horizontally to achieve a narrow beam in the elevation direction and multiple beams in the azimuth direction. Usually, a single beam antenna provides coverage over a 120° sector in the azimuth plane whereas a multi-beam antenna covers the same sector with multiple narrower beams corresponding to separate cells. In this case, the data capacity is dramatically increased due to the increased number of cells. High-performance multi-beam networks are essential for expanding the capacity of existing systems. There is an urgent industrial need to develop new solutions to build wideband multi-beam arrays in wireless communication systems.

In this chapter, we present the design of a wideband Butler matrix based beam-forming network, which covers the LTE band from 1.71 GHz to 2.69 GHz. The wideband beamforming network is employed in two alternative beam-forming arrays. The challenges are mainly from the requirements for wide operating bandwidth, pattern stability and sidelobe levels, and in an environment of strong mutual coupling within arrays. Considering the existing shortcomings and challenges in the current LTE base stations, this chapter presents the following contributions: (1) a wideband three-beam beam- forming network to cover the entire LTE band with flexible beamwidth; (2) new solutions for the design of key components in the beam-forming networks including wideband quadrature couplers, phase shifters and power dividers; (3) dual-polarized antenna arrays using compact elements with stable patterns and steerable beams that meet LTE base station criteria; and (4) excellent antenna array performance based on a reduced size element that minimizes coupling; (5) the beam-forming performance extends across the whole 4G band and have been verified by experiment.

This section is organized as follow. Section 7.2 describes the diagram of beam-forming arrays to meet LTE base station criteria. Section 7.3 discussed the theory and design procedures of the beam-forming network. The simulated and measured performances of the key components are also presented. Section 7.4 gives thorough descriptions of the radiating element as well as arrays used in the multi-beam arrays. The simulated and tested results of beam-forming arrays are presented to confirm all the designs.

7.2 Beam-Forming Antenna Array System

LTE base station antennas with multiple beams usually consist of beam-forming networks and an array of dual-linearly polarized antenna columns. The beam-forming networks divide the coverage area in the azimuth plane into n (in our case three) parts. If the coverage sector is of angular width α, then each beam should cover a sector of (α/n). In LTE base stations, three arrays are typically arranged to cover 360° arc and thus α is 120° for each array. The crossover point is defined as the intersection point of two adjacent beams, which may have different levels relative to the beam peak depending on the array configurations. Basic Butler matrices are such that if the outputs are connected to omnidirectional elements, the beam crossovers occur at -3 dB. For LTE multi-beam antennas the crossover level should normally be at about -10 dB so, to achieve this, beams must be made narrower which can be achieved if the array is lengthened.

To this end, we extend the arrays from 3 elements to 5 or 6 elements as shown in Figure 7.1, which shows block diagrams of the 5- and 6-element realizations. We refer to such a beam- forming network as an augmented Butler matrix. This achieves beam crossover values in the range from -10 dB to -15 dB, which is suitable for LTE applications. Here we intend to generate three beams in the azimuth plane to cover the 120° sector with three separate beams each covering a sector of 40°. Each beam-forming array is composed of two three-beam Butler matrices, power dividers/delay lines and a dual-linearly polarized array. Apart from its ability to control the crossover level between the beams, the augmented Butler matrix necessarily provides an amplitude taper across the array aperture which results in a reduced sidelobe level. Some control of the sidelobe level can be exercised by selecting the split ratio of the power dividers. A suitable arrangement of a 5- and 6-element beam-forming arrays are shown in Figure 7.1. Table 7.1 and 7.2 show the ideal power levels and phase distributions on the two arrays.

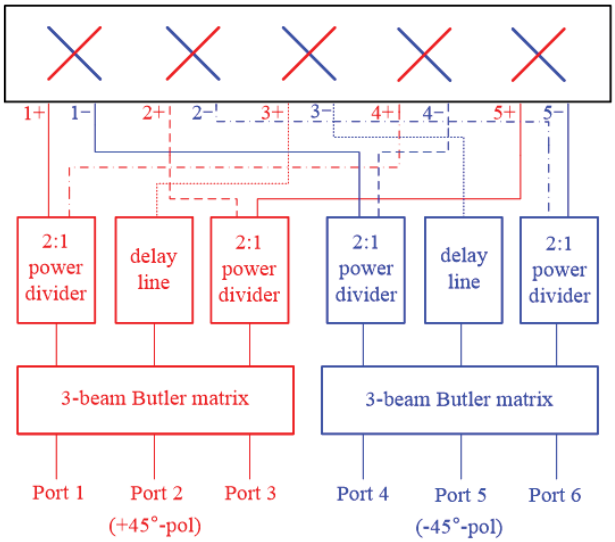

(a)

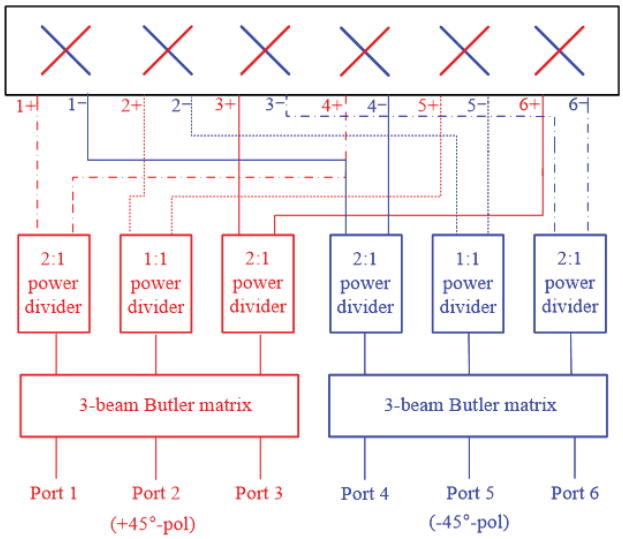

(b)

Figure 7.1 Configurations of two beam-forming arrays for LTE base stations: (a) using 5-element array; (b) using 6-element array.

Table 7.1 Power and Phase Distribution on the 5-Element Array

Element No.		1	2	3	4	5
Power Level		1/3	2/3	1	2/3	1/3
Amplitude (dB)		-4.77	-1.77	0	-1.77	-4.77
Phase (°)	Port 1	0	120	-120	0	120
	Port 2	0	-120	120	0	-120
	Port 3	0	0	0	0	0

Table 7.2 Power and Phase Distribution on the 6-Element Array

Element No.		1	2	3	4	5	6
Power Level		1/3	1/2	2/3	2/3	1/2	1/3
Amplitude (dB)		-4.77	-3	-1.77	-1.77	-3	-4.77
Phase (°)	Port 1	0	120	-120	0	120	-120
	Port 2	0	-120	120	0	-120	120
	Port 3	0	0	0	0	0	0

The three-beam Butler matrix is an essential part of the beam-forming network. To produce three beams, phase increments of 0°, 120° and -120° are required between the outputs for the three required beams. These fixed phase relationships are required over the whole operating band. The Butler matrix is composed of quadrature couplers and fixed phase shifters. All of these components are required to be wideband devices. Figure 7.2 shows how a three-way Butler matrix with the correct output amplitudes and phases can be constructed from quadrature couplers and fixed phase shifters. The design of the three-way Butler Matrix is detailed in Section 7.3.

For each antenna element in the LTE base station, ±45°- polarization is required and separate beam-forming networks and dual-polarized radiating elements are needed for the two polarizations. In the cellular environment, the three inputs to the Butler matrix correspond to three adjacent beams and are fed with signals for three separate cells. The single multi-beam antenna is used as an alternative to three independent antennas with different pointing fed from three separate cells.

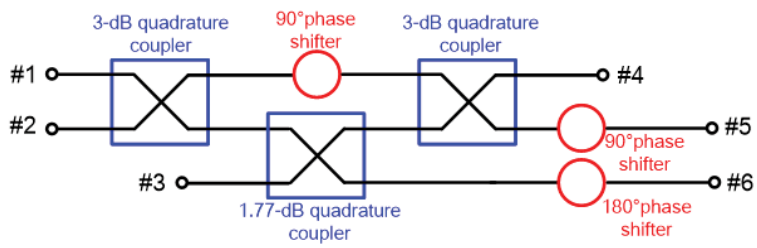

Figure 7.2 Configuration of the proposed wideband three-beam Butler matrix for LTE base stations.

7.3 Wideband Beam-Forming Network

In this section, we provide the theory and engineering design of the essential

components within the proposed wideband beam-forming network, including the three-way Butler Matrix and the wideband power dividers.

7.3.1 Three-Beam Butler Matrix

7.3.1.1 Theory of the Three-Beam Butler Matrix

For an ideal three-beam beam-forming network with perfect port matching and ideal isolation, the scattering matrix of the three-beam Butler matrix with ports 1, 2 and 3 as inputs and ports 4, 5 and 6 as outputs can be expressed as:

$$S = \begin{bmatrix} 0 & T \\ T & 0 \end{bmatrix} \tag{7.1}$$

where

$$T = \frac{1}{\sqrt{3}} \begin{bmatrix} 1 & e^{j\frac{2\pi}{3}} & e^{-j\frac{2\pi}{3}} \\ 1 & e^{-j\frac{2\pi}{3}} & e^{j\frac{2\pi}{3}} \\ 1 & 1 & 1 \end{bmatrix} \tag{7.2}$$

The matrix of the transmission block of S, is a symmetrical unitary matrix. From (2) one can observe the phase differences between any two adjacent elements of each row (the former element minus the latter one) are $-2\pi/3$, $2\pi/3$ and 0, respectively. To construct such a beam-forming network, quadrature couplers and fixed phase shifters are needed to provide appropriate power division and phase at each output port. The quadrature coupler can be represented with an orthogonal transmission matrix Q, which is written as:

$$Q = \begin{bmatrix} a & j\sqrt{1-a^2} \\ j\sqrt{1-a^2} & a \end{bmatrix} \tag{7.3}$$

where a is the signal magnitude at one output port, and the signal magnitude at the other port is $\sqrt{1-a^2}$. There is 90° phase difference between two output ports due to the orthogonal property of the quadrature coupler. For the equal- split quadrature coupler Q_1 with power division ratio of 1:1 ($a = 1/\sqrt{2}$) and unequal-split quadrature coupler Q_2 with power division ratio of 2:1 ($a = 1/\sqrt{3}$), the transmission matrices become, respectively:

$$Q_1 = \begin{bmatrix} \frac{1}{\sqrt{2}} & j\frac{1}{\sqrt{2}} \\ j\frac{1}{\sqrt{2}} & \frac{1}{\sqrt{2}} \end{bmatrix} \tag{7.4a}$$

$$Q_2 = \begin{bmatrix} \frac{1}{\sqrt{3}} & j\frac{\sqrt{2}}{\sqrt{3}} \\ j\frac{\sqrt{2}}{\sqrt{3}} & \frac{1}{\sqrt{3}} \end{bmatrix} \tag{7.4b}$$

The transmission block T can be written as:

$$T = P_1 T_1 P_2 \tag{7.5}$$

where

$$T_1 = \begin{bmatrix} Q_1 & \\ & 1 \end{bmatrix} \begin{bmatrix} j & \\ & Q_2 \end{bmatrix} \begin{bmatrix} Q_1 & \\ & 1 \end{bmatrix} \tag{7.6a}$$

$$P_1 = \begin{bmatrix} e^{j\frac{\pi}{3}} & & \\ & e^{j\frac{\pi}{6}} & \\ & & 1 \end{bmatrix} \tag{7.6b}$$

$$P_2 = \begin{bmatrix} 1 & & \\ & j & \\ & & -1 \end{bmatrix} \tag{7.6c}$$

Here, T_1, P_1 and P_2 are all diagonal matrices: T_1 is the center part of T composed of three components: two equal-power quadrature couplers Q_1 ($a = 1/\sqrt{2}$) and one unequal-power quadrature coupler Q_2 ($a = 1/\sqrt{3}$) with a 90° phase shifter. P_1 and P_2 refer to two phase shifting networks, by which P_1 will add phase shifts on the row elements while P_2 will add phase shifts on the column elements of T_1.

In (7.2), the phases of the first elements of each row are identical. However, it makes no difference what this value is, which means the phase shift block P_1 in (7.5) can be neglected, and the transmission block T of an ideal three-beam Butler matrix can be simplified to T_r as:

$$T_r = T_1 P_2 = \frac{1}{\sqrt{3}} \begin{bmatrix} e^{j\frac{2\pi}{3}} & e^{j\frac{4\pi}{3}} & 1 \\ e^{j\frac{5\pi}{6}} & e^{j\frac{\pi}{6}} & e^{j-\frac{\pi}{2}} \\ e^{-j\pi} & e^{-j\pi} & e^{-j\pi} \end{bmatrix} \tag{7.7}$$

It is seen that the phase differences between adjacent elements in each row are $-2\pi/3$, $2\pi/3$ and 0, respectively, which satisfy the phase requirements of a three-beam Butler

matrix. Based on the analysis above, the three-beam Butler matrix can be configured as shown in Figure 7.2. The configuration is quite simple as it is composed of two 3-dB and one 1.77-dB quadrature couplers, and three phase shifters with 90° and 180° phase shifts. Since the design is aimed at LTE band range from 1.71 GHz to 2.69 GHz, wideband components operating over this band need to be developed accordingly.

7.3.1.2 Quadrature Couplers

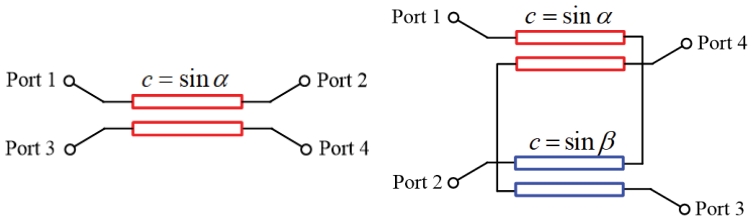

(a) (b)

Figure 7.3 Equivalent transmission line models of two quadrature couplers: (a) traditional type; (2) tandem type.

Following the analysis above, we aim to develop a new type of quadrature couplers that can realize equal and unequal coupling power ratio with wide operating band range. To satisfy the requirements of the bandwidth and power ratio, directional couplers with coupled-lines using striplines are investigated. Figure 7.3(a) shows the configuration of a traditional backward wave directional coupler with four ports. The overall length of the coupler is 90° at the center frequency, and the coupling factor of the coupled-line section is c. As mentioned in the last section, the output amplitude at two ports is a and $\sqrt{1-a^2}$, and if we write $c = \sin\alpha$, the scattering matrix of the coupler S_{c1} becomes [109]:

$$S_{c1} = \begin{bmatrix} 0 & \cos\alpha & j\sin\alpha & 0 \\ \cos\alpha & 0 & 0 & j\sin\alpha \\ j\sin\alpha & 0 & 0 & \cos\alpha \\ 0 & j\sin\alpha & \cos\alpha & 0 \end{bmatrix} \tag{7.8}$$

where α is an angle depending on the power division ratio (PDR) of the coupler. For a 3-dB coupler when the PDR equals to 1:1, $\cos\alpha = \sin\alpha = 1/\sqrt{2}$ and $\alpha = 45°$; for a 1.77-dB coupler when the PDR equals to 2:1, $\cos\alpha = 1/\sqrt{3}$, $\sin\alpha = \sqrt{2}/\sqrt{3}$ and $\alpha = 54.74°$. Ports 2 and 3 refer to the direct port and coupled port, where there is 90° phase difference between them; hence the term "quadrature coupler".

For an unequal directional coupler with a PDR of 2:1, the coupling factor is about 0.82, which is so high that it is difficult to realize using planar structures. To tackle the problem,

a tandem structure shown in Figure 7.3(b) is used. Assuming that the coupling factors of the two coupled-line sections are α and β, the output signal magnitude in this case can be calculated as:

- port 2: $\cos\alpha\ \cos\beta - \sin\alpha\ \sin\beta = \cos(\alpha+\beta)$
- port 3: $j\cos\alpha\sin\beta + j\sin\alpha\cos\beta = j\sin(\alpha+\beta)$

Therefore, the scattering matrix of the cascaded quadrature coupler S_{c2} can be written as:

$$S_{c2} = \begin{bmatrix} 0 & \cos(\alpha+\beta) & j\sin(\alpha+\beta) & 0 \\ \cos(\alpha+\beta) & 0 & 0 & j\sin(\alpha+\beta) \\ j\sin(\alpha+\beta) & 0 & 0 & \cos(\alpha+\beta) \\ 0 & j\sin(\alpha+\beta) & \cos(\alpha+\beta) & 0 \end{bmatrix} \tag{7.9}$$

If $\alpha = \beta$, the scattering matrix can be simplified as:

$$S_{c2} = \begin{bmatrix} 0 & \cos 2\alpha & j\sin 2\alpha & 0 \\ \cos 2\alpha & 0 & 0 & j\sin 2\alpha \\ j\sin 2\alpha & 0 & 0 & \cos 2\alpha \\ 0 & j\sin 2\alpha & \cos 2\alpha & 0 \end{bmatrix} \tag{7.10}$$

Compared (7.10) with (7.8), it is found that the two-stage cascaded structure is able to realize a coupling factor that is twice that of the single stage coupler for the same degree of coupling of the lines. The even- and odd-mode impedance can be calculated by the following equations:

$$Z_{0e} = Z_0\sqrt{\frac{1+c}{1-c}} \tag{7.11}$$

$$Z_{0o} = Z_0\sqrt{\frac{1-c}{1+c}} \tag{7.12}$$

In the cascaded structure, the coupling factor of the coupled-line is half that of the overall coupler. Therefore, for the 3-dB coupler, the even- and odd-mode impedances are 74.8 Ω and 33.4 Ω; for the 1.77-dB coupler, the even- and odd-mode impedances are 82.2 Ω and 30.4 Ω, respectively. All ports of the quadrature couplers should be matched at all frequencies, requiring that the even and odd mode velocities are equal across the band. Microstrip construction has unequal velocities and can only be approximately compensated [110]. Stripline inherently has equal even and odd mode velocities and normally provides much better performance where coupled lines are required.

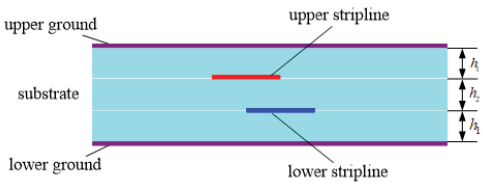

(a)

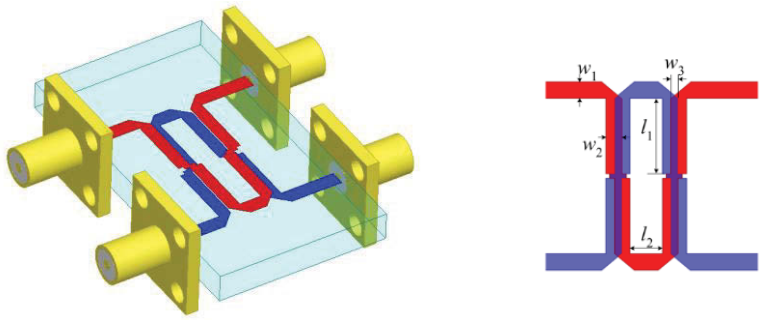

(b)

Figure 7.4 Configuration of (a) Cross-sectional view of the stripline implementation used in the design of quadrature coupler; (b) 3D model of the constructed quadrature coupler.

Figure 7.4(a) shows the cross-section view of the proposed stripline, which has three stacked substrate boards each with dielectric constant of ε_r and thickness of h_1, h_2 and h_1, respectively. There are metal layers on the top and bottom of the substrates acting as grounds. Broadside coupling occurs between the upper and lower striplines, which are located on two sides of the middle substrate.

Table 7.3 Related Parameters of Two Quadrature Couplers

3-dB coupler		1.77-dB coupler	
Parameters	Values (mm)	Parameters	Values (mm)
l_1	9.2	l_1	8.8
l_2	3.0	l_2	3.0
w_1	1.96	w_1	1.96
w_2	1.5	w_2	1.52
w_3	0.24	w_3	0.76

Figure 7.4(b) shows the 3D structure of the quadrature coupler. In this work, two different couplers with coupling coefficient of 3-dB and 1.77 dB are built in Ansys EM

Desktop, and the relevant dimensions of two couplers are listed in Table 7.3. The coupling coefficient can be controlled by changing the line width as well as the overlap between the upper and lower stripline. The substrate used for the design is Rogers RO4356B with ε_r of 3.48 and h_1, h_2 equal to 1.52 mm and 0.76 mm, respectively.

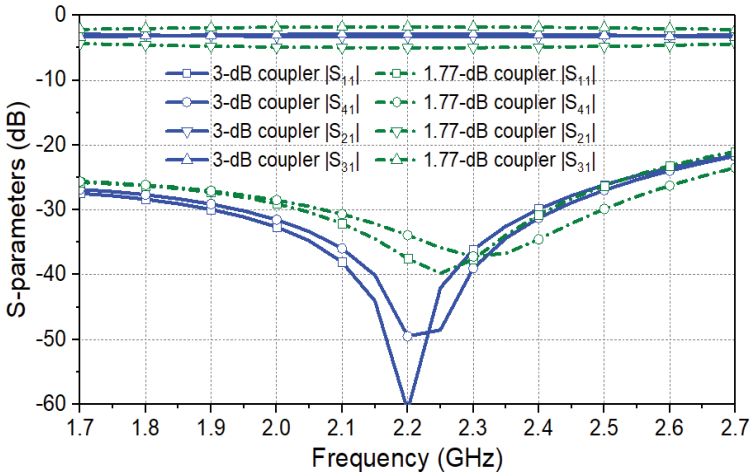

(a)

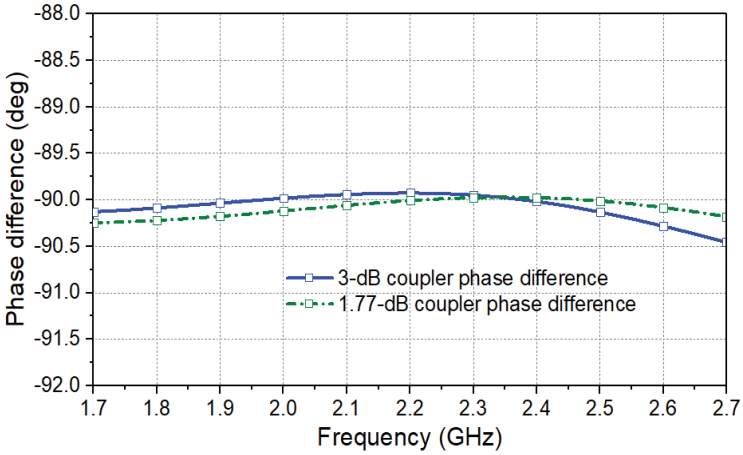

(b)

Figure 7.5 Simulated reflection coefficients of the antenna with ideal circuit feed network and its physical realization.

Simulation results are shown in Figure 7.5. Figure 7.5(a) shows that the power magnitude at port 2 and port 3 of two quadrature couplers with PDR of 1:1 and 2:1. For the equal PDR case, $|S_{21}|$ and $|S_{31}|$ is about -3.1±0.3 dB across the frequency range from 1.7 GHz to 2.7 GHz compared with the ideal power level -3 dB. For the unequal coupler, $|S_{21}|$ and $|S_{31}|$ is about -1.9±0.2 dB and -4.7±0.3 dB, which is very close to the ideal value of -1.77 dB and -4.77 dB. Figure 7.5(b) demonstrates that both designs achieve excellent port matching and isolation across the whole band. Moreover, the phase difference

between two output ports is constant and stable around 90°, representing the orthogonality property of the quadrature couplers.

7.3.1.3 Wideband Fixed Phase Shifter

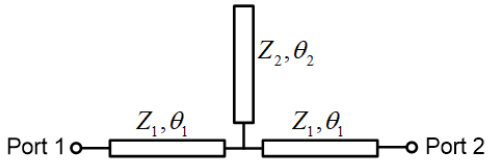

(a)

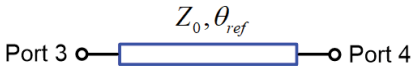

(b)

Figure 7.6 Equivalent transmission line models of the wideband phase shifter: (a) phase shifter; (b) reference line.

In addition to wideband quadrature couplers, fixed phase shifters are also critical components in the Butler matrix. To achieve a stable phase, excellent matching and transmission property and small phase deviation are extremely important. To that end, a novel type of wideband phase shifter is designed. Figure 7.6(a) shows the equivalent circuit of a suitable phase shifter. It comprises two transmission lines (Z_1, θ_1) and an open-ended stub (Z_2, θ_2) at the center point of two transmission lines. A reference line, as shown in Figure 7.6(b), is required for comparison with the phase shifter section. The operating principle of the phase shifter is that if the inputs of the phase shifter and reference line (port 1 and port 3 in Figure 7.6) are fed with equal, in-phase signals, the outputs maintain an almost constant phase difference across the band. The ABCD matrix of the phase shifter can be calculated by:

$$[A] = \begin{bmatrix} \cos\theta_1 & jZ_1\sin\theta_1 \\ j\dfrac{1}{Z_1}\sin\theta_1 & \cos\theta_1 \end{bmatrix} \cdot \begin{bmatrix} 1 & 0 \\ j\dfrac{1}{Z_2}\tan\theta_2 & 1 \end{bmatrix} \cdot \begin{bmatrix} \cos\theta_1 & jZ_1\sin\theta_1 \\ j\dfrac{1}{Z_1}\sin\theta_1 & \cos\theta_1 \end{bmatrix} \tag{7.13}$$

Subsequently, using the ABCD-to-*S*-matrix conversion, the S-parameters of the phase shifter are derived as:

$$S_{11} = \frac{B - CZ_o^2}{2Z_oA + B + CZ_o^2} \tag{7.14a}$$

$$S_{21} = \frac{2Z_o}{2Z_oA + B + CZ_o^2} \tag{7.14b}$$

where

$$A = \cos(2\theta_1) - \frac{Z_1}{2Z_2}\sin(2\theta_1) \cdot \tan\theta_2$$

$$B = j \cdot \left[Z_1 \sin(2\theta_1) - \frac{Z_1^2}{Z_2}\sin^2\theta_1 \cdot \tan\theta_2\right]$$

$$C = j \cdot \left[\frac{1}{Z_1}\sin(2\theta_1) - \frac{1}{Z_2}\cos^2\theta_1 \cdot \tan\theta_2\right]$$

The differential phase shift can be calculated by comparing the phase of the proposed structure with that of the reference line, which is expressed as:

$$\Delta\phi = \angle S_{21_ps} - \angle S_{21_{ref}} = \theta_r - \tan^{-1}\left[\frac{B + CZ_o^2}{2j \cdot Z_oA}\right] \tag{7.15}$$

For an ideal wideband phase shifter, it is required to have $|S_{21}| = 1$, $|S_{11}| = 0$, and $\Delta\phi = \theta_r - 180°$. In this case, the related value can be determined as: $\theta_1 = 90°$ and $\theta_2 = 180°$. These phase shifters can achieve a wide and constant differential phase across the desired operating band. To obtain 90° phase shift, the length of the reference line should be selected as $\theta_r = 270°$. The impedance of Z_1 and Z_2 will affect the return loss, insertion loss and phase deviation within the operating band range. In this design, to cover the wide band range and keep a minimized phase deviation, Z_1 and Z_2 are selected as 30 Ω and 33 Ω, respectively. To verify the design, full-wave simulation is done using the stripline structure. Figure 7.7 shows the 3D configuration of the phase shifter. It is noted that only one layer of stripline is used, which means the distances between the metal conductor and two grounds are different as h_1 and $h_1 + h_2$, respectively.

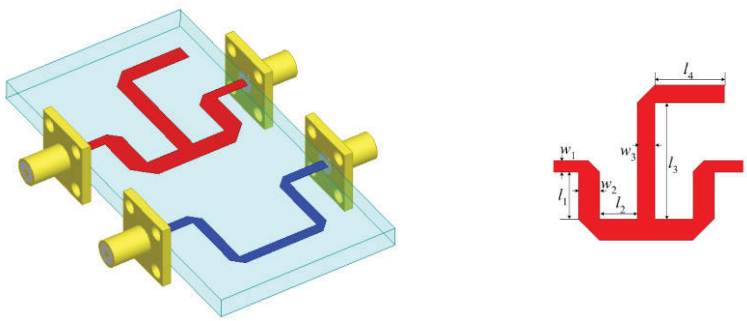

Figure 7.7 3D model of the constructed phase shifter.

Figure 7.8 shows the comparison between the synthesized and full-wave simulation results of the structure. The full-wave simulation is done in the EM environment Ansys EM Desktop using the same substrate configuration as for the quadrature couplers. The optimized dimensions of the phase shifter are found to be: $l_1 = 4.9$, $l_2 = 5.14$, $l_3 = 20$, $l_4 = 13.9$, $w_1 = 1.96$, $w_2 = 3.6$, $w_3 = 1.4$, all in mm. The full-wave simulated result demonstrates that over the 1.7 GHz to 2.7 GHz band, the return loss is more than 20 dB and insertion loss is close to 0 dB. Three resonant poles can be observed which greatly broaden the operating band. With regards to the differential phase, $\Delta\phi$ is around $90 \pm 2°$ across the same band range, which makes it very suitable for minimizing the phase deviation of the beam-forming network. It is noted that another 180° phase shifter is also required in constructing the 3-beam Butler matrix; however, since 180° requires an extremely small value of impedance that is not practical to realize, it is feasible to use two 90° phase shift units to replace the 180° one in the following design process.

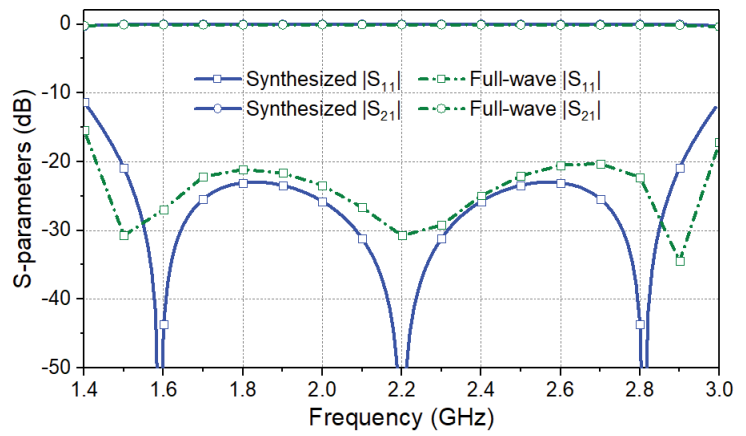

(a)

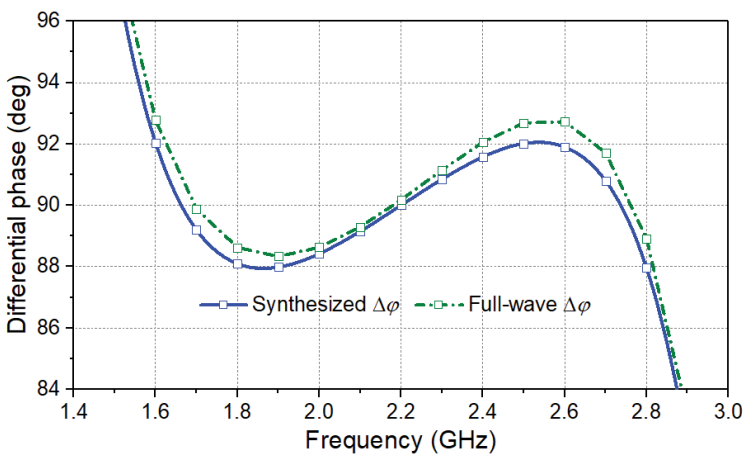

(b)

Figure 7.8 Synthesized and full-wave simulation results of the phase shifter: (a) S-parameters; (b) differential phase.

7.3.1.4 Realization of Butler Matrix

After the wideband quadrature couplers and phase shifters are designed, a three-beam Butler matrix can be created using the configuration shown in Figure 7.2. Figure 7.9(a) shows the 3D model of the Butler matrix built in the full-wave environment Ansys EM Desktop. Stripline structure using the same substrate is used. To satisfy the requirement of differential phases at each port, appropriate length delay lines are implemented as meandered lines, making the structure more compact. Two 3-dB and one 1.77-dB quadrature couplers are used as indicated in the configuration of the beam-forming network shown in Figure 7.2. Several 90° phase shifters provide 90° phase shift while two units are in series connection to provide 180° phase shift at port 6, which is in line with the configuration of the three-beam Butler matrix shown in Figure 7.2. Specific dimensions of the structure are given in Figure 7.9(b).

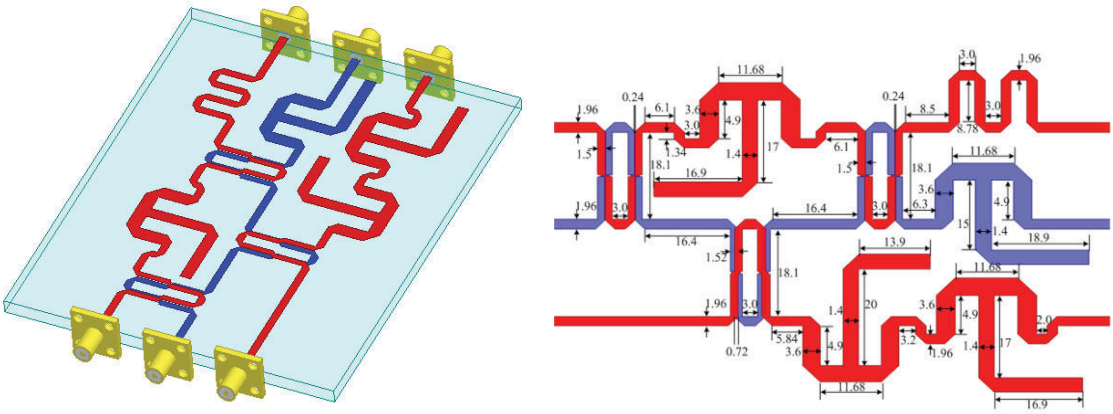

(a) (b)

Figure 7.9 3D model of the proposed three-beam Butler matrix for LTE base stations.

7.3.1.5 Experimental Results of Butler Matrix

Figure 7.10 shows the performance of the three-beam Butler matrix. As shown in Figure 7.10(a), excellent matching at all ports and isolation between input ports is obtained with $|S_{ii}|$ and $|S_{ij}|$ $(i, j = 1, 2 \text{ or } 3)$ are all less than -20 dB across the band. The transmission from input to output terminals are given in Figure 7.10(b), which are around -4.4 to -5.8 dB, and comparing well with the theoretical value of -4.77 dB at each) port, the overall insertion loss is around 0.4 dB. Figure 7.10(c) shows the differential phase in all cases. To realize the multiple-beam antenna arrays, it is required to have differential phases of $-120°$, $120°$, and $0°$, respectively, when port 1, port 2 and port 3 are excited.

The Simulated phase deviation is around ±10°.

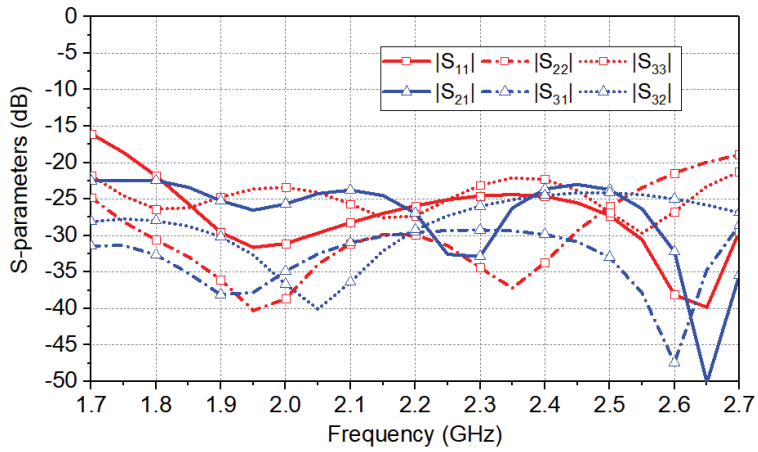

(a)

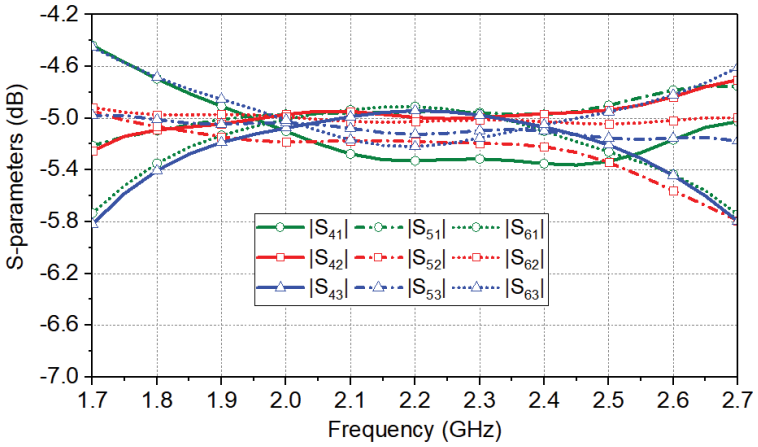

(b)

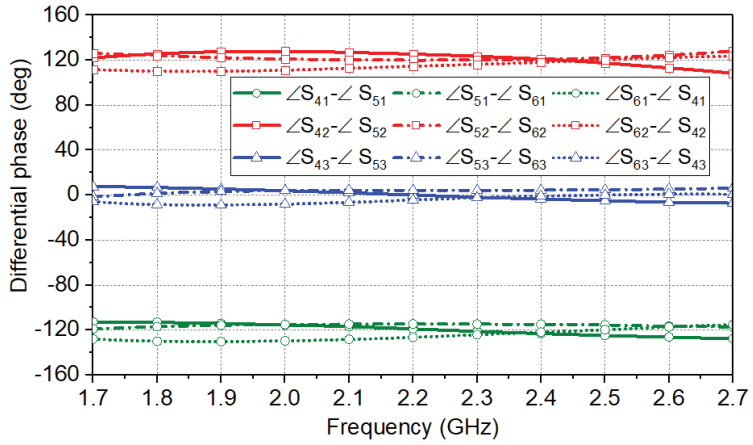

(c)

Figure 7.10 Simulated S-parameters of the fabricated Butler matrix: (a) return loss and isolations; (b) transmission coefficients; (c) differential phases.

A prototype of the beam-forming array are built and tested for validation, as shown in Figure 7.11. Since the design is implemented in stripline technology, the top and bottom

layer are ground while the tracks are in the central layers and are not visible. Its overall performance is shown in Figure 7.12. The measured results agree well with the predictions. As observed from Figure 7.12(a), within the band, all return loss values from input ports and isolation values between any two input ports ($|S_{ii}|$ and $|S_{ij}|$, $i, j = 1, 2$ or 3) are greater than 15 dB. The transmission properties of $|S_{ji}|$ ($i = 1, 2$ or 3, and $j = 4, 5$ or 6) are -5.8±1.0 dB, which means the insertion loss is around 1.0 dB for all signals. The tested differential phases at all ports are $-120°$, $120°$, and $0°$ when port 1, port 2 and port 3 are excited with around $\pm 10°$ deviation, which is the same as the simulation. These results guarantee that the three beams of the multi-beam arrays are preserved across the LTE band.

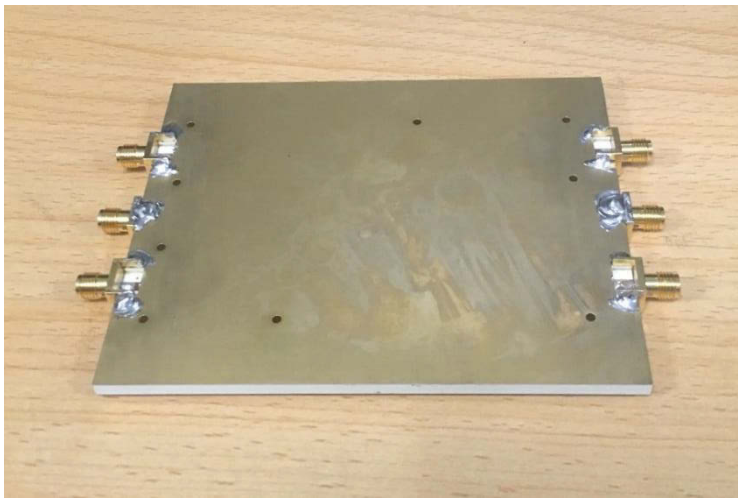

Figure 7.11 Photograph of the fabricated Butler matrix prototype.

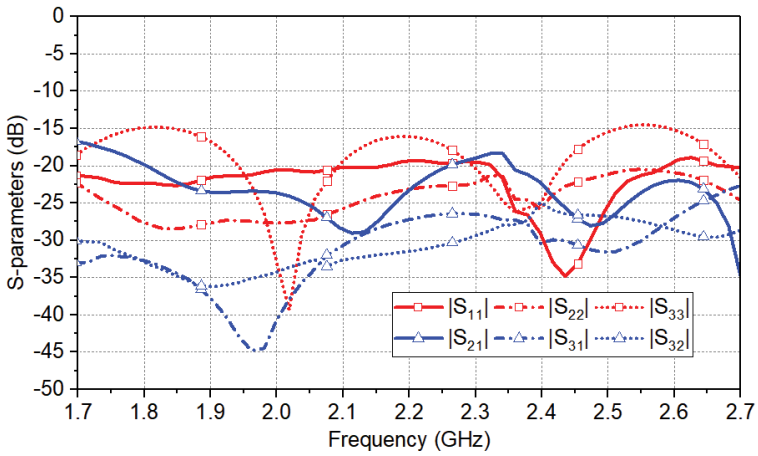

(a)

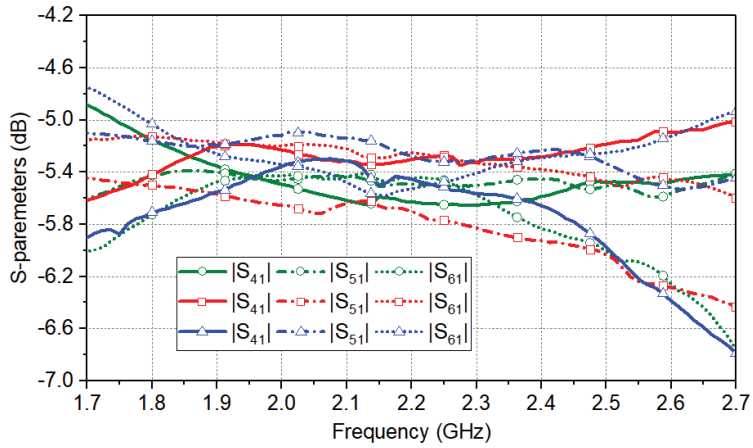

(b)

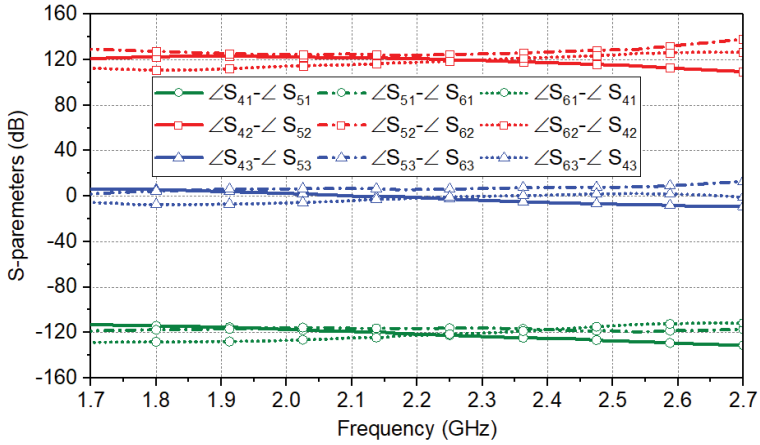

(c)

Figure 7.12 Measured S-parameters of the fabricated Butler matrix: (a) return loss and isolations; (b) transmission coefficients; (c) differential phases.

7.3.2 Wideband Power Dividers

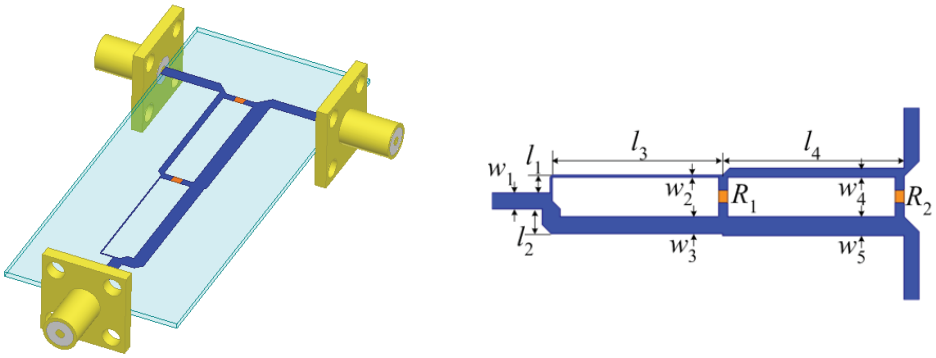

(a)

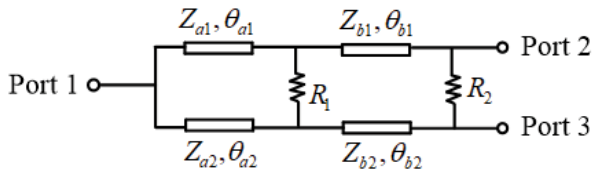

(b)

Figure 7.13 Wideband Wilkinson dividers: (a) the printed circuit board realization; (b) equivalent circuit.

To build the beam-forming networks shown in Figure 7.1, equal and unequal power dividers with equal phase outputs are needed. The power dividers help to generate the tapered power distribution to reduce the side-lobe levels.

Figure 7.13 shows the configuration of the dividers and their equivalent circuit using ideal transmission lines. To satisfy the requirement for wide operating bandwidth, two-section divider, composed of four transmission lines (Z_{a1}, θ_{a1}), (Z_{a2}, θ_{a2}), (Z_{b1}, θ_{b1}), and (Z_{b2}, θ_{b2}) and two isolation resistors (R_1, R_2), is used, as indicated in Figure 7.13(b). For wideband performance, the electrical length of each transmission line should be a quarter-wavelength at the center frequency. For an unequal power divider, we require $S_{11} = S_{22} = S_{33} = S_{32} = 0$ and the amplitude ratio of outputs is $|S_{21}|/|S_{31}| = k$, and

$$S_{21} = \frac{k}{\sqrt{k^2 + 1}} \tag{7.16}$$

$$S_{31} = \frac{1}{\sqrt{k^2 + 1}} \tag{7.17}$$

where k represents the square root of power division ratio k^2 at two output ports. Obviously, the total output power should be equal to the input power. To obtain symmetrical power level distributions on the upper and lower lines, the following equation should be satisfied so as to avoid dissipation of power in R_1 and R_2:

$$k^2 = \frac{Z_{b1}}{Z_{a1}} = \frac{Z_{b2}}{Z_{a2}} \tag{7.18}$$

Meanwhile, a suitable selection of isolation resistors R_1 and R_2 are given by:

$$R_1 = 2Z_0 \tag{7.19}$$

$$R_2 = \left(k^2 + \frac{1}{k^2}\right) Z_0 \tag{7.20}$$

Here, two power dividers are needed – one with equal power division $(k^2 = 1/1)$ and

one with unequal division ($k^2 = 2/1$).

Based on the analysis above, the S-parameters of two power dividers can be synthesized as given in Figures 7.14(a) and (b). For the equal power divider, it is found that $|S_{21}| = |S_{31}| = -3$ dB and $|S_{11}|$, $|S_{22}|$, $|S_{33}|$ and $|S_{22}|$ are all below -25 dB. For the unequal case, $|S_{21}|$ and $|S_{31}|$ are -1.8 and -4.8 dB respectively, with a difference of 3 dB indicating the power division of 2:1. The return loss at all ports and the isolation are greater than 20 dB across a wide band. The phase response of the unequal power divider is shown in Figure 7.14(c). It is observed that the phase difference between the two paths is smaller than ±1° across the whole band, which can be regarded as an in-phase power divider. An EM structure is built and the related dimensions are listed in Table 7.4. The simulated results agree well with the predicted ones, indicating that the design can provide proper power levels at outputs of the beam-forming networks and small reflections across such wideband range, which guarantee the overall performance of whole beam-forming network when integrated into systems.

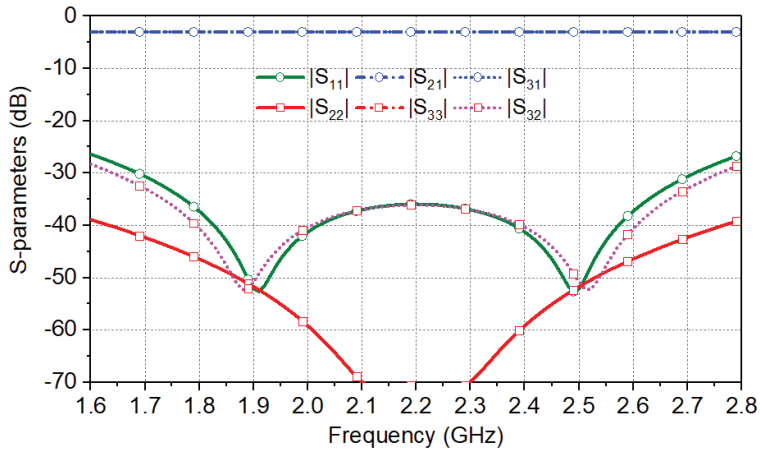

(a)

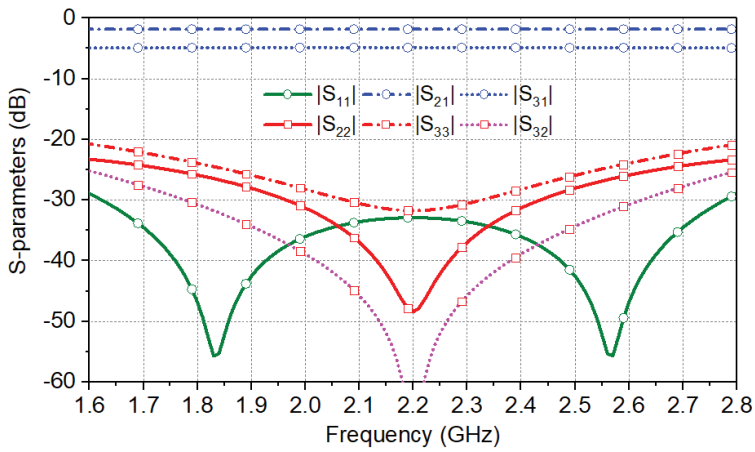

(b)

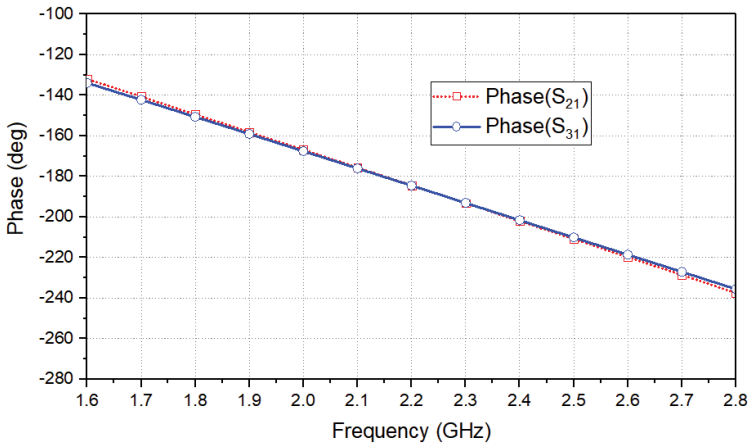

(c)

Figure 7.14 Simulated (a) magnitude of S_{11} and S_{21}, (b) magnitude of S_{31} and S_{41}, and (c) phases of S_{21} and S_{31} of the wideband power divider.

Table 7.4 Related Parameters of Two Power Dividers

1:1 power divider		2:1 power divider	
Parameters	Values (mm)	Parameters	Values (mm)
l_1	1.9	l_1	2.05
l_2	1.9	l_2	2.85
l_3	19.2	l_3	19.46
l_4	20.1	l_4	20.56
w_1	1.7	w_1	1.7
w_2	0.69	w_2	0.15
w_3	0.69	w_3	1.94
w_4	1.33	w_4	0.94
w_5	1.33	w_5	2.17
R_1	100 Ω	R_1	100 Ω
R_2	200 Ω	R_2	240 Ω

7.4 Beam-Forming Arrays

This section shows the design and performance of the radiating element and the realized beam-forming arrays. To obtain stable patterns and minimize the effect of mutual coupling between elements, a compact structure of the dual-polarized element is proposed and verified. Simulations have been conducted on a single isolated radiating element as well as on the beam-forming arrays. Prototypes of the beam-forming network as well as the arrays have been built and tested, with results provided in the following subsections.

7.4.1 Configuration and Performance of the Radiating Element

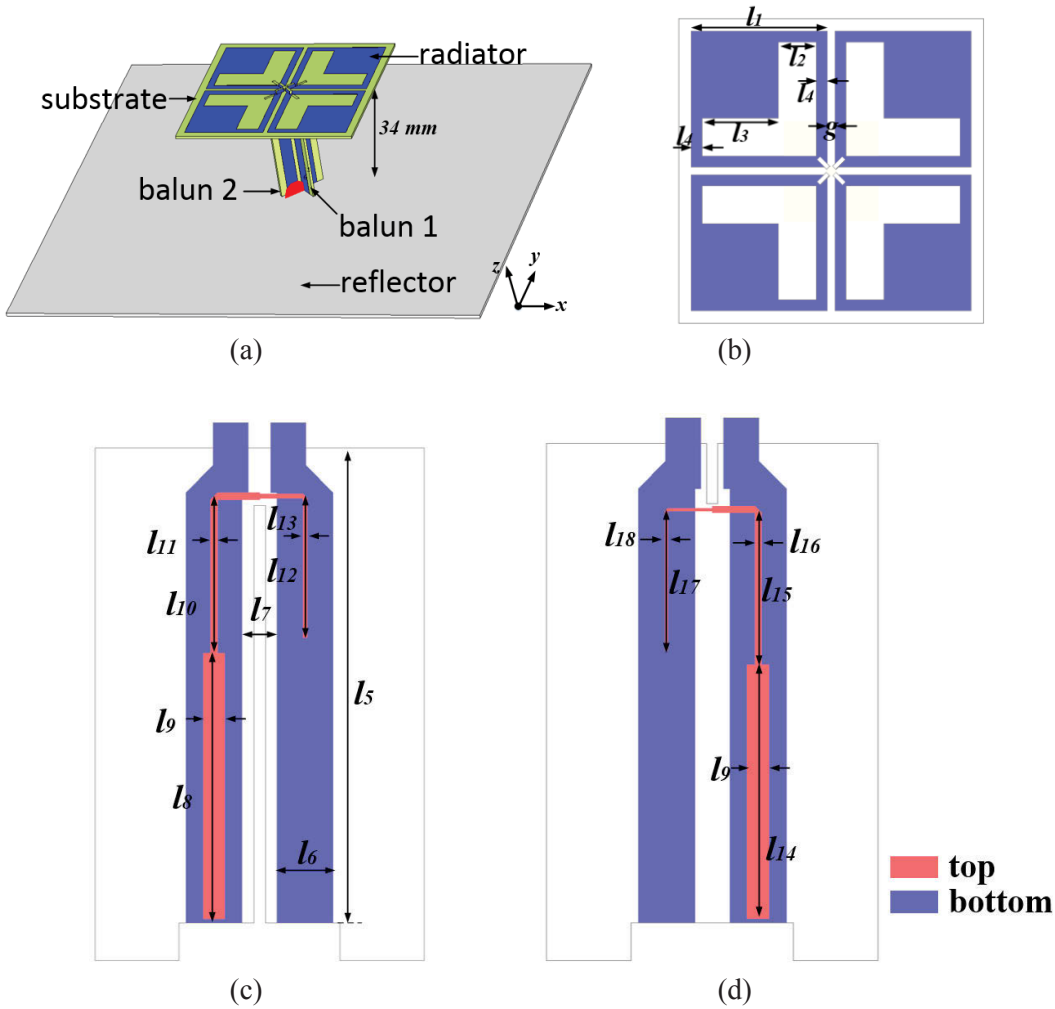

Figure 7.15 Configuration of (a) the ±45°-polarized antenna element; (b) radiator; (c) balun 1; and (d) balun 2.

The configuration of the ±45°-polarized antenna element is shown in Figure 7.15. The reason for this selection is the small size of the element which permits a half-wavelength spacing. This helps minimize the mutual coupling between elements in an array. Each element consists of a square-shaped cross-dipole, two perpendicular baluns, and a flat square ground reflector. For each dipole arm, a square metal piece is added in the square loop for convenient matching and minimizing the radiator's size. The cross-dipole is printed on the top of a substrate of dielectric constant 4.3 and thickness 1.0 mm. Two baluns are designed to excite the cross-dipole to achieve ±45° polarizations. The optimized dimensions of the element are listed in Table 7.5. The element features a compact size of 51.4 × 51.4 mm^2.

Table 7.5 Optimized Parameters of the ±45°-polarized antenna element

Parameters	Values (mm)	Parameters	Values (mm)
l_1	25	l_2	7
l_3	14	l_4	2
l_5	34	l_6	4
l_7	2.5	l_8	19
l_9	1.55	l_{10}	11.25
l_{11}	0.5	l_{12}	10.15
l_{13}	0.3	l_{14}	18
l_{15}	11	l_{16}	0.45
l_{17}	10	l_{18}	0.2
g	1.4		

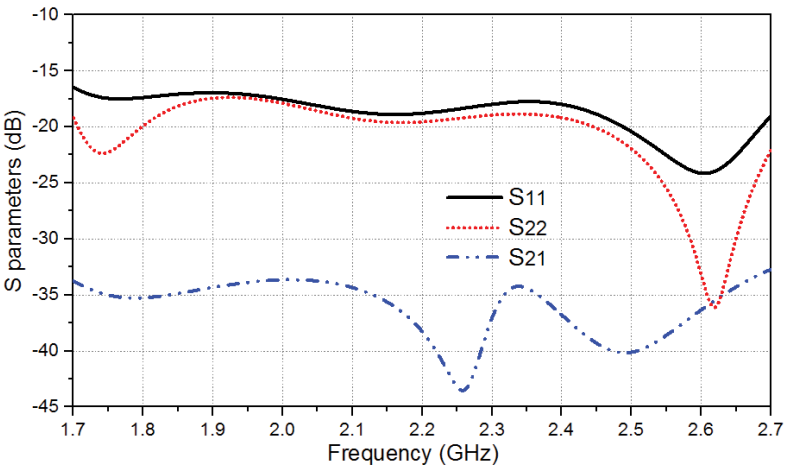

Figure 7.16 Simulated S-parameters of the ±45°-polarized single antenna element.

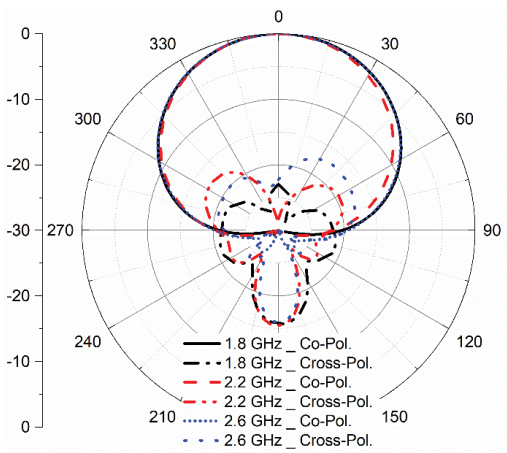

Figure 7.17 Simulated radiation pattern at 1.8 GHz, 2.2 GHz, and 2.6 GHz for the ±45°-polarized antenna element.

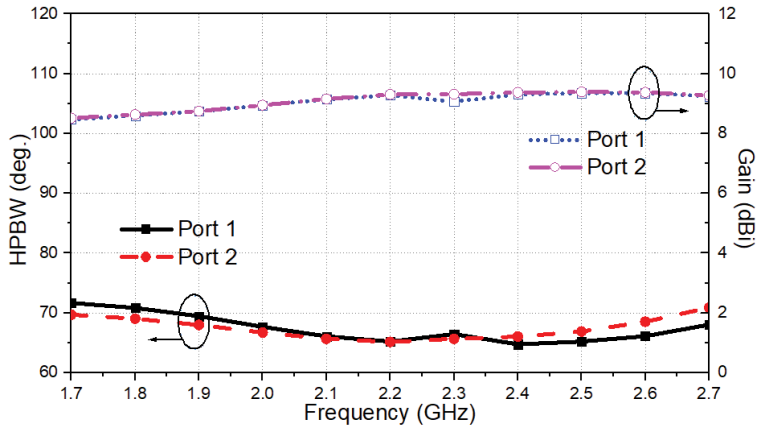

Figure 7.18 Simulated HPBW and gain for the ±45°-polarized antenna element.

The simulated S-parameters for a single isolated element is shown in Figure 7.16. The antenna elements at both polarizations are well-matched with $|S_{11}|$ and $|S_{22}|$ below -16.5 dB across the band. The coupling between the two polarizations is less than -33 dB across the band. The radiation pattern of the element for one polarization at 1.8 GHz, 2.2 GHz, and 2.6 GHz is given in Figure 7.17, from which very stable radiation patterns can be observed, with a cross-polarization level less than -22 dB at boresight. The simulated horizontal HPBW and gain performance are shown in Figure 7.18, which shows that the HPBW varies within 68°±2° and the gain fluctuates around 9.0 dBi from 1.7 GHz to 2.7 GHz for the two polarizations. The good performance of the antenna element contributes to the reliable pattern of antenna arrays used in the beam-forming arrays. While the elements were designed in isolation, the performance of the array is calculated in the presence of mutual coupling.

7.4.2 Configuration of Beam-Forming Arrays

Two arrays are designed as shown in Figure 7.19. The spacing between the elements is of critical importance for the side lobe level (SLL) and grating lobe level (GLL) for beams offset from boresight. The small size of the elements provides freedom for the array arrangement. The spacing between the elements is important in arrays. For the 5-element and 6-element arrays, the distances are set to be 70 mm (~ 0.50 λ_0) and 75 mm (~ 0.54 λ_0), respectively. These are optimized to minimize the SLL and GLL across the band. The antenna arrays are fed from two sets of beam-forming networks for the two polarizations.

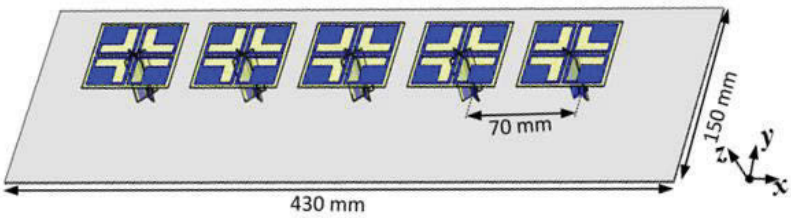

(a)

(b)

Figure 7.19 Configuration of (a) 5-element antenna array, and (b) 6-element antenna array.

7.4.3 Experimental Results

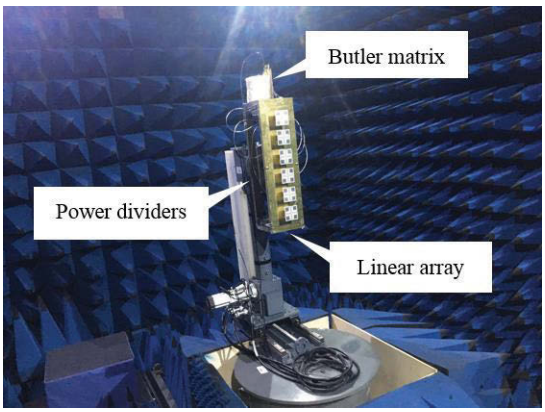

(a)

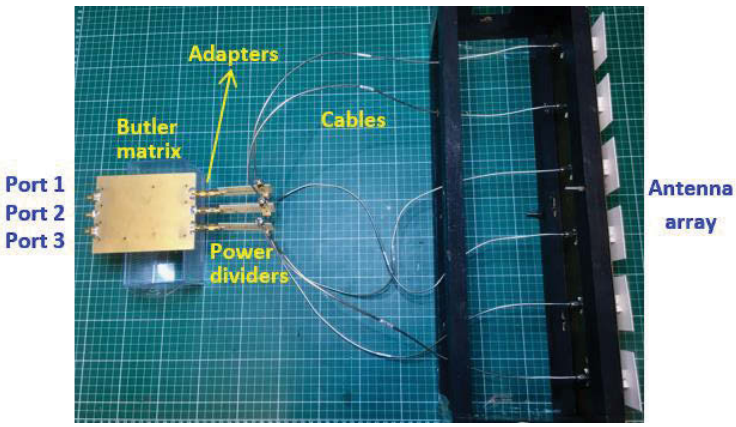

(b)

Figure 7.20 The tested LTE beam-forming array including the beam-forming network and 6-element antenna array: (a) test environment; (b) overall structure.

The test environment and the overall structure of the beam-forming arrays and are shown in Figure 7.20(a) and (b). The three-beam Butler matrix is cascaded with the three power dividers using adapters, and then the output ports of power dividers are connected with six array elements using cables. Since the two beam-forming arrays are similar in terms of structure and testing procedure, only the case of +45°-polarization of the 6-element array is given here. It is noted that due to the limitations of the test equipment, we rotated the array by 90 degree and tested the pattern in the elevation plane.

Figure 7.21 shows the measured return losses ($|S_{11}|$, $|S_{22}|$, and $|S_{33}|$) and isolation ($|S_{21}|$, $|S_{31}|$, and $|S_{32}|$) of the two beam- forming arrays comprising the beam-forming networks and antenna arrays. In both systems with 5-element or 6-element arrays, good matching with return loss greater than 12.2 dB is achieved across the band from 1.6 GHz to 2.8 GHz. Some reflections are caused by the cables, adapters and connectors used within the beam-forming arrays. Isolation better than 11 dB is obtained over the band.

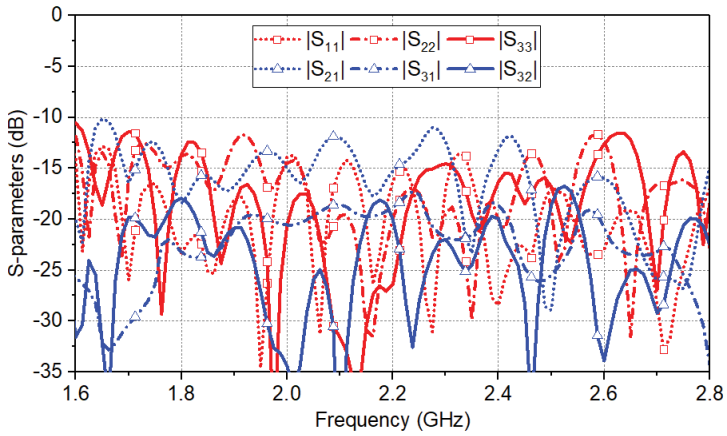

(a)

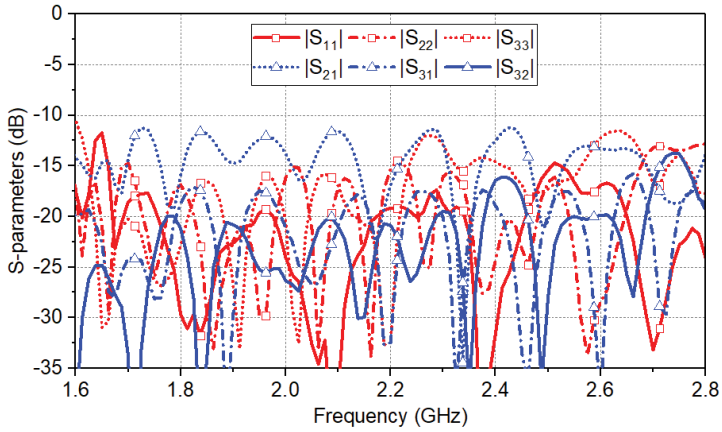

(b)

Figure 7.21 Measured return loss and isolation at input ports of two beam-forming arrays: (a) using 5-element array; (b) using 6-element array.

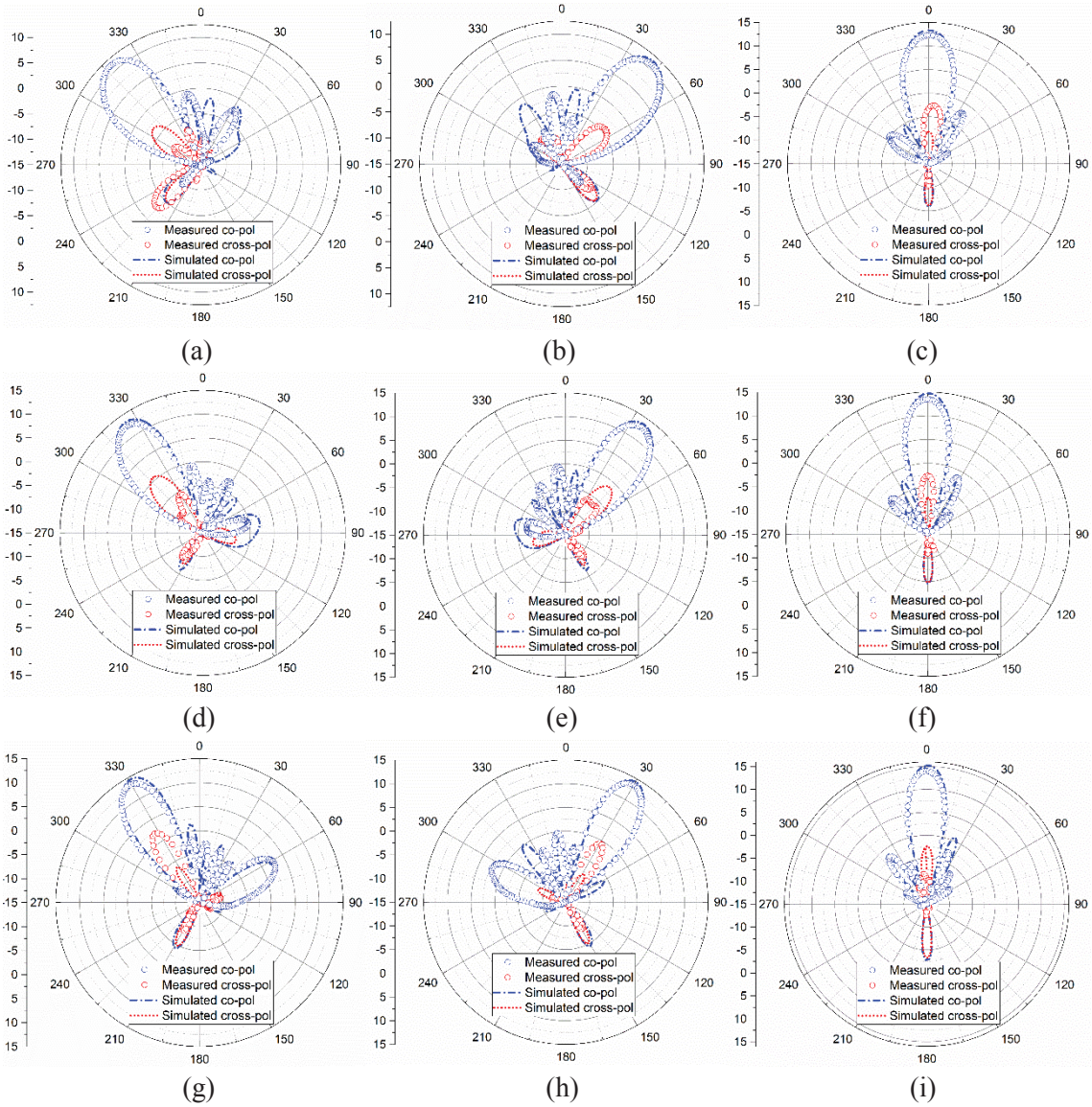

Figure 7.22 Simulated and measured radiation patterns at 1.8 GHz, 2.2 GHz, and 2.6 GHz for the 6-element antenna array fed by the beam-forming network: (a) beam 1 at 1.8 GHz; (b) beam 2 at 1.8 GHz; (c) beam 3 at 1.8 GHz; (d) beam 1 at 2.2 GHz; (e) beam 2 at 2.2 GHz; (f) beam 3 at 2.2 GHz; (g) beam 1 at 2.6 GHz; (h) beam 2 at 2.6 GHz; (i) beam 3 at 2.6 GHz.

The radiation patterns obtained from the 6-element array fed by the beam-forming network are presented in Figure 7.22. Three spaced beams beam 1, beam 2 and beam 3 are generated when port 1, port 2 and port 3 are excited, respectively. Since the beams obtained using the 5-element and 6-element arrays are similar, only the patterns of the 6-element array are shown. The simulated and measured patterns are provided at three frequencies, 1.8 GHz, 2.2 GHz and 2.6 GHz. Good agreement between the simulated patterns and the measured ones is achieved. Three contiguous beams with different pointing angles are realized by the beam-forming network across the LTE band. As shown

in Figures 7.22(a)-(c), beams at 1.8 GHz point at −42°, 42° and 0° when port 1, port 2 and port 3 of the beam-forming network are excited respectively. The measured horizontal HPBW of these three states are 23°, 23° and 20°, which are exactly those predicted. The realized gain is around 11.8 to 13 dBi and the SLL is below -12 dB. At 2.2 GHz as shown in Figures 7.22(d)-(f), the beams point at −36°, 36° and 0° and HPBWs are around 20°, 20° and 16° when port 1, port 2 and port 3 are excited. The realized measured gain is around 12.6 to 13.8 dBi, compared with the simulated value of 13 to 14.8 dBi. The SLL is below -13 dB and cross-polarization level less than -15 dB at the center of each beam. Figures 7.22(g)-(i) display the radiation patterns at 2.6 GHz with three beams pointing to −30°, 30° and 0°, respectively. The HPBW is around 16°, 16° and 13°, and realized gain is 13.5 to 14.6 dBi. The SLL is below -17 dB and cross-polarization level less than -16 dB.

Table 7.6 Overall Performance of the 6-element Array Fed By the Beam-Forming Network

	1.8 GHz			2.2 GHz			2.6 GHz		
	Port 1	Port 2	Port 3	Port 1	Port 2	Port 3	Port 1	Port 2	Port 3
Beam angle	−42°	42°	0°	−36°	36°	0°	−30°	30°	0°
HPBW	23°	23°	20°	20°	20°	16°	16°	16°	13°
Realized Gain (dBi)	12	11.8	13	13	13.2	14.8	14.8	14.6	15.1
Cross-pol Level (dB)	-22	-16	-15	-18	-19	-15	-11	-14	-22
Side-lobe Level (dB)	-13	-14	-14	-13	-13	-15	-15	-14	-17

The overall performance of the beam-forming arrays is given in Table 7.6. As expected, as the operating frequency increases from 1.8 GHz to 2.6 GHz, the beam-pointing angle slightly moves to the boresight, the HPBW becomes narrower, and the realized gain is slightly increased. The side-lobe level is improved as the operating frequency increases, but a grating lobe rises. These effects are mainly due to the variation of the spacing in wavelengths between elements. The variation of the pattern across the band is not significant and the beam crossover level between adjacent beams is almost constant. The achieved crossover values for the 5- and 6-element arrays are -10 dB and -15 dB, which are exactly in line with the target. It is noted that the mutual coupling of the arrays has been included in all simulations. The patterns hardly change between 1.71 GHz and 1.8

GHz as well as between 2.6 GHz and 2.69 GHz.

7.5 Summary

In this chapter, a novel wideband beam-forming network and two multiple beam-forming arrays for LTE base stations have been presented and verified. The designs are described in detail and are directly applicable to other configurations covering the LTE band. A thorough analysis of a beam-forming network generating three beams has been given. The design of wideband components including quadrature couplers, phase shifters and power dividers are reported. Since the stripline techniques are used throughout the whole design, the overall loss of the circuit is extremely small. To implement the function of the beam-forming network, two different LTE sub-system configurations are designed and verified with antenna arrays composed of five and six ±45° linearly-polarized elements. Measurements have been conducted successfully on the beam-forming networks as well as on the two beam-forming arrays. The results show that the proposed design can increase system capacity by producing multiple beams in free space, which can be used in a wide range of multi-beam LTE base stations.

Chapter 8: Conclusion and Future Work

8.1 Conclusion

The rapid evolution of mobile communication systems and the increasingly crowded data traffic have placed higher requirements on the cellular base station antennas. Driven by that, this dissertation focuses on the innovation of design techniques associated with cellular base station antennas.

Firstly, the key concepts and general industrial requirements of the base station antennas are briefly introduced. The state-of-the-art techniques related to base station antennas are thoroughly reviewed. Following that, three research focuses are studied, including the developments of antenna elements, multi-band antenna arrays, and multi-beam antenna arrays. Novel techniques to improve antennas' performance characteristics and configurations are investigated for each research focus. Eight antenna elements, two multi-band antenna arrays, and two multi-beam antenna arrays have been theoretically analyzed, simulated and experimentally confirmed.

For the development of antenna elements, three configurations for the required ±45˚-polarized radiation are studied, including square-dipole-array, cross-dipole, and dual-dipole configurations. They are presented in Chapters 3, 4, and 5 respectively. Chapter 3 focuses on the design of square-dipole-array antennas. Theoretical study of the square-dipole-array radiators and design guideline of wideband matching networks are presented. Method of stabilizing radiation pattern and reducing beam squint is investigated. Two square-dipole-array elements are designed with excellent wideband radiation performance characteristics and simple and low-profile structures. The circuit theory model of the wideband matching network presented in this chapter provides valuable guidance for the general feed network design of current and future base station antennas. It has been used to design the antenna feed networks in the next several chapters.

Chapter 4 investigates the design principle and bandwidth enhancement technique of cross-dipole antennas. Firstly, a design strategy of the tightly-coupled cross-dipole antennas based on a simplified dipole array model is introduced, following which an optimized cross-dipole antenna with desired wideband performance is designed. Secondly, a novel technique to broaden the bandwidth of the cross-dipole antenna with a

compact size is presented. The bandwidths of the modified cross-dipole antennas are enhanced by more than 15% without increasing antenna size or damaging other performance characteristics.

Chapter 5 describes the planarization of wideband dual-LP antenna elements using dual-dipole radiators and discusses further integration of the structure. As the main challenge of realizing the planar configuration is the miniaturization of baluns, the circuit model of baluns is designed to facilitate their integration with radiators in a planar form. Two planarized dual-dipole antennas are realized with simple and compact structures and good wideband radiation performances. To demonstrate the advantage of planarized configuration in antenna integration, a dual-CP antenna is realized by integrating a wideband coupler into the planar dual-LP structure. The antenna is tested to have a wide well-matched bandwidth and stable radiation performance with a very compact structure.

All the designed antennas feature consistent wideband performances with simple and robust structures, thus being suitable to be used as base station antenna elements. Following the innovative designs of antenna elements, antenna arrays, which are more often used in practice, are studied. Multi-band antenna arrays and multi-beam antenna arrays are the two concentrations, and they are discussed in detail in Chapters 6 and 7, respectively.

For Multi-band antenna arrays, the research is focused on suppressing cross-band scattering between antennas operating at different bands. The method proposed is to modify LB radiators with chokes to reduce HB scattering current on the LB arms. Working principles and capabilities of reducing scattering currents of three different chokes are studied. They are implemented in the dual-band antenna array environment to verify their performances. Two dual-band antenna arrays operating at 3G and 4G bands, and 4G and 5G bands are constructed with choked LB elements. It is demonstrated that by choking the LB radiator, the cross-band scattering is suppressed, and radiation patterns are restored. Similar choking methods can be adopted to solve the cross-band scattering issue in other multi-band antenna systems.

For multi-beam antenna arrays, we focused on the bandwidth enhancement and beam stabilization. Two three-way beam-forming arrays for LTE base station applications are presented. In the designs, cross-dipole antennas with compact configuration, good matching capability, and stable radiation performances are chosen as array elements. The wideband beam-forming network is formed by Butler matrices using phase shifters and

hybrid couplers to provide correct phase increments and power levels for antenna elements. A thorough analysis of wideband components used in the beam-forming network is provided. The proposed design can increase system capacity by producing multiple beams in free space, which can be used in a wide range of multi-beam LTE base stations.

8.2 Future Work

Apart from the advanced antenna techniques and designs presented in this thesis, more efforts could be made to further improve performance characteristics of cellular base station antennas.

1. For antenna elements discussed in Chapter 3, 4, and 5, configurations could be further improved to lower antenna profile and reduce antenna size while preserving high performance characteristics. These properties reduce mutual coupling and ease antenna arrangement when applied in arrays, and also reduce wind load and tower load in practice.

2. For multi-band antenna arrays presented in Chapter 6, matching of the choked element across the entire 4G band is still very challenging. More efforts should be made on choking techniques or other techniques to have wideband scattering suppression capabilities with minimized influence on the antenna matching.

3. For multi-beam antenna arrays presented in Chapter 7, the beam forming network can be expanded to form more beams to further increase the system capability. Reconfigurable beam-forming networks to produce an adjustable number of beams would also be worth studying.

References

[1] Z. N. Chen and K. M. Luk, *Antennas for Base Stations in Wireless Communications*, McGraw-Hill, 2009.

[2] M. Hejnicki, A base station antenna for every application. CommScope. 2015. [Online]. Available: https://www.commscope.com/Blog/A-Base-Station-Antenna-for-Every-Application/.

[3] B. Abbas, et. al, Understanding the RF path. CommScope. 2018. [Online]. Available: https://www.commscope.com/Resources/eBooks/Understanding-the-RF-Path-eBook/.

[4] H. –W. Lai and K. –M. Luk, "Dual polarized patch antenna fed by meandering probes," *IEEE Trans. Antennas Propag.*, vol. 55, no. 9, pp. 2625-2627, Sep. 2017.

[5] K. S. Ryu and A. A. Kishk, "Wideband dual-polarized microstrip patch excited by hook shaped probes," *IEEE Trans. Antennas Propag.*, vol. 56, no. 12, pp. 3645-3649, Dec. 2008.

[6] F. Zhu, et. al, "Ultra-wideband dual-polarized patch antenna with four capacitively coupled feeds," *IEEE Trans. Antennas Propag.*, vol. 62, no. 5, pp. 2440-2449, May. 2014.

[7] K. M. Mak, X. Gao, and H. W. Lai, "Low cost dual polarized base station element for long term evolution," *IEEE Trans. Antennas Propag.*, vol. 62, no. 11, pp. 5861-5865, Nov. 2014.

[8] Y. Jin and Z. Du, "Broadband dual-polarized F-probe fed stacked patch antenna for base stations," *IEEE Antennas Wirel. Propag. Lett.*, vol. 14, pp. 1121-1124, 2015.

[9] Y. –X. Guo, K. –M. Luk, and K. –F. Lee, "Broadband dual polarization patch element for cellular-phone base stations," *IEEE Trans. Antennas Propag.*, vol. 50, no. 2, pp. 251-253, Feb. 2002.

[10] S. Gao and A. Sambell, "Dual-polarized broad-band microstrip antennas fed by proximity coupling," *IEEE Trans. Antennas Propag.*, vol. 53, no. 1, pp. 526-530, Jan. 2005.

[11] K. Ghorbani and R. B. Waterhouse, "Dual polarized wide-band aperture

stacked patch antennas," *IEEE Trans. Antennas Propag*., vol. 52, no. 8, pp. 2171-2174, Aug. 2004.

[12] M. Barba, "A high-isolation, wideband and dual-linear polarization patch antenna," *IEEE Trans. Antennas Propag*., vol. 56, no. 5, pp. 1472-1476, May 2008.

[13] D. Su, J. J. Qian, H. Yang, and D. Fu, "A novel broadband polarization diversity antenna using a cross-pair of folded dipoles," *IEEE Antennas Wirel. Propag. Lett*., vol. 4, pp. 433–435, 2005.

[14] D. Su, D. Fu, T. N. C. Wang, and H. Yang, "Broadband polarization diversity base station antenna for 3G communication system," *J. Electromagn. Waves Appl*., vol. 22, no. 4, pp. 493–500, 2008.

[15] Q. X. Chu, D. L. Wen, and Y. Luo, "A broadband ±45° dual-polarized antenna with Y-shaped feeding lines," *IEEE Trans. Antennas Propag*., vol. 63, no. 2, pp. 483–490, Feb. 2015.

[16] H. Huang, Y. Liu, and S. Gong, "A broadband dual-polarized base station antenna with sturdy construction," *IEEE Antennas Wirel. Propag. Lett*., vol. 16, pp. 665–668, 2017.

[17] Y. Cui, R. Li, and H. Fu, "A broadband dual-polarized planar antenna for 2G/3G/LTE base stations," *IEEE Trans. Antennas Propag*., vol. 62, no. 9, pp. 4836–4840, Sept. 2014.

[18] Z. Bao, X. Zong, Z. Nie, and S. Yang, "Design and discussion of a broadband cross-dipole with high isolation and low cross-polarisation utilising strong mutual coupling," *IET Microw. Antennas Propag*., vol. 8, Iss. 5, pp. 315–322, March 2014.

[19] Y. Gou, S. Yang, J. Li, and Z. Nie, "A compact dual-polarized printed dipole antenna with high isolation for wideband base station applications," *IEEE Trans. Antennas Propag*., vol. 62, no. 8, pp. 4392– 4395, Aug. 2014.

[20] Z. Bao, Z. Nie, and X. Zong, "A novel broadband dual-polarization antenna utilizing strong mutual coupling," *IEEE Trans. Antennas Propag*., vol. 62, no. 1, pp. 450–454, Jan. 2014.

[21] D. L. Wen, D. Z. Zheng, and Q. X. Chu, "A wideband differentially fed dual-polarized antenna with stable radiation pattern for base stations," *IEEE Trans. Antennas Propag*., vol. 65, no. 5, pp. 2248-2255, May 2017.

[22] D. Z. Zheng and Q. X. Chu, "A multimode wideband ±45° dual-polarized antenna with embedded loops," *IEEE Antennas Wirel. Propag. Lett*., vol. 16, pp. 633-636, 2017.

[23] D. Z. Zheng and Q. X. Chu, "A wideband dual-polarized antenna with two independently controllable resonant modes and its array for base-station applications," *IEEE Antennas Wirel. Propag. Lett*., vol. 16, pp. 2014-2017, 2017.

[24] L. Wu, R. Li, Y. Qin, and Y. Cui, "Bandwidth enhanced broadband dual-polarized antennas for 2G/3G/4G and IMT services," *IEEE Antennas Wirel. Propag. Lett*., Early Access, 2018.

[25] Y. Cui, L. Wu, and R. Li, "Bandwidth enhancement of a broadband dual-polarized antenna for 2G/3G/4G and IMT base stations," *IEEE Trans. Antennas Propag*., Early Access, 2018.

[26] Y. Liu, H. Yi, F. W. Wang and S. X. Gong, "A novel miniaturized broadband dual-polarized dipole antenna for base station," *IEEE Antennas Wirel. Propag. Lett*., vol. 12, pp. 1335–1338, 2013.

[27] Y. Luo, Q.-X. Chu, and D.-L. Wen, "A plus/minus 45 degree dualpolarized base-station antenna with enhanced cross-polarization discrimination via addition of four parasitic elements placed in a square contour," *IEEE Trans. Antennas Propag*., vol. 64, no. 4, pp. 1514–1519, Apr. 2016.

[28] Y. Luo, Q. X. Chu and J. Bornemann, "Enhancing cross-polarisation discrimination or axial ratio beamwidth of diagonally dual or circularly polarised base station antennas by using vertical parasitic elements," *IET Microw. Antennas Propag*., vol. 11, Iss. 9, pp. 1190-1196, June 2017.

[29] Y. Luo, Q. -X. Chu, and J. Bornemann, "Enhancing cross-polarisation discrimination or axial ratio beamwidth of diagonally dual or circularly polarised base station antennas by using vertical parasitic elements," *IET Microw. Antennas Propag*., vol. 11, Iss. 9, pp. 1190-1196, July 2017.

[30] K. M. Luk and H. Wong, "A new wideband unidirectional antenna element," *Int. J. Microw. Opt. Technol*., vol. 1, no. 1, pp. 35-44, Jun. 2006.

[31] B. Q. Wu and K. M. Luk, "A Broadband Dual-Polarized Magneto-Electric Dipole Antenna With Simple Feeds," *IEEE Antennas Wirel. Propag. Lett*., vol. 8, pp. 60–63, 2009.

[32] L. Siu, H. Wong, and K. M. Luk, "A dual-polarized magneto-electric dipole with dielectric loading," *IEEE Trans. Antennas Propag*., vol. 57, no. 3, pp. 616–623, Mar. 2009.

[33] M. Li and K. M. Luk, "Wideband magnetoelectric dipole antennas with dual polarization and circular polarization," *IEEE Antennas Propag. Mag*., vol. 57, no. 1, pp. 110–119, Feb. 2015.

[34] S. G. Zhou, Z. H. Peng, G. L. Huang, and C. Y. D. Sim, "Design of a novel wideband and dual-polarized magnetoelectric dipole antenna," *IEEE Trans. Antennas Propog*., vol. 65, no. 5, May 2017.

[35] Q. Xue, S. W. Liao, and J. H. Xu, "A differentially-driven dualpolarized magneto-electric dipole antenna," *IEEE Trans. Antennas Propag*., vol. 61, no. 1, pp. 425–430, Jan. 2013.

[36] F. Wu and K. M. Luk, "A reconfigurable magneto-electric dipole antenna using bent cross-dipole feed for polarization diversity," *IEEE Antennas Wirel. Propag. Lett*., vol. 16, pp. 412–415, 2017.

[37] F. Wu and K. M. Luk, "Single-port reconfigurable magneto-electric dipole antenna with quad-polarization diversity," *IEEE Trans. Antennas Propag*., vol. 65, no. 5, pp. 2289-2296, May. 2017.

[38] Y. H. Huang, Q. Wu, and Q. Z. Liu, "Broadband dual-polarized antenna with high isolation for wireless communication," *Electron. Lett*., vol. 45, no. 14, pp. 714–715, July 2009.

[39] D. L. Wen, D. Z. Zheng, and Q. X. Chu, "A dual-polarized planar antenna using four folded dipoles and its array for base stations," *IEEE Trans. Antennas Propag*., vol. 64, no. 12, pp. 5536–5542, Dec. 2016.

[40] S. G. Zhou, P. K. Tan, and T. H. Chio, "Low-profile, wideband dual-polarized antenna with high isolation and low cross polarization," *IEEE Antennas Wirel. Propag. Lett*., vol. 11, pp. 1032–1035, 2012.

[41] Y. Dong and T. Itoh, "Miniaturized cavity-backed dual-polarized slot antenna," *Proc. Antenna and Propag. Society Int. Symp*., USA, 2012.

[42] W. W. Li, C. Wang, Y. Q. Lai and J. H. Zhou, "A compact dual-polarized cavity-backed annular slot antenna for indoor MIMO systems," *Microw. Opt. Tech. Lett*., vol. 57, no. 2, pp. 384-388, 2015.

[43] W. W. Li, X. J. Chen, J. H. Zhou and B. Q. You, "Dual-polarised cavity-backed annular slot antenna of compact structure," *Electronics Lett*. vol. 50, no. 23, pp. 1655-1656, 2014.

[44] Q. Zhang, D. Jiang, W. Wu, "An integrated diversity antenna based on dual-feed cavity-backed slot," *IEEE Antennas Wirel. Propag. Lett*., vol. 13, pp. 301-304, 2014.

[45] R. C. Paryani, P. F. Wahid and N. Behdad, "A wideband, dualpolarized, substrate-integrated cavity-backed slot antenna," *IEEE Antennas Wirel. Propag. Lett*., vol. 9, pp. 645-648, 2010.

[46] Y. Cui, Y. Niu, C. Qi, and R. Li, "A broadband flush-mountable dual-polarized dual-slot antenna," *IEEE Antennas Wirel. Propag. Lett*., vol. 17, no. 3, pp. 501-504, 2018.

[47] Y. Cui, Y. Niu, Y. Qin, and R. Li, "A new high-isolation broadband flush-mountable dual-polarized antenna," *IEEE Trans. Antennas Propag*., vol. 66, no. 12, pp. 7342-7347, Aug. 2018

[48] Y. Chen, R. G. Vaughan, "Crossed slot antenna with simple feed for high polarization isolation," *Proc. IEEE Antennas Propag. Soc. Int. Symp. (APSURSI)*, USA, Jul. 2013, pp. 650–651.

[49] S. W. Wong, G. H. Sun, L. Zhu and Q. X. Chu, "Broadband Dual-Polarization and Stable-Beamwidth Slot Antenna Fed by U-Shape Microstrip Line," *IEEE Trans. Antennas Propag*., vol. 64, no. 10, pp. 4477-4481, Oct. 2016.

[50] R. Lian, Z. Wang, Y. Yin, J. Wu and X. Song, "Design of a low-profile dual-polarized stepped slot antenna array for base station," *IEEE Antennas Wirel. Propag. Lett*., vol. 15, no. , pp. 362-365, 2016.

[51] R. Wu and Q. -X. Chu, "A wideband dual-polarized antenna for LTE700/GSM850/GSM900 applications," *IEEE Antennas Wirel. Propag. Lett*., vol. 16, pp. 2098-2101, 2017.

[52] Y. H. Cui, R. L. Li, P. Wang, "A novel broadband planar antenna for 2G/3G/LTE base stations," *IEEE Trans. Antennas Propag*., vol. 61, no. 5, pp. 2767-2774, May 2013.

[53] Y. Cui, X. Gao, and R. Li, "A broadband differential fed dual-polarized planar antenna," *IEEE Trans. Antennas Propog*., vol. 65, iss. 6, pp. 3231-

3234, June 2017.

[54] Y. Cui, X. Gao, H. Fu, Q. X. Chu and R. Li, "Broadband Dual-Polarized Dual-Dipole Planar Antennas: Analysis, Design, and Application for Base Stations," *IEEE Antennas Propag. Mag*, vol. 59, no. 6, pp. 77-87, Dec. 2017.

[55] L. H. Wen, S. Gao, Q. Luo, C. X. Mao, W. Hu, Y. Yin, Y. Z, and Q. Wang, "Compact dual-polarized shared-dipole antennas for base station applications." *IEEE Trans. Antennas Propag*., Early access, 2018.

[56] F. Tefiku and C. A. Grimes, "Design of broad-band and dual-band antennas comprised of series-fed printed-strip dipole pairs," *IEEE Trans. Antennas Propag*., vol. 48, no. 6, pp. 895 - 900, Jun. 2000.

[57] W. X. An, H. Wong, K. L. Lau, S. F. Li and Q. Xue, "Design of broadband dual-band dipole for base station antenna," *IEEE Trans. Antennas Propag*., vol. 60, no. 3, pp. 1592-1595, Mar. 2012.

[58] Alieldin, Y. Huang, and M. Stanley, "Design of dual-band dual-polarized swastika-shaped antenna for mobile communication base stations," *12th EuCAP*, UK, 2018.

[59] X. Liu, S. He, H. Zhou, J. Xie and H. Wang, "A novel low-profile, dual-band, dual-polarization broadband array antenna for 2G/3G base station," *Proc. IET Int. Conf. IET Wireless, Mobile Multimedia Netw. (ICWMNN),* Hangzhou, China, 2006.

[60] S. Chen and K. M. Luk, "High performance dual-band dual-polarized magneto-electric dipole base station antenna," *Proc. Asia-Pacific Microw. Conf. (APMC)*, Japan, 2014.

[61] Y. He, Z. Pan, X. Cheng, Y. He, J. Qiao and M. M. Tentzeris, "A novel dual-band, dual-polarized, miniaturized and low-profile base station antenna," *IEEE Trans. Antennas Propag*., vol. 63, no. 12, pp. 5399-5408, Dec. 2015.

[62] H. Huang, Y. Liu and S. Gong, "A novel dual-broadband and dual-polarized antenna for 2G/3G/LTE base stations," *IEEE Trans. Antennas Propag*., vol. 64, no. 9, pp. 4113-4118, Sept. 2016.

[63] H. Huang, Y. Liu and S. Gong, "A dual-broadband, dual-polarized base station antenna for 2G/3G/4G applications," *IEEE Antennas Wireless Propag. lett*., vol. 16, pp. 1111-1114, 2017.

[64] G. Cui, S. –G. Zhou, G. Zhao, and S. –X. Gong, “A compact dual-band dual-polarized antenna for base station application,” *Prog. Electromagn. Res. C*, vol. 64, pp. 61-70, 2016.

[65] Y. He, W. Tian and L. Zhang, “A novel dual-broadband dual-polarized electrical downtilt base station antenna for 2G/3G applications,” *IEEE Access*, vol. 5, pp. 15241-15249, 2017.

[66] Y. Liu, S. Wang, N. Li, J. Wang, and J. Zhao, “A compact dual-band dual-polarized antenna with filtering structures for sub-6 GHz base station applications,” *IEEE Antennas Wirel. Propag. Lett*., vol. 17, iss. 10, pp. 1111-1114, Oct. 2018.

[67] Y. –B. Jung and S. –Y. Eom, “A compact multiband and dual-polarized mobile base-station antenna using optimal array structure,” *Int. J. Antennas Propag*., 2015.

[68] L. Y. Nie, X. Q. Lin, Y. J. Chen, J. Zhang, B. Wang, Z. Q. Yang, and Y. Fan, “A low-profile coplanar dual-polarized and dual-band base station antenna array,” *IEEE Trans. Antennas Propag*., early access, 2018.

[69] B. Jones, O. Isik, and C. Shang, “Dual-band interspersed cellular basestation antennas,” EP. Patent 2 769 476 B1, Dec. 24, 2012.

[70] Y. Zhang, X. Y. Zhang, L. H. Ye and Y. M. Pan, “Dual-band base station array using filtering antenna elements for mutual coupling suppression,” *IEEE Trans. Antennas Propag*, vol. 64, no. 8, pp. 3423-3430, Aug. 2016.

[71] M. Li, Q. Li, B. Wang, C. Zhou, and S. Cheung, “A miniaturized dual-band base station array antenna using band notch dipole antenna elements and AMC reflectors,” *IEEE Trans. Antennas Propag*, vol. 66, no. 6, pp. 3189-3194, Jun. 2018.

[72] X. Y. Zhang, D. Xue, L. H. Ye, Y. M. Pan and Y. Zhang, “Compact dual-band dual-polarized interleaved two-beam array with stable radiation pattern based on filtering elements,” *IEEE Trans. Antennas Propag*, vol. 65, no. 9, pp. 4566-4575, Sept. 2017.

[73] X. Tang, K. Mouthaan and J. C. Coetzee, “Dual-band decoupling and matching network design for very closely spaced antennas,” *Proc. Eur. Microw. Conf*, Amsterdam, 2012.

[74] J. Weber, C. Volmer, K. Blau, R. Stephan and M. A. Hein, “Miniaturized

antenna arrays using decoupling networks with realistic elements," *IEEE Trans. Microw. Theory Tech*, vol. 54, no. 6, pp. 2733-2740, June 2006.

[75] L. Zhao and K. L. Wu, "A dual-band coupled resonator decoupling network for two coupled antennas," *IEEE Trans. Antennas Propag*, vol. 63, no. 7, pp. 2843-2850, July 2015.

[76] Butler, J. and R. Lowe, "Beam-forming matrix simplifies design of electrically scanned antennas," *IEEE Trans. Electron. Devices*, 170–173, 1961.

[77] H Hayashi, D A. Hitko, and C. G. Sodini, "Four-Element Planar Butler Matrix Using Half-Wavelength Open Stubs," *IEEE Microw. Wireless Compon. Lett*., vol. 12, no. 3, pp. 73-75, Mar. 2002.

[78] M. Bona, L. Manholm, I. P. Starski, and B. Svensson, "Low-loss compact Butler matrix for a microstrip antenna," *IEEE Trans. Microw. Theory Tech*, vol. 50, no. 11, pp. 2069-2075, Sep. 2002.

[79] M. Nedil, T.-A. Denidni, and L. Talbi, "Novel butler matrix using CPW multilayer technology," *IEEE Trans. Microw. Theory Tech*., vol. 54, no. 1, pp. 499–507, Jan. 2006.

[80] S. Gruszczynski and K.Wincza, "Broadband 4×4 Butler matrices as a connection of symmetrical multisection coupled-line 3-dB directional couplers and phase correction networks," *IEEE Trans.Microw. Theory Tech*., vol. 57, no. 1, pp. 1–9, Jan. 2009.

[81] S. Gruszczynski, K. Wincza, and K. Sachse, "Compact broadband Butler matrix in multilayer technology for integrated multibeam antennas," *Electron. Lett*., vol. 43, no. 11, pp. 635–636, May 2007.

[82] L. M. Abdelghani, T. A. Denidni, and M. Nedil, "Ultra-broadband 4×4 compact Butler matrix using multilayer directional couplers and phase shifters," *IEEE MTT-S Int. Dig*., Jun. 2012, pp. 1–3.

[83] Mohamed Ali, N. J. G. Fonseca, F. Coccetti, and H. Aubert, "Design and implementation of two-layer compact wideband Butler matrices in SIW technology for Ku-Band applications," *IEEE Trans. Antennas Propag*., vol. 59, no. 2, pp. 503–512, Feb. 2011.

[84] M. Martir, I. M. Fernandez, and A. O. Monux, "Wideband slot-coupled

butler matrix," *IEEE Microw. Wireless Compon. Lett*., vol. 24, no. 12, pp. 848–850, Dec. 2014.

[85] Collado, A. Grau, and F. De Flaviis, "Dual-band Butler matrix for WLAN systems," *Proc. IEEE MTT-S Int. Microw. Symp*., 2005, vol. 4, pp. 2247–2250.

[86] J. K. Lee and K. Chang, "Dual-band switched beam array fed by dual-band Butler matrix," *Electron. Lett*., vol. 47, no. 21, pp. 1164–1165, Oct. 2011.

[87] H. Ren, J. Shao, R. Zhou, B. Arigong, and H. Zhang, "Compact phased array antenna system based on dual-band operations," *Microw. Opt. Technol. Lett*., vol. 56, no. 6, pp. 1391–1396, Jun. 2014.

[88] K. Wincza, S. Gruszczynski, and K. Sachse, "Integrated four-beam dualband antenna array fed by broadband Butler matrix," *Electron. Lett*., vol. 43, no. 1, pp. 7–8, Jan. 2007.

[89] K. Wincza, K. Staszek, I. Slomian, and S. Gruszczynski, "Scalable multibeam antenna arrays fed by dual-band modified Butler matrices," *IEEE Trans. Antennas Propag.,* vol. 64, no. 4, pp. 1287–1297, Apr. 2016.

[90] T. N. Kaifas and J. N. Sahalos, "On the design of a single-layer wideband Butler matrix for switched-beam UMTS system applications," *IEEE Antennas Propag. Mag*., vol. 48, no. 6, pp. 193–204, Dec. 2006.

[91] Corona and M. J. Lancaster, "A High-Temperature Superconducting Butler Matrix," *IEEE Trans. Appl. Supercond*, vol. 13, no. 4, December 2003, pp. 3867-3872.

[92] W. Wang, T. G. Ma, and C. F. Yang, "A new planar artificial transmission line and its application to a miniaturized Butler matrix," *IEEE Trans. Microw. Theory Tech*., vol. 55, no. 12, pp. 2792–2801, Dec.2007.

[93] H. X. Xu, G. M. Wang, and X. Wang, "Compact butler matrix using composite right/left handed transmission line," *Electron. Lett*., vol. 47, pp. 1081–1082, 2011.

[94] Y. S. Jeong and T.W. Kim, "Design and analysis of swapped port coupler and its application in a miniaturized Butler matrix," *IEEE Trans. Microw. Theory Techn*., vol. 58, no. 4, pp. 764–770, Apr. 2010.

[95] E. Gandini, M. Ettorre, R. Sauleau, and A. Grbic, "A lumped-element unit

cell for beam-forming networks and its application to a miniaturized Butler matrix," *IEEE Transactions on Microwave Theory and Techniques*, vol. 61, no. 4, pp. 1477-1487, 2013.

[96] K. Ding, X. Fang, Y. Wang and A. Chen, "Printed dual-layer three way directional coupler utilized as 3×3 beamforming network for orthogonal three-beam antenna array," *IEEE Antennas and Wireless Propagation Letters*, vol.13, pp.911-914, 2014.

[97] H. Nachouane, A. Najid, A. Tribak, and F. Riouch, "Wideband 3×4 Butler matrix using Wilkinson divider for MIMO applications," *International Conference on Next Generation Networks and Services (NGNS)*, pp. 101-105, 2014.

[98] J. P. Wang and W.-J. Chen, "Two-layer three beam generation matrix for broadband beamforming with microstrip," *IEEE International Symposium on Antennas and Propagation (AP-S)*, July 2017.

[99] C. A. Balanis, *Antenna Theory: Analysis and Design*, 3rd ed. Wiley, 2005.

[100] R. Xu, J. –Y. Li, J. Liu, S. –G. Zhou, k. Wei, and Z. –J. Xing, "A simple design of compact dual-wideband square slot antenna with dual-sense circularly polarized radiation for WLAN/Wi-Fi Communications," *IEEE Trans. Antennas Propag*., Early access, June 2018.

[101] Q. Luo, S. Guo, and L. Zhang, "Wideband multilayer dual circularly-polarised antenna for array application," *Electron. Lett*., vol. 51, no. 25, pp. 2087-2089, Dec. 2015.

[102] J. Wu, Y. J. Cheng, H. B. Wang, Y. C. Zhong, D. Ma, and Y. Fan, "A wideband dual circularly polarized full-corporate waveguide array antenna fed by triple-resonant cavities," *IEEE Trans. Antennas Propag*.,vol. 65, no. 4, pp. 2135-2139, Apr. 2017.

[103] S. –G. Zhou, G. –L. Huang, and T. –H. Chio, "A lightweight, wideband, dual-circularly-polarized waveguide cavity array designed with direct metal laser sintering considerations," *IEEE Trans. Antennas Propag*., vol. 66, no. 2, pp. 675-682, Feb. 2018.

[104] Y. Cai, Y. Zhang, Z. Qian, W. Cao, and S. Shi, "Compact wideband dual circularly polarized substrate integrated waveguide horn antenna," *IEEE Trans. Antennas Propag*., vol. 64, no. 7, pp. 3184-3189, Apr. 2016.

[105] R. Sammeta, and D. S. Filipovic, "Reduced size planar dual-polarized log-periodic antenna for bidirectional high power transmit and receive applications," *IEEE Trans. Antennas Propag*., vol. 62, no. 11, pp. 5453-5461, Nov. 2014.

[106] S. Zheng, et al. "A broadband dual circularly polarized conical four-arm sinuous antenna," *IEEE Trans. Antennas Propag*., vol. 66, no. 1, pp. 71-79, Jan. 2018.

[107] A. Greenberg, "Simple trap construction for the multiband antenna," *QST*, Oct. 1956.

[108] D. L. Smith, "The trap-loaded cylindrical antenna," *IEEE Trans. Antennas Propag*., vol. AP-23, no. 1, pp. 20-27, Jan. 1975.

[109] M. Pozar, *Microwave Engineering*, 2nd ed. Wiley, 1997.

[110] K. C. Gupta, R. Garg, I. Bahl, and P. Bhartia, *Microstrip Lines and Slotlines*, 2nd ed. Artech House, 1996.